WAVE-INDUCED SEDIMENT TRANSPORT ON AN ESTUARINE INTERTIDAL FLAT

Tony J. Dolphin

A thesis submitted in fulfilment of
the requirements for
the Degree of
Doctor of Philosophy

The University of Waikato
Te Whare Wānanga o Waikato

March 2004

"Well, George, we knocked the bastard off"

Sir Edmund Hillary

May 29, 1953

This thesis was submitted on May 29th 2003,
the 50th anniversary of Hillary's successful ascent of
Mt Everest

ABSTRACT

Waves and tides are the primary processes responsible for sediment entrainment on estuarine intertidal flats, however a detailed understanding of the temporal and spatial variability of wave processes, and the way in which these control estuarine sediment transport, is lacking. The aim of this thesis is to redress this deficiency.

Wave, current and suspended-sediment meters were deployed along a 1600-m-long cross-shore transect of the Wiroa Island intertidal flat (Manukau Harbour, New Zealand) for a period of ten weeks. Additional data were obtained by four further experiments: a pilot experiment in the shallow estuarine fringes; field experiments to test an antifouling device and to develop a way of correcting data from biofouled optical backscatter sensors; field trials of pressure and velocity sensors under estuarine and open-coast waves; and experiments to test whether optical and acoustic backscatter sensors could be used to separately measure the concentration of suspended silts and suspended sands.

Comparison of pressure and velocity data revealed an inconsistency in some wave data from the Wiroa flat and in Green and MacDonald's (2001) data from the Okura estuary: wave amplitudes estimated from pressure were significantly smaller (factor of 2–50) than corresponding amplitudes estimated from velocity data, and there was a phase lag (45–90°) between the pressure and velocity signals. The inconsistency could be interpreted as evidence of standing waves, however, data from some instruments do not support this. Tests of linear theory and sensor performance in estuarine and open-coast settings, the effect of sensor orientation, and comparisons with observed sand entrainment, suggest that the inconsistency is due to imperfect pressure-sensor frequency response.

Waves vary systematically in response to changes in fetch, which in turn are associated with the submergence and emergence of intertidal banks during the rise and fall of the tide. For a given wind, growth in fetch on a rising tide equates to growth in wave height and period. Variation in the bed-orbital speed, $U_{w,bed}$, is due to different combinations of wave height (H), period (T) and depth ($\bar{h}$). When the depth is large, bed-orbital speeds are small due to poor penetration of wave motions through the water column. On the other hand, when depth is smaller, or when period is longer, penetration is more

effective and bed-orbital speeds are larger as a result. Consequently, in some instances, $U_{w,bed}$ is largest at high tide (when fetch, H and T are large) and smaller near the start and finish of the inundation. At other times, $U_{w,bed}$ is smallest around high tide (when $\bar{h}$ is too large for wave orbitals to penetrate effectively to the bed). Depth-limited wave breaking was not observed, but whitecaps were common.

Sand and silt suspensions were switched on and off by wave activity (when the pure-wave skin friction, θ'_w, exceeded the sand threshold, $\theta_{cr,sand}$), but not by tidal currents. Silt held in the local bed was released when sand was entrained, but there was no obvious relationship between the silt reference concentration and θ'_w because a component of the silt was advected from elsewhere in the estuary and silt in the intertidal flat is supply-limited (<2% abundance). Sand reference concentration, C_0, plots in three distinct clusters against θ'_w, which presumably correspond to rippled, transitional and flat beds. The three clusters collapsed onto a single line when flow contraction over ripple crests was accounted for, as observed by Nielsen (1986). The transitional data have not been previously identified and may represent the co-existence of rippled and flat beds. Suspended-silt concentrations were vertically homogeneous, but suspended-sand concentrations follow the simple exponential profile model (Nielsen, 1984), where the mixing length is controlled by ripple height, settling velocity and bed-orbital speed.

Silt concentrations were highest in the edge of estuarine water body known as the turbid fringe (Green *et al.*, 1997). Enhanced settling and onshore-directed wave-orbital asymmetry are thought to aid silt deposition observed on the upper flats. Patterns in sand transport are complex because the primary drivers – tidal currents and the wave-induced concentration field – are independent of each other and both vary with location across the flat and in time through the tidal cycle. This was explored by schematic modelling, which showed that combinations of different tidal regimes and fetch types produce different spatial and temporal patterns in current and concentration fields, and therefore in sediment transport. The field data showed drainage currents can be responsible for offshore transport, while asymmetry in wave-orbital motions was a means for onshore sand transport.

Spatial patterns in processes align with sedimentary and geomorphic features. Silts were found to be abundant on the channel margins, where $\theta'_w < \theta_{cr,sand}$. The intermittently inundated region near the top of the flat has the lowest slopes, and is a potential deposition zone for sands transported to the tidal edge and stranded there during the receding ebb tide. Patterns in time-integrated work due to waves, W_w, also correspond to changes in slope: slope was lowest on the upper flat where W_w was greatest, but steepened where W_w declined as a result of high tidal-translation rates across the middle flats.

Allen's (1971) model describes spatial trends in waves and tides across intertidal flats; wave activity at the bed increases at higher elevations while tidal currents decrease. The Wiroa data reveal a more complex situation: $U_{w,bed}$ and W_w are controlled by variations in wind speed and direction, fetch length, wave height, wave period, penetration, and the tidal translation rate. Thus, while Allen established a paradigm that implies zonation in transport processes, spatial and temporal interactions between waves and tidal currents can create both more subtle and more profoundly different patterns.

ACKNOWLEDGEMENTS

I would like to say a huge thanks to Dr Malcolm Green, for encouraging me to take up the PhD challenge. Mal is an excellent mentor, guide and a great friend. I am very grateful for the opportunity to have worked with him, and to have learnt so much from him.

Thanks to the whole Coastal Marine Group. Prof. Terry Healy was always one to urge me forward, thanks Terry. Thanks also Dr Kerry Black, and to Dr Willem de Lange for taking the helm when Kerry resigned. A special thanks to Dr Karin Bryan, whose assistance with Chapter 3 and the standing wave possibility were invaluable. Also to Dr Richard Gorman (aka The Wizard) for sharing his vast knowledge of Matlab and for sharing the results of his SWAN modelling of Manukau Harbour.

Thanks to the Department of Earth Science for funding this PhD by way of an Assistant Lectureship. The author is also the recipient of a University of Waikato Doctoral Scholarship, for which he is grateful. Also thanks to NIWA, for providing extensive logistic support from field equipment and vehicles to office space and staff time.

To the field crew: Hamish, Nardia, Jason, Jens, Bronwen, Rachael, Paul and Peter in the student category; and Ian, Iain, John H, Rod, Andy, Ron, John R in the field technicians category. Special thanks to Ian Blair for helping to get me through the initial deployment and to Claire Hamilton for being fabulously well organised with the hundreds of samples we gathered. John Radford designed the proto-type OBS brushes.

Thanks to Amy Fuller who helped me find the courage to start this journey, and throughout has provided encouragement and kind words. Amy also made an excellent field assistant.

Thanks to my grammar girls, Janice and Janey…oh all right, and you Mal. And to Iain MacDonald, who taught me a thing or two about Matlab.

"Sad sorry souls studying inside on sunny Saturdays and Sundays": To the PhD Club! Joanna, Vonda and Alf. I salute you – this is our year! It's time to retire the club, so, in one man's famous words 'Get back to work!'.

Scott, Sharon, Sonia, Michael, Pip, Juan y Rosita, The Hobbits, Iain, Mal, Janice, Geoff, Andrew, Lisa, Richard, Nigel, Karen, Harley, Andrew, Kerry, Maurice, Terry, Aslan, Ed, Catherine, Mark, Narelle, Nicole – great friends are what makes it all worth while, and you are. Thanks also to Scully, Maurice, Caramel, Nat and Moke for the cuddles.

A very special thanks to Jane Havemann. Janey, your support and love for me through some tough times has been unwavering. I wouldn't have got through without your thoughtful words and hugs and your uncanny ability to make me laugh when Mr Grumpy was out. You relax me :) You make good diagrams too. LUMTUCI YFA

Mum and Kylee, you guys were always there and it means so much to me, now more than ever.

As it is now 5.27 am, I apologise for any poor grammar in my acknowledgements, and also to anyone I have forgotten.

TABLE OF CONTENTS

TABLE OF FIGURES

TABLE OF TABLES

NOTATION

Symbology

A_0	ABS system constant
a_s	sediment particle radius
a_w	wave-orbital radius (otherwise known as the wave-orbital semi-excursion distance)
B	ABS beam spreading
C	sediment concentration (mg/L)
C_{h-U_w}	coherence between h and U_w
c	speed of sound
d_s	sediment particle diameter
d_w	wave-orbital diameter (otherwise known as the wave-orbital excursion distance)
D_*	dimensionless grain diameter
$D_{\theta'_w > \theta_{cr}}$	duration for which $\theta'_w > \theta_{cr}$
g	acceleration due to gravity (9.81 m/s)
G	sensor gain
f	frequency
f'_w	skin-friction wave friction factor
$h(t)$	"hydrostatic depth" time-series
$\overline{h}$	mean water depth (m)
H_{max}	Maximum wave height
H_{rms}	root-mean-square wave height
H_s	significant wave height
H_z	zero up-crossing wave height
I	Irribarren number
k	wavenumber
kh	relative water depth
k_{ABS}	acoustic wavenumber
k_s	hydraulic roughness
$k_{s,N}$	Nikuradse roughness
K_s	shoaling coefficient
m_n	nth moment of $S_\eta(\omega)$
l_s	mixing length
N	number of samples/data points
O	sensor offset
p	pressure (Pa)
p_A	atmospheric pressure (Pa)
$\langle p \rangle^2$	ABS backscattered pressure
q	cross-shore sand flux
Q	sediment flux
R	sensor response (V)
r	range from transducer
r^2	correlation coefficient
s	ρ_s / ρ_f
$S(\omega)$	power spectrum
$S^2_{a_s}$	ABS backscatter efficiency
S	sensitivity (1/G)

$\overline{S}$	wave-orbital speed asymmetry
t	time
T_z	zero upcrossing wave period
$\overline{T}$	mean spectral wave period
T_p	peak spectral wave period
T_s	significant wave period
x, y	cartesian coordinates/axes
u_{CM}	velocity component measured on a current meter's x axis
u'_*	skin-friction friction velocity
$\overline{U}$	mean current
U_3	3rd moment of wave orbital speed
U_{rms}	root-mean-square wave orbital velocity
U_s	significant wave orbital speed
$U_w(t)$	time-series of wave orbital speed
$U_{w,peak}$	peak wave orbital speed during a wave cycle
Ur	Ursell parameter
Ur_{crit}	critical Ursell parameter
v_{CM}	velocity component measured on a current meter's y axis
ν	spectral width parameter
ν	kinematic viscosity
V	current speed
$\vec{V}$	velocity vector = $[V, \phi]$
V_E	velocity component along east-west axis
V_N	velocity component along north-south axis
w	vertical velocity component
w_s	settling velocity of sediment
w_{silt}	settling velocity of silt
w_{sand}	settling velocity of sand
W_w	work done by waves
W_c	work done by the mean current
X	constant in eqn 5.20
z	elevation with respect to the bed
z_p	elevation above the bed of a pressure sensor
z_u	elevation above the bed of a velocity sensor
z_0	roughness length
Φ_w	wave propagation axis
$\Gamma_h(\omega)$	frequency dependent depth attenuation factor of pressure
$\Gamma_{Uw}(\omega)$	frequency dependent depth attenuation factor of wave orbital motion
α	ABS attenuation coefficient
β	sea bed gradient
χ	1/sinh(kh)
χ^*	1/cosh(kh)
χ^2	chi-square statistic
$\chi(f)_{AB}$	co-spectrum of A and B at frequency f
χ	attenuation of U_w at $z_u = 0$
ε_b	bed load efficiency factor (0.21)
ε_s	sediment diffusivity (eddy diffusion coefficient for sediment particles)
ε_m	eddy viscosity for momentum

ϕ	current direction (wrt true North)
ϕ_w	direction of wave propagation
γ	wave height to depth ratio (H/h)
$\eta(t)$	time-series of sea surface elevation
η_{min}	minimum sea-surface elevation during a single wave cycle
η_{max}	maxmum sea-surface elevation during a single wave cycle
η_r	ripple height
η_{bar}	bar height
φ_{h-U_w}	phase between h and U_w
φ	angle of repose
$\varphi_{U_w-\bar{U}}$	acute angle between wave direction and current direction
κ	von Karman constant (0.41)
λ	wavelength
λ_r	ripple wavelength
λ_{bar}	bar wavelength
θ_{cr}	critical Shields parameter
θ'_c	dimensionless skin friction due to currents
θ'_w	dimensionless skin friction due to waves
$\theta'_{w,r}$	enhanced skin friction due to flow contraction over ripple crests
ρ_f	fluid density
ρ_s	sediment density
$\bar{v}$	on-offshore component of the time-averaged tidal current
ω	wave radian frequency
ω_L	low radian frequency cut off
ω_H	high radian frequency cut off
ψ	mobility number
$\Diamond$	bearing of the lubber line

Subscripts

$\square_h$	derived from hydrostatic depth
$\square_{Uw}$	derived from wave orbital speed
$\square_{rms}$	root-mean-square
$\square_s$	"significant"
$\square_{bed}$	denotes the bed
$\square SD$	denotes the standard deviation
$\square\sigma$	denotes variance
$\square_\infty$	denotes deep-water conditions
$\square_p$	denotes pressure sensor
$\square_u$	denotes current meter
$\square_{ABS}$	denotes Acoustic Backscatter Sensor
$\square_{OBS}$	denotes Optical Backscatter Sensor
$\square_z$	derived from zero up-crossing analysis
$\square_s$	of sediment
$\square_w$	of water
$\square_{pred}$	predicted
$\square_{obs}$	observed

Acronyms

ABS	Acoustic Backscatter Sensor
ADV	Acoustic Doppler Velocimeter
EMCM	Electromagnetic Current Meter
LAT	Lowest Astronomical Tide = Chart Datum
NIWA	National Institute of Water and Atmospheric Research
OBS	Optical Backscatter Sensor
SSC	Suspended Sediment Concentration

1.1 INTRODUCTION

It has long been recognised that two geophysical processes – tides and waves – control sediment redistribution, evolution, geomorphology and equilibrium on estuarine intertidal flats (e.g., van Straaten and Kuenen, 1958; Postma, 1961; Krone, 1966; Klein, 1967; Reineck, 1967; Anderson, 1983). Tide-related sediment-transport processes have received considerable attention in the estuarine literature, presumably because tidal currents and water levels are periodic and easily measured/predicted. In comparison, wave-induced sediment-transport processes have received little attention (for examples of this see Black *et al.*, 1998; Eisma *et al.*, 1998) despite their recognition as an important sediment-transporting process across intertidal flats, particularly in shallow regions where tidal currents are weak (e.g., Allen, 1971; Evans and Collins, 1975; Dyer, 1989).

Table 1.1 lists investigations that consider wave activity in some way – there are few such studies and most are conducted on mud flats (Table 1.1, brown highlights), facts which are manifest in Black's (1998) 29-paper compilation entitled "Sediment Processes in the Intertidal Zone" that features only one sand flat investigation and few which consider waves. In studies where linkages between waves and sedimentation are made, they tend to be tenuous. Some investigators characterise waves from observation or wind-speed inference (e.g., Anderson, 1972; Anderson and Pejrup, 2001), while others utilise instrumentation inappropriate to short choppy seas typical of estuarine settings (e.g., Sanford, 1994; dt<2Hz). Where high sampling-frequency wave gauges are used, they are often single-point studies (e.g., Schoellhamer, 1995; Green *et al.*, 1997) which provide some insights to intertidal flat processes, but are not as useful for investigating spatial variations in tides and waves, and the affects these have on sediment grading and intertidal flat shape, for example. Finally, measuring sediment concentrations in rapidly fluctuating mixed-size suspensions, which the author suggests are typical of estuarine intertidal flats under waves (and other coastal settings), requires sediment-concentration meters with high sampling rates and an ability to separately measure each size constituent in the suspension. Previous attempts at measuring concentration under estuarine waves have not considered size bi-modality or the effects

of time-varying particle size distributions on concentration estimates, to which many sensors are sensitive (White, 1988; Bunt *et al.*, 1999). Some of these difficulties may explain the recurrent lack of wave/sediment-transport research in estuaries which continues to hinder our understanding of intertidal-flat and estuarine sedimentation (Malvarez *et al.*, 2001).

The research presented in this thesis seeks to redress the deficiency in intertidal-flat wave/sediment-transport literature by measuring and modelling waves, tides and sediment concentrations across an intertidal flat, identifying the key processes and transport mechanisms responsible for sediment mobilisation and transport, and relating the spatial patterns in forcing processes to sediment distribution and geomorphology. Studies of this type will facilitate the development of conceptual models to describe morphodynamics and classify intertidal flats, and furthermore to extend morphodynamic models (e.g., Masselink and Short, 1993) for which estuarine intertidal flats are an end-member in the spectrum of beach morphologies.

Author	Waves		Wave source		Bed slope	Width (km)	Tidal range	Sediments	
	Observed	Measured	Local	Ocean				Mud	Sand
Van Straaten	✓		✓		1:1000	5	5 m	✓	
Reineck	✓		✓	✓?	1:1400	5 ?	3.6 m	✓	✓
Anderson		✓	✓		?	0.1	?	✓	
Carling		✓	✓		1:200	1.4	8 m		✓
Ward	✓		✓		1:500		0.4 m	✓	✓
Pejrup	✓		✓		1:1700	3	1.5 m	✓	
Brydsten	✓		✓	✓				✓	
Sanford		~✓*	✓					✓	
Dolphin/Green		✓	✓		1:600	2	3.4 m		✓
Schoellhamer		✓	✓		?	?	1 m		✓
Moeller		✓	✓	✓	1:400	2	3 m		✓
French		✓	✓		?	?	2 m	✓	
Le Hir		✓	✓		1:800	4	5 m	✓	
Anderson & Pejrup	✓				1:900	1.2	1.8 m	✓	

Table 1.1: Summary of published research which investigates waves on estuarine intertidal flats, and their associated characteristics. Most studies are from the United Kingdom and the barrier-enclosed European North Sea coast. Mud flats are highlighted in brown and sand flats in yellow. Author and location Key below.

Key:

Author(s):	Location
van Straaten and Kuenen (1958)	Dutch Wadden Sea, The Netherlands
Reineck (1967)	Jade Bay, North Sea coast, Germany
Anderson (1972)	Adams Cove, Great Bay, New Hampshire, U.S.A.
Carling (1982)	Burry Inlet, Carmarthen Bay, South Wales
Ward *et al.* (1984)	Choptank River, Chesapeake Bay, U.S.A.
Pejrup (1986)	Ho Bugt, Wadden Sea, Denmark
Brydsten (1992)	Öre estuary, northern Sweden
Sanford (1994)	Upper Chesapeake Bay, U.S.A.
Dolphin *et al.* (1995)	Manukau Harbour, New Zealand
Schoellhamer (1995)	Old Tampa Bay, Florida, U.S.A
Green *et al.* (1997)	Manukau Harbour, New Zealand
Möeller *et al.* (1999)	Stiffkey, Norfolk, England
French *et al.* (2000)	Blyth estuary, Suffolk, England
Le Hir *et al.* (2000)	Brouage mudflat, Marrennes-Oléron Bay, France
Anderson and Pejrup (2001)	Kongsmark, Rømø, Wadden Sea, Denmark

1.2 AIMS AND OBJECTIVES

The primary aim of this research project is to gain an understanding of the spatial and temporal variation in physical processes as they relate to sediment transport and geomorphology across an estuarine intertidal flat. A focal point of the research is the role of waves in the intertidal-flat sediment-transport equation. To achieve this aim the following specific objectives were identified and pursued:

Preliminary field experiments were conducted on an estuarine intertidal flat to ascertain characteristics of bed shear stresses and sediment suspensions under waves and currents in the shallow margins of the estuarine water body, and to aid in the design of a comprehensive process/sediment-transport experiment.

Biofouling is a problem for optical sediment-transport sensors, particularly in tropical and temperate shallow marine environments. To overcome biofouling, a mechanical cleaner was devised and field tested with the aim of producing 'clean' measurements over time scales of weeks to months. In addition, the data collected from field trials were utilised for development of an analytical correction method in the event that sensors were biofouled.

The ability of the instrumentation suite to measure processes and sediment transport over estuarine intertidal flat was investigated using data from laboratory and field experiments. Specifically investigated were:

- the ability of current meters and pressure sensors to measure wave-orbital motions in estuaries; and
- the use of combined optical and acoustic sensor arrays to measure concentration in mixed-size sediment suspensions (silts and sands).

In the main experiment, waves, currents and suspended-sediment concentrations were measured along a cross-shore transect in order to quantify physical processes, transport mechanisms, and sediment fluxes. In order to investigate relationships between geomorphology and physical processes, the transect surface was surveyed and sediment samples collected and analysed.

1.3 STUDY SITES

Field experiments were conducted at five sites around New Zealand's North Island (Figure 1.1). The main field site was an intertidal flat in Manukau Harbour, which is a large estuary (340 km^2) situated adjacent to the city of Auckland. Ancillary data were obtained from experiments conducted in the Poutawa Channel (also in Manukau Harbour) and at an open-coast wave tower on the Taranaki coast (240 km south of Manukau Harbour). Additionally, datasets from experiments conducted at Mangawhai Beach (Green, 1999; Green and Black, 1999) and the Okura estuary (Green and MacDonald, 2001), both of which are on the North Island's north-east coast (Figure 1.1), were made available for use in this study. Here the main field site is described; details of other sites can be found in Chapter 2.

Manukau Harbour is a large, meso-tidal, barrier-enclosed estuary that connects to the high-energy west coast of North Island, New Zealand (Figure 1.1). The estuary is shallow and infilled, with over 40% of its surface area exposed at low tide (Heath *et al.*, 1977). Large intertidal and subtidal flats are dissected by deep tidal-channels which follow the course of the ancestral Manukau River (Tonkin and Taylor, 1986). Semi-diurnal tides have spring and neap ranges of 4.4 m and 1.2 m, respectively. Shallow water, strong tidal flows (up to 200 cm/s) and low fluvial inputs contribute to a water body which is 'well-mixed' and which has salinity > 30 ppt in most areas (Vant, 1995). Tidal currents on intertidal flats are weak (0–40 cm/s).

The estuary is sheltered from oceanic swells by a sizeable Pleistocene barrier (the Awhitu Peninsula, Figure 1.1) and a very large and shallow ebb-tidal delta (1250×10^6 m^3; Hicks and Hume (1996)). In the absence of swell, short-period waves are generated as winds blow across the estuary. Fetch lengths extend up to 25 km and waves > 1 m may form, however optimum conditions for wave generation require coincidence of very strong winds with high spring tides, when the harbour fetch is at its maximum (see Chapter 3 and Dolphin *et al.*, 1995).

The intertidal flat adjacent to Wiroa Island, in the eastern Manukau Harbour (Figure 1.1), was chosen as the primary field site because of its exposure to the prevailing south-westerly wind (i.e., potential for wave activity) and good instrument security – the site is regularly patrolled by Auckland International Airport security. The Wiroa

intertidal flat is approximately two kilometres wide, relatively featureless and mainly comprises well-sorted fine sands. Muddy sediments found on the flanks of the Papakura Channel give way to slightly muddy-sands and the low gradient of the intertidal flat. In these lower reaches (1.3–1.5 km from shore) the percentage of mud decreases away from the channel (< 4 %) and low relief linear bars can be found (Green *et al.*, 1997). Landward, the intertidal flat comprises a low gradient (1:600–1:1000), is often wave rippled, and has a sandy surface (< 2 % mud). Low-amplitude multiple bars are common on the upper flat (Dolphin, 1992) whilst close to shore open sand flat or mangroves (muddy sediments) separate the intertidal flat from the steep, shelly, coarse-sand, beach face.

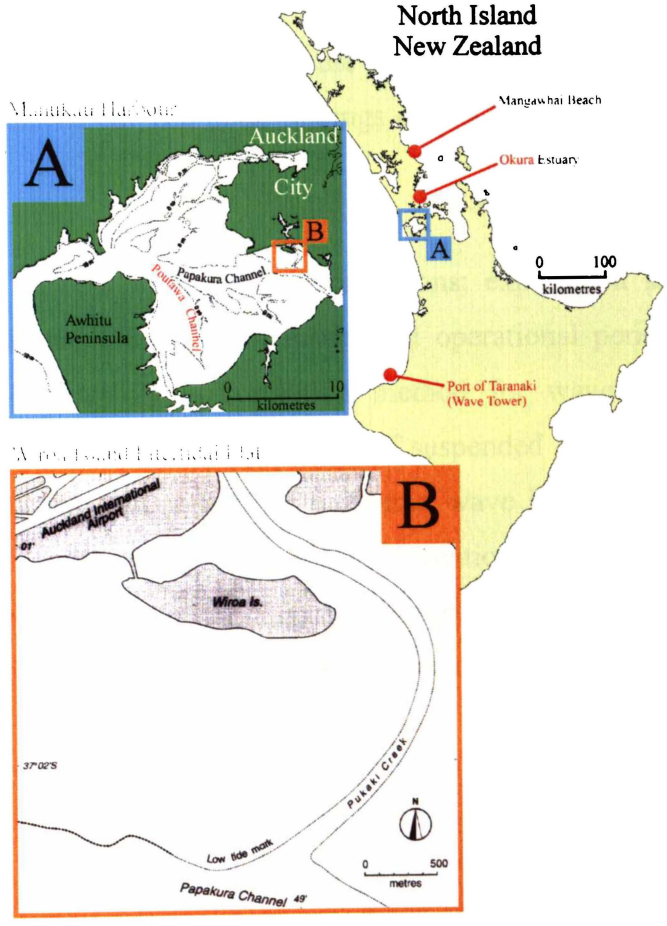

Figure 1.1: Location maps of field experiment sites: Manukau Harbour, Okura estuary, Mangawhai Beach and the coastal wave tower adjacent to the Port of Taranaki. Further details are given in Chapter 2.

1.4 THESIS LAYOUT

Notation used in this thesis is detailed in the prologue. Chapter 2 provides overviews of experiments and instrumentation, conversion of raw data into engineering units and estimation of wave parameters. In Chapter 3 wave measurements made by pressure sensors and current meters are intercompared, linear wave theory is investigated, and hypotheses are proposed for an inconsistency observed in the data. Chapter 4 describes the factors controlling estuarine wave generation and characterises the waves which arrive at the Wiroa intertidal flat. The processes controlling sand and silt entrainment, suspension, advection and flux are investigated in Chapter 5. Spatial variation in the driving processes and transport mechanisms which control the shape and evolution of the Wiroa intertidal flat are considered in Chapter 6. In particular, the links between wave processes and geomorphology, and the effects of increasing and decreasing tidal range/energy, are discussed. The main findings of this investigation are summarised in Chapter 7.

Eight appendices include: instrument specifications; experiment sampling strategies; instrument calibrations; a timeline of instrument operational periods for the transect experiment (see Chapter 2); a correction method for wave measurements using horizontally displaced sensors; measurement of suspended sediment concentration for mixed-size suspensions; comparison of measured wave height distributions with the Rayleigh model; a published paper on the prevention and analytical correction of biofouled optical backscatter sensor data; and scenarios of cross-shore sand flux and the cross-shore gradient in the cross-shore sand flux for varying tidal and concentration conditions.

2.1 INTRODUCTION

The methodology chapter provides an overview of the experiments, instrumentation, and sampling schemes used in this study. The conversion of raw data into engineering units and estimation of wave parameters from subsurface gauges is also detailed. The purpose of the chapter is to introduce the reader to the experiments conducted and the treatment of raw data in preparation for detailed analyses. Experiment details serve as a reference as such information is not usually reiterated in subsequent chapters.

2.2 OVERVIEW OF FIELD EXPERIMENTS

This study is based upon data from five field experiments that were conducted at four locations around the North Island (Figure 2.1). Included in some analyses are data from field deployments at Mangawhai Beach and Okura Estuary, which were kindly made available by Dr M. Green. This section briefly introduces each experiment and the basic aims.

1. Preliminary field experiments (Turbid Fringe Experiments) were conducted on the upper section of the Wiroa intertidal flat. Waves, currents and suspended-sediment concentration (SSC) were measured in the turbid fringe, which is the shallow turbid edge of the estuarine water body that appears during wave activity on the intertidal flats (Green and Bell, 1995), in order to gain a better understanding of turbid fringes form and what controls the very high SSC there. There are mixed views on the mechanisms controlling turbid fringe development (compare Green *et al.*, 1997 and Black *et al.*, 1999). The experiments were made during four separate tidal inundations at Wiroa Island (Figure 2.1; insets A and B) and served as pilot experiments, aiding in the design of intertidal-flat experiments which followed. Turbid fringes were also measured during deployments in the central Manukau Harbour (Bimodal-Size Suspension Experiments). Results from the Turbid Fringe Experiments are published in the Proceedings of the combined 13th Australasian Coastal and Ocean Engineering Conference and 6th Australasian Port and Harbour Conference (see Dolphin and Green, 1997).

2. Analysis of suspended sediment particle size (Turbid Fringe Experiments) was to show that suspensions on the intertidal flat were bimodal, containing variable sand/silt mixtures. As silt and sand have different settling properties, an understanding of sediment transport requires separate concentration measurements of each size mode. Furthermore, many available SSC measuring devices are sensitive to the size characteristics of suspension (White, 1988; Bunt *et al.*, 1999). As a result, Bimodal-Size Suspension Experiments were designed to investigate the response of suspended-sediment-concentration meters to mixed-size sediment suspensions in the laboratory (turbidity tank) and in the field (Poutawa Channel, Figure 2.1; inset A). As many suspended-sediment-concentration meters are sensitive to changes in particle size, the purpose of these experiments was to find a way to make successful measurements of concentration in the mixed-size suspensions of Manukau Harbour. Field experiments were conducted in Poutawa Channel because SSC in the tidal channel is approximately constant over the time interval needed to collect a pump sample there. In comparison, pump samples from flats, where suspensions are wave-induced, are difficult to interpret because concentration varies over time intervals shorter than the pumping duration. The Poutawa Channel sediments have the same size and mineral characteristics as those on the Wiroa flat. Results of this experiment are included here and have been published in the Proceedings of Coastal Sediments '99 (Green *et al.*, 1999). The data have also been used to investigate sediment dynamics and transport pathways in tidal channels (see Green *et al.*, 2000).

3. Previous experience in Manukau Harbour indicates that instruments can become biofouled in as little as three days (e.g., Bell *et al.*, 1997). Whilst most marine instruments are not seriously affected by biofouling, data from optical backscatter sensors used for measuring SSC may become contaminated as encrusting organisms obscure the sensing elements. Biofouling preventative devices were built and then tested in a 160-day Biofouling Experiment on the Wiroa flat (Figure 2.1; insets A and B). The data from clean and progressively biofouled sensors were used to develop an analytical method for making corrections to contaminated optical data. Results from the Biofouling Experiment are published in the Journal of Coastal Research (see Dolphin *et al.*, 2001) and are incorporated in Appendix VIII.

4. Estuarine waves exhibit a number of characteristics (e.g., short periods) that can make estimation of wave characteristics from pressure data challenging. Several experiments, collectively titled Pressure–Velocity Experiments, were designed to investigate whether or not near-bed pressure and velocity sensors could accurately measure waves. Specifically, the effect of sensor orientation on the functioning of pressure sensors, and the transformation of pressure and velocity data to wave statistics (e.g., wave height, period and orbital velocity) using linear (Airy) wave theory. Pressure and velocity data from both ocean (coastal) and estuarine deployments were used (Figure 2.1) in the analysis of the problem.

5. In the main experiment, 16 instruments were deployed along a cross-shore transect at Wiroa Island (Figure 2.1) to measure waves, currents, and SSC. The intertidal-flat Transect Experiment was designed to investigate the primary research aims (see Chapter 1): investigating processes responsible for sediment entrainment and suspension, spatial variability in the wave-induced and tide-induced bed shear stresses, and the relationships between spatio-temporal characteristics of forcing processes and intertidal-flat geomorphology and sedimentation.

2.3 Field and Laboratory Measurements/Data

Twelve different instrument types/models were used for measuring waves, currents and suspended-sediment concentration. Table 2.1 shows the basic instrument suite (for details see Appendix II). All instruments make single-point measurements, with the exception of Alice (Figure 2.2), which is a benthic tripod that measures vertical profiles of currents and SSC in the lower two metres of the water column (Green, 1996).

The specifications for the instruments listed in Table 2.1 are given in Appendix 1. Summary information follows.

Manufacturer	Model	Measurements				
		Pressure	Velocity			SSC
			V_x	V_y	V_z	
NIWA	Dobie-A	✓				
NIWA	Dobie-O	✓				✓
Falmouth Scientific	3D-ACM WAVE	✓	✓	✓	✓	
Sontek	ADV		✓	✓	✓	
WHISL/NIWA	Alice	✓	✓	✓		✓
InterOcean	S4A	✓	✓	✓		✓
InterOcean	S4DW	✓	✓	✓		

Table 2.1: Field instruments and measurement capabilities. V_x, V_y and V_z are the horizontal (x and y) and vertical (z) components of velocity. NIWA is the National Institute of Water and Atmospheric Research; WHISL is Woods Hole Instrument Systems Ltd

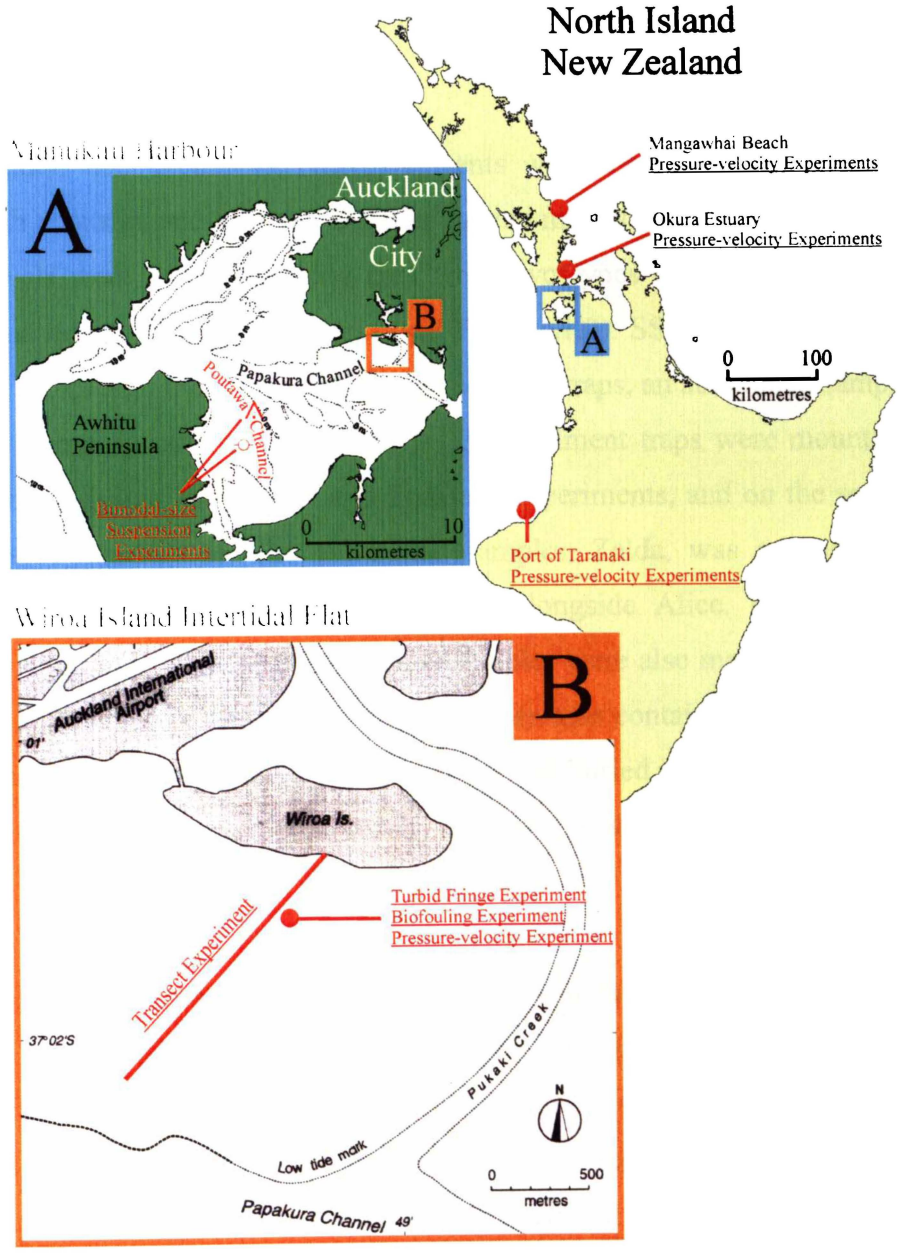

Figure 2.1: Location maps. Experiment titles (underlined) are explained in Section 2.2. ∧ and ○ mark Alice and Dobie deployments during the Bimodal-Size Suspension Experiments.

Figure 2.2: Instrumented tripod, Alice, partially inundated by the flooding tide during a wave event at Wiroa Island.

Steady (tidal) and oscillating (wave) currents were measured with electromagnetic, direct-path acoustic, and acoustic Doppler current meters (see Table A1.1, Appendix I). Water levels were estimated using data from two types of pressure sensors – strain gauges and quartz crystal oscillators (see Table A1.2). SSC was physically measured by taking samples of the suspension using sediment traps, an automated sampler, and by manually pumping samples (see Table A1.3). Sediment traps were mounted on Alice during Bimodal-Size Suspension and Transect Experiments, and on the sea bed during the Transect Experiment. The automated sampler, Zelda, was purpose built at the University of Waikato and usually operates alongside Alice. During some storms (Turbid Fringe and Transect Experiments) samples were also manually pumped from a series of frame-mounted intakes. A floating inner tube containing a carousel of sample bottles and the pump was tethered to an anchor and buried pipes connected the pump to the intakes. The pump was operated by two people standing on the submerged flat (Figure 2.3).

Two types of sediment suspension meter, Optical Backscatter Sensors (OBS) and Acoustic Backscatter Sensors (ABS), were used to remotely sense SSC. In comparison with pumped samples, OBS and ABS (Table A1.3) are unmanned and collect data (in bursts) with a greater temporal resolution and at regular intervals throughout the experiment. The OBS operates by transmitting infrared (IR) light into the surrounding water and measuring the amount of light backscattered from particles in suspension. The backscattered signal is proportional to the sediment concentration, but is also

affected by other factors that are discussed later. The ABS operates by transmitting a sound pulse and 'listening' for the backscattered sound from particles in suspension. The backscatter intensity can be related to the concentration and is also discussed later (Section 2.4.3). The Aquatec three-frequency ABS was mounted on Alice, whilst OBSs were mounted on both Alice and Dobie-O's.

Additional sensors deployed during the Transect Experiment include a sonar, which was mounted on Alice, and an autonomous video camera, which was attached to the top of a 4-m-high marine pylon. The Imagenex 675 kHz sonar measures bedforms under Alice; the sector scanner gives a plan view of the sea floor while the pencil beam measures surface elevations of the bed along a 1 m transect. The video camera was deployed to record sea-surface conditions.

2.3.1 Turbid Fringe Experiments

Experiments were conducted at Wiroa Island when strong onshore winds were predicted. On four occasions waves, currents, and suspended sediments were measured some 400 m from shore and in high-tide water depths of 0.7–1.1 m. On two occasions moderate-strong onshore winds (6–9 m/s; 11–15 m/s) generated large waves (up to 35-cm high), whilst during the remaining two times winds were offshore and waves were small (< 5 cm).

Several sensors were mounted on an instrumented frame (Figure 2.3): a bottom-mounted Dobie-A wave gauge, an ADV, and an OBS attached to a Campbell Scientific CR10X data logger. The interval between bursts was minimised to provide detail of the changing wave and suspension characteristics over the tidal cycle. The sampling strategy and sensor elevations are detailed in Table A2.1 (Appendix II). Ten-minute averages of wind speed and direction, as well as the maximum gust, were recorded hourly at the nearby Auckland International Airport meteorological station.

Water samples were collected using the floating pump and a carousel of sample bottles (Figure 2.3). Collecting samples was challenging as large waves made it difficult to remain standing and wet battery terminals gave regular electric shocks to the operators (a switch was later installed for operator comfort). Nevertheless, two 500-ml samples were collected every 10 minutes for sediment mass and grain-size analysis.

2.3.2 Bimodal-Size Suspension Experiments

Prior to the Bimodal-Size Suspension field experiments, comparative tests of the OBS and ABS were conducted in a purpose-built turbidity tank. The tank is constructed from perspex sheets and an angle-iron frame (Figure 2.4). The tank is box shaped (140 cm by 38 cm^2) with a funnel at the base and has a fluid capacity of 180 L. The water/sediment mixture recirculates as follows. An open-impeller pump (modified to allow the passage of suspended solids) at the base pumps the mixture to the top of the tank in a single hose (2.5-cm i.d.) where it is split into four smaller hoses (@ 0.8-cm i.d.) and distributed in a uniform manner just below the water surface. The mixture then sinks down the column past any installed suspended sediment meters. OBSs were installed (one at a time) inside the tank at a depth of 55 cm and facing diagonally across the tank, whilst the ABS was mounted at the top of the tank facing down the column. SSC in the tank was independently determined by filtering samples taken from a retractable port located at 55-cm depth (refer Appendix VI and Dolphin, *et al.*, 1999). Sand tests were made with sieved sediments (100–200 μm) from the Poutawa Channel bed. Silt tests were made using wet-sieved sediment (10–30 μm) extracted from the Poutawa Channel water column at slack water low tide.

Field data were collected from the Poutawa Channel, which is a deep (12–15 m) tidal channel south-west of the Wiroa intertidal flat (Figure 2.1; inset A). Alice was deployed in the channel to measure velocity, silt-concentration and sand-concentration profiles (sampling details in Table A2.2). Suspended sediments were also sampled using traps mounted on Alice and by pumping water samples from a boat. A Dobie-A was deployed on an adjacent intertidal flat to measure waves. Experiments took place during the peak tidal flows (> 50 cm/s) associated with spring tides.

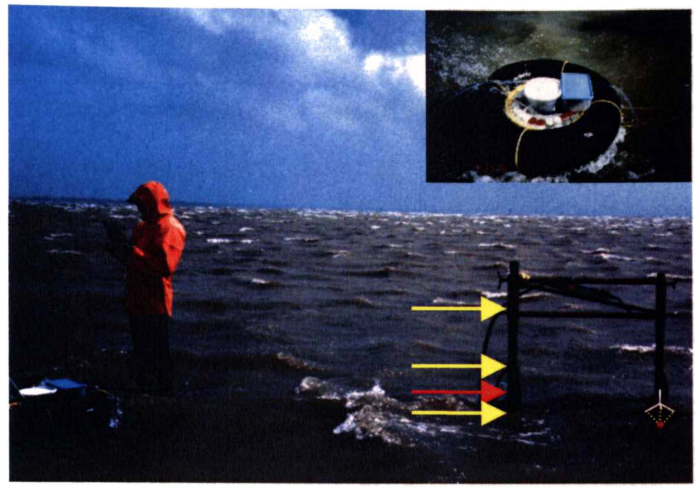

Figure 2.3: Manual sampling for SSC during a wave resuspension event (Turbid Fringe Experiment). Samples were collected with a manually activated pump. Sample bottles (inset) were connected to an intake on the frame (red arrow). Additional intakes (yellow arrows) were used in Transect Experiments (described later in this section). The location of the submerged ADV probe is drawn in (lower right).

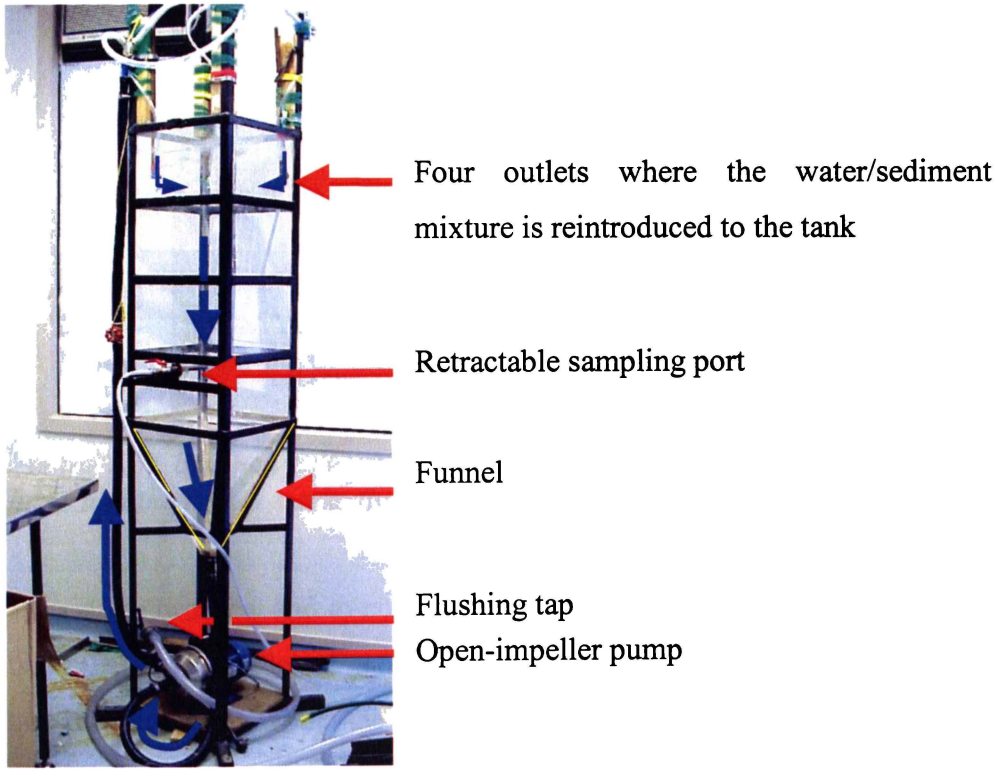

Figure 2.4: The perspex turbidity tank supported by an angle-iron frame. An open-impeller pump recirculates the sediment:water mixture and an flushing tap is used to flush the tank clean between tests.

2.3.3 Biofouling Experiment

Optical backscatter sensors are highly sensitive to the effects of biofouling as the growth of organisms on the sensor obscures the sensing elements. Concerns over biofouling of OBSs lead to the development of a pneumatic brush to prevent fouling and maintain a clean sensor face (Figure 2.5). Although automated cleaning is not a new idea (e.g., Black *et al.*, 1994; Ridd and Larcombe, 1994), the design of this system does have advantages over previous cleaners. It is well suited to OBS arrays (e.g., Alice) as many brushes can be driven by a single controller, the system endurance outlasts most deployments (thousands of sweeps limited only by the capacity of the air source) and its dimensions are small (1x10 cm) and easily adapted to different optical sensors.

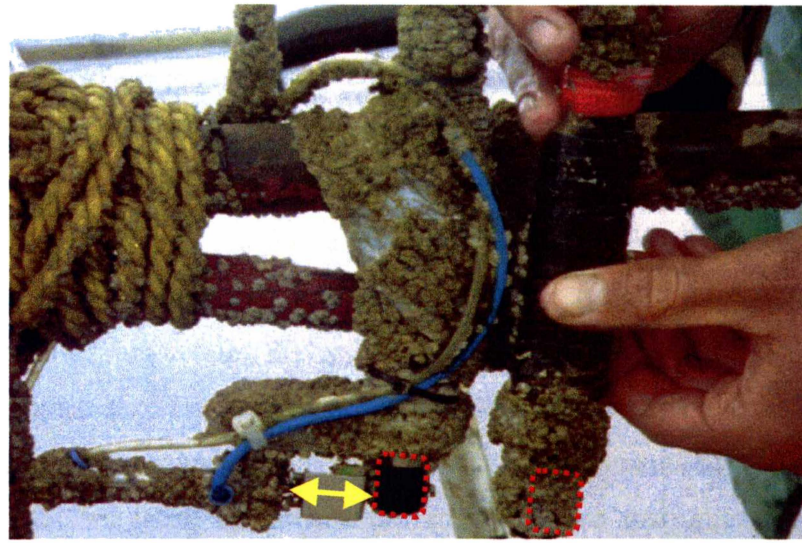

Figure 2.5: Brushed (clean) and biofouled OBSs. Red dashed lines mark the sensor faces and the arrow marks the retracted brush head.

To test the brushes, and to collect data on the performance of a biofouled OBS sensor, two OBSs were deployed at Wiroa Island for 160 days. One OBS was unprotected and became biofouled while the other was deployed with the pneumatic brush and the sensing elements remained clean (Figure 2.5). Both OBSs were mounted on a small frame, 60 cm above the bed, and facing into the expected incident wave field. This orientation was chosen to minimise variations in the suspension that might be caused by the presence of the frame. OBS data were logged synchronously on a CR10X and a Dobie-A wave gauge was mounted at the base of the frame to measure waves and water levels. The pneumatic brush was activated during OBS power-up some 10 s prior to

commencement of logging. A single out-and-back stroke was performed. The sampling strategy used is given in Table A2.3.

2.3.4 Pressure–Velocity Experiments

Pressure and velocity sensor performance and linear-wave-theory transformations were tested with four datasets; two estuarine and two open-coast. The estuary data were used to test for inconsistencies in the estimates of wave statistics under short-period waves. Further testing was conducted using instruments deployed seawards of two open-coast surf zones where the waves were longer. In all examples the data span similar *relative water depths* (i.e., depth/wavelength).

The first estuary site was Okura estuary, which is a funnel-shaped drowned river valley with a mesotidal range and which is exposed to large fetch lengths (> 60 km in some directions). Alice was deployed on an intertidal sand flat near the mouth of the estuary; sampling details may be found in Green and MacDonald (2001) and Table A2.4.1.

The second estuary site was the Wiroa intertidal flat in Manukau Harbour. Dobie-A and 3D-ACM gauges were deployed on the intertidal flat (Figure 2.1) to investigate the effect of dynamic pressure on the estimation of wave characteristics for a range of sensor orientations. Two Dobies and two 3D-ACMs were deployed. One Dobie and one 3D-ACM were counter sunk into the bed so that the instruments had a low profile and the pressure sensors faced upwards. The remaining two instruments were mounted horizontally (i.e., pressure sensors facing sidewards). The horizontal 3D-ACM faced into the approaching incident wave field, whilst the horizontal Dobie, which was weighted with a lead plate, was reoriented (relative to the wave direction) several times during the tidal cycle. Instruments were closely spaced (< 2 m apart). Sampling parameters are given in Table A2.4.2.

The first open-coast site was Mangawhai beach (Figure 2.1), which experiences low swell (< 1 m) punctuated by infrequent storm waves during the passage of subtropical cyclones. Alice was deployed just seaward of the longshore bar in depths of 7 m and 12 m. The data used have been published by Green (1999) and sampling details can be found in the aforementioned reference as well as in Table A2.4.3.

The second open-coast site was the wave tower operated by the Port of Taranaki (Figure A2.1), which is adjacent to the city of New Plymouth and some 240 km south of the Manukau Harbour entrance (Figure 2.1). The wave climate in the Taranaki region is forced by polar and subtropical winds generated in the Southern Ocean and Tasman Sea, and swell waves > 1 m in height are common. Nine wave gauges (Dobies, S4s and 3D-ACMs) used during the Transect Experiment (see Section 2.3.5) were redeployed on the wave tower: three Dobies were clamped to the tower's lower cross-member whilst S4s and 3D-ACMs were mounted on taut mooring lines between the upper and lower cross-members (Figure A2.1). The tower is also fitted with a meteorological station and a vented pressure transducer. Sampling details for the 9-day deployment are given in Table A2.4.4.

Finally, data from the main Transect Experiment (see Section 2.3.5) were used to describe and investigate pressure/velocity inconsistencies.

2.3.5 Transect Experiment

During the main field experiment a suite of up to 16 instruments (30 sensors) were deployed along a SW oriented, 1.6-km transect at Wiroa Island (Figure 2.1; inset B). The transect arrangement was chosen to provide data on how waves, currents and suspended sediment concentrations vary across the flat and along the wave propagation axis corresponding to the prevailing SW wind. Wave, current, and suspended-sediment meters were operational for a period of 10 weeks.

The experiment was divided into two periods, Phases I and II, for which the arrangement and number of sensors on the transect differed (Figure 2.6, Figure 2.7). In Phase I, suspended-sediment meters were spread evenly across the transect with Alice on the lower flat, whilst in Phase II, suspended-sediment meters were deployed on the upper flat with Alice midway on the transect. Wave gauges were regularly spaced across the flat during Phase I and Phase II. Regular instrument spacing was chosen to provide measurements across the full range of intertidal elevations and geomorphic subzones. Full details on instrument locations, sensor elevations, and sampling strategies can be found in Tables A2.5.1, A2.5.2 and A2.5.3.

Moorings and instruments were carried by hand across the intertidal flat, with the exception of Alice, which was transported to and from the site by helicopter (Figure 2.8). The instrument locations and the transect were surveyed using a Geodimeter 464 Total Station.

Data from bottom-mounted instruments were supplemented by automated video camera recordings from a local marine pylon (z = 4 m), measurements of SSC using pump samples, and grain size information from pump, trap and bed samples. Suspended-sediment samples were pumped manually using intakes mounted on a frame to which the ADV was attached (see Figure 2.3; red and yellow arrows mark intakes for this experiment). The use of sediment traps, some OBSs (without cleaning brushes), instruments with memory limitations, prototype instruments with low power endurance (Dobie-O), and the manual collection of water samples during storms, called for regular visits to the field site (at least twice weekly).

Ten-minute averages of wind speed and direction, as well as the maximum gust, were recorded hourly at the nearby Auckland International Airport meteorological station.

A timeline detailing the instrument operational and failure periods can be found in Appendix IV.

The timing of the experiment (October–December) coincided with seasonally strong SW winds. Winds blowing from this sector have a 20–25 km fetch and can generate large waves (over one metre high) on the Wiroa Island intertidal flat (Dolphin et al., 1995). Several storms were measured during the experiment, providing much of the data required to address the research aims.

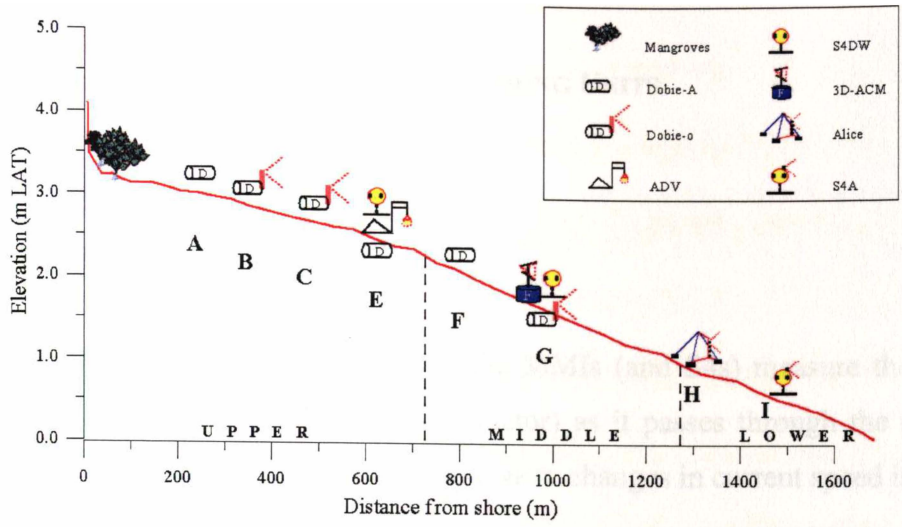

Figure 2.6: Location of instruments during Phase I of the Transect Experiment. The letters used to identify each station correspond to the last character of the station ID in Table A2.5.1.

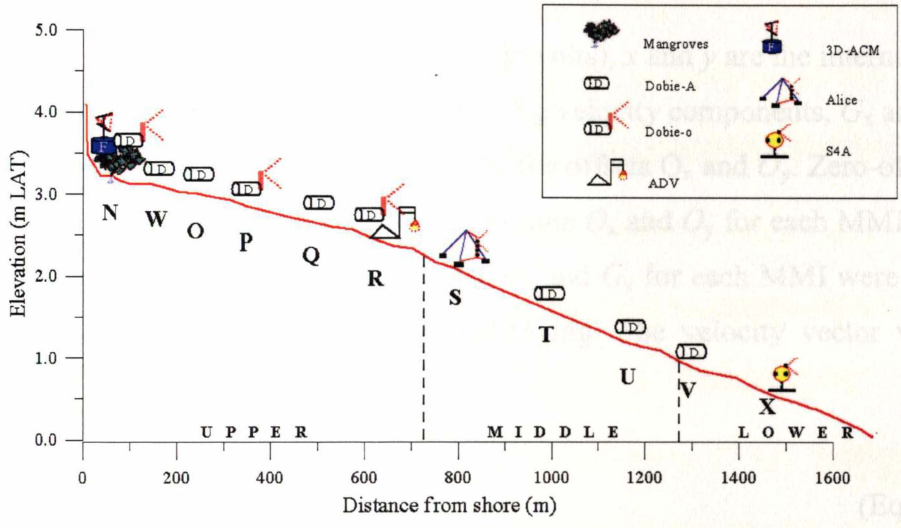

Figure 2.7: Location of instruments during Phase II of the Transect Experiment. The letters used to identify each station correspond to the last character of the station ID in Table A2.5.2.

Figure 2.8: Helicopter deployment of Alice on the Wiroa Island intertidal flat.

2.4 CONVERSION OF RAW DATA TO ENGINEERING UNITS

2.4.1 Currents

Marsh-McBirney EMCMs

The diametrically placed electrode pairs on the MMIs (and S4s) measure the voltage resulting from the motion of water (the conductor) as it passes through the magnetic field generated by the current meter. The response to changes in current speed is linear:

$$u_{CM} = G_x R + O_x$$
$$v_{CM} = G_y R + O_y \qquad \text{(Eqn 2.1)}$$

where R is the MMI sensor response (measured in volts), x and y are the internal axes of the current meter, u_{CM} and v_{CM} are the corresponding velocity components, G_x and G_y are the gains for each electrode pair and likewise for the offsets O_x and O_y. Zero-offset tests were conducted in a bucket of still water to determine O_x and O_y for each MMI, prior to each experiment (see Appendix III for details). G_x and G_y for each MMI were supplied by the manufacturer and assumed to be unchanging. The velocity vector was then determined as:

$$\vec{V} = [V, \phi] \qquad \text{(Eqn 2.2)}$$

where the current speed is

$$V = (u_{CM}^2 + v_{CM}^2)^{1/2} \qquad \text{(Eqn 2.3)}$$

and the current direction (with respect to true north) is

$$\phi = \tan^{-1}(u_{CM} / v_{CM}) + \Diamond \qquad \text{(Eqn 2.4)}$$

The velocity component v_{CM} is parallel to the bearing of the lubber line $\Diamond$, which is corrected for local magnetic declination.

$\vec{V}$ is computed internally by the S4, using a compass to convert current direction to an earth reference. It is possible for the user to adjust for any known variations in zero offset and gain, however, this was not done and the S4 User's Manual (InterOcean, 1994) recommends against it.

Falmouth 3D-ACM

The 3D-ACM computes vertical (w) and earth-reference horizontal velocity components (V_E and V_N) internally. Velocity estimates are based on the phase shift of sound transmitted along four acoustic paths (Falmouth Scientific Inc., 1998). The phase shift is dependent on the speed of sound in the fluid, which is a function of water temperature, salinity, and pressure. Variations in the water temperature have the greatest effect on the speed of sound and are taken into account internally using thermistor measurements. In coastal environments, the speed of sound is relatively insensitive to pressure and salinity variations, and only user-defined constants are required. The predicted error due to variations from preset pressure and salinity constants gives a maximum error of 1.3% for this study (for details refer to Falmouth Scientific Inc., 1998).

Sontek ADV

The ADV computes the horizontal and vertical velocity components, u_{CM}, v_{CM}, and w_{CM} internally. Measurement is based on a change in frequency between transmitted and received (reflected) sound waves (Doppler effect). Again the estimation of the speed of sound is important in determining velocity. The manufacturer has available Matlab routines that correct the velocity components for differences between preset values of temperature and salinity and actual values, however, neither temperature nor salinity were measured, so corrections have not been made. Salinity and temperature information from previous studies (Turbid Fringe Experiments and Vant, 1995) suggest that the speed of sound calculations have an error of < 1% (for details refer to SonTek Inc., 1997). The ADV calibration, applied internally, does not change unless the probe has been physically damaged (SonTek Inc., 1997).

2.4.2 Pressure

The Dobie and S4 pressure sensors (strain gauges) respond linearly to changes in pressure:

$$p = G_p R + O_p \qquad \text{(Eqn 2.5)}$$

where R is the response measured in volts, and G_p and O_p are the sensor gain and offset, respectively. G_p and O_p were established by the manufacturers for Dobie-A and S4 pressure sensors and by calibration in a sealed chamber with an independent pressure sensor mounted in its wall (Appendix III) for Dobie-O.

The Druck and Paroscientific pressure sensors used on the 3D-ACM and Alice estimate pressure from the change in oscillation frequency of a quartz crystal. In both cases the conversion into units of pressure is more complicated than in eqn 2.5. The pressure and temperature coefficients required to convert R into units of pressure are determined by the manufacturers, are assumed to be unchanging and are applied internally.

For convenience, and in preparation for analysis, all pressure data were converted into 'hydrostatic depth' as

$$h(t) = \frac{(p(t) - p_A)}{\rho_f g} + z_p \qquad \text{(Eqn 2.6)}$$

where $h(t)$ is the time series of hydrostatic depth (m), $p(t)$ is the time series of pressure measured in Pascals (Pa), ρ_f is the density of sea water (1025 kg/m^3), g is acceleration due to gravity (9.807 m/s^2), and z_p is the elevation of the pressure sensor above the bed (m). S4s and Dobies use a nominal value for atmospheric pressure (p_A) and evaluate eqn 2.6 internally. Correction for true atmospheric pressure is made using the measured time series $p_A(t)$ in post-processing. This requires solving eqn 2.6 for $p(t)$, subtracting the nominal atmospheric pressure and then introducing $p_A(t)$ for p_A back into eqn 2.6. Alice and 3D-ACMs report absolute pressure and so eqn 2.6 is applied directly in post-processing, again using $p_A(t)$ for p_A.

The burst mean water-depth $\bar{h}$ is derived as the time-average of $h(t)$:

$$\bar{h} = \frac{\sum_{i=1}^{N} h(t)_i}{N}$$

where N is the number of points per data burst. Although time-averaging $h(t)$ yields $\bar{h}$, $h(t)$ does not, in fact, equate to the time series of instantaneous sea-surface elevations (i.e., $h(t) \neq \eta(t)$) since the frequency-dependent attenuation of pressure fluctuation with depth has not been accounted for.

2.4.3 Suspended-Sediment Concentration

SSC was estimated using OBSs, an ABS and physical samples. The OBS, which operates by transmitting IR light into the surrounding water and measuring the amount of light backscattered from particles in suspension, responds linearly to changes in the concentration up to ~10^4 mg/L (Kineke and Sternberg, 1992):

$$C = G_{\mathrm{OBS}} R + O_{\mathrm{OBS}} \qquad \text{(Eqn 2.7)}$$

where C is the concentration expressed in mg/L, R is the OBS response, measured in volts, and G_{OBS} and O_{OBS} are the sensor gain and offset respectively. G_{OBS} and O_{OBS} are determined for each sensor in laboratory and/or field calibrations.

Interpreting OBS data is not always as straightforward as eqn 2.7 implies because, in addition to concentration, OBSs also respond to changes in aspects of the suspension such as particle size (Ludwig and Hanes, 1990; Conner and De Visser, 1992; Green and Boon, 1993; Black and Rosenberg, 1994; Xu, 1997; Bunt *et al.*, 1999) and refractive index (Bunt *et al.*, 1999; Hatcher *et al.*, 2000; Sutherland *et al.*, 2000). Calibration and interpretation of OBS data are discussed further in Section 5.3 and Appendix VI.

The ABS is a sonar device which transmits sound and relates the echo (sound backscattered from particles (sediment) in the water column) to the SSC at a number of discrete elevations, to give a concentration profile or C-profile. Following transmission, the ABS employs a range-gating technique, 'listening' for the backscattered return at

discrete time intervals, each of which corresponds to a small section (a bin) of the water column/C-profile. The relationship between backscattered sound and C in each bin is defined by:

$$C(r) = \frac{\rho_s \langle P \rangle^2}{A_0^2 c} . \exp(-4\alpha r) \frac{1}{B^2(r) S^2(a_s)} \qquad \text{(Eqn 2.8)}$$

where $C(r)$ is the concentration at range r from the transducer, ρ_s is the sediment density, $\langle P \rangle^2$ is backscattered pressure (sound), c is the speed of sound, α is the attenuation coefficient, $B(r)$ describes beam spreading as a function of r, $S^2(a_s)$ describes the "efficiency" with which particles of radius a_s=d_s/2 backscatter sound, and A_0 is a system constant that is independent of scattering properties of the sediment and is determined by calibration. Standard $1/r^2$ beam spreading was assumed for the far field and for the near field the model of Downing *et al.* (1995) was used. The sediment density was assumed to be that of the predominant mineral, quartz (2.65 g/cm^3), and α was formulated to account for sound absorption by water and suspended sediments (Downing, 1992). Downing's (1992) derivation of $S^2(a_s)$, which incorporates the data of Sheng and Hay (1988), was used. The ABS 'pings' at a rate of 80 Hz, from which $\langle P \rangle^2$ is formed as the average of 16 successive returns, which gives a sampling rate of 0.20 s.

Calibration and interpretation of ABS data are discussed further in Section 5.3 and Appendix VI for similar reasons to those given for the OBS.

Physical samples provide a more direct estimate of SSC, however they have a number of limitations: the time required to collect a sample (typically ~ 10 s) is long compared to estuarine wave periods and probable associated concentration variations, and sample collection is restricted to times of site visits and pre-programmed automated samples. By comparison, ABS and OBS collect data bursts regularly and at frequencies much shorter than individual wave cycles. However, physical samples are considered important for verifying the concentration inferred from optical and acoustic backscatter data. All samples collected were treated with $HgCl_2$ solution (40 ppm) to exterminate micro-organisms which can, with time, multiply and alter the particulate mass and therefore SSC. Following standard procedure, samples were filtered and the dry mass of

sediment expressed as a proportion of the fluid volume (mg/L). The analysis is detailed in Dolphin *et al.* (1999).

2.5 Estimation of Wave Parameters

2.5.1 Sea-surface elevation

$p(t)$ was detrended and converted to $h(t)$ using eqn. 2.6. The time series of sea-surface elevation was then evaluated as:

$$\eta_h(t) = \int_{\omega_H}^{\omega_L} \Gamma_h(\omega)\, S_h(\omega) e^{i\omega t} d\omega \qquad \text{(Eqn 2.9)}$$

where $S_h(\omega)$ is the power spectrum of $h(t)$, ω is the wave radian frequency and $\Gamma_h(\omega)$ is the transfer function representing frequency-dependent attenuation of pressure with depth, described by linear wave theory:

$$\Gamma_h(\omega) = \frac{\cosh(k\bar{h})}{\cosh[k(z_p^* + \bar{h})]} \qquad \text{(Eqn 2.10)}$$

with $z_p^* = (z_p - \bar{h})$ and wavenumber, k, which satisfies the linear dispersion relation:

$$\omega^2 = gk \tanh(k\bar{h}) \qquad \text{(Eqn 2.11)}$$

at every ω. Eqn 2.11 was solved by employing the Newton-Raphson technique (Kreyszig, 1993, p. 929). Wind-generated gravity waves, defined as waves with periods 1–30 s (Kinsman, 1984), provide the frequency limits for integration in eqn. 2.9:

$\omega_L = 2\pi/30\ s^{-1}$

and

$\omega_H = 2\pi/1\ s^{-1}$ for $\omega_H \leq 2\pi/1\ s^{-1}$

$$\omega_H = \frac{\pi}{\sqrt{\pi z / g}} = \sqrt{\frac{\pi}{(z/g)}} \qquad \text{for } \omega_H > 2\pi/1 \text{ s}^{-1} \qquad \text{(Eqn 2.12)}$$

Eqn 2.12 is the high-frequency cut off to prevent amplification of noise (adapted from Hutt and Black, 1997), which has been employed previously by, for example, Green (1999) and McComb *et al.* (2001).

$\eta(t)$ was also estimated from current-meter data as follows. Firstly, time series of wave-orbital speed, $U_w(t)$, was determined from the measured velocity components $\tilde{u}_{CM}$ and $\tilde{v}_{CM}$ as:

$$U_w(t) = \sqrt{\tilde{u}_{CM}^2(t) + \tilde{v}_{CM}^2(t)}\,\cos[\phi_\Delta(t)] \qquad \text{(Eqn 2.13)}$$

where the tilde indicates time-domain high-pass filtering (cutoff = 30 s), and

$$\phi_\Delta(t) = \tilde{\phi}(t) - \bar{\phi}_w, \qquad \text{(Eqn 2.14)}$$

where $\bar{\phi}_w$, the average direction of wave propagation, was determined for each burst as the angle of maximum variance (refer Appendix V), and

$$\tilde{\phi}(t) = \tan^{-1}[\tilde{u}_{CM}(t)/\tilde{v}_{CM}(t)] + \Diamond \qquad \text{(Eqn 2.15)}$$

In a similar fashion to eqn 2.9, $\eta_{Uw}(t)$, was then evaluated as:

$$\eta_{Uw}(t) = \int_{\omega_H}^{\omega_L} \frac{1}{\omega} \Gamma_{Uw}(\omega)\, S_{Uw}(\omega) e^{i\omega t} d\omega \qquad \text{(Eqn 2.16)}$$

where $S_{Uw}(\omega)$ is the power spectrum of $U_w(t)$ and $\Gamma_{Uw}(\omega)$ is the transfer function representing frequency-dependent attenuation of wave orbital motion with depth, described by linear wave theory:

$$\Gamma_{Uw}(\omega) = \frac{\sinh(k\bar{h})}{\cosh[k(z_u^* + \bar{h})]} \qquad \text{(Eqn 2.17)}$$

Finally, the power spectrum of $w(t)$, $S_w(\omega)$, was determined as:

$$S_{\eta_w}(\omega) = S_w(\omega) \frac{1}{\omega} \Gamma_w(\omega) \qquad \text{(Eqn 2.18)}$$

where the actual phase relationship between $\eta_w(t)$ and $w(t)$ is ignored and $\Gamma_w(\omega)$ is the transfer function representing frequency-dependent attenuation of wave orbital motion with depth, described by linear wave theory:

$$\Gamma_w(\omega) = \frac{\sinh(k\bar{h})}{\sinh[k(z_u^* + \bar{h})]} \qquad \text{(Eqn 2.19)}$$

Eqn 2.18 can be integrated to give the variance of $\eta_{Uw}(t)$.

2.5.2 Wave statistics

In a sea with a narrow frequency spectrum and a linear Gaussian surface, wave heights are expected to be distributed according to the single-parameter Rayleigh model in which wave heights are normalised by the root-mean-square (RMS) wave height H_{rms} (Longuet-Higgins, 1952):

$$H_{rms} = \sqrt{8\eta_\sigma} \qquad \text{(Eqn 2.20)}$$

where η_σ is the variance of $\eta(t)$ (Longuet-Higgins, 1980). η_σ is calculated as the zero moment (m_0) of $S_\eta(\omega)$, which is determined from:

$$m_n = \int_{\omega_H}^{\omega_L} \omega^n S_\eta(\omega)\, d\omega \qquad \text{(Eqn 2.21)}$$

It is then possible to determine any number of height statistics (again assuming Rayleigh distributed heights) that are related to one another through m_0. The mean and significant wave heights:

$$\overline{H} = 0.886\sqrt{8\eta_\sigma} \qquad \text{(Eqn 2.22)}$$

$$H_s = 1.414\sqrt{8\eta_\sigma} \qquad \text{(Eqn 2.23)}$$

are used in this thesis.

Investigation of the actual wave height distributions (Appendix VII) from the Transect Experiment reveals that wave heights on the Wiroa-flat broadly follow the Rayleigh distribution and that there is no significant difference (at the 99 % level) between the empirical and Rayleigh exceedence probabilities. Similar results were recorded by Black (1983) in Whangarei Harbour. However, in most cases on the Wiroa flat (though not all) the Rayleigh distribution systematically exceeds the observed distribution in the high-wave tail of the distribution (see Appendix VII). Researchers working on open-coasts have made similar observations (e.g., Forristall, 1978; Sobey *et al.*, 1990; Green,

1994). Tayfun (1981) suggested that the deficiency in wave heights toward the high-wave extreme could be due to wave breaking by whitecaps. Thus, whitecapping, which appears to be prolific in the seas over the Wiroa intertidal flat, provides a likely explanation for the observed differences between Rayleigh and empirical distributions.

Of relevance then is the error associated with Rayleigh-based wave height statistics from Wiroa. Green (1994) quantified the error for a range of wave height statistics in a simple diagram (Figure 2.9) which utilises Tayfun's N (a descriptor of the sea state and local water depth). N, which is specified and evaluated in Appendix VII, is in the range 3–7000 for Wiroa Island. For seas with numerous whitecaps (low N) the error is approximately 3% for H_s, and for most of the waves at Wiroa Island it is < 1%. As the error is low and wave height statistics are not used to make estimates of nonlinear processes such as sediment transport, Rayleigh statistics are considered acceptable and are used forthwith.

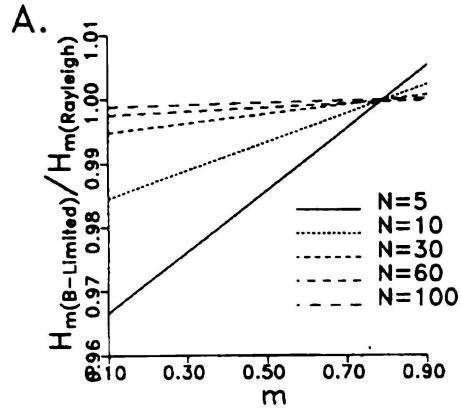

Figure 2.9: Ratio of breaking limited and Rayleigh statistics as a function of Tayfun's (1981) N-parameter. The significant wave height H_s is represented by $H_{m=1/3}$. Source: Green (1994).

The mean spectral period $\overline{T}$ and dimensionless spectral width ν are defined using spectral moments (eqn 2.21) as

$$\overline{T} = \frac{2\pi m_0}{m_1} \qquad \text{(Eqn 2.24)}$$

$$\nu = \frac{\mu_2}{\varpi^2 m_0} \qquad \text{(Eqn 2.25)}$$

where

$$\mu_2 = \frac{m_2 m_0 - m_1^2}{m_0}$$

and $\varpi = 2\pi / \overline{T}$ (Longuet-Higgins, 1975). $\overline{k}$ is the wavenumber which satisfies the linear dispersion relation (eqn 2.11) with $\overline{T}$ and $\overline{h}$, and $\overline{\lambda}$ is wavelength which is related to $\overline{k}$ as $\overline{\lambda} = 2\pi / \overline{k}$.

The Ursell parameter represents the ratio of nonlinearity to the rate of dispersion (Massel, 1996):

$$Ur = \frac{H\lambda^2}{\overline{h}^3} \qquad \text{(Eqn 2.26)}$$

The RMS and significant wave-orbital speeds at the bed were derived from linear theory as:

$$U_{\text{rms,bed}} = \sqrt{U_{w,\sigma}} \frac{1.414}{\cosh(k(z_u^* + \overline{h}))} \qquad \text{(Eqn 2.27)}$$

and

$$U_{\text{s,bed}} = \sqrt{U_{w,\sigma}} \frac{2.008}{\cosh(k(z_u^* + \overline{h}))} \qquad \text{(Eqn 2.28)}$$

respectively, where the variance $U_{w,\sigma}$ is the zero moment (m_0) of $S_{Uw}(\omega)$ as determined from eqn 2.21 and $z_u^* = (z_u - \overline{h})$. Although eqns 2.27 and 2.28 do not depend directly

upon surface wave height, their formulation is based on Rayleigh height statistics. In comparison, the 3rd orbital-speed moment, U_3, is not a Rayleigh statistic:

$$U_3 = 1.4\left[\sum_{j=1}^{N}\left|U_{w,j}\right|^3 \Big/ N\right]^{1/3} \qquad \text{(Eqn 2.29)}$$

where $U_{w,j}$ is the jth value of $U_w(t)$ and N is the number of measurements. Black and Rosenberg (1991) demonstrated that U_3, which has been shown to coincide with the 85th–90th percentile velocity (Kos'yan, 1985), is related to SSC near the bed. Linear theory was used to transform U_3 to the bed:

$$U_{3,\text{bed}} = U_3 \frac{1}{\cosh(k(z_u^* + \bar{h}))} \qquad \text{(Eqn 2.30)}$$

3.1 Consistency of Estimates of Wave Parameters

To test that wave parameters estimated from pressure data (e.g., H_s, eqn 2.23) are consistent with wave parameters estimated from velocity data (e.g., $U_{s,bed}$, eqn 2.28), a simple check was made by comparing $\eta_h(t)$ (calculated from the pressure record; eqn 2.9) and $\eta_{Uw}(t)$ (calculated from the velocity record; eqn 2.16), which were expected to be much the same. Figure 3.1 shows a typical comparison. The example shown is from the 3D-ACM during the Transect Experiment. Pressure and velocity were logged synchronously and were measured at similar elevations (< 10-cm vertical separation), meaning that differences due to attenuation with depth (i.e., Γ_h and Γ_{Uw}) were small.

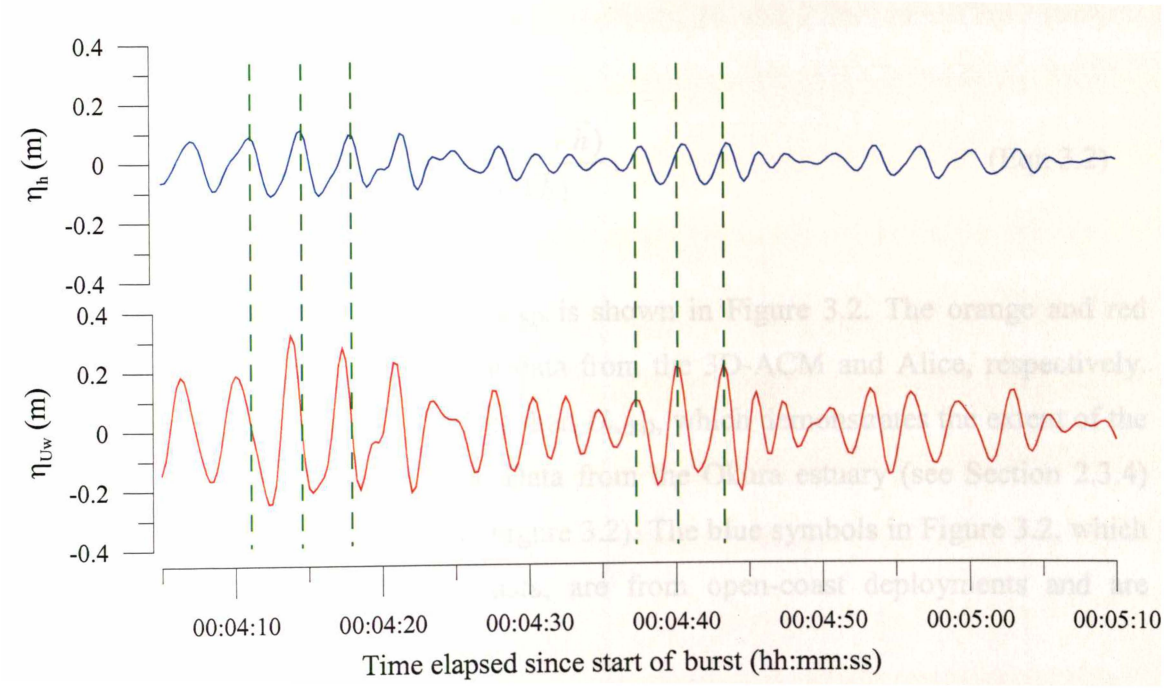

Figure 3.1: Seventy seconds of sea-surface elevation data from the 3D-ACM at site W1G (see Figure 2.1 and Figure 2.6).

At first glance, the records look comparable, with individual waves and wave groups being readily identifiable in the pressure and velocity records. However, closer inspection reveals two irregularities: the wave amplitudes in the pressure data, $\eta_h(t)$, are significantly smaller than in the velocity data, $\eta_{Uw}(t)$; and there is a phase difference between the two signals (see dashed reference marks in Figure 3.1). In this case, the

pressure and velocity data are inconsistent, in the sense that they do not simultaneously satisfy linear wave theory for a progressive wave.

The extent of this inconsistency in Transect Experiment data (Alice and the 3D-ACM) is revealed by a comparison between $U_{w,SD}$ (which is the standard deviation of wave-orbital speed estimated from velocity measurements) and $U_{w,SD,pred}$ (which is predicted from the pressure data using linear wave theory)(Figure 3.2). For this analysis, data were included only if $h_{SD,pred}$ exceeded the pressure-sensor resolution (taken as 0.01 m for Alice and the 3D-ACM), where $h_{SD,pred}$ is given by:

$$h_{SD,pred} = \frac{U_{w,SD}\sinh(\bar{k}\bar{h})\cosh(\bar{k}(z_p^* + \bar{h}))}{\omega\cosh(\bar{k}(z_u^* + \bar{h}))\cosh(\bar{k}\bar{h})} \qquad \text{(Eqn 3.1)}$$

Having passed this test, which ensures the pressure fluctuations were actually detectable by the sensor, the predicted velocity, $U_{w,SD,pred}$, was then calculated from h_{SD} and linear theory as:

$$U_{w,SD,pred} = \frac{h_{SD}\cosh(\bar{k}\bar{h}) \quad 2\pi\cosh(\bar{k}(z_u^* + \bar{h})}{\cosh(\bar{k}(z_p^* + \bar{h}))\bar{T} \quad \sinh(\bar{k}\bar{h})}. \qquad \text{(Eqn 3.2)}$$

The comparison of $U_{w,SD,pred}$ with $U_{w,SD}$ is shown in Figure 3.2. The orange and red points represent Transect Experiment data from the 3D-ACM and Alice, respectively. $U_{w,SD,pred}$ is at least a factor of two less than $U_{w,SD}$, which demonstrates the extent of the amplitude inconsistency in the data. Data from the Okura estuary (see Section 2.3.4) also exhibit the same inconsistency (Figure 3.2). The blue symbols in Figure 3.2, which show consistent pressure–velocity data, are from open-coast deployments and are discussed in later sections.

Cross-spectral analysis quantifies the phase between pressure and velocity (Figure 3.3). For the burst shown in Figure 3.1, $S_{\eta h} < S_{\eta Uw}$ at the spectral peak, where $S_{\eta h}$ and $S_{\eta Uw}$ are the sea-surface elevation spectra from pressure and velocity. Furthermore, the pressure–velocity phase, $\varphi_{h\text{-}Uw}$, is approximately -50°, meaning that η_{Uw} leads η_h by 50° across the frequencies 0.25 to 0.5 Hz, where the coherence, $C_{h\text{-}Uw}$, is high.

An indication of the range of phase lags during the Transect Experiment is shown by Figure 3.4, in which $\varphi_{h\text{-}Uw}$ at the mean spectral period ($\overline{T}$) is plotted. Data from the 3D-ACM cluster in the range -40° – -90°, whilst Alice data cover a similar range but show more scatter. Scatter in $\varphi_{h\text{-}Uw}$ from the Alice data most likely arises from the effect of directionally spread waves in the correction used to account for the horizontal separation of pressure and velocity sensors (Appendix V, refer Section 2.5.1)

For velocity and pressure data to be consistent with linear wave theory, $\eta_h = \eta_{Uw}$ and $\varphi_{h\text{-}Uw} = 0°$. For example, Doering and Bowen (1987) demonstrate that η-spectra from pressure and current (MMI) data are almost indistinguishable at frequencies between 0.10 and 0.50 Hz, while Herbers *et al.* (1992) confirm pressure and velocity are in phase. Similar results were found by Cavaleri (1980), Guza and Thornton (1980), Bishop and Donelan (1987), Guza *et al.* (1988) and Herbers *et al.* (1991).

This clearly is not the case with the Wiroa 3D-ACM and Alice data. Two questions arise. Firstly, which is "correct" – the pressure or the velocity data, or neither? Secondly, is this inconsistency indicating that linear wave theory is not applicable in this case? These questions are now addressed.

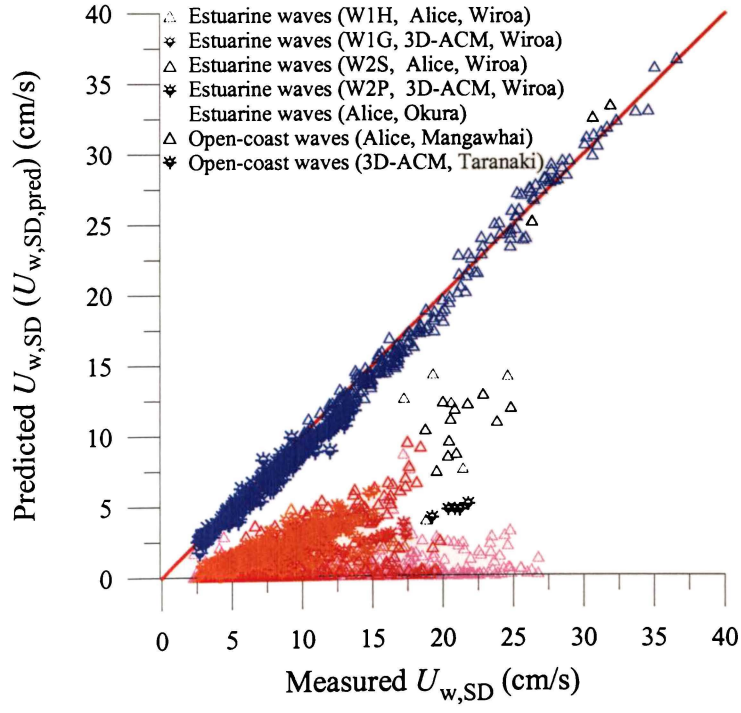

Figure 3.2: Comparison of $U_{w,SD}$ (calculated from current-meter data) with $U_{w,SD,pred}$ (predicted from pressure data and linear wave theory). The solid red line is the 1:1 line. Estuarine data is shown in shades of red (Wiroa intertidal flat and Okura estuary) while ocean data are shown in shades of blue (Mangawhai Beach and Port of Taranaki wave tower). These datasets are described in Sections 2.3.5 and 2.3.4.

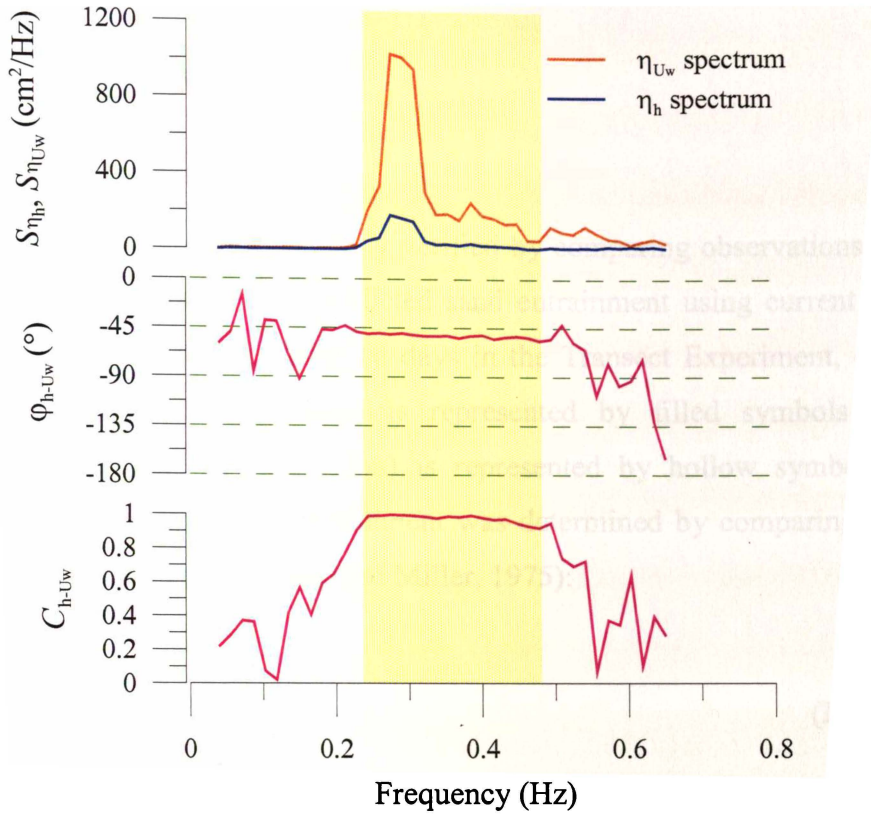

Figure 3.3: Sea-surface elevation spectra derived from pressure (h) and velocity (U_w) from burst W1G0698 (shown in Figure 3.1). Pressure–velocity phase and coherence, $\varphi_{h\text{-}Uw}$ and $C_{h\text{-}Uw}$, from cross-spectral analysis are shown in the lower two panels.

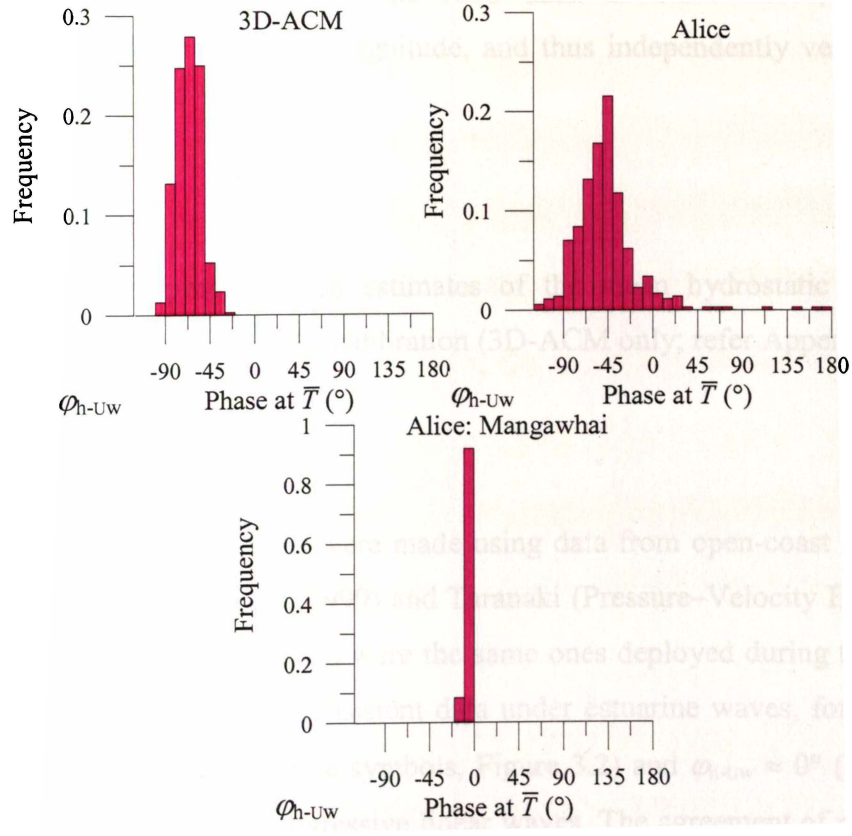

Figure 3.4: Frequency distributions of $\varphi_{h\text{-}Uw}$ at the mean spectral period ($\overline{T}$) for Transect Experiment data (top two graphs) and the Mangawhai experiment data (bottom graph).

3.2 SENSOR PERFORMANCE

Current

Current measurements were independently verified by comparing observations of sand entrainment (using ABS data) with predicted sand entrainment using current data. In Figure 3.5, which is a plot of U_s over 16 days in the Transect Experiment, observed entrainment (i.e., sand in suspension) is represented by filled symbols and no entrainment (i.e., no sand in suspension) is represented by hollow symbols (refer Section 5.4 for details). Predicted entrainment was determined by comparing U_s with the critical wave-orbital-speed (Komar and Miller, 1975):

$$\frac{\rho_f U_w^2}{(\rho_s - \rho_f) g d_s} = 0.21 (a_w / d_s)^{1/2} \qquad \text{(Eqn 3.3)}$$

following Green (1999), where d_s is the grain diameter and a_w is the wave-orbital radius. The plot shows that sand entrainment predicted by current data and eqn 3.3 equates to entrainment observed in the ABS data. In other words, the current measurements are of the expected magnitude, and thus independently verified by the ABS data.

Pressure: hydrostatic

The pressure sensors provide good estimates of the mean hydrostatic pressure as evidenced by post-experiment static calibration (3D-ACM only; refer Appendix III).

Pressure: waves

Pressure sensor tests under waves were made using data from open-coast experiments conducted at Mangawhai (Green, 1999) and Taranaki (Pressure–Velocity Experiments; Section 2.3.4). The instruments used were the same ones deployed during the Transect Experiment. In contrast to the inconsistent data under estuarine waves, for open-coast waves $\eta_h = \eta_{Uw}$ within ± 10% (blue symbols, Figure 3.2) and $\varphi_{h\text{-}Uw} \approx 0°$ (Figure 3.4), which is the expected case for progressive linear waves. The agreement of pressure and velocity measurements under ocean waves suggests that both velocity and pressure sensors are operating normally, at least for ocean conditions. This result also suggests

that linear wave theory correctly accounts for signal attenuation under waves (see Section 3.3 for details).

The relative water depth, *kh*, is similar for the estuarine and open-coast settings (Table 3.1), where *kh* is defined as the ratio of depth *h* to deep-water wavelength λ_∞:

Deep-water conditions $\quad \frac{h}{\lambda_\infty} > \frac{1}{2} \quad \text{or} \quad k_\infty h > \pi$

Intermediate-water conditions $\quad \frac{1}{2} > \frac{h}{\lambda_\infty} > \frac{1}{20} \quad \text{or} \quad \pi > k_\infty h > \frac{\pi}{10}$

Shallow-water conditions $\quad \frac{h}{\lambda_\infty} < \frac{1}{20} \quad \text{or} \quad k_\infty h < \frac{\pi}{10}$

Thus the only significant difference between the ocean and estuarine data is the wave period, which, for estuarine waves, was less than for open-coast waves (Table 3.1).

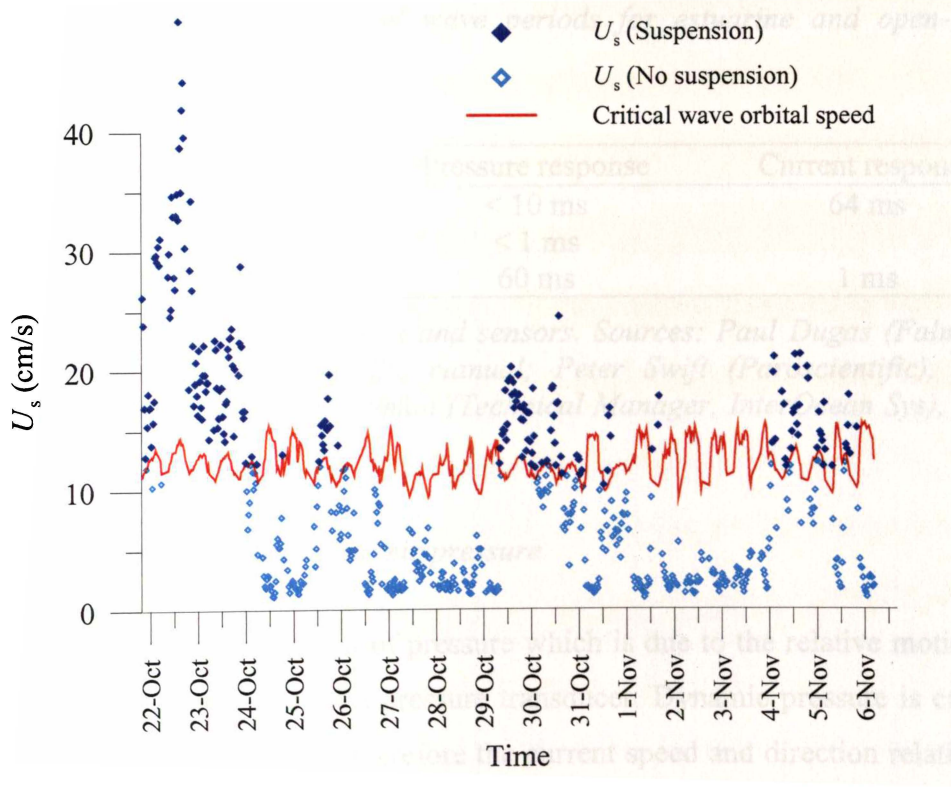

Figure 3.5: Significant wave-orbital speed (U_s) and predicted critical wave-orbital speed (Eqn 3.3) from a 16 day period. Filled and hollow symbols represent sediment "suspension" and "no-suspension" as defined from ABS data (refer Section 5.4).

As the pressure–velocity inconsistency is only present in short-period waves, it could be argued that the inconsistency is due to frequency-dependent attenuation of the wave-induced pressure fluctuations within the sensor itself; that is, an instrument frequency-response problem. While the construction of pressure sensors was not investigated in any detail, it is noteworthy that the sensors which gave inconsistent readings were both quartz crystal oscillators. Frequency-response testing was not experimentally investigated in this study as this is difficult to do. However, comments and instrument/sensor specifications from the manufacturers (Table 3.2) indicate that the pressure-sensor frequency response is adequate for the wave periods observed and the instrument sampling rates employed. However, without having actually conducted a frequency–response test, and given the unexpected results, there remains an element of uncertainty.

Experiment:	*kh* range	$\overline{T}$ range (s)
Transect Experiment	0.4–3.9	1–6
Taranaki wave-tower experiment	0.4–0.9	7–13
Mangawhai experiment	0.4–2.3	6–15

Table 3.1: Relative water depths and wave periods for estuarine and open-coast experiments.

Instrument	Logging rate (Δt)	Pressure response	Current response
3D-ACM	200 ms	< 10 ms	64 ms
Alice	250 ms	< 1 ms	
S4	500 ms	60 ms	1 ms

Table 3.2: Sampling rates from loggers and sensors. Sources: Paul Dugas (Falmouth Scientific), pers comm.; Paroscientific manual; Peter Swift (Paroscientific), pers. comm.; InterOcean manual; Joel Edelman (Technical Manager, InterOcean Sys), pers. comm.

Pressure: sensor orientation and dynamic pressure

Dynamic pressure is that component of pressure which is due to the relative motion of surrounding water particles against a pressure transducer. Dynamic pressure is caused by stagnation of the local flow and therefore the current speed and direction relative to the orientation of the transducer face controls its magnitude. As depth increases, dynamic pressure decreases and is often assumed to be a negligible component of the total pressure measured near the bed, however, the presence of dynamic pressure has potential to cause errors in the estimation of waves from pressure data (for example, Cavaleri *et al.*, 1978; Cavaleri, 1980; Lee and Wang, 1984). Under waves, the effect of

dynamic pressure is expected to be more noticeable in data from transducers oriented perpendicular to the horizontal flow than those transducers facing upward (for example), because U_w is much larger than the vertical velocity w_w (except near the surface where U_w and w_w can be a similar magnitude).

During the Transect Experiment, two pressure-sensor orientations were employed: vertical (up or down facing) and horizontal (direction not accurately recorded). The data from pressure sensors with a vertical orientation (Alice and 3D-ACM) were inconsistent when compared with collocated current data, as previously described (e.g., Figure 3.1). Pressure–velocity comparisons for the horizontal-facing pressure sensors (Dobies and S4s) were not possible because Dobies do not measure current and, whilst the S4 does, its large sampling diameter (c. 2-m diameter; Edelman, 2000) relative to typical wavelengths (c. 5–8 m) casts some doubt over the suitability of S4 current data for measuring estuarine waves.

To make comparisons of pressure-sensor orientation under an estuarine wave field, S4 pressure, 3D-ACM pressure and 3D-ACM current data (Figure 3.6) were compared during a brief period of the Transect Experiment when an S4 and 3D-ACM were deployed adjacent to one another (see Appendix II and IV). Wave-height estimates made from S4 pressure data concur with estimates from 3D-ACM current data but not with the 3D-ACM pressure data, which is smaller as previously noted. This data provides the only pressure-pressure comparison in the Transect Experiment and shows that pressure fluctuations recorded by the 3D-ACM (vertical orientation) are much smaller than those recorded by the S4 (horizontal orientation). It is also the only comparison in which pressure (S4) is consistent with velocity (3D-ACM). The S4–3D-ACM pressure comparison suggests either a problem with measurement of fluctuating pressure (but not time-averaged pressure) by the 3D-ACM, or that dynamic pressure and sensor orientation are important, despite the expectation that any errors due to dynamic pressure would appear in the S4 data (which was oriented horizontally). The agreement between 3D-ACM current and S4 pressure data (horizontal orientation), but inconsistency between 3D-ACM current and 3D-ACM pressure data, warrants further investigation as follows.

A brief field experiment (refer Section 2.3.4; Pressure–Velocity Experiments) was contrived to test whether pressure-sensor orientation could be a cause of the observed inconsistency. The experiment was conducted on the Wiroa intertidal flat during a single tidal inundation with onshore winds (WSW, 8–10 m/s, gusting up to 16 m/s) and associated wave activity. Two Dobies and two 3D-ACMs were deployed, with one of each instrument type in a vertical (up-facing) position, and the other in a horizontal position. As noted in Figure 3.7, the horizontal Dobie was occasionally reoriented relative to the observed wave direction (as observed in the field), whilst the horizontal 3D-ACM was facing offshore into the approaching waves at all times.

Figure 3.7 demonstrates that vertically-oriented pressure sensors consistently report lower wave-induced pressure fluctuations. However, the difference between vertical and horizontal pressure sensor orientations is small (factor of 1–1.4; Figure 3.7) compared to the observed pressure–velocity inconsistency (factor 2–50; Figure 3.2). Large differences were observed in data from the two Dobies during the ebb tide, but not in the data from the two 3D-ACMs. It is difficult to ascertain why this occurred because these differences coincided with Dobie reorientation and the turning of the tide. Even so, the differences were still smaller than the inconsistency. Prior to high-tide the reorientation of the horizontal Dobie with respect to wave direction appears to have had no effect on the wave-height estimates from pressure (H_s) when compared to vertical Dobie data, indicating that dynamic pressure is not significant.

The data from this experiment were limited to a single tidal inundation and do not match the pressure-velocity inconsistencies which have been noted in the Transect Experiment data. That is, $\eta_h \approx \eta_{Uw}$ and $\varphi_{h\text{-}Uw} \approx 0°$; but for all 3D-ACM Transect Experiment data $\varphi_{h\text{-}Uw} \approx -45° - -90°$. The absence of inconsistent data from this short experiment makes it difficult to reliably ascertain the importance of dynamic pressure. Further research is needed to elucidate the problem: a longer experiment, different deployment locations, an array of pressure sensors at different orientations/angles, and accompanying velocity measurements are required.

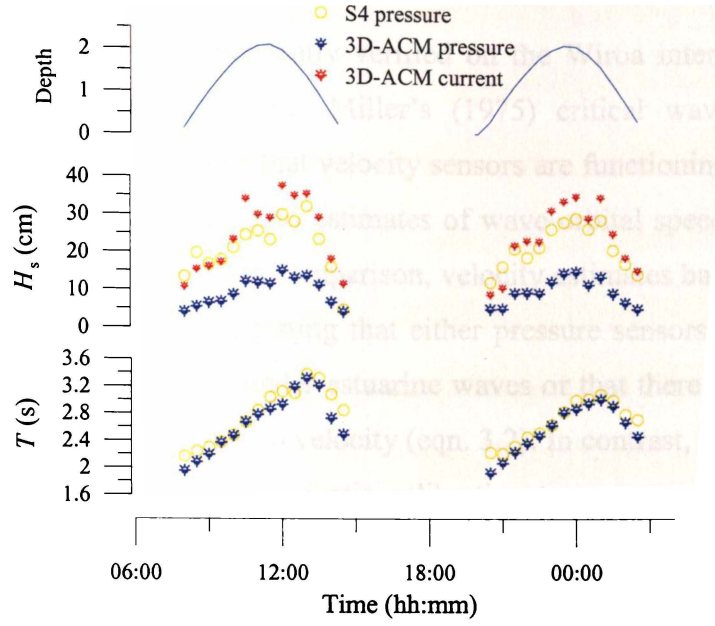

Figure 3.6: Comparison of pressure measurements (H_s) from a collocated S4 (O S4DW model) and 3D-ACM (✱). H_s derived from the 3D-ACM velocity measurements is also presented. Although the magnitude inconsistency is observed in the 3D-ACM pressure data (when compared to velocity) it is not observed in the S4 pressure data (which has a horizontal rather than a vertical orientation).

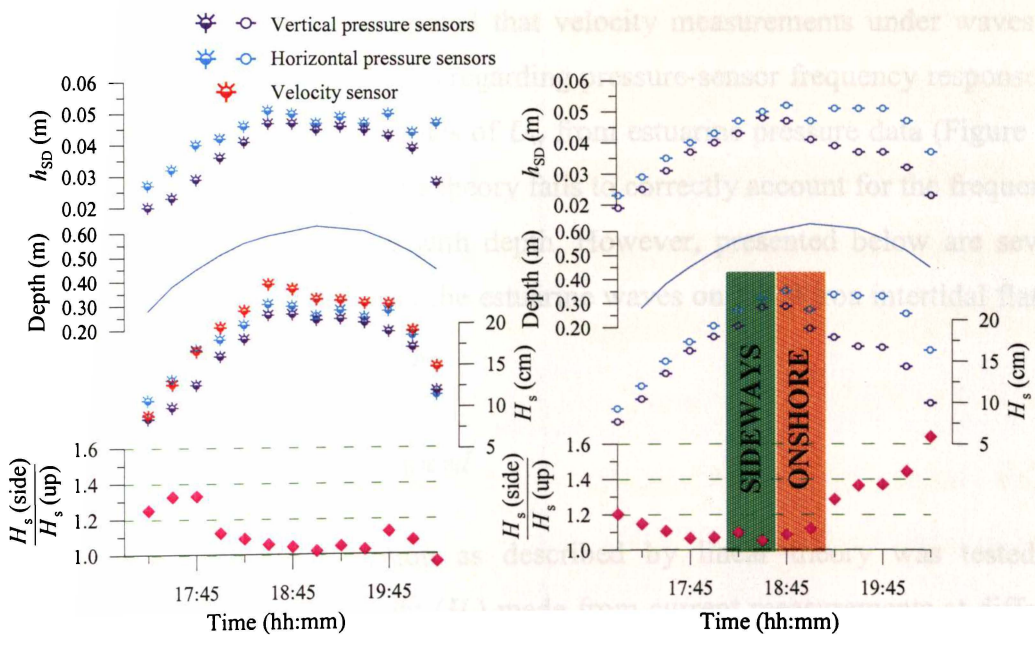

Figure 3.7: Wave statistics from the dynamic-pressure experiment using Dobie (-o-) and 3D-ACM (✱) pressure and velocity sensors. The graph on the left presents data from the two 3D-ACMs and on the right are Dobie data. As indicated by the green and orange stippled regions, the sideways facing Dobie was occasionally reoriented with respect to the wave field: onshore indicates the pressure sensor facing in the direction of wave travel, sideways is oriented facing along the wave crest, and at all other times Dobie faced into the waves.

Current measurements were independently verified on the Wiroa intertidal-flat using ABS suspension data and Komar and Miller's (1975) critical wave-orbital-speed equation (eqn. 3.3). These data show that velocity sensors are functioning normally and that current measurements provide good estimates of wave-orbital speed and sediment entrainment under estuarine waves. In comparison, velocity estimates based on pressure data (Figure 3.2) are too small, suggesting that either pressure sensors (3D-ACM and Alice) are not functioning properly under estuarine waves or that there is a problem in the theory used to transform pressure to velocity (eqn. 3.2). In contrast, S4 pressure data does compare well with velocity data. Static calibration tests, measurement of mean water depth, measurement of waves in an open-coast setting (Figure 3.2), and the manufacturers' specifications for frequency response suggest that all pressure sensors should be functioning normally. Investigations into the effect of sensor orientation were inconclusive and frequency response tests were not performed.

3.3 Validity of Linear Wave Theory

Independent evidence has demonstrated that velocity measurements under waves are accurate. If the manufacturers' claims regarding pressure-sensor frequency response are to be accepted, then the underestimates of U_w from estuarine pressure data (Figure 3.2) gives the impression that linear wave theory fails to correctly account for the frequency-dependent attenuation of pressure with depth. However, presented below are several lines of evidence which suggest that the estuarine waves on the Wiroa intertidal flat are well described by linear wave theory.

Depth attenuation of wave-orbital speed

Depth attenuation of wave motion as described by linear theory was tested by comparing estimates of wave height (H_s) made from current measurements at different elevations. The current data were taken from Alice's vertical array of MMI current meters (refer Section 2.3 and Table A1.1 for details). The results presented in Figure 3.8 compare data from the lowest current meter (MMI 1; z_u = 13.5 cm) with data from current meters at higher elevations (MMI 2, MMI 3, MMI 4; z_u = 45.5, 82 and 115.5 cm). In the left panel of Figure 3.8, attenuation is obvious: measured wave-orbital speed increases with proximity to the surface, as expected. In the right panel (Figure 3.8), the

same data are transformed into the surface wave statistic H_s using eqn 2.23 (refer Section 2.5.2). All estimates of H_s are similar (Figure 3.8b), showing that depth-attenuation is reasonably well described by linear wave theory.

Measures of linearity

A number of parameters are available for indicating the "degree of wave nonlinearity". One approach defines 'regions' for different wave theories in the nondimensional space defined by the ratios $\gamma = H/h$ and relative water depth, h/λ (kh). Burst-averaged S4, 3D-ACM and Alice wave data (Transect Experiment) are plotted on a h/λ–H/h diagram (Figure 3.9). The data fall within the region of linear wave theory, although some data approach the wave steepness (Muir Wood, 1969)

$$\frac{H}{\lambda} = \frac{1}{16}\tanh(kh)$$

that represents the boundary to Stokes theory, while the limiting wave steepness defined by (Miche, 1944):

$$\left(\frac{H}{\lambda}\right)_{max} = \frac{1}{7}\tanh(kh) \qquad \text{(Eqn 3.4)}$$

is not approached by the burst-averaged data.

Bursts in which fluctuating pressure was smaller than the pressure-sensor resolution were not included in the wave analysis, since it is not possible to reliably transform such data into surface-wave statistics. Such bursts coincide with either calm sea-surface conditions (i.e., no waves) or *deep-water* waves, which explains the sharp cutoff in the data coinciding with the *deep-water* linear wave theory boundary.

The degree of wave nonlinearity may be considered by comparing the critical Ursell parameter, Ur_{crit} (Longuet-Higgins, 1956), which represents the boundary between linear and cnoidal wave theory (Figure 3.9):

$$Ur_{crit} = \frac{32\pi^2}{3} = 105.28, \qquad \text{(Eqn 3.5)}$$

with the Ursell parameter, Ur, (eqn 2.26). Ur was evaluated from Transect Experiment data with $\overline{H}$ and $\overline{\lambda}$. For all bursts, $\overline{Ur} < 40$, with the vast majority having $\overline{Ur} < 10$. Small $\overline{Ur}$ suggests that waves are linear and that nonlinear wave theories will be unable to account for the pressure–velocity inconsistency.

Finally, there are no obvious relationships between η_{Uw}/η_h and the parameters which define theory boundaries drawn in Figure 3.9 (e.g., H/h, h/λ, Ur, T, k, h, H).

Collectively, these results suggest that linear theory is a good descriptor of the estuarine waves measured, at least for velocity-based measurements.

Conclusions

The applicability of linear wave theory for estuarine waves measured on the Wiroa flat was examined using three tests – test of depth attenuation of wave-orbital motion, test using wave-theory application diagram, and test by comparison of Ur with Ur_{crit}. None of these tests suggest linear wave theory should be rejected. It is concluded that inapplicability of linear theory is unlikely to be the cause of the pressure–velocity inconsistency.

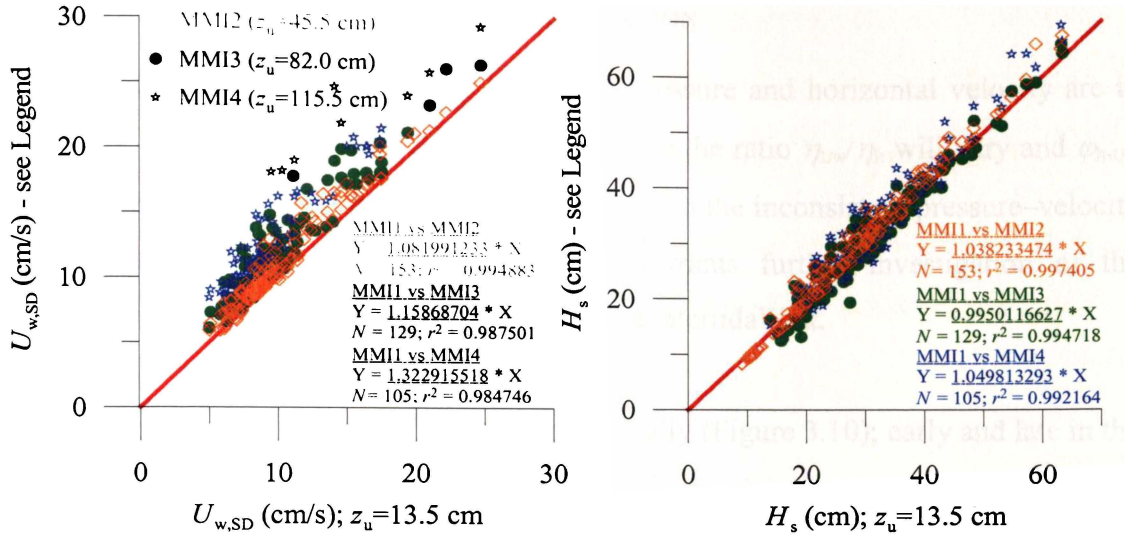

Figure 3.8: Depth attenuation of wave-orbital motions: comparison of $U_{w,SD}$ using data from *MMI 2, MMI 3 and MMI 4 with data from the lowest sensor, MMI 1 (left panel); and comparison of that same data when expressed as* H_s *(using linear theory to account for the frequency-dependent attenuation of wave motion with depth,* Γ_{Uw}*). There are fewer comparisons at higher sensor elevations due to longer exposure periods. Text indicates linear regression equations (forced though the origin) and statistics. The slopes in the regression equations (underlined) serve as a useful summary of the depth-attenuation of velocity in the first graph (left) and of the performance of* Γ_{Uw} *in the second (right).*

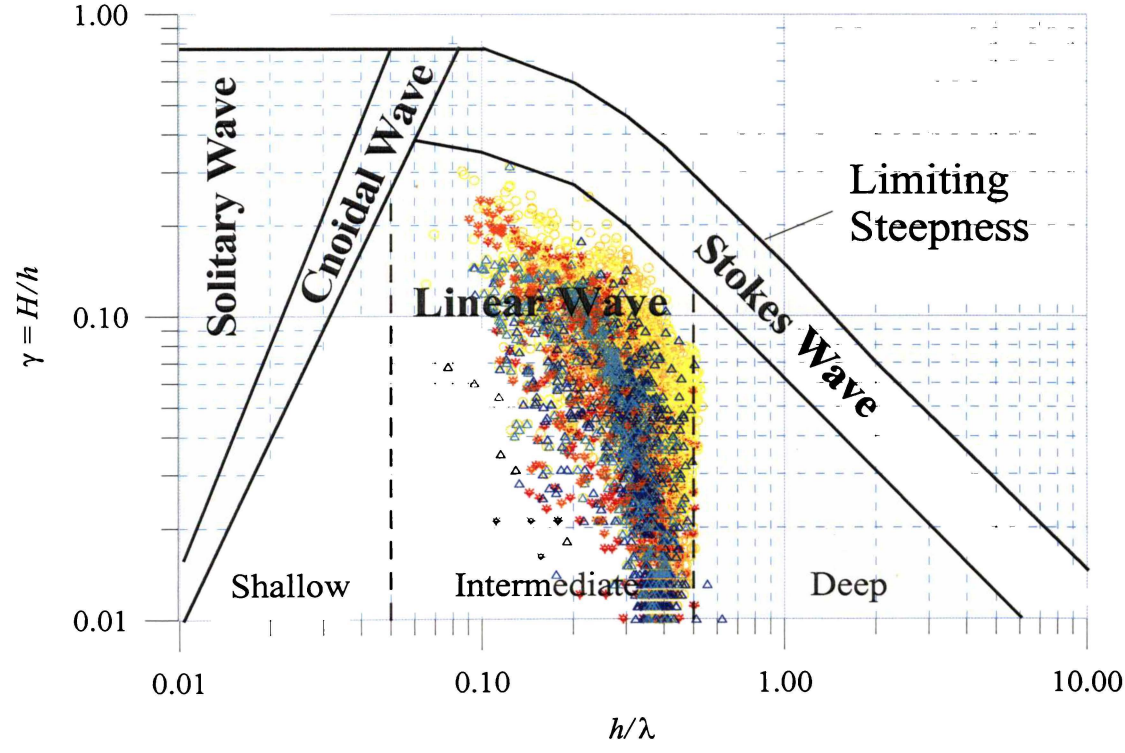

Figure 3.9: h/λ–H/h diagram illustrating regions of applicability of different wave theories and overlain with estuarine wave data (burst means) from Alice (Δ), 3D-ACMs (✱) and S4s (O) during the Transect Experiment. The diagram is arranged to give preference to most simplistic theories in those areas where there is overlap (Komar, 1998)

3.4 STANDING WAVES – A POSSIBLE EXPLANATION

Under linear progressive waves, $\eta_{Uw} = \eta_h$ and pressure and horizontal velocity are in phase ($\varphi_{h\text{-}Uw} = 0°$). However, under standing-waves the ratio η_{Uw}/η_h will vary and $\varphi_{h\text{-}Uw} = 90°$. These features are observed, to some extent, in the inconsistent pressure–velocity data from the Transect Experiment, which warrants further investigation of the possibility that standing waves exist on the Wiroa intertidal flat.

During each inundation η_{Uw}/η_h varies systematically (Figure 3.10); early and late in the inundation η_{Uw}/η_h is large, but decreases toward high tide, though never falling below ~2.5. While this pattern is persistent in Transect Experiment wave data, the size of η_{Uw}/η_h varies significantly from tide to tide and consequently scatterplots reveal no trend with depth (or other wave/tide parameters).

The phase $\varphi_{h\text{-}Uw}$ also varies over the tidal cycle: $\varphi_{h\text{-}Uw}$ decrease from 90° as the water-level rises, but never gets lower than about 25°, which occurs near high tide. As with η_{Uw}/η_h, the pattern is persistent, but the actual values vary from tide to tide. $\varphi_{h\text{-}Uw}$ was also compared with several wave/tide parameters and no relationships were evident.

Systematic variation in both η_{Uw}/η_h and $\varphi_{h\text{-}Uw}$ is suggestive of standing waves where either the nodal structure migrates with the rise and fall of the tide or where the relative energies of progressive and standing waves (in a mixed standing/progressive-wave field) changes with the state of the tide. The tendency of $\varphi_{h\text{-}Uw}$ to shift toward 0° with increasing water depth suggests that when fetch is large, progressive waves may dominate in a mixed progressive/standing wave field.

There are, however, a number of factors which cast doubt on the standing-wave hypothesis.

Firstly, inconsistent data were observed at four locations, but were always from the same two instruments, suggesting a measurement problem. Secondly, assuming the existence of standing waves, then the magnitude inconsistency (always large η_{Uw} and small η_h) suggests sensors were located close to a standing-wave node, but were never located close to an antinode (small η_{Uw} and large η_h). In four separate deployment

locations (10 week duration) across the intertidal flat it is possible, but perhaps not very likely, that sensors would always be in proximity of a standing-wave node. In any case, presumably the tide would translate any standing wave nodal structure across the flat.
To further investigate the possibility of standing waves, the ADV data from the Transect Experiment (see Table A2.1) were examined. As the ADV has no pressure sensor, the vertical component of velocity, $w(t)$, was used to determine η_w and to make magnitude (η_{Uw}/η_w) and phase ($\varphi_{w\text{-}Uw}$) comparisons with measured U_w. The expected phase relation $\varphi_{w\text{-}Uw}$ is 90° for progressive waves and 0° for standing waves. For linear progressive waves $\eta_{Uw}/\eta_w = 1$ and for standing waves η_{Uw}/η_w is variable depending on location within the node-antinode structure.

The ADV data show that $\eta_{Uw}/\eta_w \approx 1$ (Figure 3.11) and $\varphi_{w\text{-}Uw} \approx 0°$. The few bursts where η_{Uw}/η_w is large, may be explained by proximity of the sampling volume to the bed (i.e., $w \rightarrow 0$ as $z \rightarrow 0$), or contamination of the data by surface bubbles, particularly when the water depth is small. Hence the ADV data show no indication of standing-wave activity.

Conclusions

Some of the measured pressure and velocities are consistent with the existence of standing waves on the Wiroa flat, others are not. Estuarine flats receive incident wave energy at high frequencies and are probably the least ideal surface (due to the extremely low gradient) from which wave reflection might occur and standing waves develop as a result. The steep beachface on the upper flat may provide some means of reflection, however, it cannot be responsible for standing waves as it is only inundated for a short period during each tidal inundation. The standing-wave evidence is difficult to interpret because the Transect Experiment was not devised with standing waves in mind.

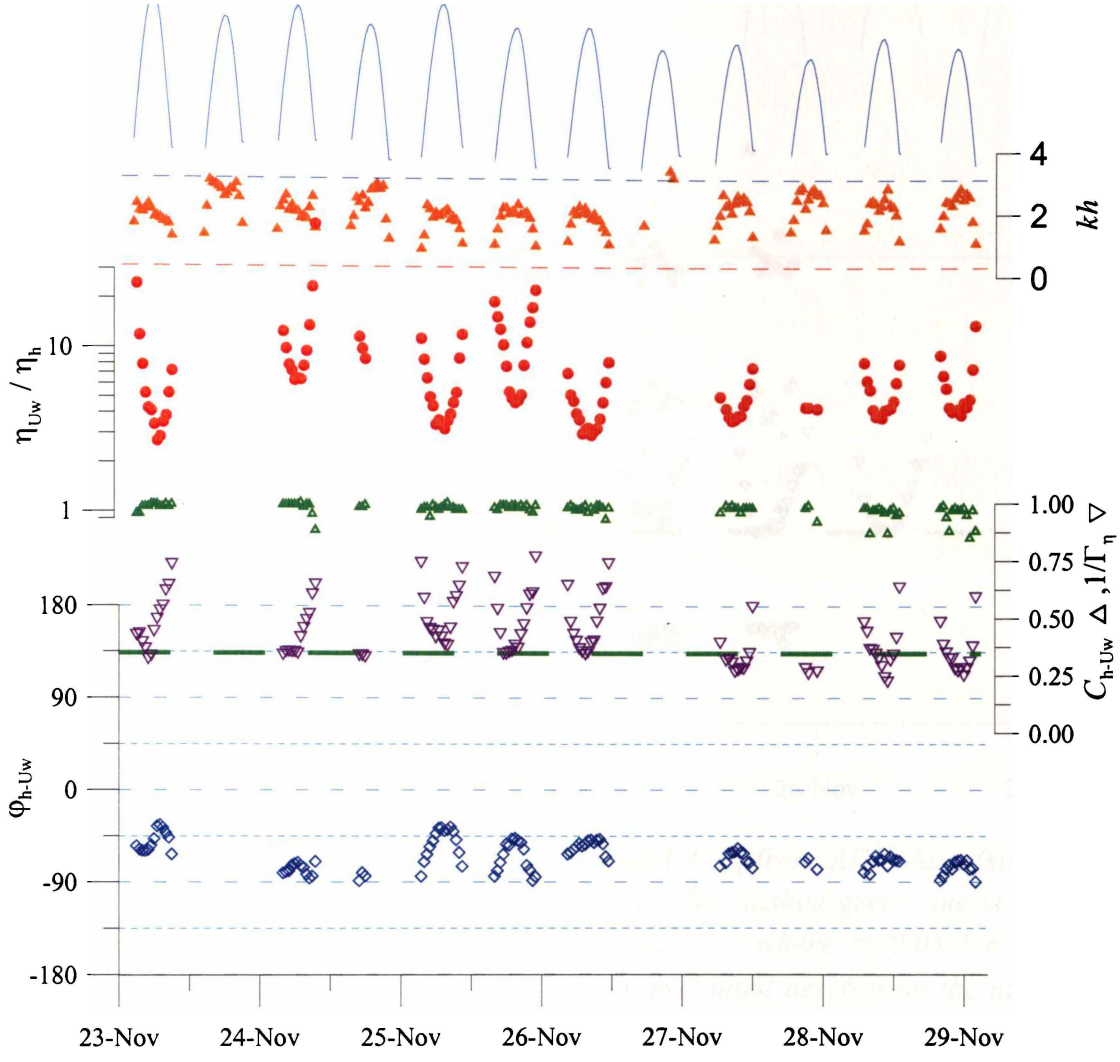

Figure 3.10: Time series of η_{Uw}/η_h, $\varphi_{h\text{-}Uw}$, $\overline{h}$, kh, and $1/\Gamma_\eta$. $\varphi_{h\text{-}Uw}$ was evaluated from the cross-spectrum at $\overline{T}$. Dashed blue and red lines on the kh panel indicate deep and shallow-water limits, respectively. The dashed green line is the 95% confidence limit for $C_{h\text{-}Uw}$, defined as $C^2_{1-\alpha} = 1-\alpha^{[2/\nu-2]}$ where α=0.05 for the 95% confidence limits and ν is the degrees of freedom evaluated as 16 from the number of spectral estimates merged (8). When $C_{h\text{-}Uw} < C^2_{1-\alpha}$ the spectrum is incoherent and due to chance alone (Emery and Thomson, 1998).

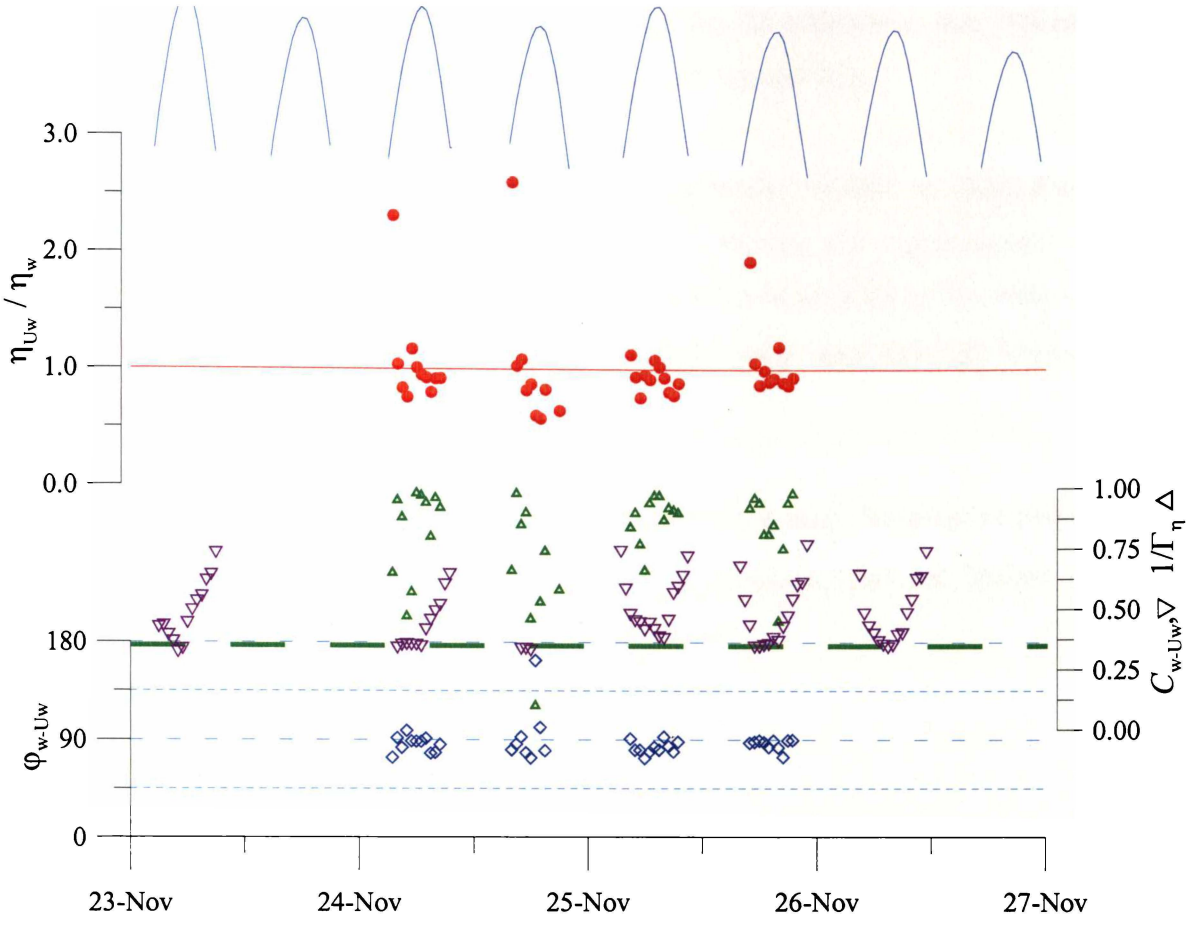

Figure 3.11: Time series of η_{Uw}:η_h, $\varphi_{w\text{-}Uw}$, $C_{h\text{-}Uw}$ and $1/\Gamma_\eta$ from ADV data (site W1E). $\varphi_{w\text{-}Uw}$ was evaluated from the cross-spectrum at $\overline{T}$. The dashed green line is the 95% confidence limit for $C_{w\text{-}Uw}$, defined as $C^2_{1-\alpha} = 1-\alpha^{[2/\nu-2]}$ where α=0.05 for the 95% confidence limits and ν is the degrees of freedom evaluated as 16 from the number of spectral estimates merged (8). When $C_{w\text{-}Uw} < C^2_{1-\alpha}$ the spectrum is incoherent and due to chance alone (Emery and Thomson, 1998).

3.5 CONCLUSIONS

There is an inconsistency between pressure and velocity measurements from two instruments at four locations on the Wiroa flat. Similar inconsistencies were also found in an analysis of Green and MacDonald's (2001) data from Okura estuary. The inconsistency ($\eta_{Uw}/\eta_h >> 1$ and $\varphi_{h\text{-}Uw} \neq 0$) could be interpreted as evidence for the existence of standing waves. However, data from other instruments refute this. Further investigation is required to adequately resolve the standing-wave possibility. Subsurface and surface-piercing gauges should be deployed so that measurements span several locations across any possible standing wave node–anti-node structure.

The pressure-velocity inconsistency is most likely due to pressure-sensor frequency response, although manufacturers' specifications do not support this.

There is no evidence to suggest the velocity measurements provide an inaccurate or unreliable description of wave-orbital motions. In particular, the current-meter data show that velocity measurements under estuarine waves can be used in the context of sediment entrainment and, by implication, bed shear stress and sediment transport calculations.

Static calibrations demonstrate that pressure measurements may be used to estimate mean water depth, however fluctuating pressure information must be treated with caution and are not used for inferring wave-orbital speeds.

4.1 INTRODUCTION

Estuarine waves are generated as the wind blows across local fetch-limited seas. In addition to fetch, factors such as water depth, estuarine geometry and bathymetry place important constraints on wave growth. The aim of this chapter is to describe factors important for estuarine wave generation and to characterise the estuarine waves which arrive at the Wiroa Island intertidal flat, including their temporal variation.

4.2 WAVE GENERATION AND EVOLUTION IN SHALLOW TIDAL ESTUARIES

Wave generation is generally considered to be a function of three factors: wind speed, which controls the rate at which energy is imparted into the sea surface (Wiegel, 1964; Bretschneider, 1966); wind duration, which is the length of time that the wind blows; and fetch length, which is the distance over which the wind blows. Both fetch and duration restrict the opportunity for wind energy to be transferred to waves (Komar, 1998). In shallow tidal estuaries, the wave field is also influenced by fetch and bottom friction which vary with the rise and fall of the tide. In addition, whitecapping mediates wave growth across the estuary. These factors are discussed as they apply to Wiroa Island/Manukau Harbour.

The Manukau Harbour (Figure 2.1) experiences locally generated, short-period wind waves (typically 2–4 s) and is effectively sheltered from energetic ocean swell by its large shallow ebb-tidal-delta (1250×10^6 m^3; Hicks and Hume (1996)), long entrance channel (~10 km) and large Pleistocene sand barrier (Awhitu Peninsula). Neilson (1998) observed some double-peaked wave spectra from a channel margin and suggested that the longer period spectral peak (c. 5 s) may represent 'remnant' swell wave energy. However, no such observations have been made on intertidal flats and the energy contribution of swell in the southern harbour is considered to be negligible (Gorman and Neilson, 1999).

Fetch length

At high tide, fetch is a function of the size and shape of the estuary ("geometry") and the direction from which the wind blows. Large waves can be generated in elongate lagoons and fjords, for example, if the prevailing winds coincide with the long fetch axis, or comparatively small waves if not (e.g., Strangford Lough, Ryan and Cooper, 1998; Malvarez *et al.*, 2001). In Manukau Harbour, the squarish geometry is favourable for large fetches in every wind direction. At Wiroa Island the longest high-tide fetches (14–18 km) are aligned with the 210–270° sector (Figure 4.1), which also delivers the prevailing wind. About some orientations (e.g., 200–210° and 270–280°), small changes in wind direction significantly alter the available fetch (see blue/red lines in Figure 4.1) and, therefore, wave conditions.

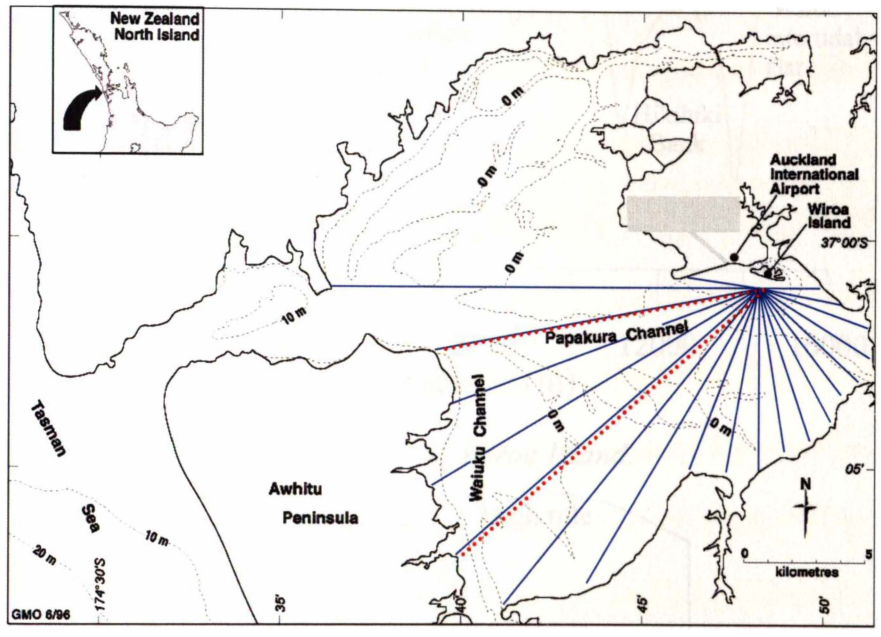

Figure 4.1: Map of Manukau Harbour showing fetch lengths for wind/wave sectors at 10° increments.

The emergence and submergence of intertidal banks causes temporal (tidal) variation in the fetch length, and therefore in the wave field. An example scenario was prepared for the SW transect (prevailing wind) leading to Wiroa Island, which includes four intertidal banks (see Figure 4.2). At low tide nearly half of the estuary floor is exposed and fetch is restricted to the deep tidal channels; for Wiroa the low-tide SW fetch is the 1.8-km-stretch across the Papakura Channel (Figure 4.2 and Figure 4.3). As the tide rises, water spills across the central harbour banks and the fetch length grows, in large steps or transitions (e.g., Hangore Bank crossing), up to a maximum of 16.4 km at high tide. The process reverses on the ebbing tide. Of course, the fetch pattern shown in Figure 4.3 only pertains to the SW wind as the bottom profile is different for each wind direction (e.g., compare contours along profiles with dashed red lines; Figure 4.1).

Temporal variations in fetch length are also influenced by the factors controlling water levels. In tidal estuaries these include: the tidal range (including tidal inequalities, lunar declination, peri/apogee, peri/aphelion, syzygy and so on), tidal asymmetry (i.e., the shape of the tidal wave), the type of tide (e.g., semi-diurnal, mixed or diurnal) and storm surge (e.g., Bartholdy and Aagaard, 2001). Thus, temporal variation in the fetch also reflects peculiarities of tidally-induced and meteorologically-induced variation in water level.

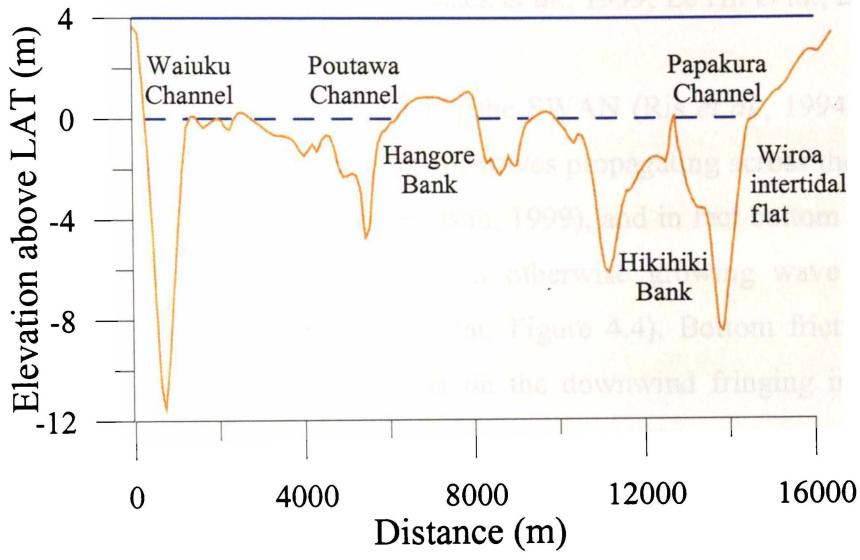

Figure 4.2: Bathymetry along SW transect to Wiroa Island.

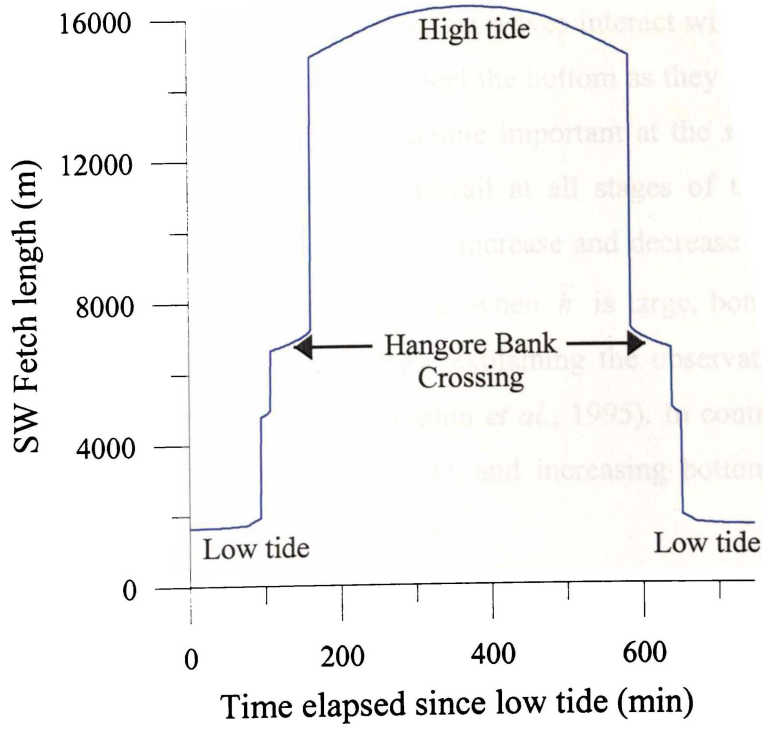

Figure 4.3: Time evolution of fetch length for a SW transect (Figure 4.2) and a 4–m spring tidal range.

Bottom friction

On the open coast, where gravity-wave wavelengths are longer and bed gradients are steeper compared to estuarine intertidal flats, waves shoal and deform across relatively short distances. Energy losses due to bottom friction are often considered to be negligible (e.g., Thornton and Guza, 1983; Dally *et al.*, 1985; Komar, 1998) and most energy losses are attributed to wave breaking. In comparison, on estuarine intertidal flats, bottom friction can be a significant, as waves travel long distances over near-flat surfaces in *intermediate* water depths (e.g., Black *et al.*, 1999; Le Hir *et al.*, 2000).

In Manukau Harbour, wave simulations using the SWAN (Ris *et al.*, 1994) numerical model indicate bottom friction is important for waves propagating across the wide, flat, central-harbour sandbanks (Gorman and Neilson, 1999), and in fact bottom friction can counter and even reduce wave heights in an otherwise growing wave field (e.g., Hangore Bank and Wiroa Island intertidal flat; Figure 4.4). Bottom friction was the single largest energy-dissipating mechanism on the downwind fringing intertidal flat (i.e., Wiroa).

Spatial patterns in *kh* can indicate zones in which bottom friction may be large, as shown in Figure 4.5. The plot, which is for a 7-m-long wave propagating across the SW transect at a tidal stage of 2.5 m, demonstrates that waves interact with the bed as they traverse *intermediate-depth* sandbanks, do not feel the bottom as they cross intervening channels, and that shoaling processes may become important at the *shallow* estuarine coastline/fringes. This general pattern may prevail at all stages of the tide under a tidally-modulated fetch as wavelength and depth increase and decrease together, which causes *kh* to change slowly. During spring tides, when $\bar{h}$ is large, bottom friction on central banks may dissipate less wave energy, explaining the observation that larger waves tend to occur on spring tides (e.g., Dolphin *et al.*, 1995). In contrast, increasing downwind wavelength equates to decreasing *kh* and increasing bottom friction over downwind sandbanks and fringing intertidal flats.

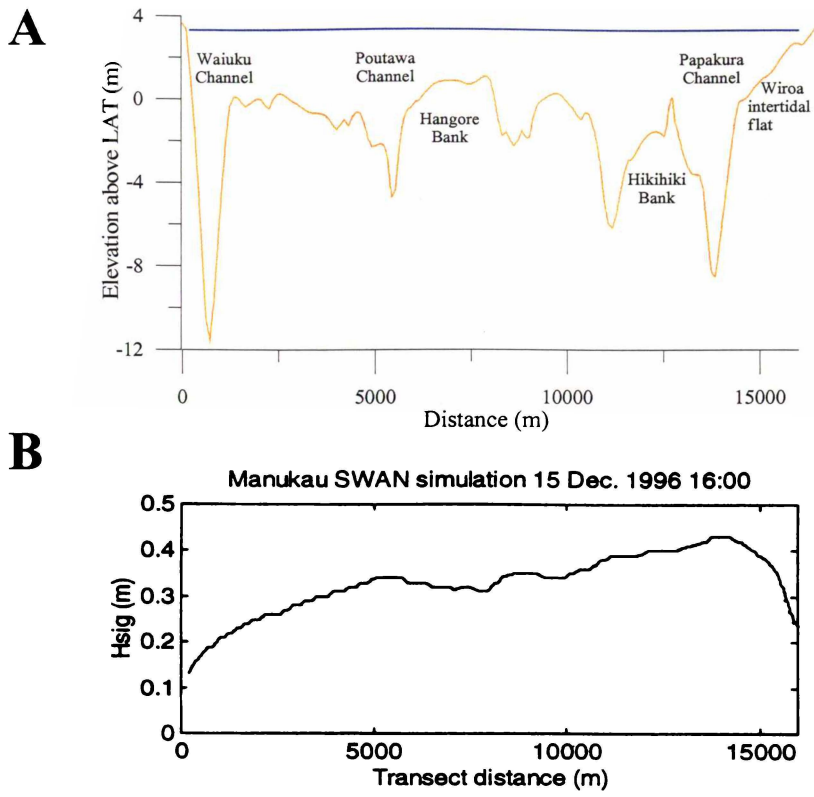

Figure 4.4: **A** *Bathymetry along the SW transect from Wiroa Island. The solid blue line indicates the water depth (3.34 m) used in* **B**, *the output from the SWAN model. The distance axes are aligned. The model run is for a steady wind of 7-m/s blowing along the harbour transect. Falling wave height associated with the bottom friction term is observed where waves propagate across shallow sandbanks, in particular the Hangore Bank and the Wiroa Island intertidal flat. Source:* (Gorman and Neilson, 1999).

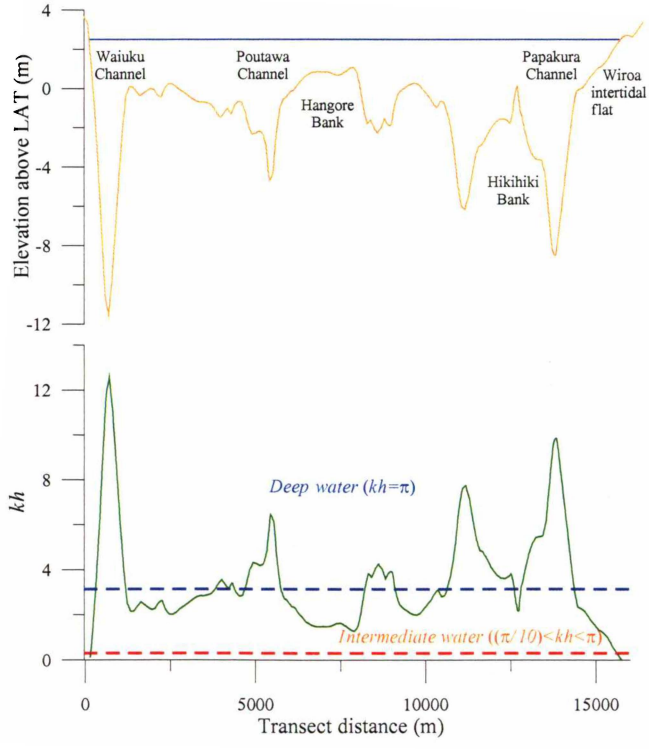

Figure 4.5: Example of kh experienced by a 7-m-long wave propagating along the SW transect for a tidal elevation (solid blue line) of 2.5 m above LAT.

Energy dissipation due to depth-limited breaking and whitecapping are other mechanisms by which wave energy/heights decrease. In semi-enclosed water bodies with locally generated seas, depth-limited wave breaking is thought to be negligible (Young and Verhagen, 1996; Gorman and Neilson, 1999), with the exception of estuarine beaches, where waves encounter sudden changes in depth. In contrast, whitecapping is common in estuaries. Whitecapping is the localised oversteepening of a wave which is distinct from the steepness-limited breaking that arises from shoaling-induced changes in H and λ. Consequently, whitecapping is unrelated to water depth and results in energy losses across large sections of the available wave fetch. Gorman and Neilson (1999) found that whitecapping was the largest source of wave energy dissipation in Manukau Harbour (although they note that the term describing whitecapping is not well formulated in the SWAN model), with the exception of the Wiroa flat, where bottom friction dominated.

4.3 WAVES AT WIROA ISLAND

The description of waves at Wiroa Island is based on analysis of Alice data from the lower intertidal flat (site W1H, Figure 2.6). Alice data were used in preference to nearby S4A data because the faster sampling rate (Δt=0.25-s cf. 0.5 s) employed by Alice is better suited to measurement of short-period waves. In addition, the current-meter array on Alice provides information on wave-orbital motions at more than one location in the water column. Surface wave-characteristics were described using data from the current-meter closest to the surface, while near-bed orbital motions were described using data from the lowest current meter.

Individual waves were defined from $\eta(t)$ using a zero upcrossing analysis, where $\eta(t)$ is inferred from $U_w(t)$ and linear wave theory (eqn 2.16). The elapsed time between successive upcrossings defines the period, T_z, and the corresponding wave height, H_z, is:

$$H_z = \eta_{max} - \eta_{min} \qquad \text{(Eqn 4.1)}$$

where η_{max} and η_{min} are, respectively, the maximum and minimum sea-surface elevations in an individual wave cycle.

The wavenumber for each wave, k_z, was determined by solving the linear dispersion relation (eqn 2.11) for T_z and $\bar{h}$. Wavelength ($\lambda_z = 2\pi / k_z$), steepness ($[H/\lambda]_z$), relative depth ($k_z \bar{h}$) and the height to depth ratio ($H_z / \bar{h}$) were also calculated.

4.3.1 Characteristics of the Sea Surface

Wave heights on the outer flat were typically 5–30 cm, with periods of 1.75–3 s and wavelengths of 400–800 cm (Figure 4.6[1]). The maximum recorded wave height (H_{max}) at W1H was 103 cm, but waves of up to 120-cm were measured 200-m further offshore at site W1I. The highest waves have periods of 2.5–5 s whilst waves of longer periods ($T_z > 5$ s) are rare and of relatively low H_z (< 20 cm). The sharp boundary on the left limb of Figure 4.6A represents limiting wave steepness, which will be discussed subsequently. Scatter plots do not reveal the typical co-varying wave heights, periods, and lengths expected to be associated with tidally-modulated fetch lengths because the variation in event magnitude (Figure 4.6 contains 10 weeks of wave data) is as large as the variation across intra-tide time scales (temporal variations are investigated later in this section).

Figure 4.7 provides a useful illustration of the degree to which waves are interacting with the bed. Most waves (95%) are of *intermediate kh* with the most common joint-categories being $k_z \bar{h}$ = 1.5–2.5 with T_z = 2–3 s. These waves 'feel' the bottom, but do not undergo significant shoaling transformations experienced by *shallow-water* waves, which make up 0.18% (28 waves) of the Alice dataset. The absence of *deep-water* waves has already been discussed (Chapter 3).

Wave direction (expressed as the direction of wave travel) on the lower flat corresponds to the two dominant wind directions, SW and NE (Figure 4.8). Given the short fetch, offshore propagating waves (NE winds) are usually very small (small height, short period) and difficult to measure with bottom mounted current meters (refer Section 4.3.2), hence there are few measured waves moving offshore. Onshore propagating waves typically have a narrow directional range once they reach the lower flat.

---

[1] In the following sections wave characteristics are graphically portrayed using combined scatter and joint-distribution plots; coloured crosses mark individual waves and show the range and extremes of each distribution, while hollow circles are proportional to the frequency in each joint-class and are used to elucidate distribution patterns in regions where the data are dense.

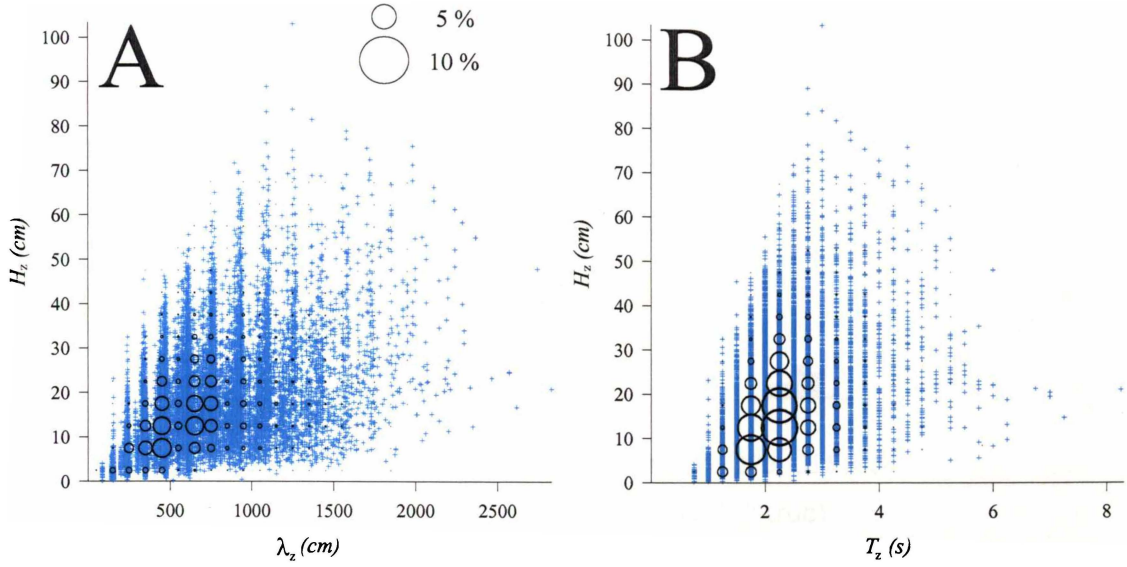

Figure 4.6: Scatter and joint distribution plots of **A.** λ_z, H_z *and* **B.** T_z, H_z. *Blue symbols represent individual waves while circles are proportional to frequency in each joint-distribution class. The 'banding' in* T_z *is due to the temporal resolution of the data (dt = 0.25 s). Banding occurs in all scatterplots of T and, to a lesser degree, T-related statistics.*

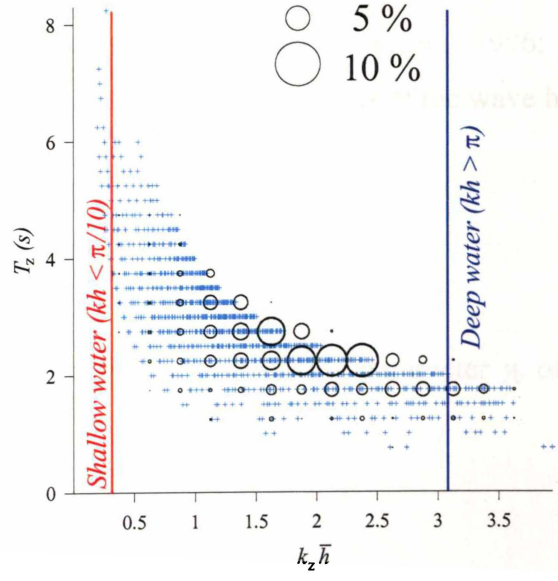

Figure 4.7: Scatter and joint distribution plot of $k_z\bar{h}$, T_z. *Blue symbols represent individual waves while circles are proportional to frequency in each joint-distribution class.*

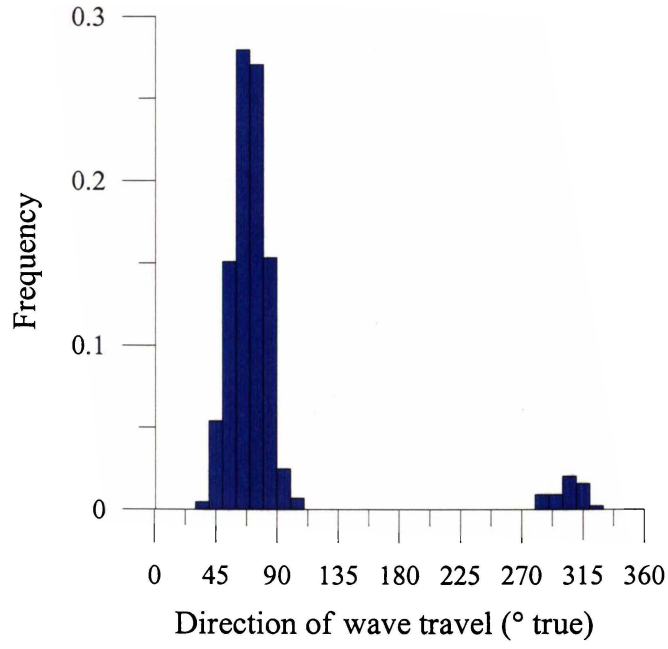

Figure 4.8: Histogram of wave direction for all W1H wave data. The wave direction, evaluated as the bearing waves are travelling toward, was determined using the velocity axis of maximum variance, scatterplots, and manual inspection of wind speed and direction (refer Appendix V for details).

Wave breaking

Depth-limited wave breaking is expected to be negligible in the locally generated seas of semi-enclosed water bodies (Young and Verhagen, 1996; Gorman and Neilson, 1999). To test this notion, individual measurements of the wave height to depth ratio:

$$\gamma_z = \frac{H_z}{\bar{h}} \qquad \text{(Eqn 4.2)}$$

were compared with the depth-limited breaking parameter γ_b of Kaminsky and Kraus (1993):

$$\gamma_b = 1.20 I^{0.27} \qquad \text{(Eqn 4.3)}$$

where I is the Irribarren number:

$$I = \frac{\beta}{\sqrt{[H/\lambda]_\infty}}, \qquad \text{(Eqn 4.4)}$$

β is the sea bed gradient, the subscript $_\infty$ denotes *deep-water conditions*, and eqn 4.3 was empirically evaluated from 17 field and laboratory datasets. H_∞ was calculated from measured wave heights and the linear shoaling coefficient:

$$\frac{H_z}{H_\infty} = K_s = \sqrt{\frac{1}{\left(1+\frac{2k_z\bar{h}}{\sinh(2k_z\bar{h})}\right)\tanh(k_z\bar{h})}} \qquad \text{(Eqn 4.5)}$$

The measured and *deep-water* heights do not differ significantly (< 10% for most waves) as shoaling only has a major influence on wave height in *shallow water* (Komar, 1998). *Deep-water* wavelength was also calculated from linear theory using the measured wave period:

$$\lambda_\infty = \frac{gT_z^2}{2\pi} \qquad \text{(Eqn 4.6)}$$

Figure 4.9 is a plot of γ_z against $k_z\bar{h}$. For most data, $\gamma_z < 0.2$ and is of *intermediate* depth. Violet symbols denote $0.9\gamma_b < \gamma_z < \gamma_b$. A small number of data points are greater than the predicted γ_b (red symbols), indicating that the model (eqn 4.3) has failed to correctly describe γ_b, at least for these data. However, the test may be unfair as $\gamma_z < 0.5$, which is outside the range for which eqn 4.3 is strictly valid ($0.6 < \gamma_b < 1.59$). Given that only 0.48% of the waves 'fail', it seems reasonable to use the model as a broad indicator of depth-induced wave breaking. In that case, one can conclude that the greater proportion of waves do not approach the depth-limit for breaking, which follows the expectations of Young and Verhagen (1996) and Gorman and Neilson (1999) for waves in fetch limited seas.

Wave steepness was compared to Miche's (1944) steepness-limit for wave breaking, $[H/\lambda]_{max}$ (eqn 3.4; magenta line in Figure 4.10B). The evidence suggests that most waves approaching $[H/\lambda]_{max}$ are whitecaps: $[H/\lambda]_z$ shows no particular trend with depth; $[H/\lambda]_z$ approaches $[H/\lambda]_{max}$ at both *shallow* and *intermediate kh*; $\gamma_z < \gamma_b$; and as whitecaps are short-lived (2–5 s) and span only short sections of wave crest (1–4 m; observations and video recordings), one might expect there to be few observations of such waves.

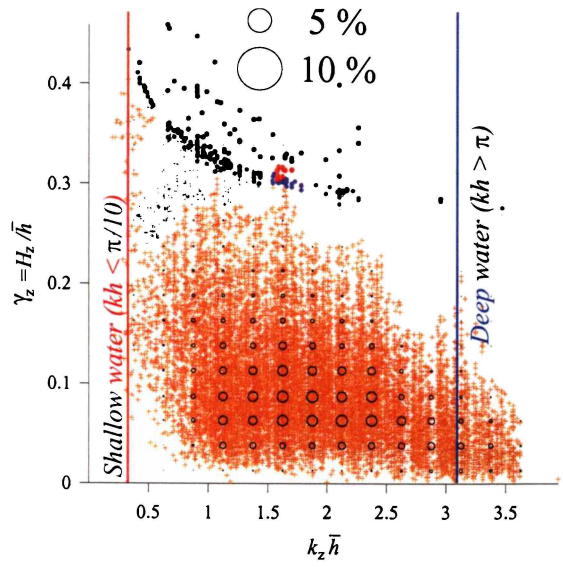

Figure 4.9: Scatter and joint distribution plot of $k_z\bar{h}$, γ_z. Orange symbols represent individual waves while circles are proportional to frequency in each joint-distribution class. Symbols coloured red are $\gamma_z > \gamma_b$ and in violet are $0.9\gamma_b < \gamma_z < \gamma_b$.

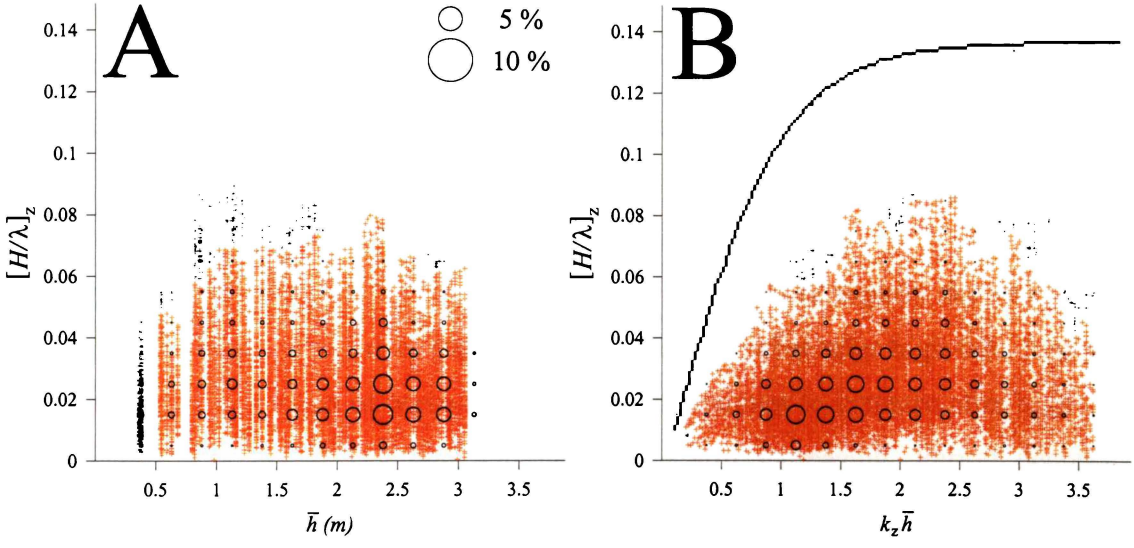

Figure 4.10: Scatter and joint distribution plots of **A.** $\bar{h}$, $[H/\lambda]_z$ *and* **B.** $k_z\bar{h}$, $[H/\lambda]_z$. *Orange symbols represent individual waves while circle size is proportional to frequency in each joint-distribution class. The pink line is Miche's (1944) equation for* $[H/\lambda]_{max}$.

Whitecaps in growing seas are distinguished from shoaling-induced wave oversteepening by the fact that they occur over wide-regions of sea, irrespective of the relative water depth. Although single-point measurements are not ideal for measurement of a whitecapping sea, video recordings suggest whitecaps can be extensive. Furthermore, Gorman and Neilson's (1999) results indicate that whitecapping is an important mechanism for energy dissipation at the sea surface, while losses due to shoaling-induced breaking are negligible.

From tide-to-tide, variation in wave characteristics is dependent on wind speed as well as the available fetch length, which is defined by the several factors discussed previously. As variation in fetch is systematically controlled by the tide, wave characteristics also exhibit temporal patterns that are strongly correlated to the tidal stage (Figure 4.11).

Notwithstanding changes in wind speed, wave height is related to fetch length (Figure 4.11), which varies on a c.12.4-h cycle in phase with the tidally varying water level. Wave heights rise and fall dramatically around the time of the fetch transition associated with the submergence and emergence of the Hangore Bank, which more than doubles the fetch on the rising tide (7→16 km) and halves it on the falling tide (16→7 km). Coinciding with fetch transitions is the anticipated change in bottom friction that occurs as relative water depth over sandbanks increases/decreases (e.g., Black *et al.*, 1999). The reduction in wave height that occurs prior to the emergence of the Hangore Bank (Figure 4.11), when local $\overline{h}$ is low, is probably due to energy dissipation on sandbanks, as previously noted.

Wave period also changes with fetch, but the pattern is usually slightly skewed (Figure 4.11). That is, wave period rises steadily and peaks somewhat after high tide, implying that penetration to the bed of wave-orbital motions continues to increase after high tide, when depth falls but wavelength and height are still increasing. Period decreases quickly when the Hangore Bank begins to emerge on the falling tide and the fetch falls from 16 to 7 km. Inspection of the S_η time-stack (Figure 4.12) illustrates the drift in the spectral peak from c. 0.5 Hz to 0.2 Hz, indicating a growing wave field. The η-spectra are generally skewed with a sharp low-frequency boundary (representing the growing face of the η-spectrum) and a long tail into higher frequencies. At, and just after high-tide, the η-spectrum has a well-defined peak due to increasing energy at lower frequencies (c. 0.3 Hz). Correspondingly, the dimensionless spectral width, ν, is low (indicating a narrow spectrum), due to a well-defined spectral peak.

The pattern in $\overline{kh}$ begins with a steep increase on the rising tide (Figure 4.11) when wave periods are short, indicating *deeper* water and reduced penetration of wave motion to the bed (Section 4.3.2). As the rate of water level rise begins to slow and the growing waves begin to lengthen, $\overline{kh}$ tends to flatten off and remains this way for most of the high tide. A slow decline in $\overline{kh}$ follows on the falling tide, which is due to simultaneous decreases in $\overline{\lambda}$ and $\overline{h}$.

In summary, waves approaching the intertidal flat exhibit regular cycles caused by tidally varying water depth and fetch length. Although wind speed causes waves to grow, in shallow tidal estuaries that wave growth is ultimately constrained by fetch length, which is controlled by wind direction and tidal elevation. Wave growth is also limited by bottom friction, which itself is controlled by water depth and wavelength (*kh*) as well as by bed characteristics. In the absence of changes in wind speed and direction (fetch), estuarine waves vary according to the tidal modulation of fetch.

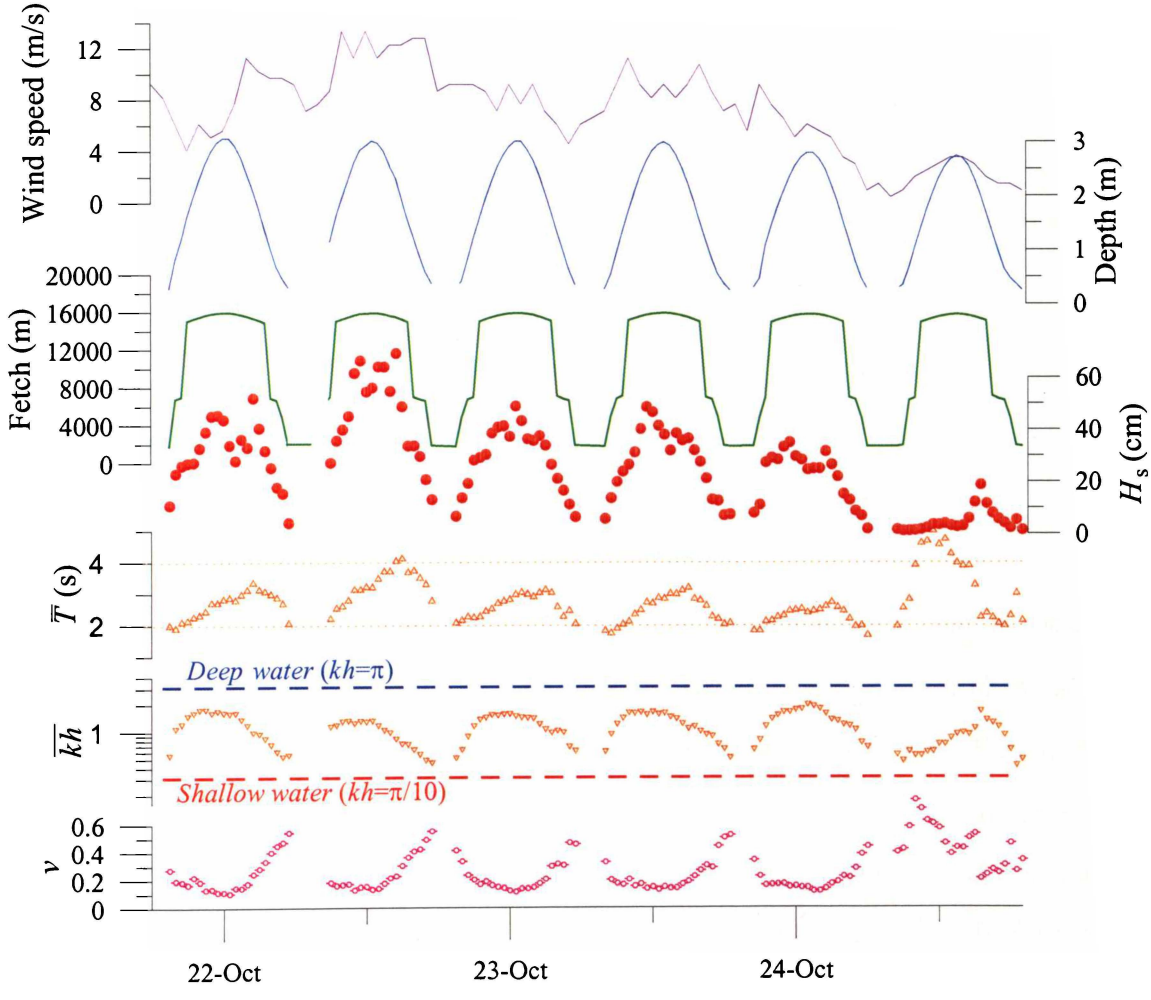

Figure 4.11: Temporal variation in wave characteristics at during a period of strong onshore winds. Burst statistics are from Alice data gathered at site W1H on the lower intertidal flat at Wiroa Island.

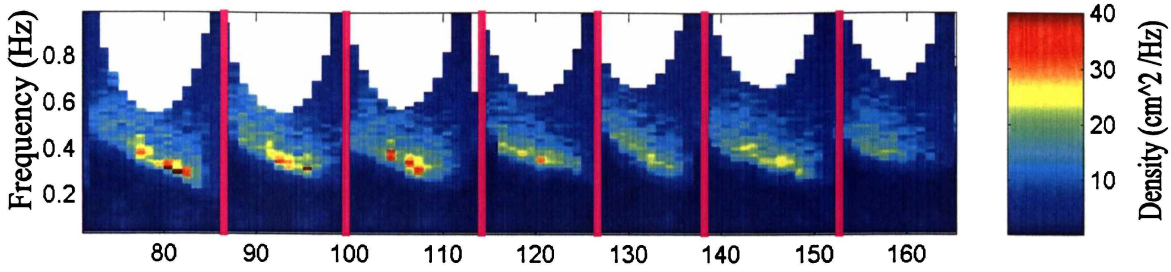

Figure 4.12: η-spectra time-stack. Colour indicates the spectral density (cm^2/Hz). The x-axis is time where the interval between bursts is 30 minutes and the pink-lines denote breaks in time between tides (when sensors were exposed). The boundary into white areas represents the depth dependent high-frequency cut-off (eqn 2.12) and also serves to indicate the stage of the tide: high-tide is when the white area is largest.

4.3.2 Near-bed Wave-Orbital Motions

Wave-orbital speed at the bed is a function of wave height, wave period and water depth. Linear wave theory describes the bed-orbital speed, U_{bed} as:

$$U_{bed} = \frac{H}{2}\omega\chi$$

where ω is the wave radian frequency (determined from T) and χ describes the penetration of U_w to the bed (determined from T and $\bar{h}$):

$$\chi = \frac{1}{\sinh(kh)}$$

The influence of H on U_{bed} is obvious. The response of U_{bed} to changes in ω and χ, however, is more complex, as an increase in T causes a decrease in ω and, at the same time, an increase in χ (Figure 4.13). The product $\chi\omega$ demonstrates that changes in χ with T dominate over changes in ω for certain combinations of T and $\bar{h}$. Furthermore, the period range in which the slope of $\chi\omega$ is steepest (Figure 4.13; lower panel) corresponds to typical wave periods observed at Wiroa. Consequently, changes in T across the 1–4-s range exert significant control on U_{bed} for a given H (Figure 4.14; pink arrows). This is investigated for the Wiroa intertidal flat in the following.

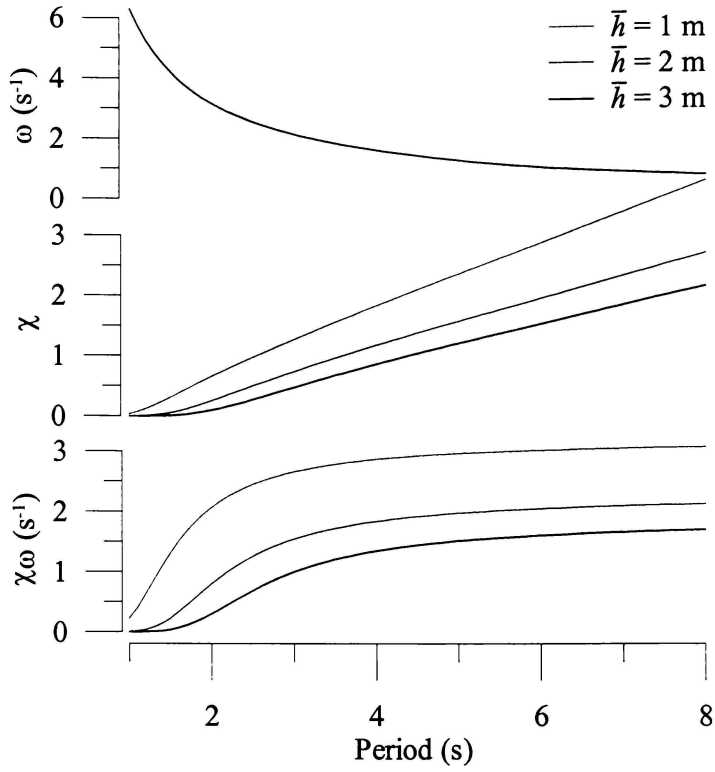

Figure 4.13: Examples of ω, and, for three depths, χ and the product χω. The depths and periods chosen represent typical Wiroa conditions.

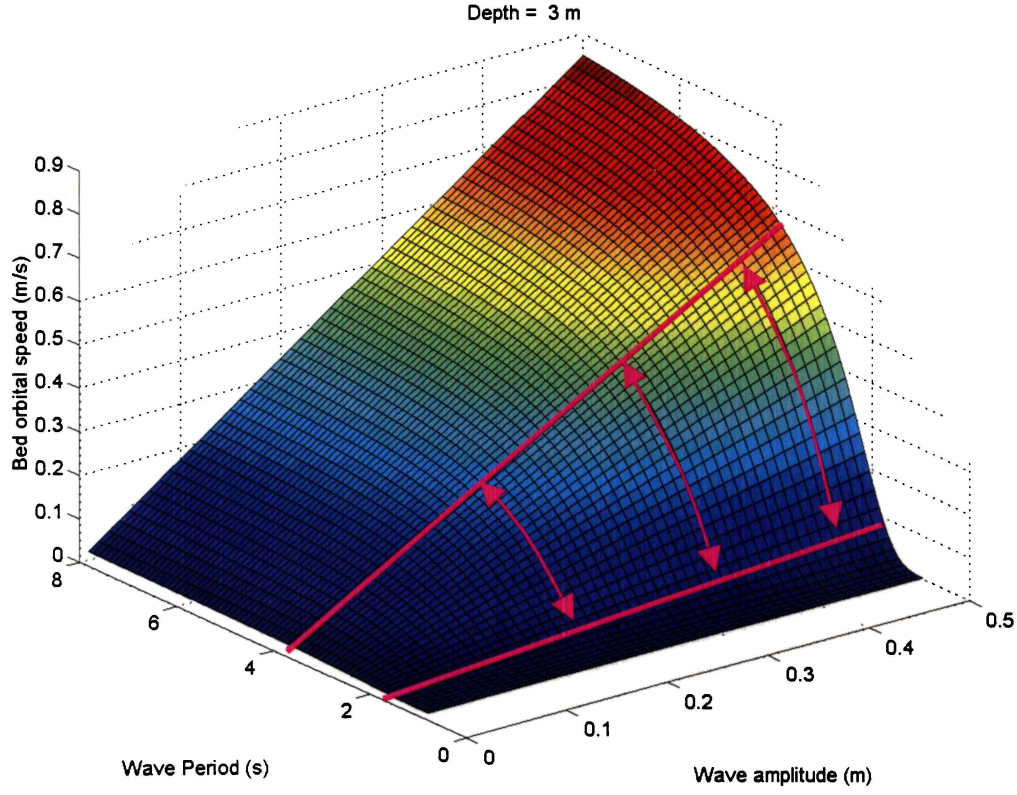

Figure 4.14: Example of the response of U_{bed} to changes in H/2 (amplitude) and period for $\bar{h}$ = 3 m. U_{bed} undergoes greatest changes in the T = 1–4 s range, as indicated by the arrows and in the lower panel of Figure 4.13.

The wave-orbital-speed distribution was mapped using $U_{peak,z}$ (Figure 4.15), which is the maximum speed recorded under each measured wave. $U_{peak,z}$ is greatest for $kh \approx 0.5–1.0$ (shallow-end of the *intermediate* depth regime), which occurs when depth becomes small and/or wave period increases. The importance of relative water depth and penetration (χ) in controlling bed-orbital speed is demonstrated by the trend of increasing $U_{peak,z}$ with decreasing $k_z \bar{h}$. Scatter in Figure 4.15A indicates variation in the magnitude of winds that cause waves. $U_{peak,z}$ is typically < 20 cm/s, with the most common classes at 4–8 cm/s in the *intermediate* range $k_z \bar{h} = 2–2.5$.

The critical entrainment speed (eqn 3.3) for sands is compared with $U_{peak,z}$ in Figure 4.15B, which shows that, for 32% of the measured waves, $U_{peak,z}$ exceeds the critical speed. Note that eqn 3.3 was not intended for use with intra-wave orbital speeds, and is used here only to show patterns and to indicate the frequency of sediment motion under these estuarine waves (detailed entrainment analysis follows in Chapter 5).

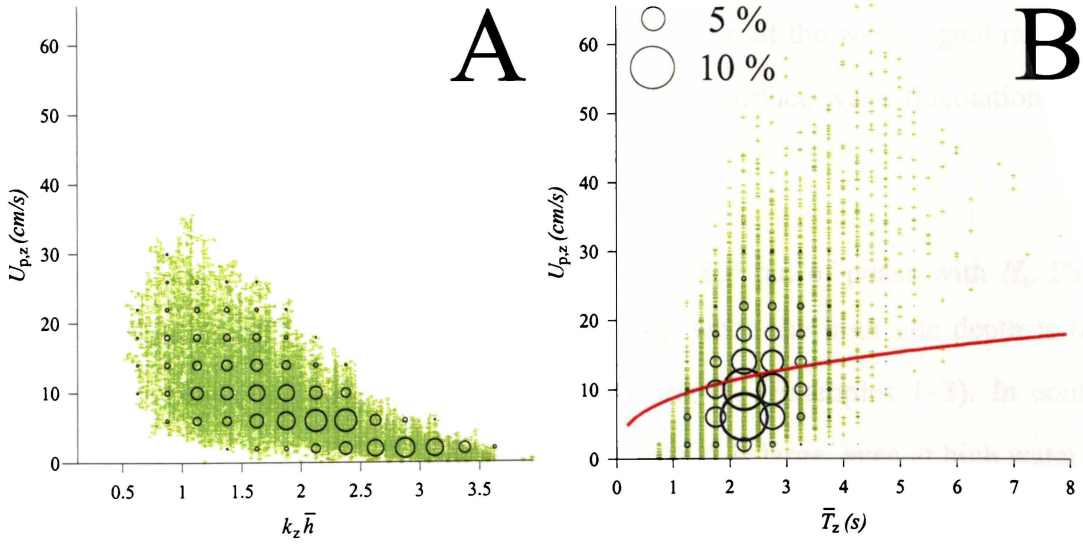

Figure 4.15: Scatter and joint distribution plots of **A.** $k_z \bar{h}$, $U_{peak,z}$ *and* **B.** T_z, $U_{peak,z}$. *Green crosses represent the peak velocity in each wave cycle,* $U_{peak,z}$, *while circles are proportional to the frequency in each joint-distribution class. The red line in the right-hand graph is the critical wave-orbital speed (eqn 3.3).*

Over a tidal cycle at Wiroa Island, temporal patterns in U_{bed} are determined by a subtle balance between $\overline{h}$, H and T, all of which have been shown to increase and decrease more-or-less simultaneously (e.g., Figure 4.11). On the rising tide, the effect of increasing depth on χ is countered by the effect of increasing period on χ and ω, and is also countered by increasing H. In the following, the Wiroa data are used to describe and explain patterns in $U_{s,bed}$.

Green *et al.* (1997) observed that $U_{s,bed}$ (eqn 2.28) on the outer Wiroa flat usually peaked near mid-tide and declined toward high tide. In comparison, the data used here are from higher locations (on the lower and middle flat) and demonstrate that, in fact, a variety of $U_{s,bed}$ patterns exist. Three cases were observed: (1) $U_{s,bed}$ is greatest at the beginning and end of the inundation, and smallest around high-tide (Examples 1–3; Figure 4.16); (2) $U_{s,bed}$ is smallest at the beginning and end of the inundation, and greatest around high tide (Examples 7–9; Figure 4.16); and (3) $U_{s,bed}$ varies in a complicated way due to variation in winds (Examples 4–6; Figure 4.16). In the following χ^* (1/cosh[kh]) is used to describe penetration of the wave signal rather than χ, as it nondimensional, scales as a proportion of the surface wave fluctuation, and is easier to interpret.

In the first case, $U_{s,bed}$ varies in phase with χ^* but 180° out of phase with H_s. During spring tides (and on the lower reaches of the flat), when the high tide depth is large, small χ^* causes $U_{s,bed}$ to decrease, despite growing H_s (Examples 1–3). In contrast, during neap tides (and on the higher parts of the flat) χ^* is large, even at high water, and $U_{s,bed}$ follows changes in H_s, becoming largest at high tide when fetch is also greatest (Examples 7–9). Such contrasting patterns in $U_{s,bed}$ during the tidal cycle can have important consequences for sediment entrainment and transport and are discussed further in Chapter 5.

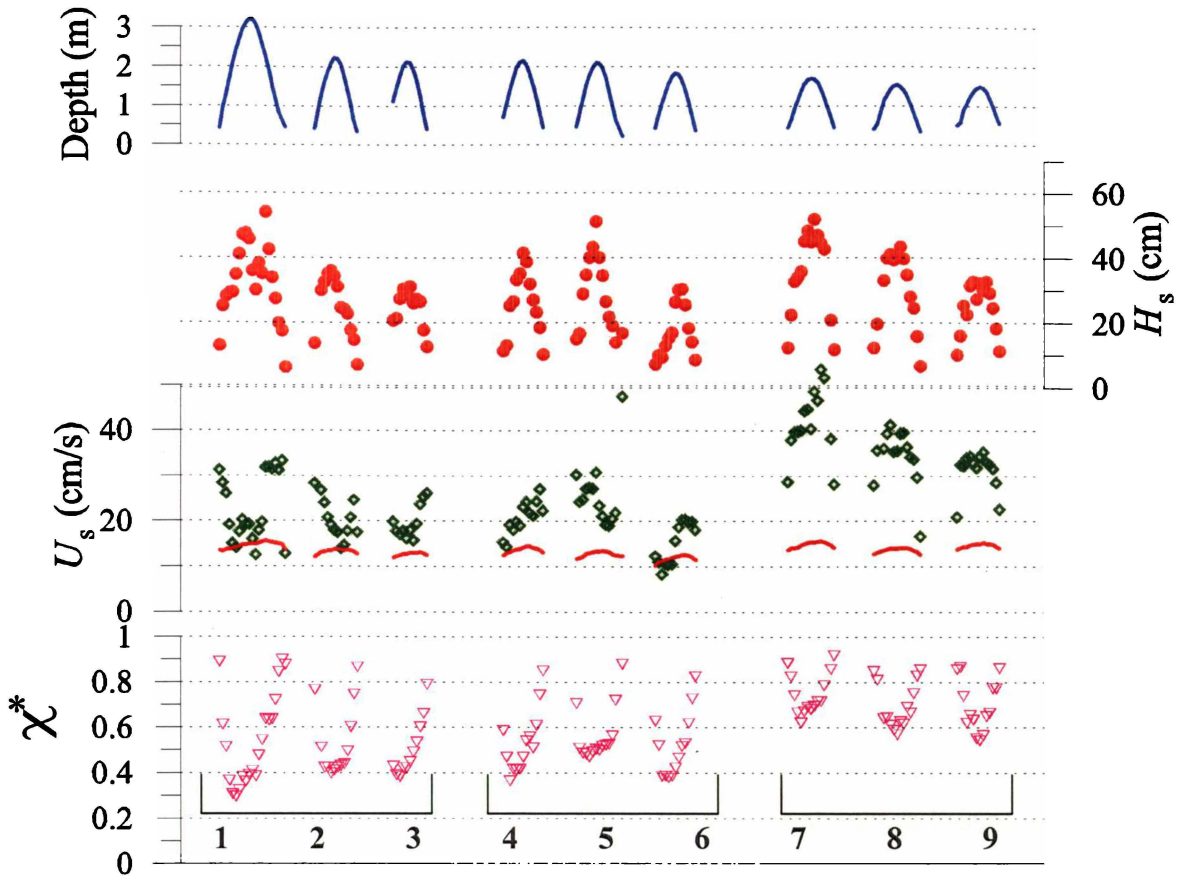

Figure 4.16: Examples of the variations in $U_{s,bed}$ during storm inundations. In groups of three from left to right, $U_{s,bed}$ trends are concave, variable and convex. Note: each inundation is mapped separately, so the time axis is discontinuous; the time interval between successive points is 30 minutes. Red lines denote the critical wave-orbital speed (eqn 3.3).

More complex patterns arise when changes in wind speed and/or direction occur during the course of a storm (Examples 4–6). For example, in event-4 wind speed rose sharply during the flood tide causing a sudden increase in H_s. This was followed shortly after by an increase in χ^* associated with increasing T. Consequently, $U_{s,bed}$ continues to rise throughout the inundation due to the consistently increasing χ^*.

Velocity asymmetry and shoaling

As waves shoal and steepen seaward of a surf zone, the wave-orbital motion becomes increasingly elliptical and asymmetric. Asymmetry of the wave-orbital speed is investigated here as it can cause a net drift, culminate in wave breaking, and influence the net sediment transport rate and direction due to the nonlinear dependence of sediment transport on the fluid velocity (Soulsby, 1997).

The near-bed wave-orbital-speed asymmetry was evaluated for each burst as $\overline{S}$:

$$\overline{S} = \frac{1}{B^*} \int_{t=0}^{B^*} U_w^2(t) U_w(t)\,dt \qquad \text{(Eqn 4.7)}$$

where B^* is the length of time between the first upcrossing and the last down crossing in a burst of data, such that only complete wave cycles are considered, and $U_w(t)$ was taken from Alice data at z_u = 13.5 cm. $\overline{S}$ is an indicator of wave skewness (i.e., non-symmetry) (e.g., Green and MacDonald, 2001). Skewness was also determined for individual waves:

$$S_z = \frac{1}{T_z} \int_{0^*}^{T_z} U_w^2(t) U_w(t)\,dt$$

The distribution of S_z for the entire Alice (W1H) dataset is shown in Figure 4.17, where a blue symbol indicates asymmetry in the onshore direction. S_z is small for most waves. Furthermore, positive and negative S_z are about equally frequent, suggesting no obvious net drift under asymmetric waves.

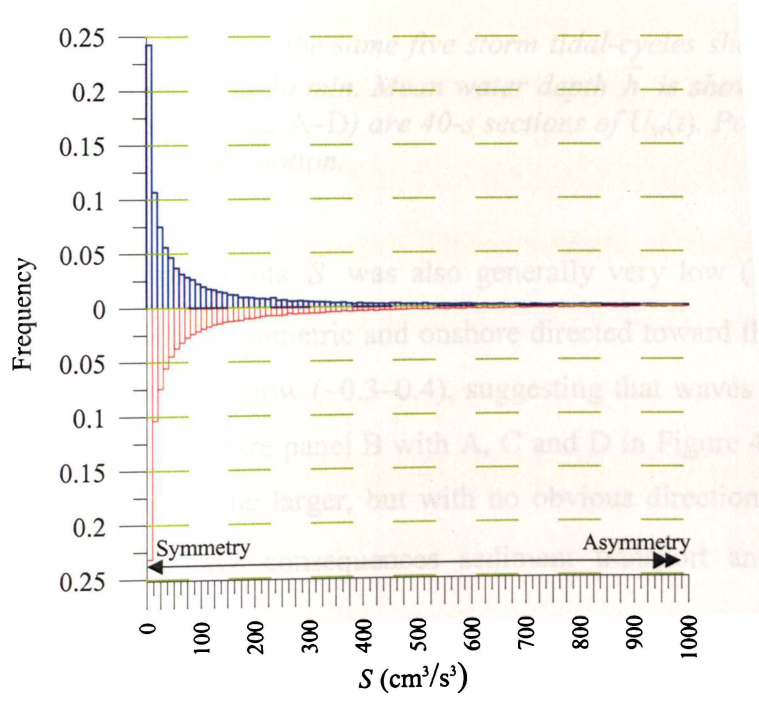

Figure 4.17: Frequency distributions (onshore/offshore) of wave skewness, S_z, for all waves measured at site W1H.

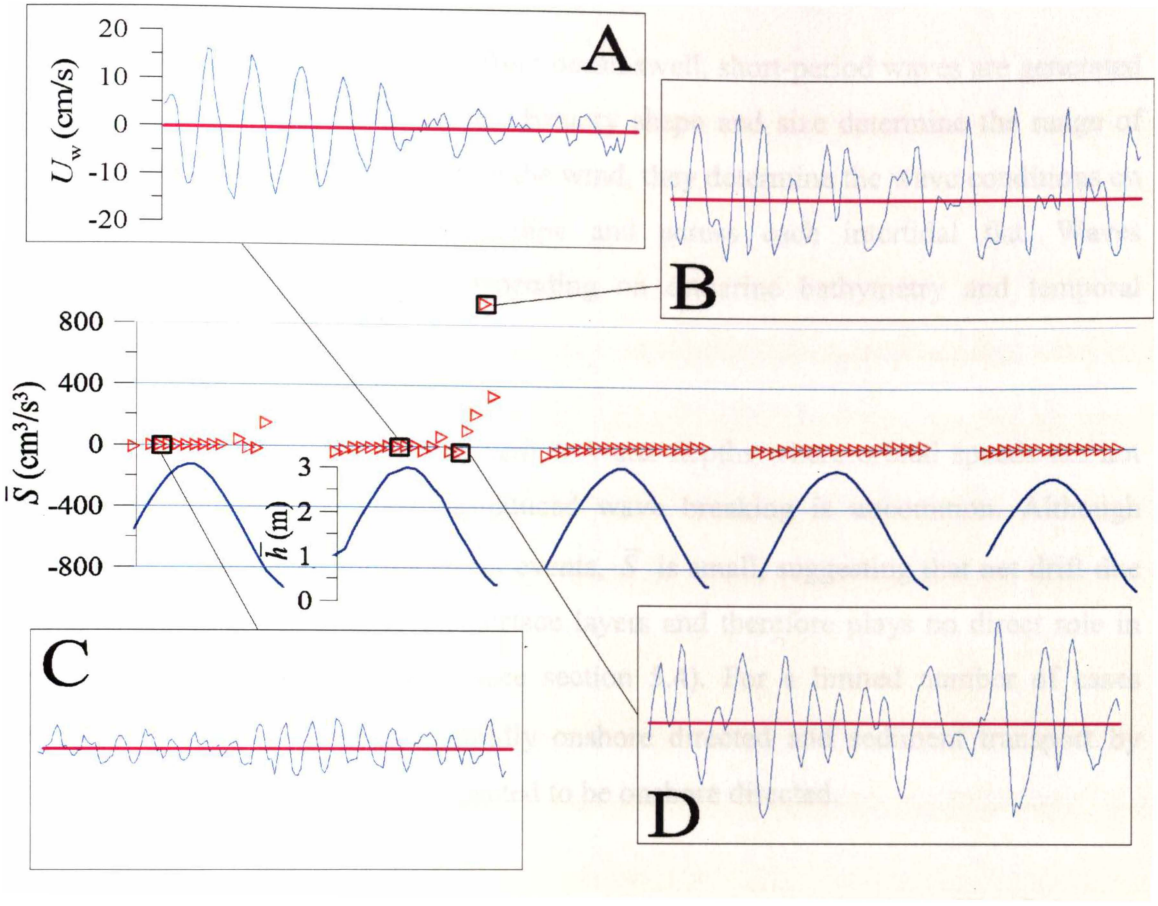

Figure 4.18: Variation in $\overline{S}$ (▷) *over the same five storm tidal-cycles shown in Figure 4.11. The interval between bursts is 30 min. Mean water depth* $\overline{h}$ *is shown by the sky-blue lines and the four insets (labelled* A–D*) are 40-s sections of* $U_w(t)$*. Positive* $U_w(t)$ *is the onshore component of the wave motion.*

During five consecutive storm events $\overline{S}$ was also generally very low (Figure 4.18), however, $\overline{S}$ can become mildly asymmetric and onshore directed toward the end of the ebb tide. During these times, *kh* is low (~0.3–0.4), suggesting that waves are shoaling and wave crests are peaked (compare panel B with A, C and D in Figure 4.18). Higher on the intertidal flat, S_z tends to be larger, but with no obvious direction (onshore or offshore) favoured. $\overline{S}$ can have consequences sediment transport and is further investigated in section 5.6.

4.4 CONCLUSIONS

In semi-enclosed estuaries protected from ocean swell, short-period waves are generated as the wind blows over local fetches. Estuary shape and size determine the range of available fetch lengths and, along with the wind, they determine the wave conditions on each section of the estuarine shoreline and across each intertidal flat. Waves approaching intertidal flats vary depending on estuarine bathymetry and temporal variation in fetch lengths.

At Wiroa, waves propagate in *intermediate* water depths where orbital speeds are not strongly asymmetric and shoaling-induced wave breaking is uncommon. Although whitecaps are ubiquitous during storm events, $\overline{S}$ is small, suggesting that net drift due to whitecapping is confined to the surface layers and therefore plays no direct role in sediment entrainment or transport (see section 5.4). For a limited number of cases (when kh was low), $\overline{S}$ became mildly onshore directed and sediment transport by waves might also, as a result, be expected to be onshore directed.

Temporal variation in $U_{s,bed}$ is due to different H and $\chi\omega$ combinations. The field data show that for shallow depths (e.g., neap tides or higher on the flat) $U_{s,bed}$ is smallest at the beginning and end of the inundation, and greatest around high tide, while for larger depths (e.g., spring tides or lower on the flat) $U_{s,bed}$ is greatest at the beginning and end of the inundation, and smallest around high-tide. Variation in the way bed-orbital motion changes over a tidal cycle is expected to influence patterns in SSC and sediment transport.

5.1 INTRODUCTION

Sediment entrainment occurs when the bed shear stress exerted by moving fluids exceeds the forces holding the sediment at rest, or when gravity destabilises a sediment surface which has steepened beyond the angle of stability or repose (i.e., avalanching). The angle of repose in water is typically around 32° (Nielsen, 1990). As the intertidal-flat gradient is less than 0.1°, movement of grains solely under the influence of gravity does not occur.

Bed shear stress on the Wiroa intertidal flat is generated primarily by tidal currents and oscillatory flows underneath local wind waves (refer Chapter 4). Wind-induced shear stress was not considered as sediment saturation is > 85% at all times (Drabsch *et al.*, 1999), which inhibits sediment motion (e.g., Sarre, 1988; Arens, 1994; Jackson and Nordstrom, 1998). Previous experiments have shown that tidal currents are too weak to entrain sediments across most of the intertidal flat, except during large spring tides on the channel margins (Dolphin *et al.*, 1995; Green *et al.*, 1997). In comparison, Figure 5.1 (shown previously in Chapter 3) indicates that maximum bed-orbital speeds are at times in excess of critical, and that during such times bed sediment is raised into suspension.

The aim of this chapter is to describe the processes of sediment entrainment and transport under waves and currents on the Wiroa intertidal flat.

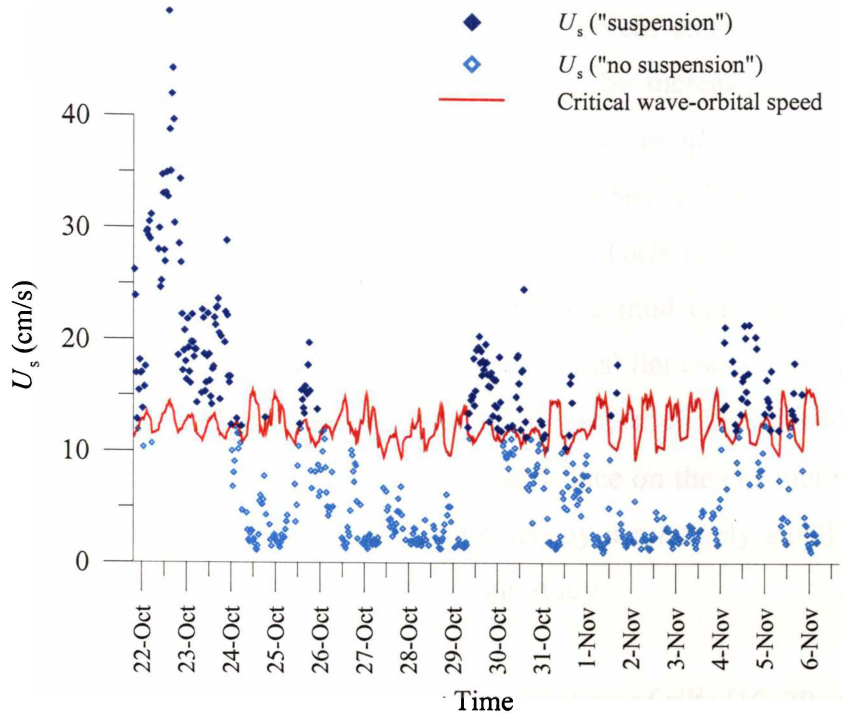

Figure 5.1: Comparison of measured sand entrainment to the critical wave-orbital speed (eqn 3.3) and wave-orbital speed at the bed ($U_{s,bed}$). The data shown are from a 15-day at siteW1H. $U_{s,bed}$ is represented by a filled symbol if sand (d_s = 180 μm) was observed to be in motion and by a hollow symbol if not (refer Section 5.4 for details). This diagram was used previously to verify velocity data (Figure 3.5).

5.2 Bed and Suspended Sediments of the Intertidal Flat

The bed sediments of the Wiroa intertidal flat have a bimodal size distribution. Across the greater intertidal flat (i.e., ~100–1500-m from shore; Figure 5.2) sediments comprise well-sorted fine sands (125–250 μm) with a minor silt mode (~20 μm; < 2% silt by volume). On the uppermost and lowermost reaches of the flat, the surficial sediments vary from those on the greater intertidal flat. On the upper flat, a steep (1:10), short (2-3 m) estuarine beach is made up of gravely-textured sediments (>1000 μm) comprising mostly broken shells and hard-packed sand. At its base the beach contacts the intertidal flat sloping at c. 1:1000. In this region there are patches of silt overlying sand. The silt patches are ephemeral (observed after storms), except in near shore stands of mangroves where silts are abundant (plot A, Figure 5.2), compacted and enduring. Silt abundance also increases to around 20% with proximity to the channel margins.

As the percentage of fine sediment in a mixed-size sediment matrix increases, cohesion comes to play an increasingly important role (for sediment entrainment/stability) by increasing the shear strength of the sediment and thereby increasing the critical bed shear stress at which grains will be entrained. McCave *et al.* (1995) suggest that sediments larger than 10 μm exhibit increasingly non-cohesive behaviour, while field and laboratory experiments compiled by Mitchener and Torfs (1996) indicate that the sediment matrix takes on cohesive behaviour when the mud content is greater than 3-15%. As the bed sediments of the greater Wiroa intertidal flat contain less than 2% silt by mass, and particles are mostly larger than 10 μm, they are considered to be noncohesive. Cohesion is likely to be of some significance on the channel margins and within mangrove stands, although these regions occupy a relatively small area of the intertidal flat, and are not directly considered in this study.

Suspended sediments are also typically bimodal, consisting of silts (10–30 μm) and fine sands (125–220 μm). Figure 5.3 presents examples of size-distributions for bed sediments (plot **A**), for suspended sediments from two storm events (plots **C** and **D**), and from different elevations during a single event (plots **B** and **D**). The relative contribution of each size-mode is observed to vary for different suspension events and at different elevations (z = 20 cm and 8 cm for plots **B** and **D**, respectively). The ratio of suspended silt/sand is generally much larger than it is for bed sediments and the volume differences with elevation suggest comparatively less sand in suspension at higher elevations.

The settling velocity of silts and sands differs by two orders of magnitude: a silt particle of 20 μm has a settling velocity (w_s) of 0.03 cm/s or 90 cm in 50 min, while a fine-sand particle of 200 μm has a settling velocity of 2 cm/s or 90 cm in 45 s (following Soulsby, 1997). Since settling speed is a first-order control on dispersal and deposition of suspended sediment, the two grain sizes in suspension at Wiroa are expected to behave quite differently from each other. Therefore, they will be treated independently in the following analysis.

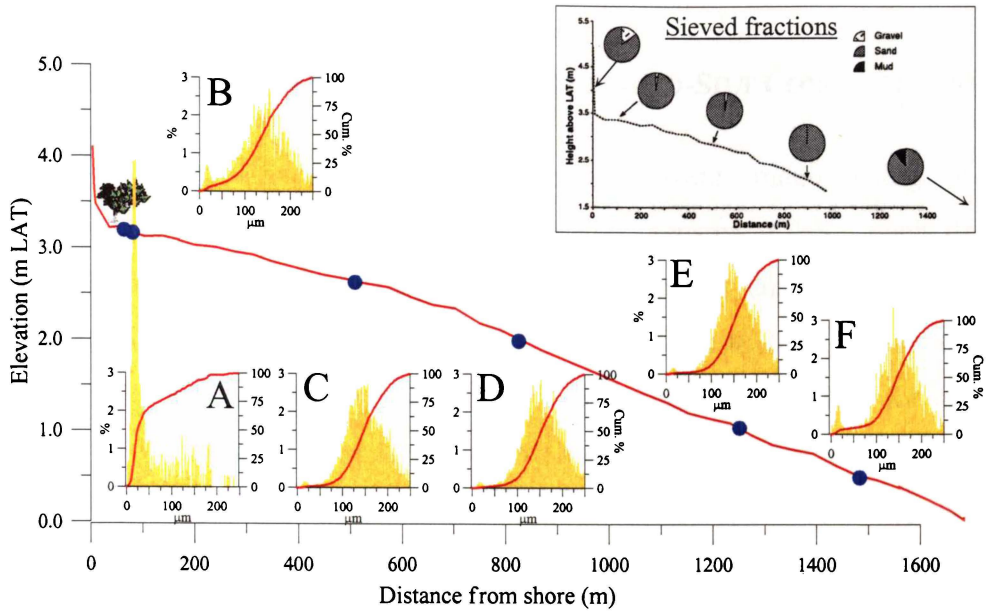

Figure 5.2: Grain size across the intertidal-flat transect. Sample collection and analysis are described in Chapter 2 and Dolphin et al. (1999). The inset shows sieved sediment size-fractions (gravel, sand, mud; Folk, 1968). On the main diagram blue circles denote locations of samples which were analysed using the Galai CIS-100 time-of-transition particle size analyser. The corresponding particle size distributions are shown with the percentage volume in each class on the left y-axis (yellow bars) and the cumulative percentage on the right y-axis (red line). Note that the samples used for plots **A** *and* **B** *were only 10-m apart; the sample in plot* **A** *was collected from a muddy depression within a mangrove stand while plot* **B** *is open sand flat adjacent to mangroves.*

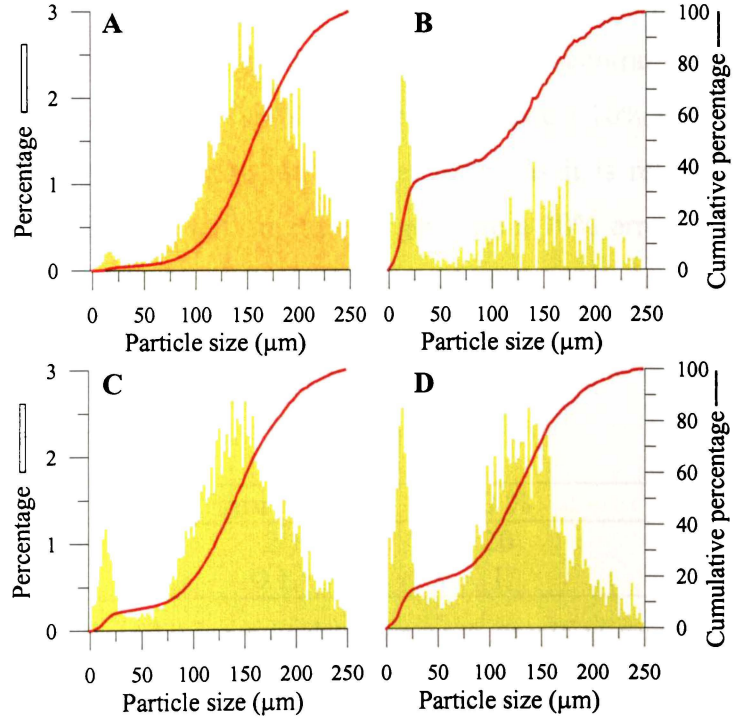

Figure 5.3: Examples of the grain size distributions from the bed (**A**) *and suspended sediments collected in sediment traps* (**B–D**) *from the Wiroa intertidal flat. The trap samples shown are from single tidal inundation. Plots* **B** *and* **D** *are from traps deployed for the same tidal inundation but whose apertures were located at z = 20-cm and 8-cm respectively.*

5.3 ESTIMATION OF SUSPENDED-SAND AND SUSPENDED-SILT CONCENTRATIONS

Suspended sediment concentration measurements were made using Acoustic Backscatter Sensors (ABS) and Optical Backscatter Sensors (OBS). Each device is sensitive to different particle size ranges – fine sediments for OBS and sands for ABS (White, 1988; Lynch *et al.*, 1994; Bunt *et al.*, 1999) – due to their different transmit wavelengths. To test if the differences in sensitivity could be exploited for measuring the silt-size and sand-size components of Manukau suspensions, experiments were conducted in the turbidity tank and in the Hangore Channel (Section 2.3.2). Details of the turbidity tank and Hangore Channel experiments can be found in Green *et al.*, (1999) and Appendix VI. Reported here are only the key findings that relate to measurement of sand and silt concentrations in a mixed silt/sand suspension.

Using Manukau sediments, the turbidity tanks tests showed that the ABS is sensitive to sand-sized suspensions and very insensitive to any silt in suspension, while the OBSs are sensitive to silt suspensions but are relatively insensitive to any sand in suspension. Key results are given in Table 5.1. The errors incurred by assuming only one size fraction is present (silts for OBS, sands for ABS) in a mixed-size suspension suggest that: the ABS can be used to estimate suspended sand concentration as it is insensitive to suspended silt (requires a 20:1 silt/sand mix to generate a 10% error); while the OBS can be used to estimate suspended silt concentration as it is relatively insensitive to suspended sand (requires a 50:50 mixture to generate a 10% error). The turbidity tank results were verified in the Hangore Channel and subsequently the ABS/OBS combination was used to investigate the silt and sand dynamics of a tidal channel (Green *et al.*, 2000).

	Error=1 %	10 %	100 %
ABS (1.97 MHz)	2	20	200
OBS	0.1	1	10

Table 5.1: Ratios of C_{silt}/C_{sand} required to generate specified errors for the 1.97 MHz ABS and ratios of C_{sand}/C_{silt} required generate specified errors for the OBS. Source: Green et al. (1999).

5.4 INITIATION OF MOTION BY CURRENTS AND WAVES

Bed shear stress on the intertidal flat is produced by steady flows associated with the passage of tides and by oscillatory flows underneath local wind waves (refer Chapter 4). Wind-driven currents may augment or diminish tidal currents (e.g., Dolphin and Green, 1997), thus enhancing or reducing bed shear stress underneath the steady flow. To investigate silt and sand movement, entrainment measurements are compared with predictions of the threshold of sediment motion.

Entrainment is inferred from OBS (silt) and ABS (sand) data, and presented as a sediment suspension/no-suspension index. There were no other data to independently verify the index as poor water clarity invalidated the use of video/photography, and attempts to measure ripple migration failed due to insufficient resolution of the sonar data.

The index was initially evaluated by comparing the mean concentration for each burst, $\overline{C}$, with a calm weather "background concentration", $\overline{C}_{\text{background}}$. For sands, the background concentration was set at 15 mg/L (z = 1 cm), which is similar to the background concentration reported by Green (1999) for the same ABS. For silts, the background concentration was set at ~25 mg/L (z = 46 cm). Data were classified as "no-suspension" if $\overline{C} \leq \overline{C}_{\text{background}}$ and as "suspension" if $\overline{C} > \overline{C}_{\text{background}}$. Bursts categorised as "suspension" were then further analysed to verify the classification. Time-series concentration data, $C(t)$, from all "suspension" bursts were inspected. Intermittent suspension was observed in some $C_{\text{sand}}(t)$, which also had low $\overline{C}$ (see Figure 5.4B). The "intermittent suspension" bursts, which are not amenable to this binary classification, were not included in further analyses.

Sediment entrainment is predicted for currents and waves by comparing estimates of the skin friction (that component of the bed shear stress which acts directly on sediment particles) with the entrainment threshold. For steady currents, the skin friction is:

$$u'_{*c} = \frac{\kappa \overline{U}(z)}{\ln(z/z'_0)} \qquad \text{(Eqn 5.1)}$$

where z_0' is the skin-friction roughness length

$$z_0' = 2.5 d_s / 30, \qquad \text{(Eqn 5.2)}$$

d_s is the particle diameter, $\overline{U}(z)$ is the steady current at elevation z, and κ is von Karman's constant (0.41). The friction velocity u_{*c}' can be nondimensionalised by:

$$\theta_c' = \frac{\rho_f u_{*c}'^2}{(\rho_s - \rho_f) g d_s} \qquad \text{(Eqn 5.3)}$$

which is then used to make comparisons with the dimensionless entrainment threshold determined from the Shields curve, θ_{cr}. For evaluating u_{*c}' and θ_c', d_s was taken as 180 μm for sand and 20 μm for silt, and $\overline{U}(z)$ was determined from current measurements made at the nominal elevation z = 13.5 cm.

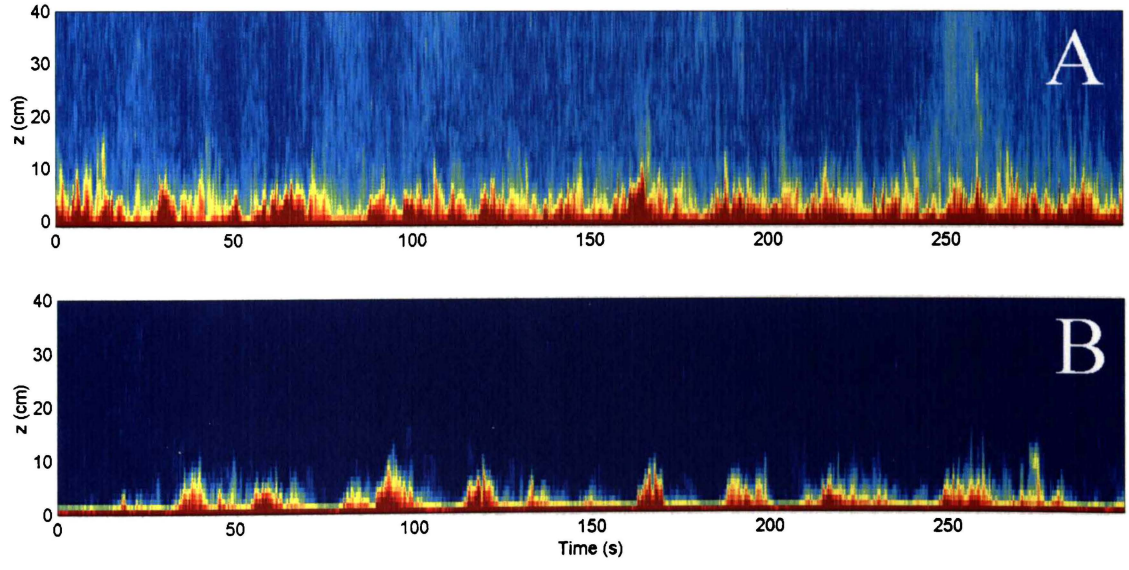

Figure 5.4: Examples of $C_{sand}(t)$ showing **A** *'continuous suspension' and* **B** *'intermittent suspension'.*

Under waves, the skin-friction friction velocity is estimated as

$$u'_{*w} = U_w \sqrt{0.5 f'_w} \qquad \text{(Eqn 5.4)}$$

where U_w is the wave-orbital speed at the bed and f'_w is the skin-friction wave friction factor based on Swart's (1974) formulation:

$$f'_w = \exp\left[5.213\left(\frac{2.5 d_s}{a_w}\right)^{0.194} - 5.977\right] \qquad \text{(Eqn 5.5)}$$

where a_w is the wave-orbital radius, which is related to the wave-orbital speed as $U_w = a_w \omega$. u'_{*w} can be nondimensionalised by:

$$\theta'_w = \frac{\rho_f u'^2_{*w}}{(\rho_s - \rho_f) g d_s} \qquad \text{(Eqn 5.6)}$$

which is then used to make comparisons with θ_{cr} to predict entrainment. Following Black and Rosenberg's (1991) work on velocity scales and sediment transport, $U_{3,bed}$ (eqn 2.30) was chosen to represent U_w for the evaluation of a_w, f'_w, u'_{*w} and θ'_w. The nondependence of U_3 on Rayleigh wave statistics (e.g., U_{rms}, U_s) also serves to free skin-friction calculations from assumptions relating to Rayleigh distributed sea-surface elevations (refer Chapter 2 and Appendix VII).

5.4.1 Sand entrainment

Figure 5.5 is a plot of θ'_w against θ'_c, where the plot symbols are filled to denote sand "suspension" and hollow to denote "no-suspension". The plot demonstrates that waves are capable of entraining sands on the intertidal flat but that currents are not, as follows. The "suspension" data approximately separate from the "no-suspension" data at the critical value $\theta'_w \approx 0.05$, which is indicative of sand entrainment under waves, but there is no such division with θ'_c, which demonstrates that steady currents are too weak to entrain sands on the intertidal flat.

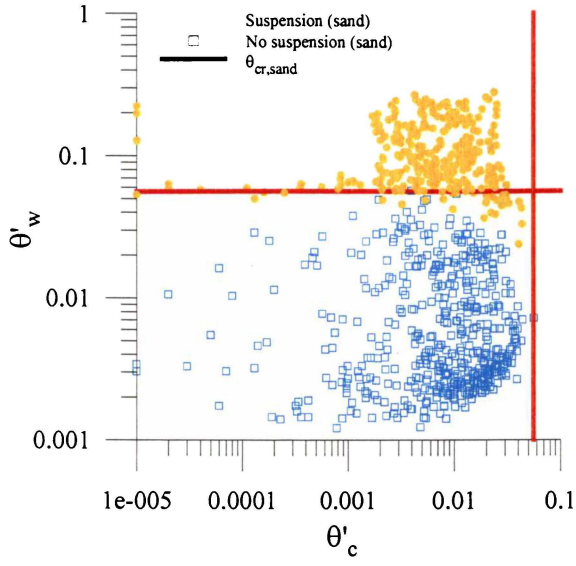

Figure 5.5: Plot of skin friction due to waves (θ'_w) and currents (θ'_c). Data are classified according to the sand suspension index where filled symbols indicate "suspension" and hollow symbols indicate "no suspension". Red lines represent the predicted sand entrainment threshold $\theta_{cr,sand}$.

The entrainment threshold inferred from the data, $\theta'_w \approx 0.05$, is similar to the predicted entrainment threshold, $\theta_{cr,sand} = 0.056$ (red lines in Figure 5.5), which was determined for Wiroa sands using the Shields curve (Soulsby and Whitehouse, 1997):

$$\theta_{cr} = \frac{0.3}{1+1.2D_*} + 0.055[1-\exp(-0.020D_*)] \qquad \text{(Eqn 5.7)}$$

where D_* is the dimensionless grain size

$$D_* = \left[\frac{g(s-1)}{\nu^2}\right]^{1/3} d_s \qquad \text{(Eqn 5.8)}$$

with $s = \rho_s/\rho_f$ and kinematic viscosity $\nu = 0.0000113$ m^2/s. The inability of steady currents to entrain sands was also correctly predicted by $\theta'_c < \theta_{cr,sand}$. Agreement between observed entrainment and the Shields curve (Figure 5.5) demonstrates that eqn 5.7 is a good predictor of $\theta_{cr,sand}$ on the Wiroa intertidal flat.

Although currents do not entrain sands, wave–current interaction can, at times, enhance the otherwise subcritical pure-wave skin friction ($\theta'_w < \theta_{cr,sand}$), resulting in entrainment. The two-layer, wave–current boundary-layer model of Larsen *et al.* (1981) was used to quantify the influence of wave–current interaction on skin friction and sand entrainment. In the wave–current boundary layer the total dimensionless skin friction, $\theta'_{total,w-c}$, is the vector sum of the maximum wave skin-friction $\theta'_{w,w-c}$ and the mean current skin-friction $\theta'_{c,w-c}$, where $\theta'_{w,w-c}$ and $\theta'_{c,w-c}$ are enhanced relative to their pure-wave and pure-current counterparts (θ'_w and θ'_c). $\theta'_{w,w-c}$ and $\theta'_{c,w-c}$ were evaluated using an iterative procedure (see Larsen *et al.*, 1981) with the steady current $\overline{U}(z)$ at $z = 13.5$ cm, the wave-orbital speed $U_{3,bed}$, the wave period $\overline{T}$, and the acute angle between the direction of the waves and the steady current $\varphi_{U_w - \overline{U}}$.

The influence of wave–current interaction on skin friction and entrainment is shown in Figure 5.6 where plot **A** is θ'_w against θ'_c, plot **B** is a test for model consistency with θ'_w (refer caption), and plots **C** and **D** are $\theta'_{w,w-c}$ and $\theta'_{total,w-c}$ against θ'_c. When the current enhanced skin-friction due to waves $\theta'_{w,w-c}$ is used in place of the pure-wave skin friction θ'_w (Figure 5.6C), the apparently anomalous data are lifted and the separation representing the entrainment threshold is slightly better defined. A similar effect is noted when $\theta'_{total,w-c}$ is used in place of $\theta'_{w,w-c}$ (or θ'_w), however some "no-suspension" bursts are also raised above the predicted threshold (Figure 5.6D) and consequently $\theta'_{total,w-c}$ provides no improvement over θ'_w.

Only a few instances of wave–current interaction causing otherwise unpredicted entrainment were observed, suggesting that wave–current interaction has only a minor influence on the entrainment of intertidal-flat sands at Wiroa. For entrainment purposes then, computing skin friction using the wave–current interaction model gives added complexity but, in this case, with only slight improvement over pure-wave estimates of the skin friction. Consequently θ'_w (eqns 5.5 and 5.6) is adopted for subsequent sand-transport calculations.

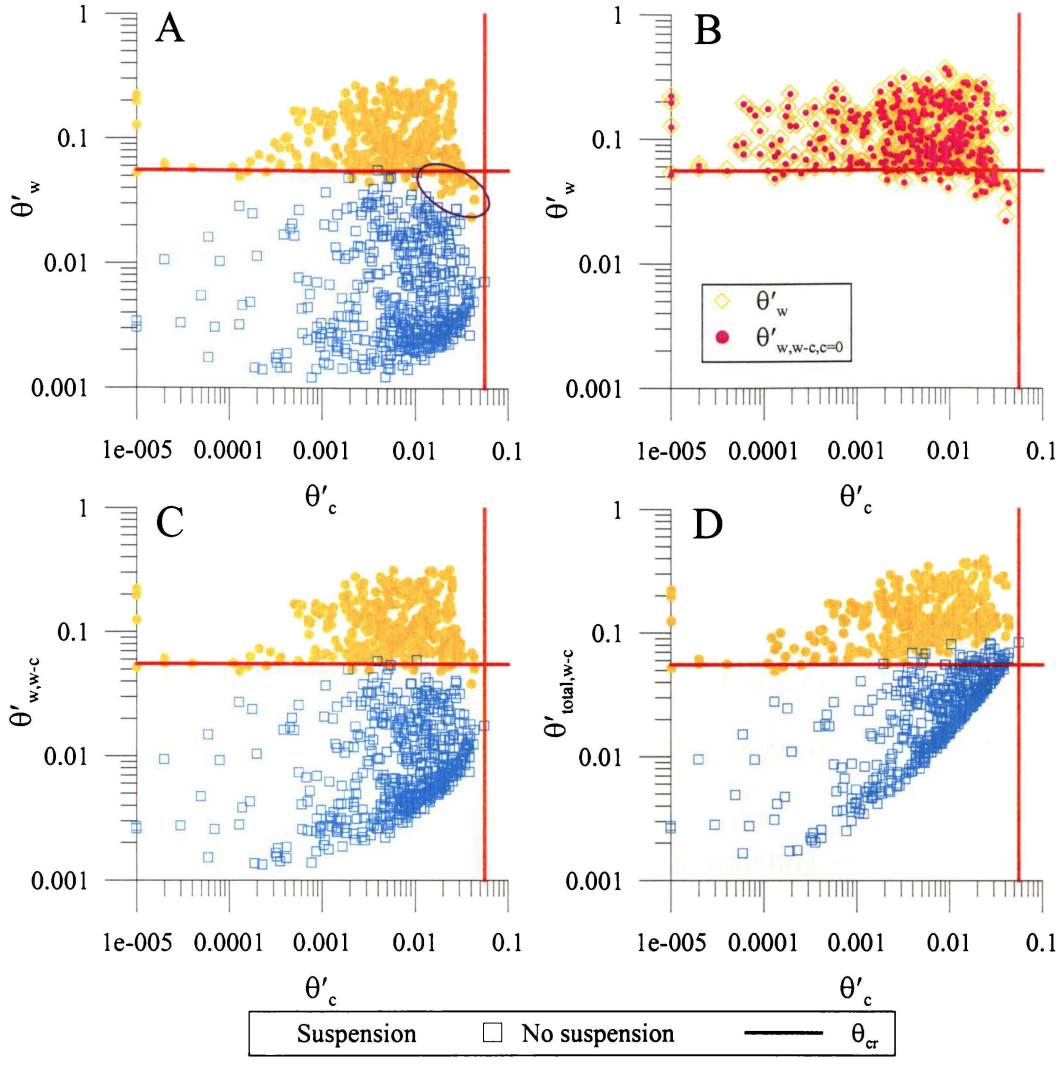

Figure 5.6: Plots of the skin friction due to steady currents and **A**: *the pure-wave skin friction* θ'_w *(i.e., Figure 5.5);* **B**: *the wave component of the total skin friction predicted by the wave–current interaction model with currents set to zero* ($\theta'_{w,w\text{-}c,c=0}$); **C**: *the wave component of the total skin friction predicted by the wave–current interaction model* ($\theta'_{w,w\text{-}c}$); *and* **D**: *the total skin-friction predicted by the wave–current interaction model* ($\theta'_{total,w\text{-}c}$). *Data are classified according to the suspension index as described previously. Red lines represent the predicted entrainment threshold* θ_{cr}. *Plot* **B** *is used to demonstrate that the wave–current interaction model's equivalent of pure wave skin friction,* $\theta'_{w,w\text{-}c,c=0}$ *(i.e.,* $\theta'_{w,w\text{-}c}$ *with currents set to zero), is the same as the pure wave skin-friction* θ'_w, *and thereby validates comparison between skin friction determined using the pure and wave–current regimes.*

5.4.2 Silt entrainment

Data on the entrainment of silts from the mixed silt/sand bed are presented in Figure 5.7, in which θ'_w is plotted against θ'_c and plot symbols are filled to denote silt "suspension" and hollow to denote "no suspension". The plots suggest that waves are capable of entraining silts from the intertidal flat but that currents are not. However, the separation of filled and hollow symbols that marks the apparent entrainment threshold for waves is not as obvious for silts (Figure 5.7A) as it was for sands (Figure 5.5). Despite the overlap of the filled and hollow symbols, "suspension" data do tend to cluster at high θ'_w while "no-suspension" data tend to cluster at low θ'_w, which demonstrates that silts are entrained with increasing θ'_w, although the critical value of θ'_w is difficult to determine. With respect to θ'_c, the absence of any separation in the "suspension/no-suspension" data indicates that steady currents do not entrain silts.

When the silt suspension index was re-examined, resulting in reclassification and removal of some data points (explained later in this section), the data appear to separate about $\theta'_w = 0.05$ (Figure 5.7B & C), which is very similar to the sand entrainment threshold observed previously. That is, $\theta_{cr,silt} \approx \theta_{cr,sand}$, which is unexpected because the predicted entrainment threshold for silts (d_s = 20 μm; $\theta_{cr,silt}$ = 0.19) is significantly larger than the predicted threshold for sands (d_s = 180 μm; $\theta_{cr,sand}$ = 0.056). The explanation for the discrepancy between observed and predicted entrainment of silts is thought to be related to the mixed-size bed, the arrangement of silt and sand grains in the sediment matrix, the formulation of θ_{cr}, and/or the contribution of non-local suspension processes.

As the relative abundance of silt in the surficial sediment matrix is very low (< 2 %) and silts in the bed are not known to overlie sands (with the exception of mangrove areas), silt particles most likely reside within the interstitial spaces between sand grains and consequently are shielded from bed shear stresses. When sands are lifted into suspension, the (interstitial) silt particles would also be exposed and entrained, so that the entrainment of silts and sands from the local bed would occur more-or-less simultaneously. In that case, $\theta_{cr,silt}$ should be the same as $\theta_{cr,sand}$, which is the observation made from the data. In addition, the low abundance of silt in the bed may

result in a lag between the time when silts are first entrained and the time when they are sufficiently concentrated to be detected above background turbidity. This may explain the "no-suspension" data observed when $\theta'_w > \theta_{cr,sand}$.

The discrepancy between observed and predicted threshold may also be related to the formulation of $\theta_{cr,silt}$ using the Shields curve. For silt particles, eqn 5.7 is said to be an improvement on the original Shields curve as it incorporates recent data (Soulsby and Whitehouse, 1997). However, the recent data is from the entrainment of silts by currents alone and includes no new data from entrainment under waves. Eqn 5.7 ($\theta_{cr,silt} = 0.19$) is arguably better than the original Shields curve, which gives a threshold value for silt ($\theta_{cr,silt} = 0.5$) that is larger than Bagnold's (1963) theoretical maximum (0.3) and that is determined from extrapolation beyond the data limits. Also, Soulsby and Whitehouse (1997) note that scatter in the wave data used to formulate the Shields curve may be due to application of different friction factors. Consequently, the Shields curve is not well-defined for silt-sized particles and, given the entrainment mechanics of silt in the intertidal-flat bed, the observed threshold is taken as the best measure for silt entrainment ($\theta_{cr,silt} \approx 0.056$).

As noted above, silt "suspension" data underwent further analysis which resulted in the reclassification and removal of several bursts. Silt particles, which have small settling speeds, may remain in suspension several hours after they are first entrained, and thus may be detected in suspension far from their origins and in subcritical flow conditions. Consequently, attempting to distinguish entrainment conditions by way of the suspension index used here may be compromised. Two examples are used to demonstrate this and also to refine the silt "suspension/no-suspension" index.

During the subcritical conditions which follow cessation of wave activity, silt concentrations return to their calm-weather background levels over 1–2 tidal cycles (e.g., Green *et al.*, 2000). Removal of post storm data (i.e., when concentrations are slowly declining toward ambient levels) eliminates a number of subcritical ($\theta'_w < \theta_{cr}$) "suspension" points (see Figure 5.7A and B). Likewise, terrigenous silts may be introduced to the estuary during floods. Identification and removal of data from rainfall events further reduces scatter in the data and thereby improves the estimate of the observed entrainment threshold (Figure 5.7C).

On the Wiroa flat (and across the estuary; Green and Bell, 1995; Green *et al.*, 2000), silt suspension rises during episodes of wave activity, which are marked by periods of wave-induced skin friction in excess of the critical skin friction required to entrain sands ($\theta_{cr,sands\ \&\ silts} = 0.056$). Silts in the intertidal-flat bed have the same threshold as sands because sand particles shield them from bed shear stresses. The small settling velocity of silt implies that observed silt suspensions will almost always comprise silts sourced from elsewhere on the intertidal flat and elsewhere in the estuary. It is not possible to distinguish the relative contributions with this dataset.

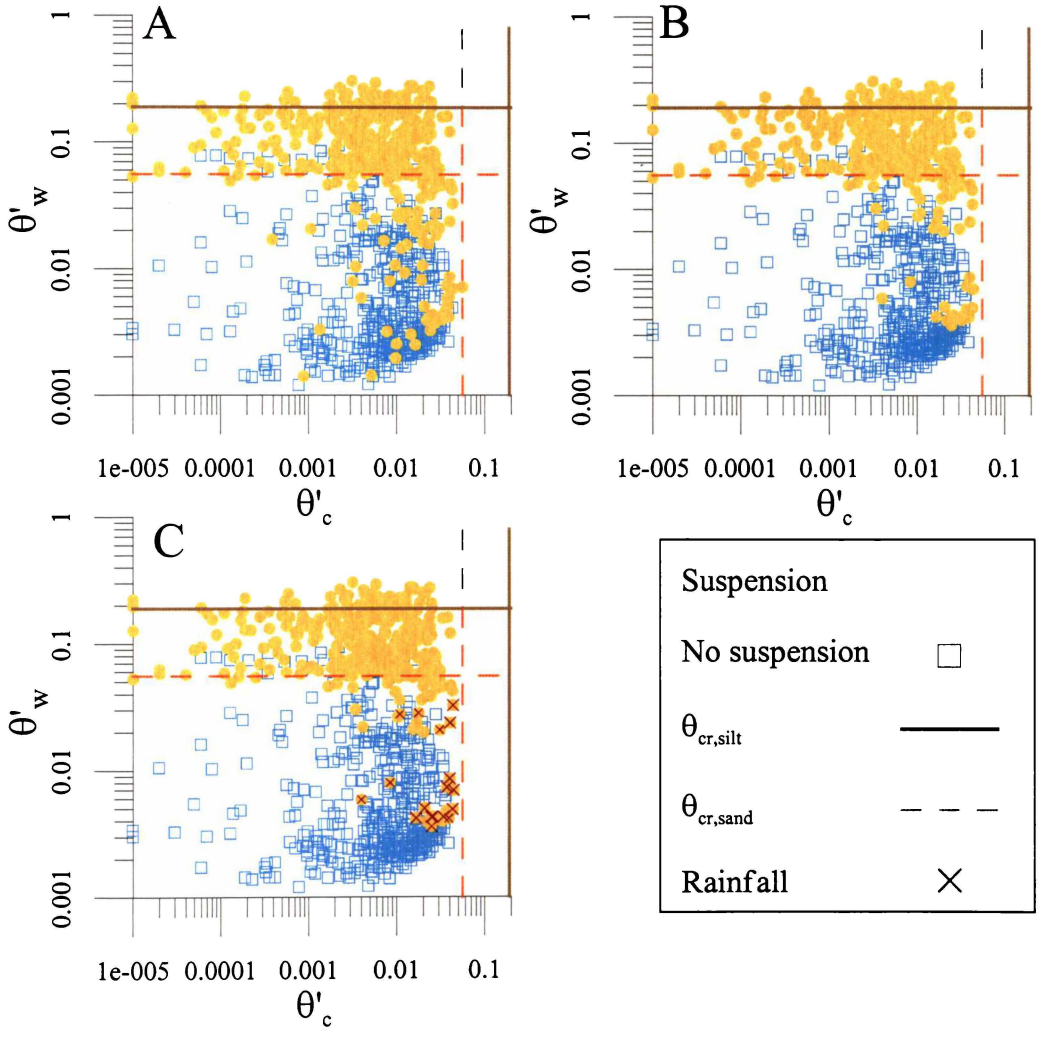

Figure 5.7: Plots of the skin friction due to waves θ'_w and steady currents θ'_c. Data are classified according to whether silt is in suspension (filled symbols) or not (hollow symbols). Predicted critical entrainment thresholds for silt and sand are marked by lines as shown in the legend. Plot **A** *includes all suspended silt data, while in plot* **B** *post wave-event data are removed (see text for explanation), and in plot* **C** *symbols marked with a* **×** *indicate suspension due to catchment runoff during rainfall events.*

5.5 SUSPENDED SEDIMENTS UNDER CURRENTS AND WAVES

5.5.1 Suspended Sand

Time-averaged suspended-sand reference concentration

For each $\overline{C}_{sand}$-profile the bed was identified and the profile referenced to elevation above the bed, as follows. In ABS data, a sharp break in the slope of the concentration profile is caused by the strong echo from the bed (see Figure 5.8). The 'base' of the ABS profile is the concentration measured 1-cm above the bed and is found at range from transducer r_{base}, while the range to the bed, $r_{bed} = r_{base} - 1$ cm, is used to reference the profile with respect to the bed for each burst as $z = r_{bed} - r$ and $z_{base} = r_{base}$ (Figure 5.8).

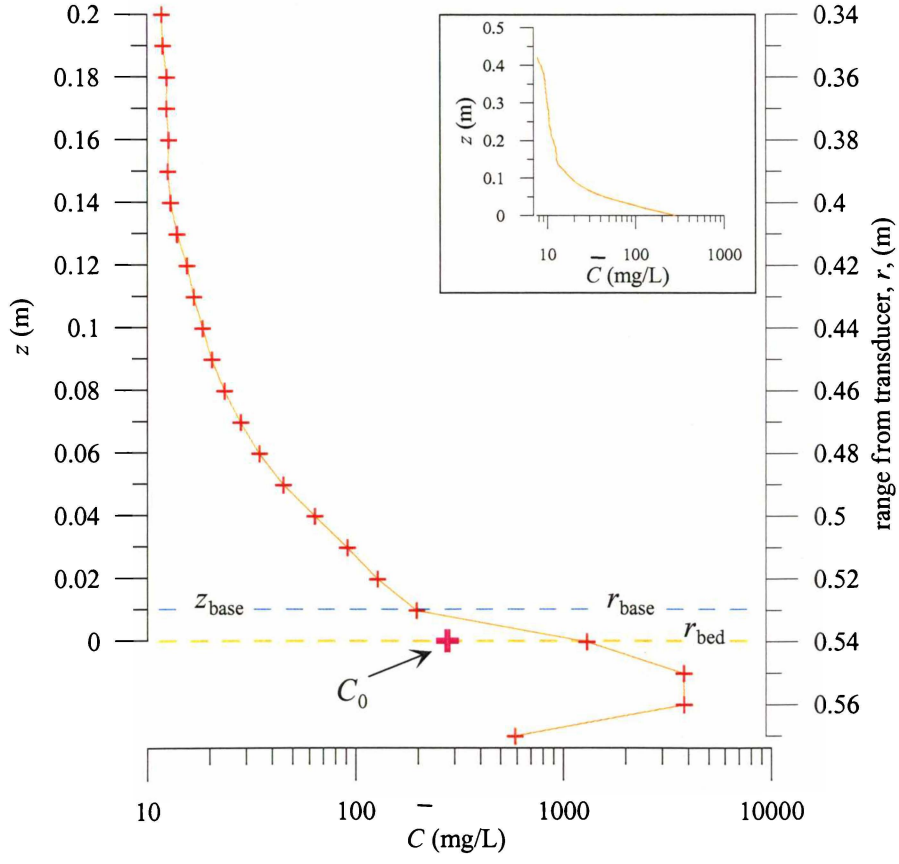

Figure 5.8: An example of a $\overline{C}_{sand}$ -profile illustrating the definition of z_{base} and C_0. The right y-axis is the range from transducer r. For each burst the elevation above the bed is determined as $z = r_{bed} - r$.

The reference concentration, C_0, was estimated using data from the near-bed section of the concentration profiles, which plotted as straight lines in $\log_{10}(\overline{C}_z) - z$ space. Following Webb and Vincent (1999) and Green and Black (1999), C_0 was calculated by fitting a straight line to the profile data over the domain

$$z_{base} + 3 \text{ cm} \geq z \geq z_{base}$$

and extrapolating the fitted line to z_{base} – 1 cm (Figure 5.8). For the fitted lines, the r^2 correlation coefficient was high in most cases ($r^2 > 0.9$ for 97% of the profiles) and the F-statistic, which was greater than the tabled F-value for 98% of the profiles, indicated a linear relationship between the parameters in $\log_{10}(\overline{C}_z) - z$ space. Bursts where $r^2 < 0.9$ and/or $F < F$-tabled were excluded from the following analysis.

Figure 5.9 is a plot of the observed reference concentration against the wave-induced skin friction. The pure-wave skin friction data ( ) fall into two groups: in the first group, for which θ'_w < c. 0.10, C_0 is proportional to the cube of θ'_w and the data are described by:

$$C_0 = 0.08\rho_s\theta'^3_w \qquad \text{(Eqn 5.9)}$$

(solid orange line, Figure 5.9), which is similar to the model of Nielsen (1986) and Green and Black (1999) for C_0 over rippled beds. In the second group, for which $0.1 \leq \theta'_w \leq 0.3$, the relationship between C_0 and θ'_w changes from a power-law to a linear model (dashed orange line, Figure 5.9):

$$C_0 = 0.0007\rho_s\theta'_w \qquad \text{(Eqn 5.10)}$$

which was not an obvious feature in the Nielsen (1986) and Green and Black (1999) datasets.

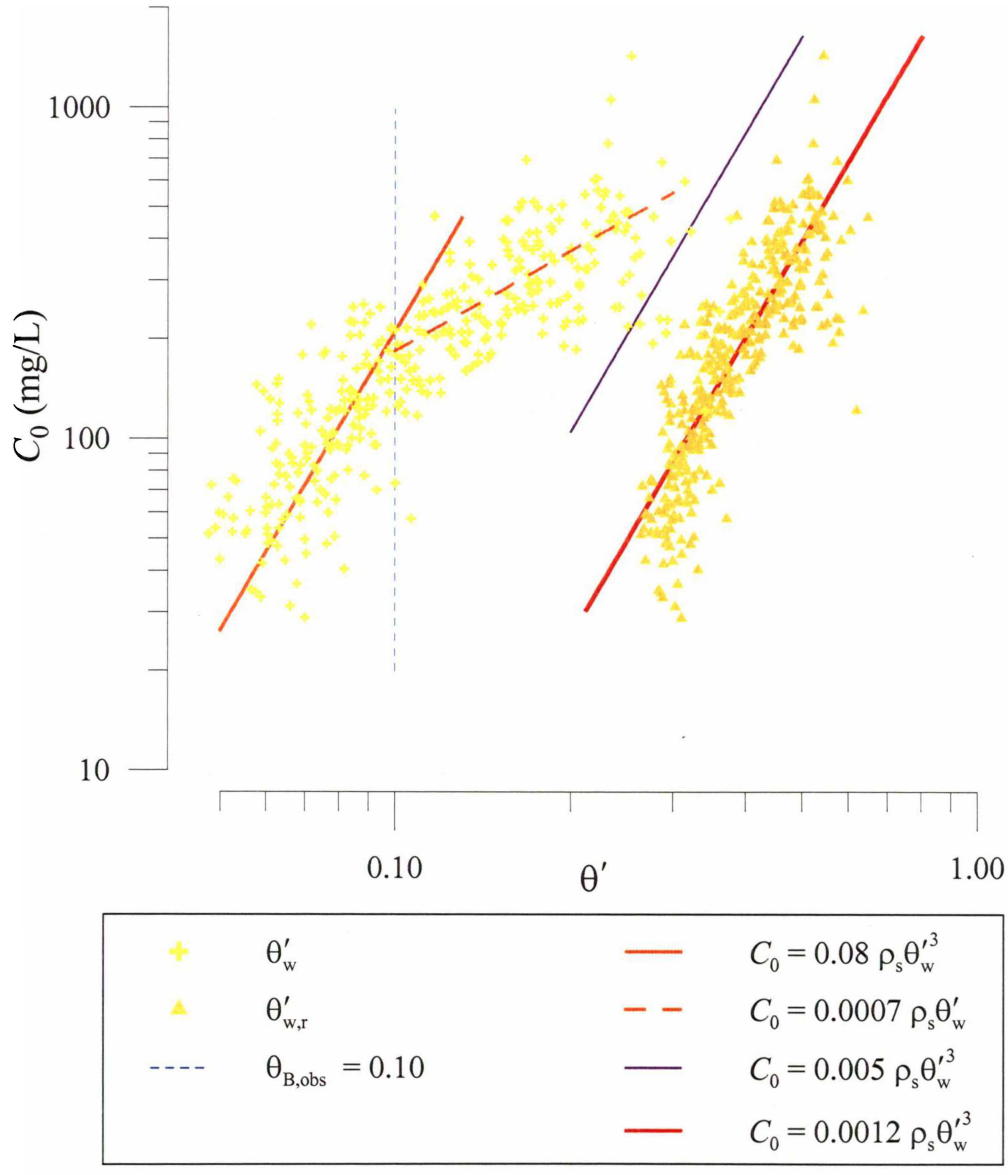

Figure 5.9: The relationship between skin friction estimates (θ'_w, $\theta'_{w,r}$) and C_0.

The differences between these two groups may be related to changes in the steepness of wave-orbital ripples $[\eta/\lambda]_r$. Nielsen (1986) showed that C_0-θ'_w data fell into two groups (solid orange and purple lines in Figure 5.9), broadly distinguished by the bed condition (ripples/flat beds). In the ripple regime, skin friction is enhanced by flow contraction near ripple crests (Du Toit and Sleath, 1981), and data cluster in a different space on C_0-θ'_w plots. To account for flow contraction over ripples, Nielsen (1986) parameterised the enhancement of skin friction over wave-formed ripples as

$$\theta'_{w,r} = \frac{0.5\rho_f f'_w}{(\rho_s - \rho_f)gd_s}\frac{U_w^2}{(1-\pi[\eta/\lambda]_r)^2} = \frac{\theta'_w}{(1-\pi[\eta/\lambda]_r)^2}, \qquad \text{(Eqn 5.11)}$$

and found C_0 data coalesced into a single group described by:

$$C_0 = 0.005\rho_s\theta'^3_{w,r} \quad \text{(Eqn 5.12)}$$

That is, eqn 5.12 predicts C_0 for both rippled and flat beds (i.e., sheet flow).

This approach, using $\theta'_{w,r}$ instead of θ'_w, was applied to the Wiroa data. As there are no ripple data (due to sonar failure) eqn 5.11 was predicted using (Nielsen, 1981):

$$[\eta/\lambda]_r = 0.342 - 0.34\sqrt[4]{\theta'_w} \quad \text{(Eqn 5.13)}$$

The θ'_w data, shown in Figure 5.9 as , collapse onto a single curve,

$$C_0 = 0.0012\rho_s\theta'^3_{w,r}, \quad \text{(Eqn 5.14)}$$

as observed by Nielsen (1986) and Green and Black (1999). This finding has two important implications. Firstly, changes in ripple steepness explain the two groups observed in C_0–θ'_w space, even though the second group in the Wiroa data (eqn 5.10) does not plot in the sheet-flow region identified by Nielsen (1986) and Green and Black (1999). Secondly, eqn 5.13 provides a reasonable estimate of $[\eta/\lambda]_r$, at least with respect to the Wiroa data and the C_0–$\theta'_{w,r}$ relationship. That is, C_0 at Wiroa Island is a function of the θ'_w and $[\eta/\lambda]_r$. These results invalidate a change in sediment availability at higher stresses, which might have otherwise been invoked to explain the differences between eqn 5.9 and eqn 5.10.

The clustering of the Wiroa data around eqn 5.14 suggests that three ripple regimes influence C_0. Firstly, when $\theta'_w < 0.1$, ripples are near maximum or *equilibrium* steepness (determined by angle of repose for the sediment) (solid orange line, Figure 5.9). Secondly, as θ'_w increases, the flow becomes too vigorous and ripple steepness declines (dashed orange line, Figure 5.9). Finally, the bed is flattened and sheet flow conditions preside (solid purple line, Figure 5.9). The point separating the first two groups (dashed blue line, Figure 5.9) is sometimes known as the *break-off point* (Grant and Madsen, 1982). The low and high skin friction regimes, representing equilibrium

ripples and flat/hummocky beds, are described by Nielsen (1986) and Green and Black (1999). However, the intermediate skin friction regime, which represents c. 50% of the Wiroa data, is not obvious in their datasets and thus received no comment.

The intermediate range, which is characterised by change in the relationship between C_0 and θ'_w (i.e., reference concentration changes from a cubic dependence on θ'_w to a linear dependence), would appear to result from a decrease in ripple steepness prior to onset of sheet flow, as described by eqns 5.11, 5.13 and 5.14 and Figure 5.9. The intermediate range observed here may simply represent a transitional state which has not been observed in other datasets because of the speed at which the bed moves from rippled to flat beds in those datasets. Alternatively, the intermediate data may represent transitional bottom and skin friction conditions in which both flat and rippled beds existed during each burst. These conditions may be expected under wave groups (e.g., Hanes, 1990), which are known to occur on Wiroa flat.

The differences between the coefficients in eqn 5.12 and eqn 5.14 may be due to overestimation of ripple steepness by eqn 5.13, however there are no ripple data to validate this assertion.

Eroded ripples are expected to give way to flattened beds and sheet flow, however there are insufficient observations at high θ'_w in the Wiroa dataset (Figure 5.9) to identify the sheet flow regime that Nielsen (1986) observed. This is taken to mean that sheet flow only rarely, if at all, occurred. Furthermore, the likely absence of sheet flow/flat beds is consistent with eqn 5.13, which cannot predict flat beds, but does correctly account for changes in C_0 due flow contraction over ripple crests. Consequently, $\theta'_{w,r}$ would be expected to deviate from eqn 5.14 (Figure 5.9) when skin friction was large, which is not apparent.

In contrast, there is some divergence from eqn 5.14 when $\theta'_{w,r}$ is comparatively low (Figure 5.9). The divergence may be due to incorrect prediction of the ripple steepness. Under low bed shear stress, empirical ripple equations are least reliable as antecedent ripples can dominate and ripple response tends to lag behind local flow conditions (Dingler and Clifton, 1984; Williams *et al.*, 2000).

Time-averaged suspended-sand profile

In the near-bed region (z < 10–12 cm), the Wiroa concentration profiles plot as straight lines in $\log_{10}(\overline{C}_z) - z$ space (Figure 5.10A) and are described by Nielsen's (1984) simple exponential profile model:

$$\overline{C}(z) = C_0 \, e^{-z/l_s} \qquad \text{(Eqn 5.15)}$$

(Figure 5.11). The mixing length, l_s, is the length scale which governs the mixing of sediment particles and can be viewed as a typical distance (elevation) over which sediment is mixed into the water column (Aagaard and Masselink, 1999). Eqn 5.15 derives from the governing equation for gradient diffusion:

$$w_s \overline{C} = -\varepsilon_s \frac{d\overline{C}}{dz} \qquad \text{(Eqn 5.16)}$$

in which the sediment diffusivity, ε_s, is vertically invariant. $d\overline{C}/dz$ is the concentration gradient and ε_s is related to the mixing length as (Nielsen, 1992):

$$l_s = \frac{\varepsilon_s}{w_s}. \qquad \text{(Eqn 5.17)}$$

In the gradient diffusion model, the downward sediment flux ($w_s \overline{C}$) is balanced by the upwards sediment flux, which in turn is given by the product of the concentration gradient and the sediment diffusivity ($-\varepsilon_s(d\overline{C}/dz)$). Time-averaged concentration profiles are often treated with diffusion alone for simplicity (e.g., Masselink and Pattiaratchi, 1998; Ogston and Sternberg, 2002), which is justifiable for near-bed suspensions as the vertical component of velocity, w, tends to zero. At higher elevations, Ogston and Sternberg (2002) found that convection accounted for less than 20% of the sediment mixing.

The sediment diffusivity profiles plotted in Figure 5.10B were determined from the $\overline{C}_{sand}$-profiles (Figure 5.10A) as:

$$\varepsilon_s(z) = \frac{-w_s \overline{C}_z}{d\overline{C}/dz}, \qquad \text{(Eqn 5.18)}$$

where the settling velocity, w_s, was estimated following Soulsby (1997) as w_s = 2 cm/s for a 180-μm diameter particle. The ε_s-profiles are approximately vertically invariant, which is expected as most of the Wiroa data can be described by the simple exponential model (eqn 5.15). The profiles in which ε_s is not vertically invariant account for only a small percentage of the suspension profiles (3%), and are further discussed later in this section.

The mixing length is shown in Figure 5.12, which was determined from the $\overline{C}_{sand}$-profiles as:

$$l_{s,obs} = \frac{dz}{d \ln \overline{C}} \qquad \text{(Eqn 5.19)}$$

where $\overline{C}$ has units of volume/volume and eqn 5.19 was applied over the domain 1 cm < z < 6 cm.

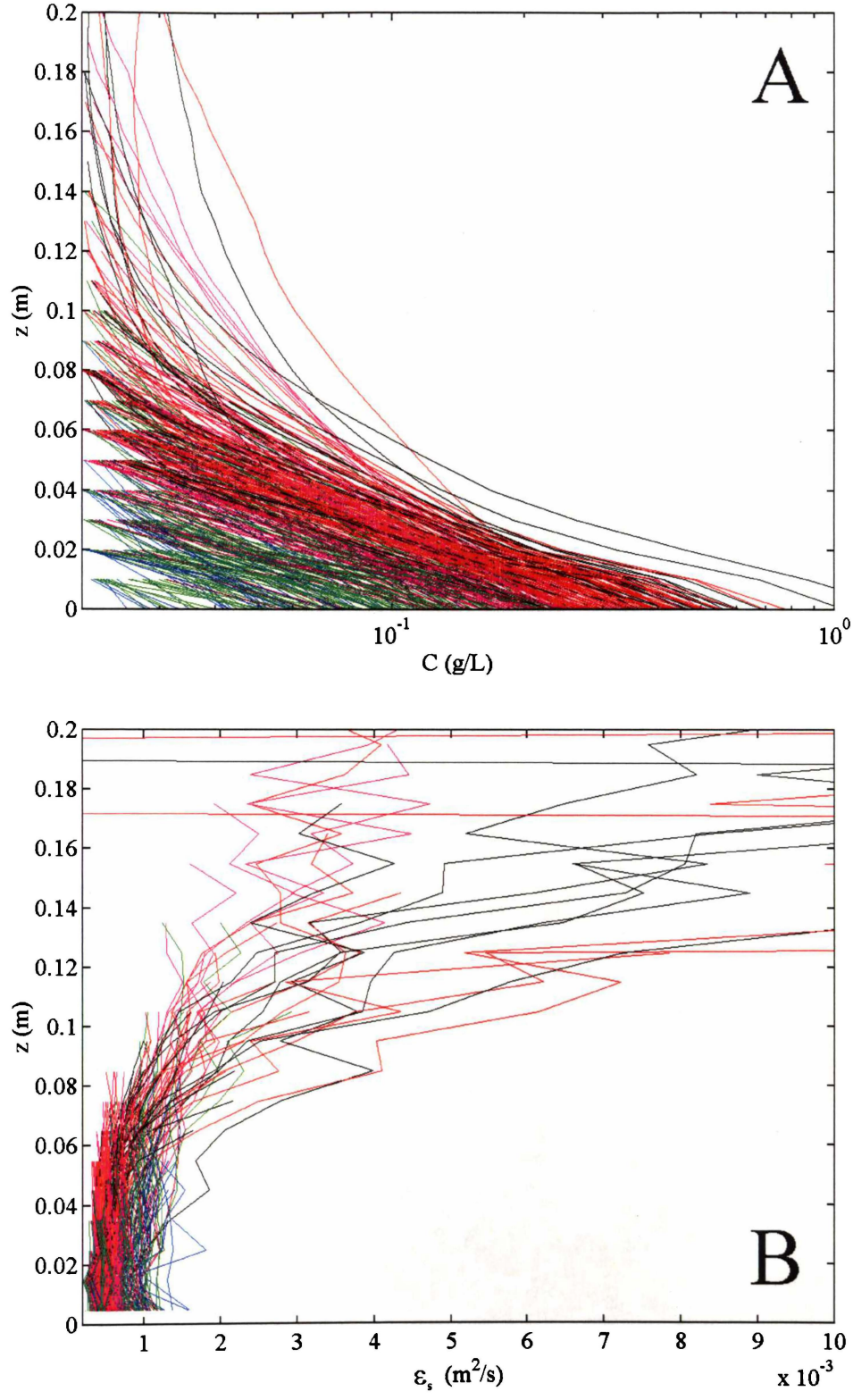

Figure 5.10: **A**: $\overline{C}_{sand}$ *-profiles from lower and middle intertidal flat (W1H and W2S).* **B**: ε_s *estimated from* $\overline{C}_{sand}$ *-profiles. Colour coding is by* u'_{*w} *: — < 5 cm/s, — 5–6 cm/s, — 6–7 cm/s, — 7–8 cm/s, and — > 8 cm/s.*

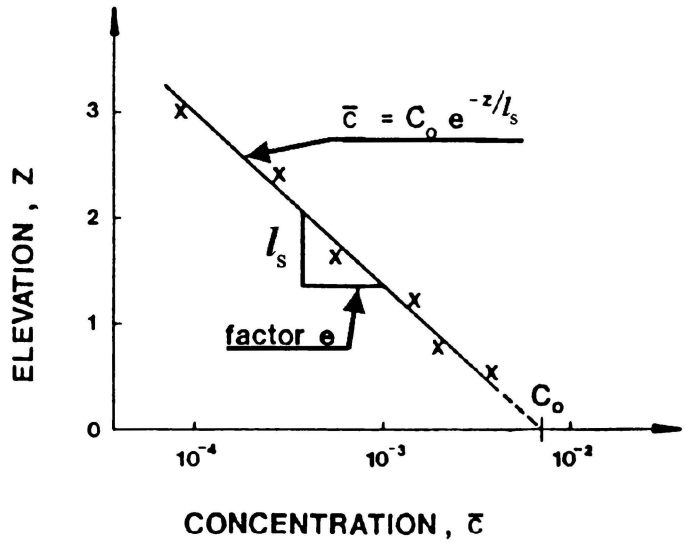

Figure 5.11: Definition of $\overline{C}$-profile parameters C_0 and l_s. (Source: Figure 7-182, Nielsen, 1990).

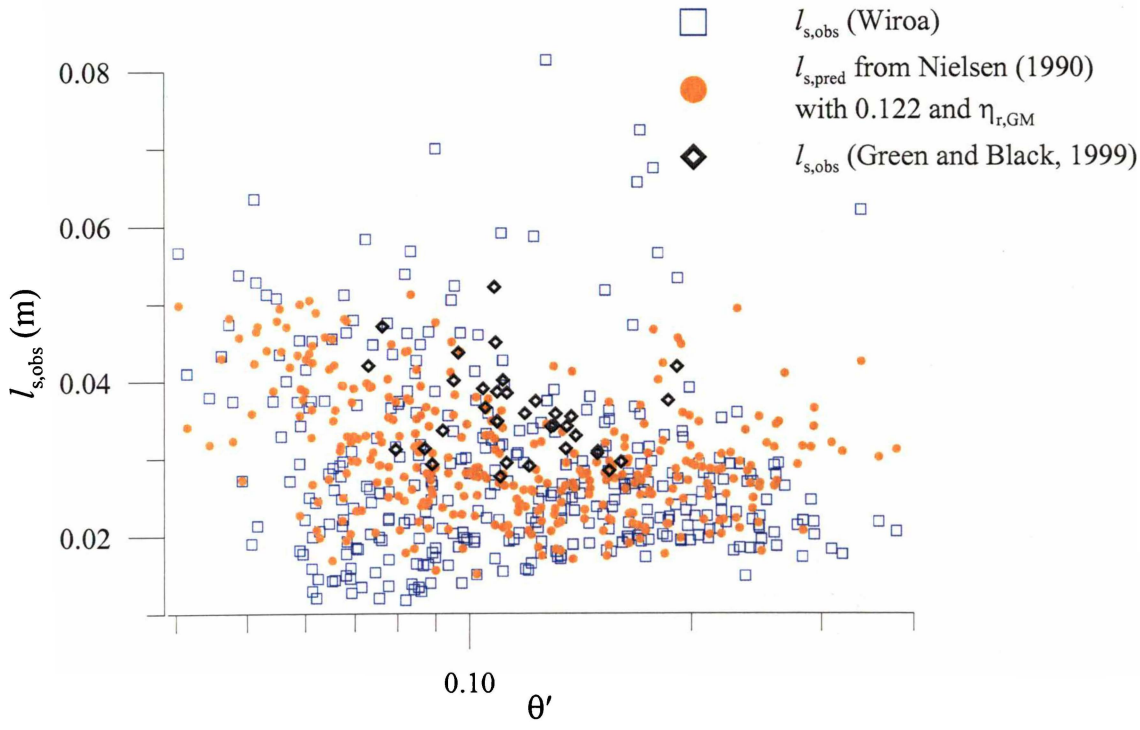

Figure 5.12: Comparison of θ'_w and l_s for Wiroa and Mangawhai (Green and Black, 1999) data, demonstrating the lack of relation between the two parameters.

As θ'_w drives ripple evolution and turbulent kinetic energy, which in turn is related to the mixing length (e.g., Kajiura, 1964; Sheng and Hay, 1995; Ogston and Sternberg, 2002), some relationship between θ'_w and l_s might be expected. However, colour coding of ε_s-profiles (and $\overline{C}_{sand}$-profiles) according to skin friction (Figure 5.10) suggests there is no θ'_w–l_s relationship, as does the scatter plot of θ'_w and l_s (Figure 5.12), which includes some open-coast (Mangawhai) data. Instead, l_s can be described by Nielsen's (1990) equation:

$$\frac{l_s}{\eta_r} = X\frac{a_w\omega}{w_s} \qquad \text{(Eqn 5.20)}$$

where the constant X = 0.122 was determined by best fit to the Wiroa data (Figure 5.13A), $U_{3,bed}$ was used for $a_w\omega$, w_s = 2 cm/s, and ripple heights (η_r) were estimated from Grant and Madsen's (1982) empirical relation:

$$\eta_{r,GM} = \begin{cases} 0.22(\theta'_w/\theta_{cr})^{-0.16}a_w & \text{for } \theta'_w \le \theta_{B,GM} \\ 0.48(D_*^{1.5}/4)^{0.8}(\theta'_w/\theta_{cr})^{-1.5}a_w & \text{for } \theta'_w > \theta_{B,GM} \end{cases} \qquad \text{(Eqn 5.21)}$$

where $\theta_{B,GM}$ is the break-off point determined from Grant and Madsen (1982) as:

$$\theta_{B,GM} = 1.8\theta_{cr}[D_*^{1.5}/4]^{0.6} \qquad \text{(Eqn 5.22)}$$

Nielsen (1990) found X = 0.075 from laboratory and field observations over natural sand bed ripples ($a_w\omega/w_s$ < 18). Those data (dark letters), as well as MacDonald's (1977) fixed ripple observations (dark symbols), are also plotted on Figure 5.13A. While there is a similar degree of scatter in all of the datasets, l_s/η_r is always proportional to $a_w\omega/w_s$, suggesting that ripples play an important role in generating bottom turbulence and enhancing mixing. The Wiroa data overlap somewhat with Nielsen's (1990) data from natural sand bed ripples.

The differences between X for the Wiroa and Nielsen datasets, and scatter between $l_{s,obs}$ and $l_{s,pred}$ (Figure 5.13B), may be explained by: inadequately defined parameters; unrealistic assumption of a constant value for w_s; and/or an additional and unaccounted

for mixing mechanism. The remainder of this section is a discussion of these possibilities.

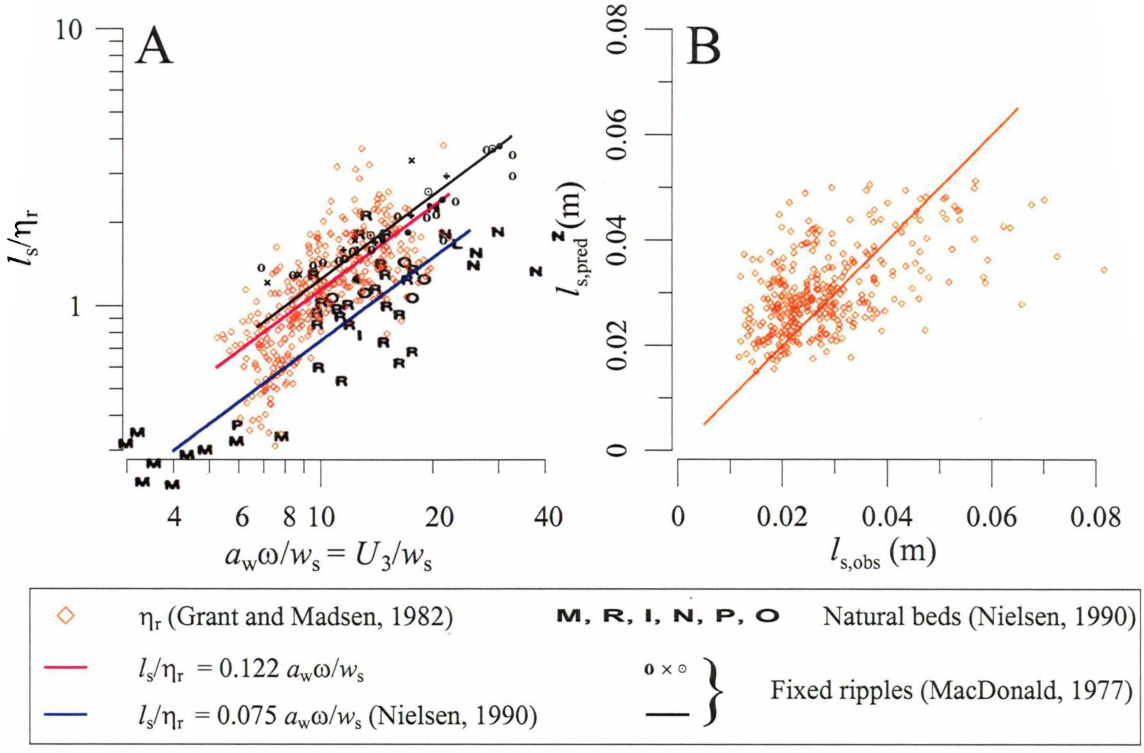

Figure 5.13: **A**: *Relative suspension length scales based on $l_{s,obs}$ and $\eta_{r,GM}$. Orange symbols are Wiroa data with $l_{s,obs}$ and $\eta_{r,GM}$, and the pink line is the line of best fit to Wiroa data (eqn 5.20). Black symbols are MacDonald's (1977) data (for different grain sizes) over a bed of wooden ripples.* **B**: *Comparison of observed ($l_{s,obs}$) and predicted with mixing length (eqn 5.20 and eqn 5.21).*

Firstly, there is some uncertainty regarding model parameters. The velocity scale, $a_w\omega$, was not specified by Nielsen, and differences in definitions of $a_w\omega$, as well as the way w_s and η_r are determined, may explain scatter in, and the differences between, the two datasets. For instance, when U_s is used instead of U_3 for $a_w\omega/w_s$ then X = 0.09, which accounts for about half of the difference in X between the Wiroa and Nielsen data. The differences are even smaller if U_{rms} is used. Similarly, differences in estimates of w_s can result from differences in measurement techniques (e.g., sieving, laser-sizing, settling tube), choice of a representative grain size (e.g., mean, median, d_{60}, d_{90}), choice of equation used to determine settling speed from particle size, and variation in particle characteristics (e.g., particle density, angularity, roughness and shape). It is thus possible to contrive a result in which the Wiroa data will fit Nielsen's relationship.

Secondly, w_s may vary due to changing suspended sand sizes. Although the Wiroa sands are well sorted, it has been shown above that small changes in particle size and settling can explain differences between the datasets. Thus, scatter may imply variation in the suspended particle sizes at an inter-burst time scale. There are currently no data on variation in suspended sand sizes for confirmation.

Thirdly, there are no bedform observations for Wiroa. The reliance on empirical ripple-height estimates is another obvious candidate to explain both differences between the two datasets and also the spread in the data (Figure 5.13). In addition to being unable to account for lag effects in bed response to local forcing (e.g., Dingler and Clifton, 1984; Williams *et al.*, 2000), ripple-height predictors are inconsistent (e.g., Figure 5.14), although they are within 1-2 cm of ripple heights observed when the flat is exposed. Grant and Madsen's (1982) model (eqn 5.21) gave predictions of η_r that were the most consistent with Nielsen's l_s model, compared to the ripple height predictions by Nielsen's (1981) regular-wave model (eqn 5.23), Nielsen's (1981) irregular-wave model (eqn 5.24) and typical ripple heights observed on the exposed flat (eqn 5.25):

$$\eta_{r,reg} = \begin{cases} (0.275 - 0.022\,\psi^{0.5})a_w & \text{for } \psi < 156 \\ 0 & \text{for } \psi > 156 \end{cases} \qquad \text{(Eqn 5.23)}$$

$$\eta_{r,irreg} = 21\,\psi^{-1.85} a_w \qquad \text{for } \psi > 10 \qquad \text{(Eqn 5.24)}$$

$$\eta_{r,const} = 0.02\,\text{m} \qquad \text{(Eqn 5.25)}$$

where ψ is the mobility number:

$$\psi = \frac{(a_w \omega)^2}{(s-1)g d_s} \qquad \text{(Eqn 5.26)}$$

The comparison is shown in Figure 5.15.

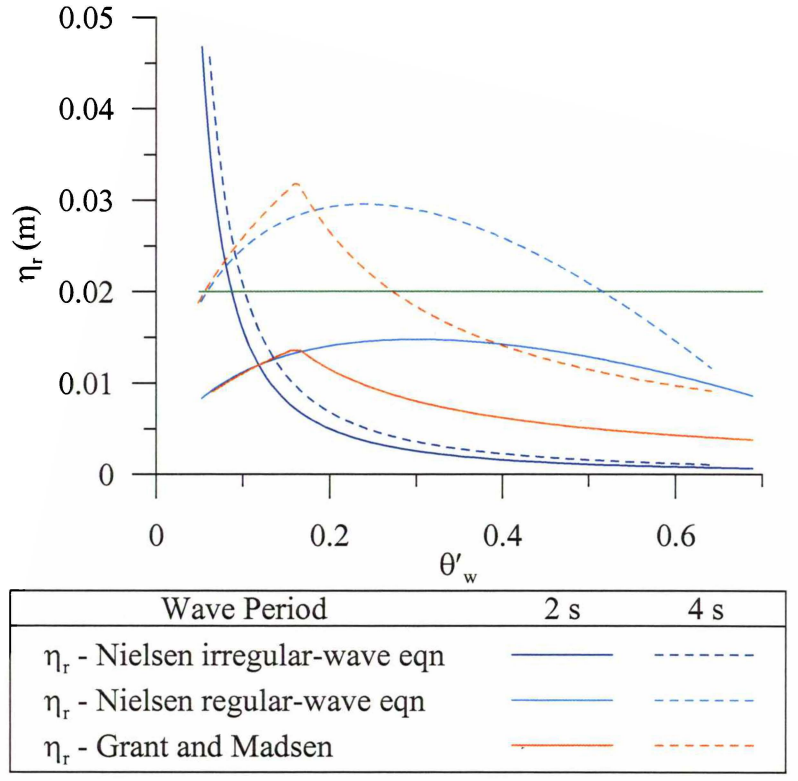

Figure 5.14: Ripple height predictions for eqns 5.21, 5.23 and 5.24. All equations are for wave-orbital ripples and each line represents the ripple height due to the skin friction associated with a given wave period. Examples are given for 2-s and 4-s waves as these span the range of measured wave periods at Wiroa.

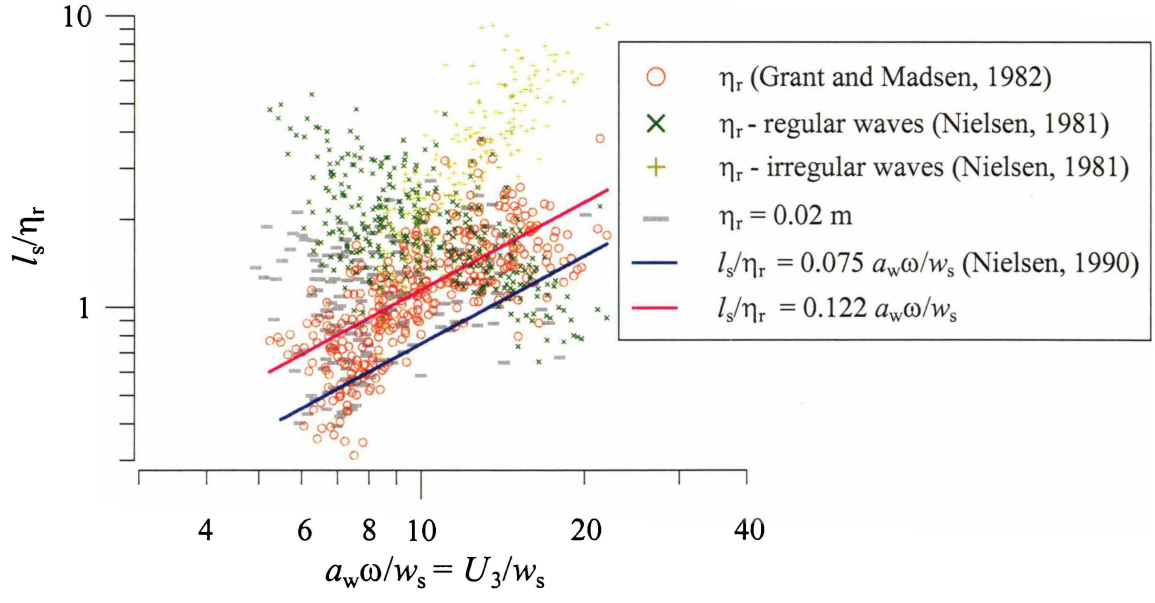

Figure 5.15: Relative suspension length scales based on $l_{s,obs}$ and η_r determined from the empirical ripple height equations of Grant and Madsen (1982), and Nielsen's (1981) irregular-wave and regular-wave equations. A fourth comparison is made using η_r = 2 cm, which is a typical ripple height observed on the exposed flat.

The final point concerning Nielsen's mixing-length model concerns the possible role of surface-penetrating turbulence under whitecaps. Ogston and Sternberg (2002) found that diffusivity under unbroken waves was invariant with elevation above the bed, which is consistent with the Wiroa observations. Under plunging breakers, however, surface-penetrating turbulence causes large ε_s which decreases with distance from the sea surface. This implies that surface-generated turbulence can penetrate to the bed (Ogston and Sternberg, 2002). Three percent of Wiroa ε_s-profiles show large ε_s decreasing from the surface (Figure 5.10B), suggesting that some of the data is affected by breaking. However, ε_s -profiles are always vertically invariant (near the bed; z = 0 to 7–10 cm), suggesting that surface-penetrating turbulence does not reach the bed as noted for plunging breakers. This observation is consistent with whitecaps and spilling breakers, whose breaking turbulence does not penetrate to the bed (Miller, 1976; Donelan 1978).

In summary, the factors contributing to scatter in the Wiroa mixing length are most likely related to the way parameters are specified and to the reliance on empirical estimates of ripple dimensions. The effect of surface-penetrating turbulence under whitecaps may explain a small percentage of the ε_s-profiles.

5.5.2 Suspended Silt

Shown in Figure 5.16 are the $\overline{C}_{silt}$ -profiles, which show silt concentrations to be more-or-less homogenous with depth. Hence, the silt reference concentration ($\overline{C}_{ref,silt}$) can be taken from any level. Also shown in Figure 5.16 is $\overline{C}_{ref,silt}$ taken at z = 45.5 cm, plotted against θ'_w.

Silt concentration profiles are vertically invariant because silt particles have a low settling speed and are therefore readily mixed throughout the water column and maintained in suspension in turbulent environments (e.g., Collins, *et al.*, 1981). There is no obvious relationship between θ'_w and $\overline{C}_{ref,silt}$, for which there are several possible reasons. Firstly, less than 2% of the bed sediment is silt. This might mean that the supply of silt from the bed is exhausted before an equilibrium silt suspension can be established. Secondly, since $w_{s,silt}$ is small, settlement time-scales may exceed the time-scales of wave events (Black, *et al.*, 1999). Hence, suspended silt encountered at any

particular location in the estuary may have originated at some other location a considerable distance "upstream". Finally, the velocity of a flow that entrains fine particles exceeds the settling rate of fines at the bed (Nielsen, 1992). Consequently, $\overline{C}_{\text{ref,silt}} \neq f(\theta'_{\text{w}})$ and, for a given erosional stress, C_{silt} increases until either yield strength at the bed changes, sediment supply is exhausted, high concentrations alter the fluid properties, or sediment is advected away from the source.

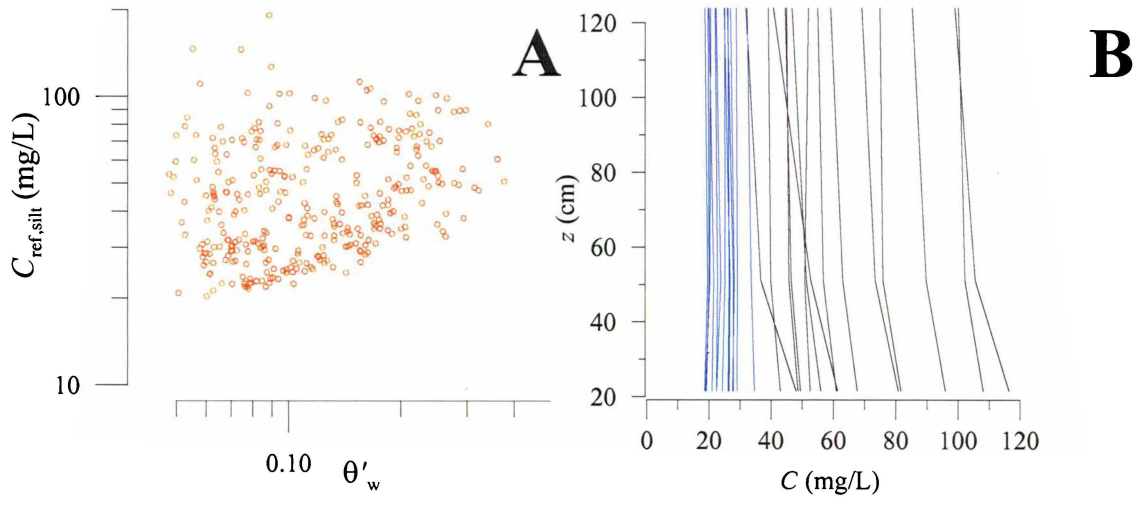

Figure 5.16: **A**: *Comparison of* θ'_{w} *with* $\overline{C}_{\text{ref,silt}}$. **B**: *Examples of* $\overline{C}_{\text{silt}}$ *-profiles.*

5.6 SEDIMENT FLUX

5.6.1 Introduction

The wave-induced sand flux, $\vec{Q}_{\text{sand,total}}$, was conceptualised as the vector sum of three components (following Green and MacDonald, 2001): the advection of the time-averaged wave-induced suspension by the mean current ($\vec{Q}_{\text{sand,wc}}$), the advection of the wave-induced suspension by waves ($\vec{Q}_{\text{sand,ww}}$), and the bed-load flux due to both waves and currents ($\vec{Q}_{\text{sand,bed,w\&c}}$):

$$\vec{Q}_{\text{sand,total}} = \vec{Q}_{\text{sand,wc}} + \vec{Q}_{\text{sand,ww}} + \vec{Q}_{\text{sand,bed,w\&c}} \qquad \text{(Eqn 5.27)}$$

Arrows in eqn 5.27 denote vector quantities and the addition is vector addition. The bedload is that part of the total load which is supported by intergranular forces and which responds instantaneously to the bed shear stress, while the suspended load is

supported by turbulence in the fluid flow (Bagnold, 1956). The fact that some particles can be supported by both intergranular forces and by fluid drag makes bedload practically unmeasurable in situations where suspended load also occurs (Nielsen, 1992). Thus, bedload was modelled while suspended load was determined using current and concentration data from Alice.

In comparison to sands and gravels, which require constant application of an upward-directed force to remain in suspension for any length of time, fine particles (e.g., silts) remain in suspension for long periods (Dyer, 1986). Also, there is no bedload component, so silt flux shortens to:

$$\vec{Q}_{\text{silt,total}} = \vec{Q}_{\text{silt,wc}} + \vec{Q}_{\text{silt,ww}} \qquad \text{(Eqn 5.28)}$$

where $\vec{Q}_{\text{silt,wc}}$ and $\vec{Q}_{\text{silt,ww}}$ are the current- and wave-advected components, respectively.

5.6.2 Estimation of Sediment Flux

Suspended-load flux

$\vec{Q}_{\text{sand,wc}}$ was determined for each burst and for $z < z_{\text{ABS}}$ as:

$$Q_{\text{sand,wc}} = \int_{z_{\text{base}}}^{z_{\text{ABS}}} \overline{C}_{\text{sand}}(z)\,\overline{U}(z)\,\mathrm{d}z \qquad \text{(Eqn 5.29)}$$

and

$$\phi_{\text{sand,wc}} = \phi_{\overline{U}} = \tan^{-1}\left(\overline{u}(z)/\overline{v}(z)\right) \qquad \text{(Eqn 5.30)}$$

where $Q_{\text{sand,wc}}$ is the flux magnitude and the flux direction, $\phi_{\text{sand,wc}}$, is the mean current direction, $\phi_{\overline{U}}$. $\overline{u}(z)$ and $\overline{v}(z)$ were calculated from current velocity measured at z = 13.5 cm. $\overline{U}(z)$ was determined using measured current speed at z = 13.5 cm in eqn 5.1 with $z_0 = k_s/30$, where k_s is the total hydraulic roughness (Nielsen, 1992):

$$k_s = \frac{8\eta_r^2}{\lambda_r} + 5\theta' d_s \qquad \text{(Eqn 5.31)}$$

and η_r and λ_r are the height and length of wave-orbital ripples (eqns 5.21 and 5.22). Concentration profiles were determined from ABS data as previously described. Similarly, $\vec{Q}_{silt,wc}$ was calculated using eqns 5.29 and 5.30, but replacing $\overline{C}_{silt}$ for $\overline{C}_{sand}$, and assuming homogenous silt concentration profiles (Section 5.5.1).

$\vec{Q}_{sand,ww}$ is controlled by the phase between the concentration and velocity fields and by asymmetry in the velocity distribution under each wave (refer Section 4.3.2). $\vec{Q}_{sand,ww}$ was determined for each burst as:

$$Q_{sand,ww} = \left[\left(\int_{z_{base}}^{z_{ABS}} \frac{1}{B} \int_0^B C_{sand}(z,t) u(z,t) \, dt \, dz \right)^2 + \left(\int_{z_{base}}^{z_{ABS}} \frac{1}{B} \int_0^B C_{sand}(z,t) v(z,t) \, dt \, dz \right)^2 \right]^{1/2} \qquad \text{(Eqn 5.32)}$$

and

$$\phi_{sand,ww} = \tan^{-1} \left(\frac{\int_{z_{base}}^{z_{ABS}} \frac{1}{B} \int_0^B C_{sand}(z,t) \, u(z,t) \, dt \, dz}{\int_{z_{base}}^{z_{ABS}} \frac{1}{B} \int_0^B C_{sand}(z,t) \, v(z,t) \, dt \, dz} \right) \qquad \text{(Eqn 5.33)}$$

where $C_{sand}(z,t)$ is the instantaneous suspended sand concentration at elevation z, and $u(z,t)$ and $v(z,t)$ are the easterly and northerly components of the instantaneous wave-orbital velocity (eqn 2.13) at elevation z. Following Osborne and Greenwood (1992), time-integrals in eqns 5.32 and 5.33 were evaluated from the co-spectrum of $C_{sand}(z,t)$ and $u(z,t)$ or $v(z,t)$ as:

$$\frac{1}{B} \int_0^B C_{sand}(z,t) \, u(z,t) \, dt = \int_{f_H}^{f_L} \chi_{C_{sand}(z,t)u(z,t)}(f) \, df$$

$$\frac{1}{B} \int_0^B C_{sand}(z,t) \, v(z,t) \, dt = \int_{f_H}^{f_L} \chi_{C_{sand}(z,t)v(z,t)}(f) \, df \qquad \text{(Eqn 5.34)}$$

where $\chi(f)$ is the co-spectrum, f is frequency, and the integration limits f_L and f_H for wind waves are 1/30 s^{-1} and 1/1 s^{-1} respectively (Kinsman, 1984). Eqn 5.34 was evaluated using resampled velocity data (Δt = 0.2 s) for $u(z,t)$ and $v(z,t)$ with $C_{sand}(z,t)$. Resampling was performed using a linear fit between measured velocity data points (Δt = 0.25 s).

The same approach was taken for calculating silt flux advected by waves, but replacing C_{silt} for C_{sand} in eqns 5.32–5.34, and assuming homogenous silt concentration profiles (Section 5.5.1).

For $z \geq z_{ABS}$ sand flux is taken to be zero, which is reasonable since sand suspension is confined to the near-bed region (refer Section 5.5.1). Measurements of sand concentrations when $\overline{h} < z_{ABS}$ are not available. Hence, the remainder of the analysis concerns flux only in water depths greater than ~ 50 cm. Green *et al.* (1997) and Dolphin and Green (1997) have reported some measurements in the "turbid fringe", for which water depth was less than 50 cm, but these are not used here as it was not possible to distinguish the sand and silt components in their concentration measurements.

Bedload Flux

Bedload is difficult to measure where suspended load also occurs, particularly for fine sands (e.g., c. 150 μm), which are entrained virtually directly into suspension (Collins *et al.*, 1981; Dyer, 1986). Thus, at Wiroa, the bedload is anticipated to be a minor component of the total sand load. The energetics bedload model Bailard and Inman (1981) and Bailard (1981), was used to reveal patterns in bedload. As bedload was not measured, the model is uncalibrated and direct comparisons between bedload magnitude and other flux components are not made.

The bedload model assumes an instantaneous response to change in current velocity. Green and MacDonald (2001) tested the Bailard model for phase lag between bedload and current velocity in the range of 10–20° (e.g., Jonsson and Carlsen, 1976; Sleath, 1978) and found that it had little effect on estimates of transport rate and direction. They also noted that the model performed well when compared to sediment tracer

experiments (Hicks and Green, 2001). Following Green and MacDonald (2001), instantaneous response was assumed and the burst-averaged bedload flux carried by combined waves and currents $\vec{Q}_{\text{sand,bed,w\&c}}$ was determined as:

$$Q_{\text{sand,bed,w\&c}} = \left\{ \left[\left(\frac{\rho_s C_d \varepsilon_b}{g \tan\varphi} \right) \frac{1}{B} \int_0^B U^2(z,t)\, u(z,t)\, \mathrm{d}t \right]^2 + \left[\left(\frac{\rho_s C_d \varepsilon_b}{g \tan\varphi} \right) \frac{1}{B} \int_0^B U^2(z,t)\, v(z,t)\, \mathrm{d}t \right]^2 \right\}^{1/2} \quad \text{(Eqn 5.35)}$$

and

$$\phi_{\text{sand,bed,w\&c}} = \tan^{-1} \left(\frac{\frac{1}{B} \int_0^B U^2(z,t)\, u(z,t)\, \mathrm{d}t}{\frac{1}{B} \int_0^B U^2(z,t)\, v(z,t)\, \mathrm{d}t} \right) \quad \text{(Eqn 5.36)}$$

where C_d is the drag coefficient relevant for elevation z, ε_b is the bedload efficiency (taken as 0.21; see Bailard (1981)), $\tan\varphi$ is the angle of repose (0.61), and $U(z,t)$ is the total current speed due to combined waves and currents. Eqns 5.35 and 5.36 were evaluated using current measured at z = 13.5 cm for $U(z,t)$, $v(z,t)$ and $v(z,t)$ and $C_d = 0.0025$ (Soulsby, 1997). C_d was taken as a constant because bed roughness was not measured.

5.6.3 Results – Sand

Figure 5.17 summarises the sand flux, $\vec{Q}_{\text{sand,total}}$ and its components $\vec{Q}_{\text{sand,wc}}$ and $\vec{Q}_{\text{sand,ww}}$, at the two Alice sites on the lower and middle flat. $\vec{Q}_{\text{sand,bed,w\&c}}$ is deliberately separated and has no scale, as explained previously.

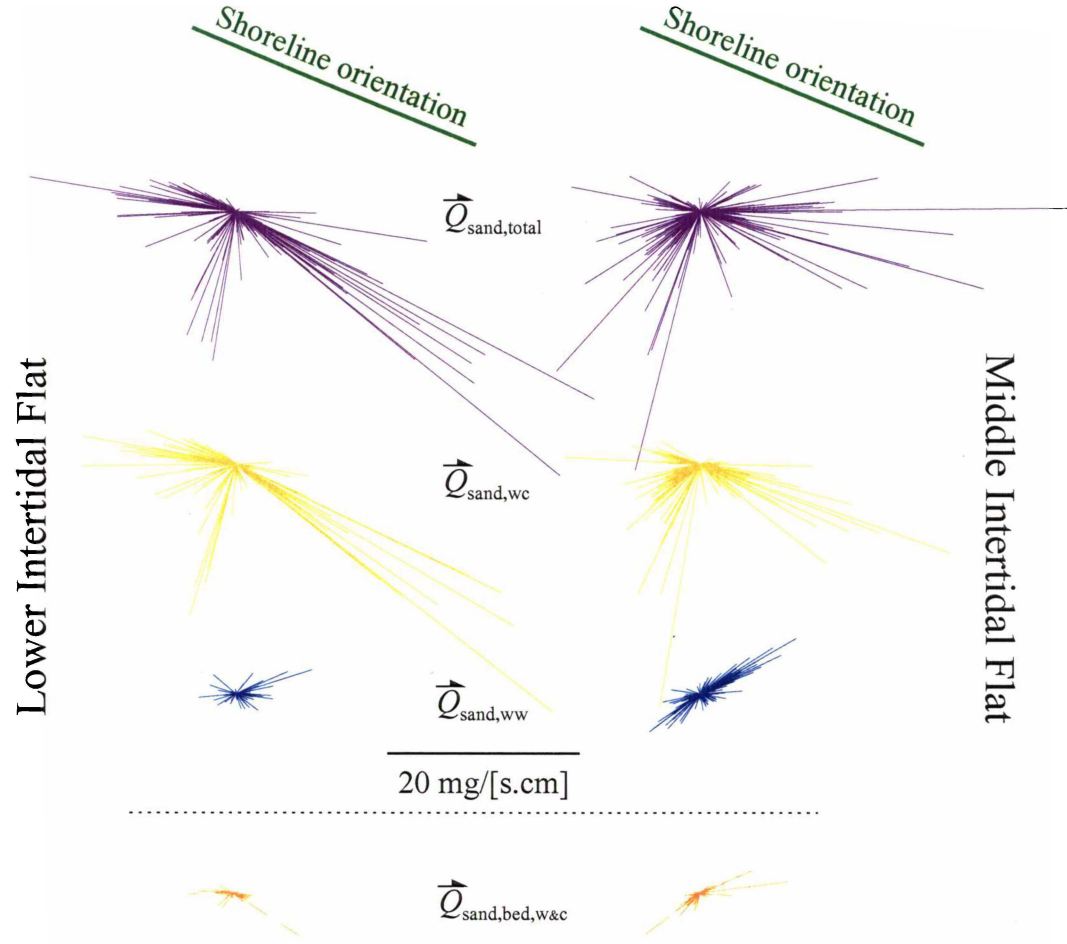

Figure 5.17: Sand transport vectors and components from Alice deployments on the middle and lower Wiroa flat.

5.6.4 Results – Silt

Figure 5.18 summarises silt flux at the two Alice sites on the lower and middle flat. $\bar{Q}_{silt,total}$ is shown with its components $\bar{Q}_{silt,wc}$ and $\bar{Q}_{silt,ww}$; the dashed line indicates a change in scale (see caption).

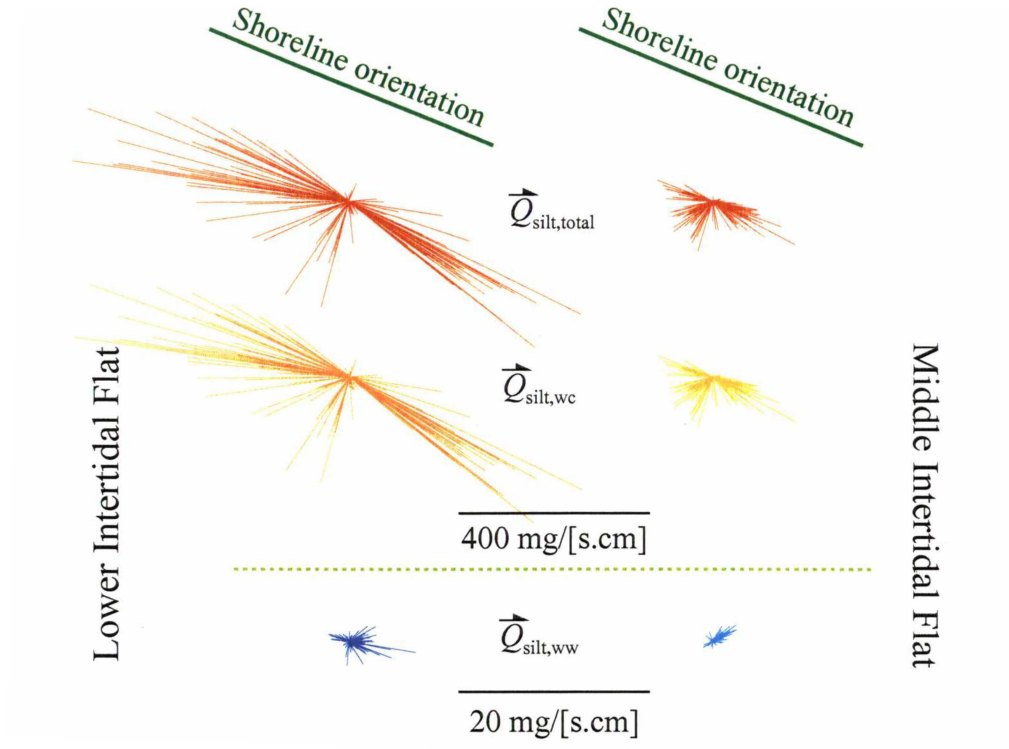

Figure 5.18: Silt transport vectors. $\bar{Q}_{silt,total}$ *is the vector sum of* $\bar{Q}_{silt,wc}$ *and* $\bar{Q}_{silt,ww}$*. Note* $\bar{Q}_{silt,total}$ *and* $\bar{Q}_{silt,wc}$ *have been scaled down by a factor of 20 to fit on the page (compare scale bars).*

5.6.5 Discussion – Sand

A prerequisite for sand transport on the flat is wave action, however, transport of sands *per se* is determined by the interaction of the tidal currents with the wave-induced concentration field, which are independent of one another and which both vary with location across the flat and with time through the tidal cycle.

At any given stage of the tide, tidal currents decrease with elevation (distance) up the flat due to bottom friction (Dyer, 1989). Furthermore, tidal currents weaken on the upper flat (above the mid-tide mark) due to decreasing tidal currents at the time of inundation which are associated with slowing tidal flows across the estuary around high tide slack water). At Wiroa, peak spring tidal flows decline from 25 cm/s on the lower flat to 16 cm/s on the upper flat. All else being equal, sand transport would therefore decrease with elevation up the flat.

Tidal inequalities and estuarine bathymetry/geometry control local circulation patterns and therefore tidal-current direction. Consequently, current direction can vary and there

may not be a consistent pattern in net transport. All else being equal, net transport direction would be controlled by local circulation patterns. For example, on the lower Wiroa flat, sand transport is alongshore for the first part of the ebb tide and offshore for the second part, whereas on the middle flat, ebb transport is primarily offshore (Figure 5.17 and Figure 5.20).

Wave-induced suspended-sand concentrations increase with elevation up the flat due to increasing bed-orbital motion, which arises from interactions amongst fetch, H, T, $\bar{h}$, χ and ω, as discussed in Chapter 4. All else being equal, sand transport would increase with elevation up the flat.

As inundation duration decreases with elevation up the flat, so the time interval available for sediment transport shortens. At Wiroa, the inundation duration decreases from c. 11–12 hours on the lower flat to 0–4 hours on the upper flat. All else being equal, inundation duration would reduce net transport at higher elevations. For example, events C and I from the lower and middle flat (Figure 5.20 and Figure 5.21) had similar wave conditions and sand flux (c.f. 3.9 g/cm per hour versus 3.8 g/cm per hour), but due to longer inundation, the net transport was significantly larger on the lower flat (c.f. 180 g/cm versus 112 g/cm).

As the tidal current and concentration fields are independent of each other, different spatial/temporal combinations give rise to a range of transport patterns. On the mid/lower Wiroa flat, high concentrations and strong tidal currents typically combine in the early and late stages of the inundation to give large $Q_{sand,wc}$, but toward high tide, $Q_{sand,wc}$ declines as tidal currents decrease, regardless of concentration (e.g., compare events A and B in Figure 5.20 and events G and H in Figure 5.21). In contrast, at higher elevations up the flat, and/or during neap tides, concentration can initially be small when currents are strong, peak around high tide when currents are weak (e.g., Figure 5.19), which thus yields smaller transport vectors and smaller net sand flux. The duration for which high concentrations combine with strong tidal currents also affects transport patterns and net sand flux. For instance, $Q_{sand,wc}$ is larger in event A than D because sand concentrations are high for longer periods during peak tidal flow. Flood/ebb differences in the concentration field affect the net transport direction, which at times may be counter to the direction favoured by the dominant phase of the tidal current (e.g., event E).

Sand is also transported by wave-orbital motions ($\vec{Q}_{sand,ww}$). $U_{w,bed}$, $\overline{S}$ and $\vec{Q}_{sand,ww}$ all increase with elevation on the flat, due to shallower water depths and exposure to longer fetch. On the lower Wiroa flat, there are no obvious wave-induced transport patterns, but on the middle flat $\vec{Q}_{sand,ww}$ vectors are onshore/offshore and $\vec{Q}_{sand,bed,w\&c}$ vectors switch from an alongshore to cross-shore alignment (Figure 5.17). Increasing $\overline{S}$ on the upper flat suggests that $\vec{Q}_{sand,ww}$ would increase further with elevation on the flat, with the caveat that $\vec{Q}_{sand,ww}$ is also influenced by bedform evolution, which in turn influences the phase between concentration and velocity through the vortex shedding process (e.g., Osborne and Greenwood, 1992). $\vec{Q}_{sand,ww}$ was not measured on the upper flat.

Alongshore gradients in sand transport are controlled by patterns in local circulation, which were not investigated here. Cross-shore gradients in sand transport at Wiroa are due to several factors. Concentration increases in a shoreward direction, while the mean current and inundation time decrease in a shoreward direction. The ebb tidal flow, which is larger on the middle flat, transports sand offshore and deposits it on the lower flat. In contrast, there is some evidence to suggest that net onshore transport under waves increases with elevation on the flat, which would return sand to the upper flat.

The Wiroa data demonstrate that patterns in the mean current, concentration field and wave flux control patterns in sand transport, which will translate into sedimentary and geomorphic change. Sand-transport processes elucidated here may be applicable to other flats with meso-tidal range and tidally modulated fetch. Different patterns are expected when fetch is constant (e.g., deep estuaries) and as tidal range/energy increases or decreases. These factors are addressed in the following chapter.

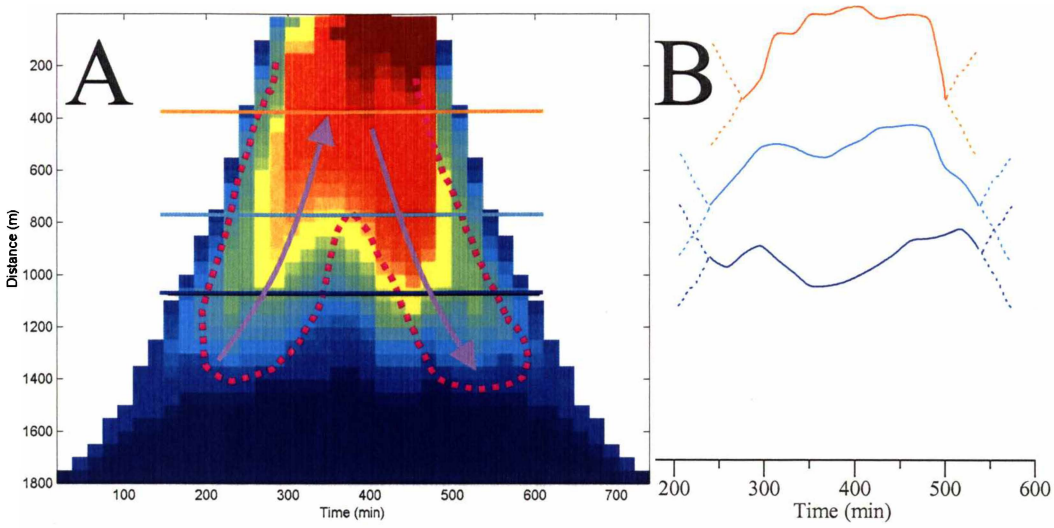

Figure 5.19: **A**: *Schematic of space-time variation in concentration along a shore-normal profile and* **B**: *cross-sections illustrating temporal patterns at three locations. Dashed lines indicate the uncertainty of sand concentrations in the shallow edge of the estuarine waters for which there are no measurements of sand concentration (i.e., when* $\overline{h} < z_{ABS}$*).*

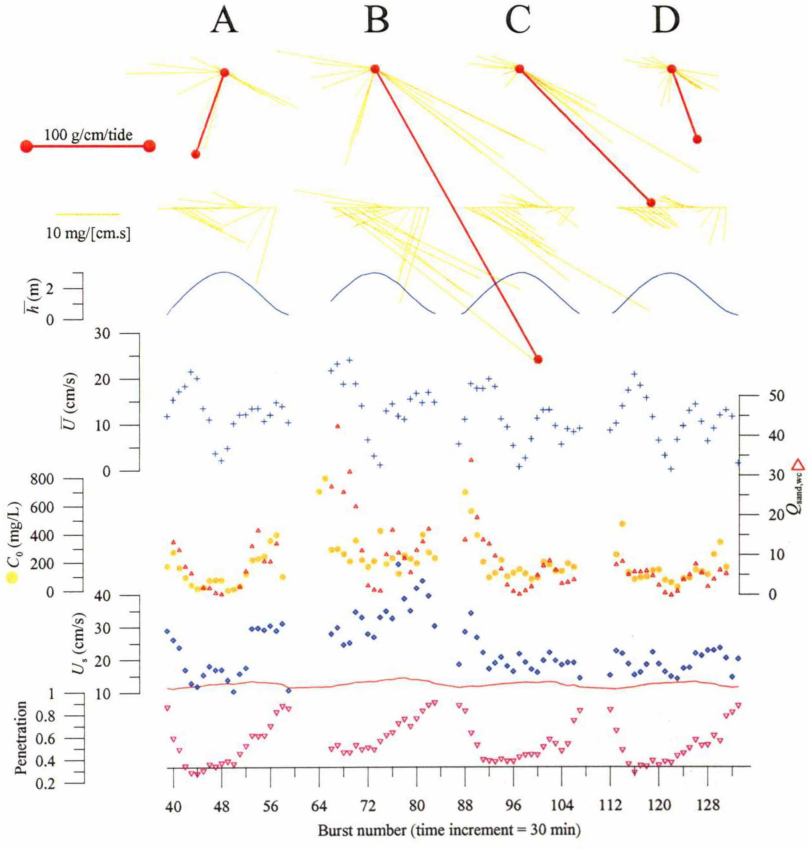

Figure 5.20: Sand transport vectors $\vec{Q}_{sand,wc}$ *for four events on the lower flat (Alice; W1H). The red vector sticks on the polar plots (top panel) represent the event integrated transport* (g/cm/tide). *Accompanying the depth-integrated transport vectors* (mg/[cm.s]) *are the associated temporal variations in some of the processes that contribute to* $\vec{Q}_{sand,wc}$*. The red line on the* U_s *panel is the critical wave-orbital speed (eqn 3.3).*

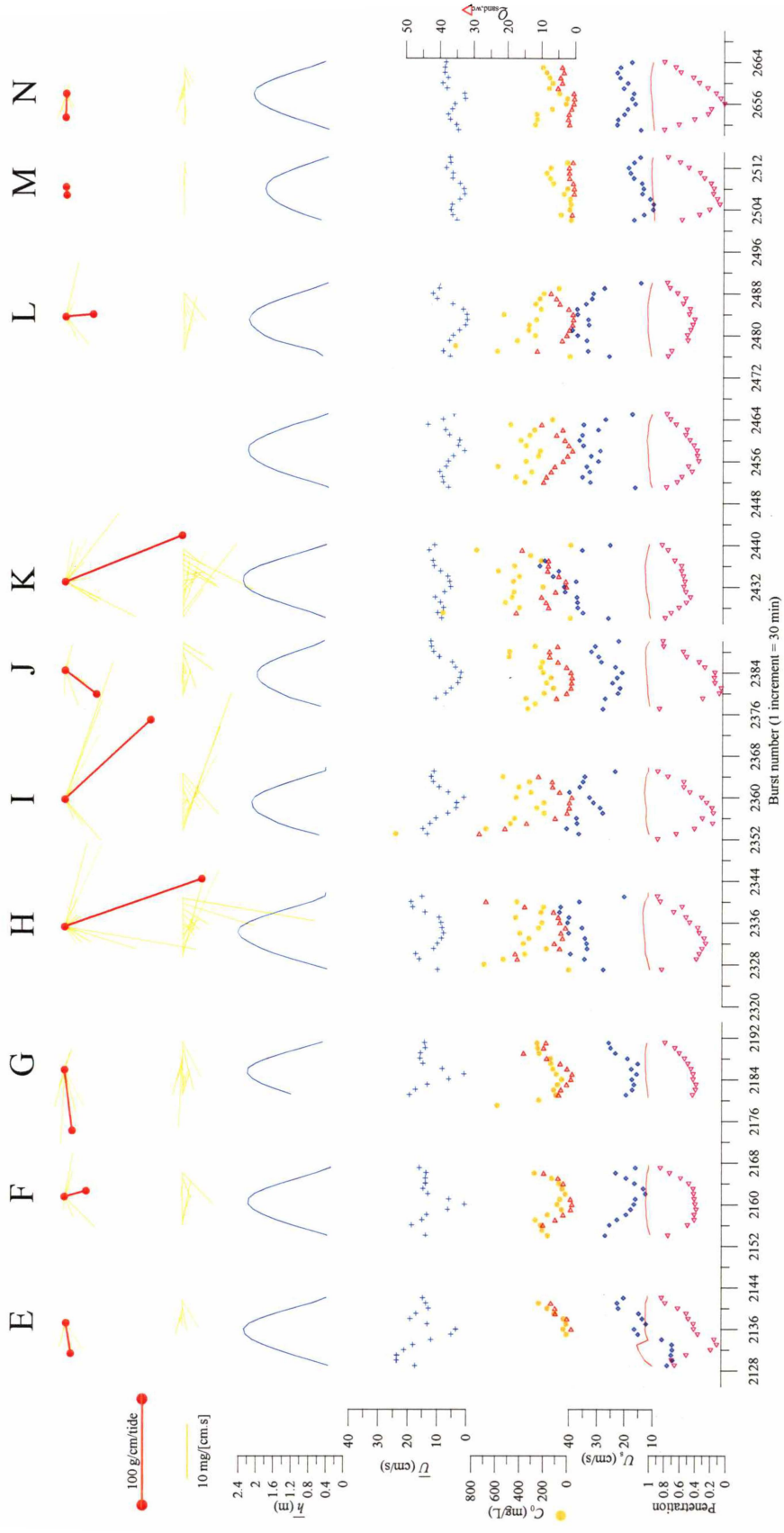

Figure 5.21: Sand transport vectors $\vec{Q}_{\text{sand,wc}}$ *for a selection of events on the middle flat. The red vectors sticks on the polar plots (top panel) represent the event integrated transport* (g/cm/tide). *Accompanying the transport vectors are the associated temporal variations in some of the processes that contribute to* $\vec{Q}_{\text{sand,wc}}$. *The red line on the* U_s *panel is the critical wave-orbital speed (eqn 3.3).*

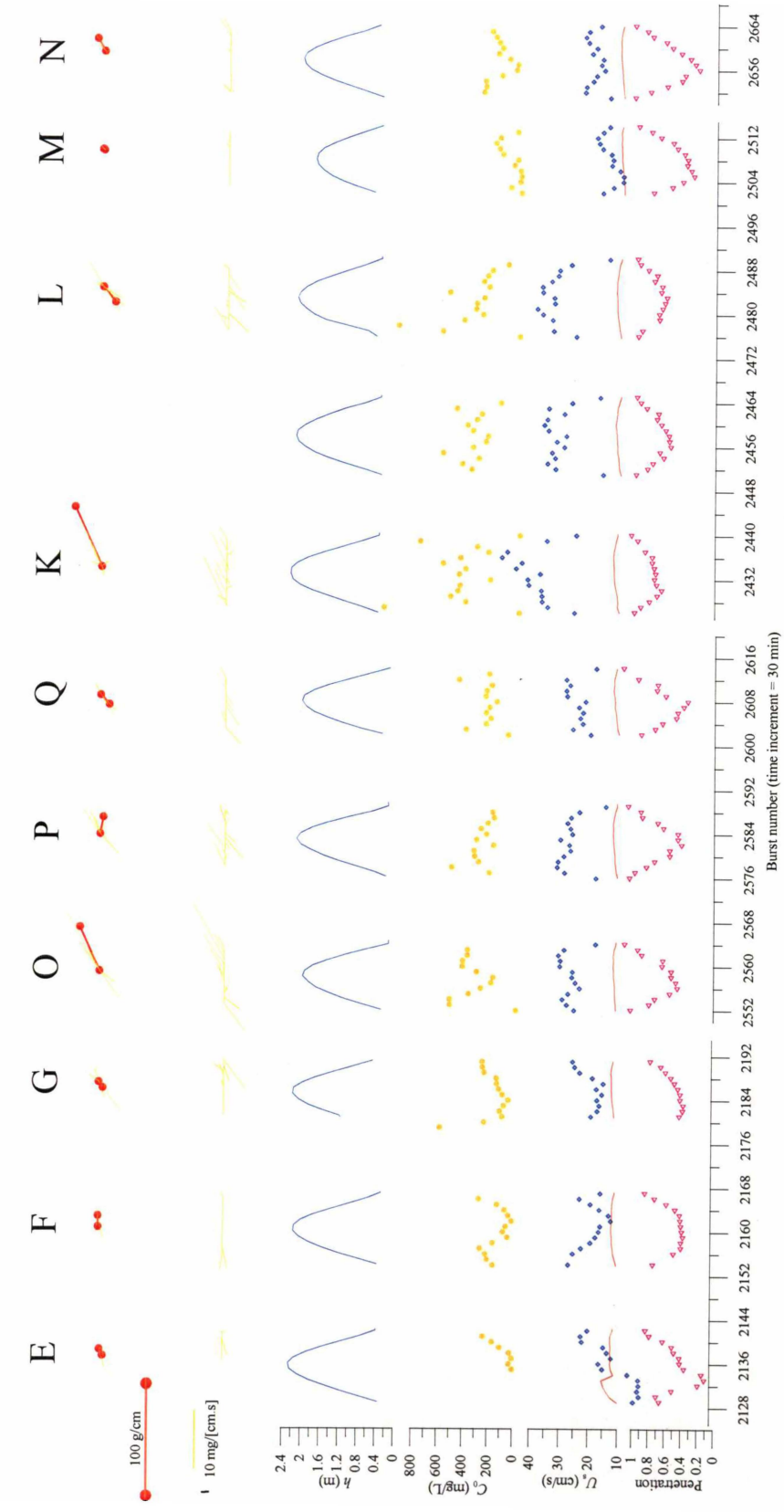

Figure 5.22: Sand transport vectors $\vec{Q}_{\text{sand,ww}}$ *for a selection of events from the middle flat. The red vectors sticks on the polar plots (top panel) represent the event integrated transport* (g/cm/tide). *Accompanying the transport vectors are wave, depth and mean concentration statistics. The red line on the* U_s *panel is the critical wave-orbital speed (eqn 3.3).*

5.6.6 Discussion – Silt

Silt transport is more difficult to understand because it presumably originates from distant locations, as well as being released from the bed locally when waves exceed the critical for sand motion. In the discussion that follows, silt transport across the intertidal flat is considered from an heuristic perspective, drawing upon data collected here and in other Manukau Harbour studies.

There are several possible causes for elevated silt concentrations in Manukau Harbour: catchment runoff; wave erosion of siltstone cliffs and platforms in the northern estuary (Tonkin and Taylor, 1986); and resuspension from the estuarine bed. In many North Island estuaries, resuspension (by tidal currents and/or waves) is the most common cause of elevated turbidity as fluvial inputs are low and bed sediments are predominantly marine derived (Tonkin and Taylor, 1986; Hume and Herdendorf, 1992).

The highest silt concentrations are found in the turbid edge of the estuarine water body during periods of wave activity (e.g., > 1500 mg/L; Dolphin and Green, 1997). Green *et al.* (1997) called this body of water the "turbid fringe" and defined it as the region of high sediment concentrations where Nielsen's (1986) pure-wave model underestimates the reference concentration. Green *et al.* (1997) hypothesised that the underestimates were the result of processes unaccounted for in Nielsen's model, such as turbulence due to breaking waves.

Black *et al.* (1999) were able to model the basic features of the turbid fringe (though not the absolute concentrations) using a pure-wave entrainment model that did not invoke any additional processes. The success of their modelling hinged on limiting sediment availability for different size classes, and a Lagrangian modelling approach which tracked resuspended particles. In their model, the turbid fringe initiates on the channel margins and picks up and accumulates silt particles as it migrates across the flat with the rising and falling tide. Dobie-O OBS data (Figure 5.23) support this result, showing the turbid fringe tends to concentrate with elevation as it moves up the flat (and throughout the tidal cycle), however the data are difficult to interpret because of the presence of suspended sands at the measurement elevation. The advection and accumulation of fine sediments was considered by Black *et al.* to account for the anomaly observed by Green *et al.*, however there are no silt-only concentration measurements in the turbid fringe to

confirm[2]. Future turbid fringe experiments need to employ measurement techniques which separately estimate C_{silt} and C_{sand} in order to gain a better understanding of sediment dynamics and thereby assess the Black *et al.* model.

The Wiroa data may be used to refine the observations that arise from Black *et al.*'s (1999) model. According to the model, as the turbid fringe migrates across the flat, accumulation of silt (increasing concentration) is countered by horizontal diffusion (decreasing concentration) and concentration in the turbid fringe declines. However, the Dobie-O data suggest concentration in the fringe increases up the flat (Figure 5.23), implying that horizontal diffusion is opposed by some mechanism which was not accounted for in the model. That mechanism may be $\bar{Q}_{silt,ww}$, which drives silt onshore (Figure 5.18). If the silt concentration and velocity phase is ~0° then increasing $\overline{S}$ with elevation on the flat would suggest $\overline{S}$ contributes to onshore silt transport and maintenance of the turbid fringe.

Furthermore, during initiation of the turbid fringe, the model probably underestimates $\overline{C}_{silt}$ (refer Figure 2(g), Black *et al.*, 1999) as the silt fraction on the channel margin occupies 10 times the volume allocated in the model. This is because abundance in the model was based on samples taken at higher elevations on the flat where silt abundance is low. Underestimates of $\overline{C}_{silt}$ during initiation of the turbid fringe on the channel margins has implications for the suspended silt mass and deposition (discussed subsequently).

In the Alice data ($\overline{h} > 50$ cm), silt suspensions always decline as $\overline{h}$ increases (and vice-versa), which is characteristic of a migrating turbid fringe (Figure 5.24, Figure 5.25). On the lower flat, high $\overline{C}_{silt}$ in the turbid fringe coincides with peak tidal flow and the resultant alongshore directed silt flux is large (> 400 mg/[cm.s]). However, the passage of this sediment has little consequence for sedimentation on the flat as settling only occurs at high tide slack current, when the settling distance (i.e., depth) is large and by which time concentrations are low as the turbid fringe has passed; and at low tide slack current, when water is confined to channel margins and silt particles probably settle on

[2] OBS measurements alone can not be used to accurately describe C_{silt} in a mixed silt/sand suspension where C_{silt}/C_{sand} is unknown.

channel margins. Thus, Nielsen's (1992) wash load analogy gives an appropriate description of the large silt fluxes that pass over the lower intertidal flat: "wash load is, in a sense, similar to water vapour over a dry or drying surface".

Unlike on the lower flat, where $\bar{Q}_{\text{silt,wc}}$ is high but is of little consequence for sedimentation, on the upper flat wave asymmetry and enhancement of settling processes are hypothesised to aid deposition of the turbid-fringe silts. As the tide begins to retreat, $\bar{h}$ falls and silt particles in the narrow turbid fringe may begin to settle at an enhanced rate due to the combined effects of settling velocity and change in water depth ($w_s' = w_s + d\bar{h}/dt$). On the rising tide the opposite occurs. Onshore-directed $\bar{S}$ may hinder horizontal diffusion and the ebb retreat of suspended silts with the tide such that silts become stranded on upper sections of the flat (e.g., < 100 m from shore; Figure 5.26).

Stranded silts are deposited in veneers up to 2-cm-thick and are ephemeral, being swept away in 1–2 tidal cycles. Consequently, they have little long-term effect on sedimentation, with the exception of those silts deposited in mangroves, which are protected by pneumataphores and canopy vegetation. As the mangrove area has grown, silt accumulation has become a more permanent feature (observations). The root-modified boundary layer provides shelter from waves (e.g., Wallace and Cox, 1997) and the long exposure periods on the upper flat increase evaporative losses from the silt matrix and thereby enhance consolidation processes and cohesive sediment strength (Nichols and Biggs, 1985). Stranding of silts only occurs at the top of the intertidal flat, which implies that strengthening tidal flows on the ebbing tide close the window of opportunity for settlement as the tide falls away from the upper flat. In summary, waves provide an important mechanism for onshore transport of silt in the turbid fringe and can contribute to the potential growth of intertidal flats in sheltered/vegetated regions.

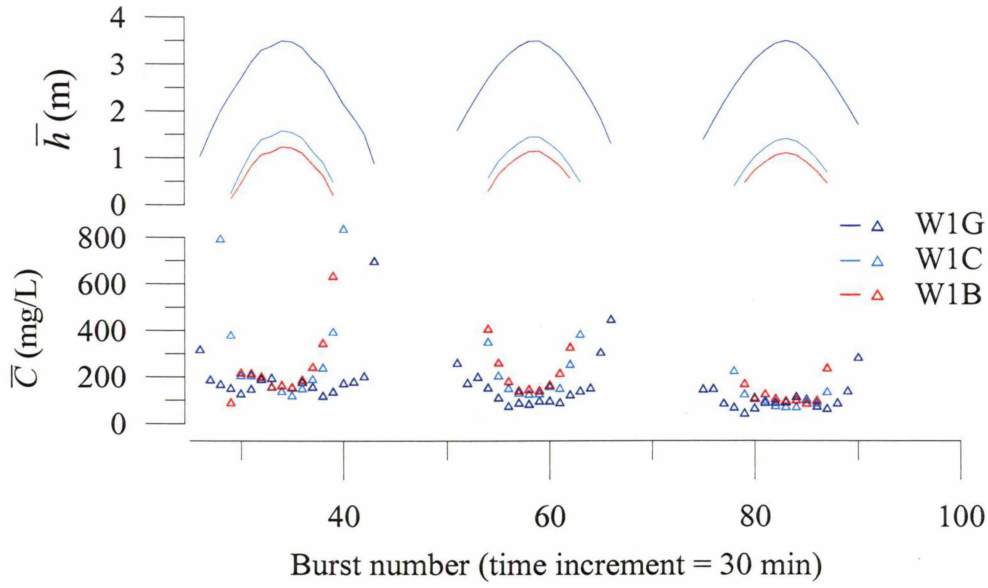

Figure 5.23: Turbid fringe events as measured by OBSs on the Dobie-O's. The progression from dark blue through to red marks increasing elevation on the intertidal flat. Refer to Figure 2.6 for site locations.

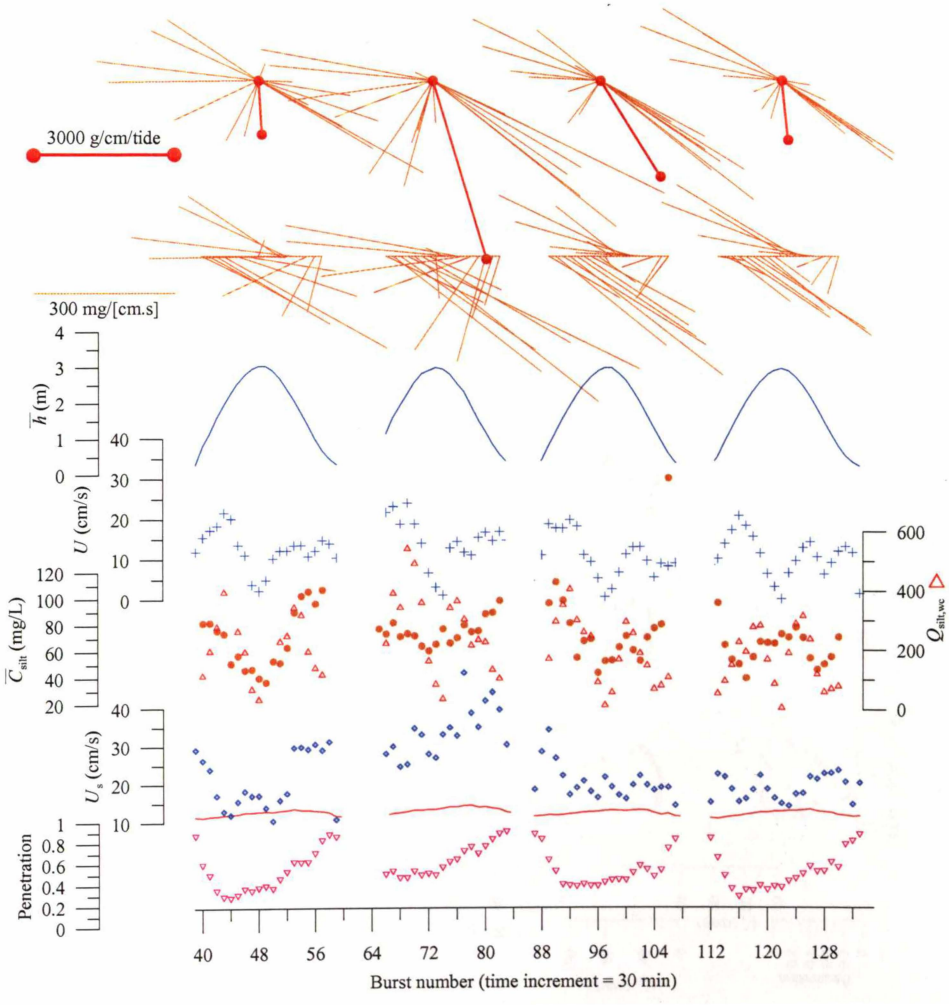

Figure 5.24: Silt transport vectors, $\bar{Q}_{silt,wc}$, for four events from the lower flat. The red vector sticks on the polar plots (top panel) represent the event-integrated transport (g/cm/tide). *Accompanying the transport vectors are wave, depth and mean silt concentration statistics.*

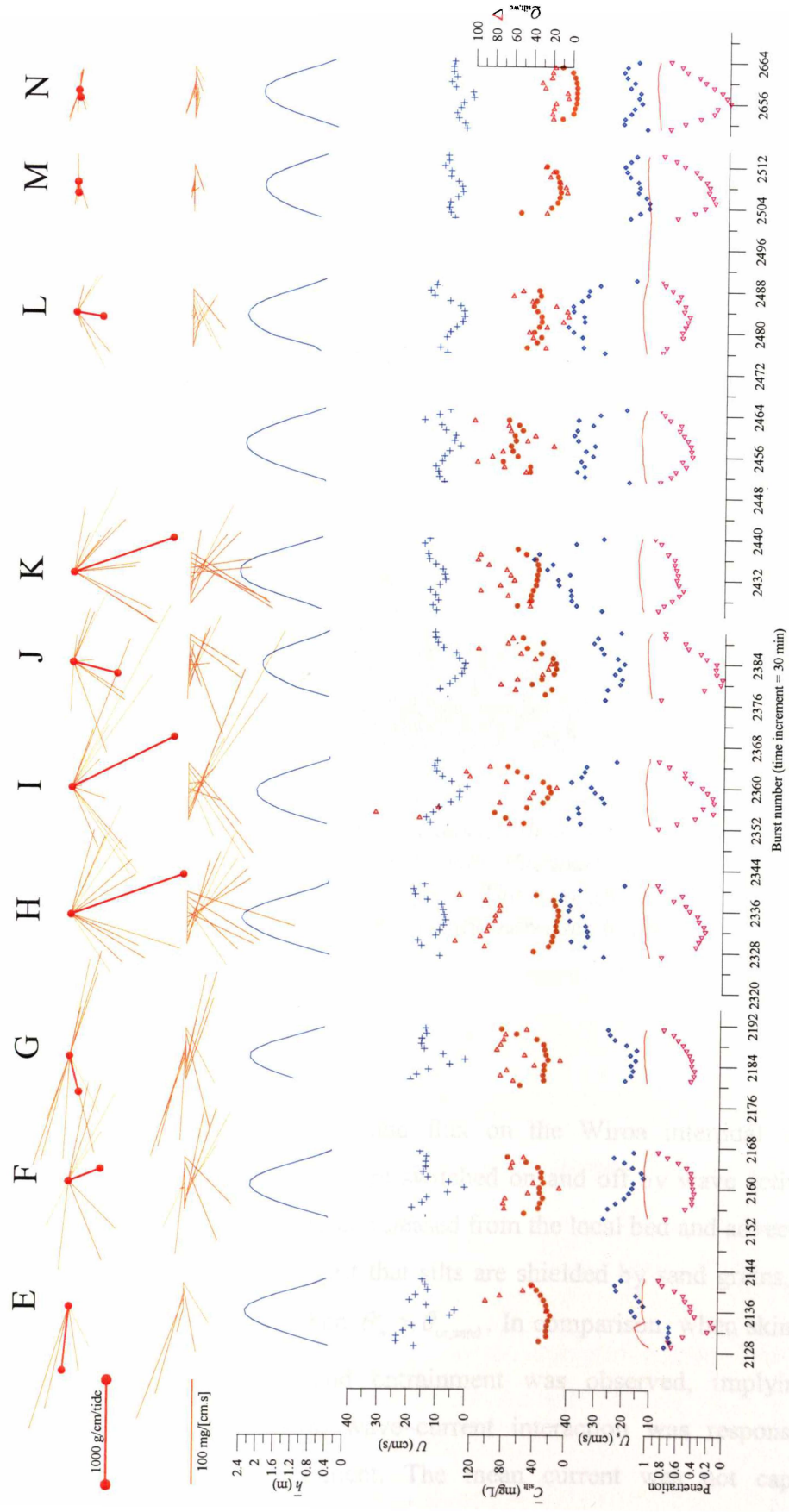

Figure 5.25: Silt transport vectors, $\bar{Q}_{\text{silt,wc}}$, for a selection of events from the middle flat. The red vectors sticks on the polar plots (top panel) represent the event integrated transport (g/cm/tide). *Accompanying the transport vectors are wave, depth and mean silt concentration statistics.*

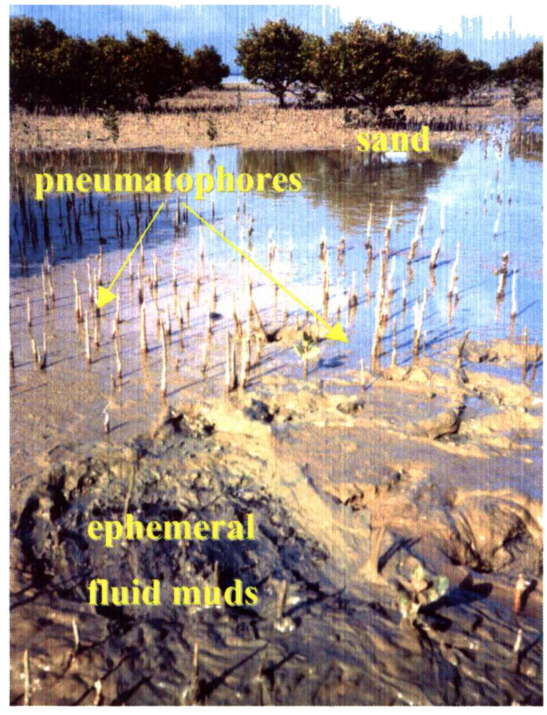

Figure 5.26: Fluid mud layer (1–2 cm) deposited in a depression on the upper intertidal flat during the receding tide of a storm. Blackened (anaerobic) fine-sands are visible where mud has been scraped away (foreground). Pneumatophores, the mangrove's 'breathing' roots, protrude the sediment surface. The seaward edge of the mangrove stand occupies the background – mangrove density increases in the landward direction (to the left in the image).

5.7 CONCLUSIONS

The mechanisms controlling silt and sand flux on the Wiroa intertidal flat were investigated. Sand and silt entrainment are switched on and off by wave activity. Silt suspensions on the flat comprise material released from the local bed and advected from distant source regions. The data suggest that silts are shielded by sand grains, and are only entrained from the local bed when $\theta'_w > \theta_{cr,sand}$. In comparison, when skin friction due to waves exceeds critical, sand entrainment was observed, implying sand suspensions are local. On occasion wave–current interaction was responsible for otherwise unpredicted sand entrainment. The mean current was not capable of mobilising sediment.

Although the silt flux is greatest over the lower flat, there is little silt deposition because settlement only occurs at high water slack current when settling distances are large, and

at low tide slack water, when the tide is just leaving the flat. On the upper flat, onshore-directed wave-orbital asymmetry and $\bar{Q}_{\text{silt,ww}}$ maintain a narrow turbid fringe, counteracting horizontal diffusion and advection during the falling tide. Consequently, on the falling tide, silts become stranded on the upper flat, although they are typically swept away within one to two tidal cycles, unless deposited in mangrove stands. $\bar{Q}_{\text{silt,ww}}$ is thus an important mechanism for confinement of the turbid fringe, and for promoting silt deposition on the upper sections of intertidal flats.

The sand reference concentration data show three regimes: when $\theta'_w < 0.1$, steep ripples dominate and $C_0 \propto \theta'^3_w$; as θ'_w increases, ripples become rounded and $C_0 \propto \theta'^1_w$; and eventually the bed is flattened and $C_0 \propto \theta'^3_w$. There were insufficient observations at high θ'_w to identify the flat-bed regime observed by Nielsen (1986). The intermediate conditions may reflect the co-existence of ripples and flat beds, or a transitional state which has not been previously observed.

$\overline{C}_{\text{sand}}$-profiles follow Nielsen's (1984) simple exponential model, which implies vertically invariant sediment diffusivity. Mixing length was reasonably well described by Nielsen's (1990) empirical equation (eqn 5.20). Scatter about eqn 5.20 is most likely to be related to the way parameters are specified and to the reliance on empirical estimates of ripple dimensions. At times, mixing in the region $z > 8$ cm was influenced by surface-penetrating turbulence under whitecaps. Under shoaling induced breakers, surface-generated turbulence may penetrate closer to the bed, however other research (e.g., Donelan, 1978; Ogston and Sternberg, 2002) suggests that only turbulence associated with plunging breakers, which are not expected on intertidal flats, reaches the bed.

Patterns in sand transport on the intertidal flat are complex because the primary transport factors, tidal currents and the wave-induced concentration field, are independent and both vary with location across the flat and with time through each tidal cycle. A variety of transport patterns result. Although the cross-shore component of $\bar{Q}_{\text{sand,wc}}$ was difficult to predict, drainage currents provided a means of offshore sand transport while wave-orbital asymmetry provided a mechanism for onshore sand transport.

Chapter 6: Spatial Variation in Intertidal Flat Sediment Transport and Geomorphology

6.1 INTRODUCTION

Sediment deposition and erosion arise from spatial gradients in sediment transport. Therefore, over the long-term, morphology is shaped by sediment-flux divergence, rather than sediment transport *per se*. The aim in this chapter is to investigate patterns of sediment transport, and to identify links between these patterns and intertidal-flat morphology. This will be done by using numerical models of the Wiroa transect, and also by way of schematic modelling. The numerical models (described in Section 6.2.1) simulate waves, currents and tidal elevations across Manukau Harbour, including the Wiroa flat. The schematic modelling includes simulations for intertidal flats with tidally-modulated fetches as well as constant fetches. Relationships between sediment transport processes and geomorphology, as well as the effects of tidal energy/range, are discussed.

The investigation of sediment flux patterns will address sand only. Spatial patterns in silt flux are not investigated because silt concentration is related to far-field processes, not local bed shear stresses, and therefore can not be modelled at the 'local' intertidal flat scale. For an understanding of silt dynamics an estuary-wide perspective is required. In the absence of such data (field measurements or modelled), the transport of silt is not considered further in this study.

6.2 WIROA TRANSECT

6.2.1 Patterns in Waves, Currents and Geomorphology

The top two panels of Figure 6.1 show features of the Wiroa transect. The transect is divided into five geomorphic zones corresponding to breaks of slope and changing particle size distributions: the *beach*, which is steep and comprises hard-packed sands and imbricated shells; the *upper flat*, which is divided into two sections, (*U1*, which has a gradient of 1:1000 and mangrove stands with muddy beds interspersed with fine-sand open flats, and *U2*, which is open flat with a 1:700 gradient); the *middle flat*, which has the steepest gradient on the flat (1:400) and also comprises fine-sands; the *lower flat*,

which has a lower slope than the middle flat (1:450) and an increasing mud content near its outer margins; and the Papakura tidal *channel*, which is steep sided with a cohesive muddy bed. On the upper flat, shore-parallel low-amplitude multiple bars ($\eta_{bar} \approx 0.2$ m, $\lambda_{bar} \approx 30$ m) are common (Dolphin, 1992; Dolphin *et al.*, 1995), while on some sections of the lower-flat, channel aligned bars ($\eta_{bar} \approx 0.05$ m, $\lambda_{bar} \approx 50$ m) are found (Green *et al.*, 1997). Wave-orbital ripples are ubiquitous, suggesting that wave action mobilises sand at all intertidal-flat locations.

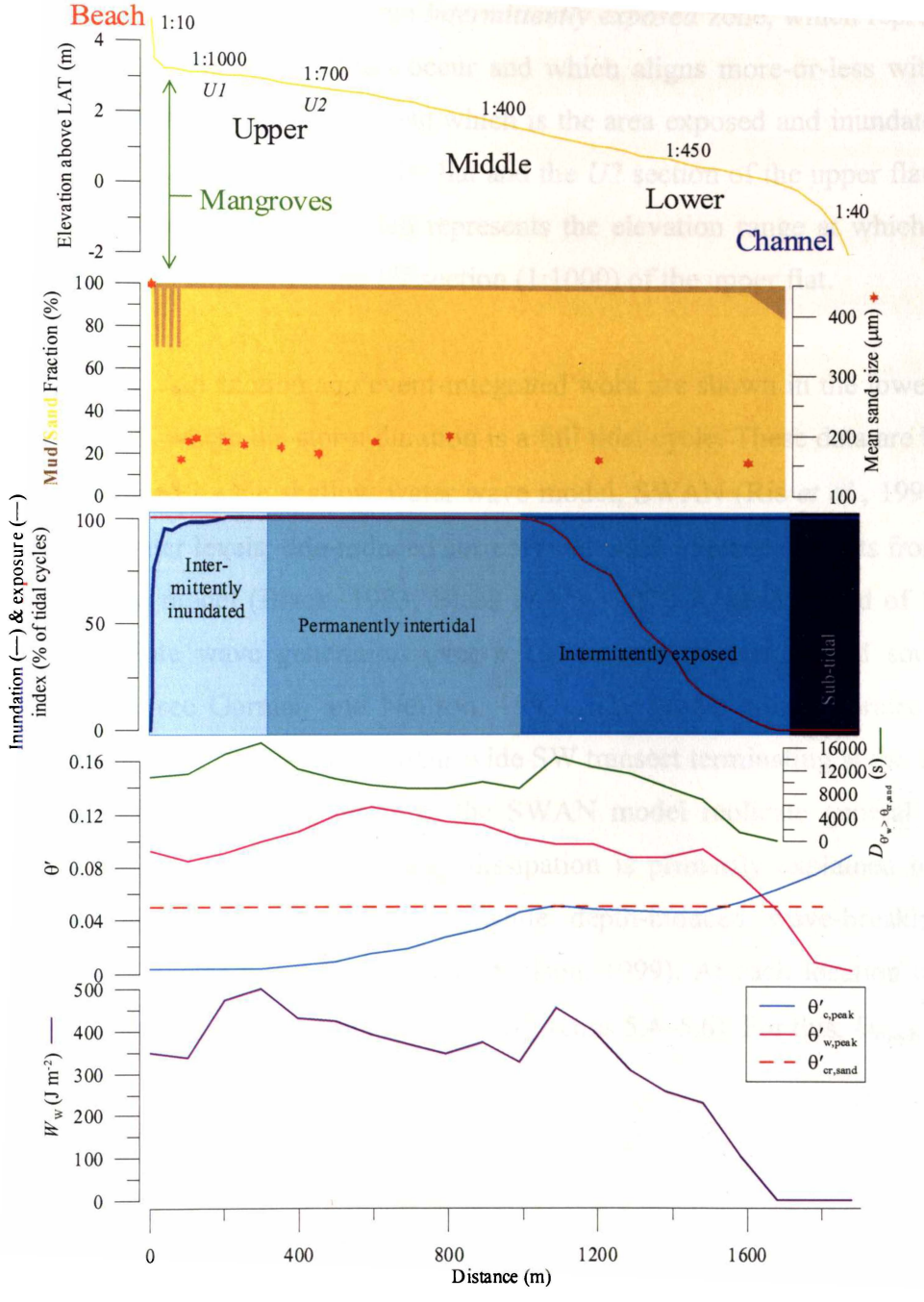

Figure 6.1: Spatial patterns in geomorphology, inundation, peak skin friction, and work. Skin friction and work are based on SWAN model output for a single tidal cycle with steady SW winds of 8 m/s. The inundation/exposure index is based on tidal predictions for a two year period.

Inundation patterns on the Wiroa transect were determined from two years of tidal elevation data predicted from Bell *et al.*'s (1998) finite-element model of Manukau Harbour. The positions of each high and low tide were mapped on the Wiroa transect and expressed as an inundation/exposure index, which is the number of inundations and exposures expressed as percentage of the number of tidal cycles, for each location. Four inundation zones were identified (central panel, Figure 6.1): the permanently inundated *subtidal* zone, which delineates the seaward margin of the flat and is characterised by increasing slope and mud abundance; the *intermittently exposed* zone, which represents the elevation range at which low tides occur and which aligns more-or-less with the lower flat; the *permanently intertidal* zone which is the area exposed and inundated on every tide, and which occupies the middle flat and the *U2* section of the upper flat; and the *intermittently inundated* zone, which represents the elevation range at which high tides occur, and which aligns with the *U1* section (1:1000) of the upper flat.

Patterns in the peak skin friction and event-integrated work are shown in the lower two panels of Figure 6.1, where the storm duration is a full tidal cycle. These data are based on η-spectra predicted by the shallow water wave model, SWAN (Ris *et al.*, 1994), in conjunction with water levels, tide-induced currents and wind-induced currents from the 3DD hydrodynamic model (Black, 1983; Black *et al.*, 1993). A steady wind of 8 m/s was used to simulate wave generation over a 100-m grid of central and southern Manukau Harbour (see Gorman and Neilson, 1999). The model was calibrated with several wave gauges positioned on a harbour-wide SW transect terminating at the Wiroa flat (Neilson, 1998). The source terms in the SWAN model replicate general wave conditions on the Wiroa flat: wave energy dissipation is primarily explained by the bottom friction and white-capping terms, while depth-induced wave-breaking is uncommon (refer Chapter 4 and Gorman and Neilson, 1999). At each location on the Wiroa transect, η-spectra were used to calculate θ'_w (eqns 5.4–5.6). For this, $U_{rms,bed}$:

$$U_{rms,bed} = \frac{\pi H_{rms}}{\overline{T}\sinh(k\overline{h})},$$

was used for U_w, and eqns 2.20 and 2.24 were used for H_{rms} and $\overline{T}$, respectively. Likewise, $\overline{U}$ at each location was used to determine θ'_c (eqns 5.1–5.3). The peak skin

friction terms, $\theta'_{c,peak}$ and $\theta'_{w,peak}$, are the maxima for each point on the transect during the inundation.

The map of $\theta'_{c,peak}$ (fourth panel, Figure 6.1) demarcates zones of competency in $\overline{U}$ (i.e., where $\overline{U}$ exceeds the entrainment speed). $\theta'_{c,peak}$ declines with distance up the flat and is subcritical at all locations, except on the channel margins, which is consistent with field data. Thus, currents do not resuspend bottom sediments. The decline in $\overline{U}$ with elevation above the middle flat reduces $\theta'_{c,peak}$ and thereby acts to decrease $Q_{sand,wc}$, as noted previously.

In contrast, $\theta'_{w,peak} > \theta_{cr,sand}$ across the entire flat (fourth panel, Figure 1.1), implying that sand moves at all locations for some stage(s) of the inundation. Spatial variation of θ'_w is determined by variation in H, $\overline{T}$ and $\overline{h}$. The modelling shows that there are in fact two peaks in $\theta'_{w,peak}$, one at ~1500 m and the other at ~ 600 m. The former peak (at 1500 m), occurs near low tide, when small waves in shallow water produce a maximum in bed-orbital speed. The latter peak (at 600 m), occurs nearer to high tide, where larger H and $\overline{T}$ (under the longer fetch) combine to produce a maximum in bed-orbital speed. $\theta'_{w,peak}$ decreases shoreward of 600 m ($\overline{h}_{local} = 0.4 - 0.8$ m) because absolute levels of wave energy decrease due to dissipation (both bed friction and whitecapping).

Integrating skin friction ($\theta' > \theta_{cr,sand}$) over the inundation period yields work done. For waves, the work per unit area, W_w, was determined as

$$W_w = \frac{1}{2}\int_0^T \rho_f f_w |U_w| U_w^2 \, dt \qquad \text{for } \theta'_w > \theta_{cr,sand} \qquad \text{(Eqn 6.1)}$$

where the integration period, T, is a single tidal cycle and eqn 6.1 has units of kg.(m^2/s^2).m^{-2} or J.m^{-2}. W_w is plotted across the transect in the bottom panel of Figure 6.1. As $\theta'_{c,peak} < \theta_{cr,sand}$, W_c was not calculated.

Spatial variability in W_w is controlled by $D_{\theta'_w > \theta_{cr,sand}}$, which is the duration for which $\theta'_w > \theta_{cr,sand}$ (Figure 6.1). $D_{\theta'_w > \theta_{cr,sand}}$, in turn, is a function of the inundation time (which

decreases with elevation) and patterns in bed-orbital speed across the transect. The modelling shows two peaks in $D_{\theta'_w > \theta_{cr,sand}}$, one on the upper flat at 300 m, and one on the middle flat at 1100 m (fourth panel, Figure 1.1). These two peaks in $D_{\theta'_w > \theta_{cr,sand}}$ also translate into two peaks in W_w at the same locations (lowest panel, Figure 1.1), indicating that $D_{\theta'_w > \theta_{cr,sand}}$ is the primary control on W_w at Wiroa, rather than inundation. On the lower flat, inundation time is high, but χ^* is small in the relatively deeper water, which means that θ'_w exceeds $\theta_{cr,sand}$ only early and late in the tide. Nevertheless, there is a location on the mid/lower flat where bed-orbital speeds are high enough for long enough to produce a peak in W_w. Between the two peaks in W_w, the tide translates the zone of "competent" bed-orbital speeds too quickly to achieve much work.

6.2.2 Relationship between morphology and patterns in waves and currents

Spatial patterns in peak parameters differ from spatial patterns in time-integrated parameters. $\theta'_{c,peak}$ and $\theta'_{w,peak}$ show the regions in which currents and waves are capable of mobilising sand, for at least part of the inundation. However, peak parameters can be misleading, as they fail to take into account variability in skin friction during each inundation (e.g., Amos, 1995). In contrast, time-integrated terms represent cumulative effects, and so the inundation/exposure index and W_w can be expected to show some relationships with geomorphic features, which is the case for Wiroa, as follows.

The lowest bed slopes, which are found on the upper flat (1:700 – 1:1000), correspond to *intermittent inundation* and maximum W_w. The former represents the range of high-tide shoreline positions and is a potential deposition zone for sands transported toward the tidal edge by, for example, $\vec{Q}_{sand,ww}$, and stranded there by the receding ebb tide. The low-gradient upper flat also corresponds to the zone of maximum W_w. This suggests that intertidal flats are an ultra-dissipative energy regime (Masselink and Short, 1993) since where energy increases, sandy coastal deposits tend to decrease in slope in order to more effectively dissipate incoming wave energy. The break of slope leading to the steeper middle flat corresponds to lower W_w, which is the result of lower wave energy due to shorter fetch (the Hangore transition; see Chapter 4) and lower $D_{\theta'_w > \theta_{cr,sand}}$, which in turn is due to the higher tidal translation rate. As for the latter, the tide moves fastest over the middle flat, and thus quickly translates the zone of large θ'_w (when χ^* is large).

As $d\bar{h}/dt$ is large, changes in $\bar{h}$ act to reduce χ^*, θ'_w and $D_{\theta'_w>\theta_{cr,sand}}$. On the lower flat, the fetch is similar, but $\bar{h}$ stays shallower for longer, due to the slower tidal translation rate. As a result, there is a secondary peak in W_w.

In making comparisons between sediment transport processes and the geomorphology, it should be noted that the morphodynamic response is limited by sediment availability, which is not taken into account. Also, the form of the intertidal flat is the cumulative effect of waves and tides operating for time scales much longer than the single storm inundation used to calculate peak and time-integrated parameters. For a more accurate picture of the morphodynamics, longer time-scales are required.

6.3 SCHEMATIC MODELLING

6.3.1 Introduction

Tidal modulation of fetch is an important control on wave evolution and sediment transport over intertidal flats. When the fetch is tidally modulated, H and T grow as fetch increases (for a given wind). The effect of increasing wavelength on bed-orbital motion is tempered by increasing depth over flats. That is, the tide acts to simultaneously increase χ by way of increasing fetch and T, and to decrease it by way of increasing local water depth. This 'phase-locking' of fetch, depth and wave characteristics minimises changes in kh and, in the case of Wiroa, maintains *intermediate* depth conditions and inhibits the onset of shoaling and breaking associated with shallow kh. Consequently, wave-induced entrainment and transport is driven by wave orbital motions under non-breaking waves of intermediate kh.

In contrast, when fetch is constant (e.g., Okura and Newtonards; Green and MacDonald, 2001; Malvarez *et al.*, 2001) for a given wind, larger and longer waves, compared to a tidally-modulated fetch, may result as event duration and wave growth are not hindered by periodic emergence and submergence of banks. Under constant fetches, χ and $U_{s,bed}$ are determined by the timing, magnitude and duration of the storm event relative to $\bar{h}$ at any given tidal stage (or location). At high-tide, bottom friction and whitecapping are the primary energy dissipating terms, which is also the case for tidally-modulated fetches. However, as the tide falls, wave characteristics at the edge of the flat are effectively unchanged since fetch is constant (± width of intertidal flat). Consequently,

kh over the flat declines and *shallow* water conditions may be encountered in which waves may shoal, deform, and break (e.g., Green and MacDonald, 2001).

The tidally-modulated/constant-fetch dichotomy is used as one part of the conceptual basis of the schematic modelling. The other part concerns the tidal currents, for which five scenarios were considered: flood and ebb dominant, symmetrical, flood pulse and ebb drainage. Each scenario is described further in the following section.

The two fetch cases and the five current cases are investigated in various combinations in the schematic modelling.

6.3.2 Model description

The model is formulated for a single transect across an intertidal flat. Cross-shore sand flux (specifically, the advection of the mean suspended-sand field by the on-offshore component of the tidal current) and cross-shore gradient in cross-shore sand-flux over a single tidal cycle are calculated.

Cross-shore sand flux as a function of cross-shore location on the sand flat, x, and time within the tidal cycle, t, is given by:

$$q_{\text{sand,wc}}(x,t) = <\overline{\upsilon}_{x,t}><\overline{C}_{x,t}> \qquad \text{(Eqn 6.2)}$$

where $\overline{\upsilon}$ is the on-offshore component of the time-averaged tidal current and the angle brackets denote depth-averaged terms. For both $q_{\text{sand,wc}}$ and $\overline{\upsilon}$ positive is onshore and negative is offshore. Note that $<\overline{\upsilon}_{x,t}>$ and $<\overline{C}_{x,t}>$, the velocity and concentration fields, respectively, are specified independently (described later).

$q_{\text{sand,wc}}(x,t)$ is time-integrated across the tidal cycle to give the net sand flux at each location on the transect:

$$q'_{\text{sand,wc}}(x) = \int_0^T q_{\text{sand,wc}}(x,t)\,dt = \int_0^T <\overline{\upsilon}_{x,t}><\overline{C}_{x,t}>\,dt \qquad \text{(Eqn 6.3)}$$

The cross-shore gradient in q' is then given by

$$q''_{\text{sand,wc}}(x_n) = \frac{q'_{\text{sand,wc}}(x_n) - q'_{\text{sand,wc}}(x_{n+1})}{x_n - x_{n+1}} \qquad \text{(Eqn 6.4)}$$

Specification of the concentration fields

The concentration fields used in the schematic modelling are shown in Figure 6.2. Two event magnitudes, 'mild' and 'large', are simulated. The diagrams are time stacks of concentration along a shore-normal transect. White areas are exposed sections of the flat. The Wiroa transect was used for the bathymetry.

For the tidally-modulated fetches, the concentration field is based on patterns at Wiroa in which large waves reach the flat at or just after high tide, and, at the same time, orbital motions penetrate more deeply through the water column, due to longer periods. The concentration field is slightly asymmetric in time.

For constant fetches, the wave field is assumed to be in equilibrium with a steady wind and thus waves approaching the flat do not evolve over the tidal cycle and the concentration field is symmetrical in time. During the constant-fetch mild event, waves shoal and dissipate much of their energy on the channel margin at low-tide; here concentrations are high. As the water level rises, χ^* declines and waves dissipate their energy slowly as they move over the flats; in this case, concentrations are lower and span a wider area. During the major event, there is a relatively narrow band of high concentrations, which reflects a similarly narrow band in which bed-orbital speeds are high. (Note, units are not shown on graph axes because the data is synthetic and the intention of the model is to identify patterns, not absolute magnitudes).

Specification of the current fields

The current fields used in the schematic modelling are shown in Figure 6.3. The diagrams are time stacks of current along a shore-normal transect. Again, white areas are exposed sections of the flat and the Wiroa transect was used for the bathymetry.

Five different scenarios were considered for tidal currents: flood dominance and ebb dominance, in which the currents were stronger but occurred for a shorter duration in

the direction of dominance; a symmetrical tide, in which the current speed and duration were equal during the flood and the ebb; a unidirectional current, that represents drainage from the flat during the ebb tide; and a unidirectional current that represents an onshore flow during the flood phase only. An arbitrary decay factor was applied to the symmetrical, flood dominant and ebb dominant scenarios to simulate diminishing tidal currents with distance across the flat, as noted in the literature (e.g., Amos, 1995) and observed in the data.

6.3.3 Results

$q_{\text{sand,wc}}(x,t)$ was calculated at each time over the tidal cycle and each location on the transect using eqn 6.2 together with the concentration and current fields shown in Figures 6.2 and 6.3, respectively.

The results for all scenarios are plotted in Figure 6.5 (full-size plots can be found in Appendix IX). For each scenario (i.e., combination of concentration and current fields), results are shown by way of four graphs (refer to Figure 6.4 throughout the following description of how to read the results). Firstly, in the top two graphs $q_{\text{sand,wc}}(x,t)$ and $q''_{\text{sand,wc}}(x,t)$ are depicted as a function of time through the tidal cycle (vertical axis) and location on the transect (horizontal axis). Secondly, in the lower two graphs, $q'_{\text{sand,wc}}(x)$ and $q''_{\text{sand,wc}}(x)$ are depicted as a function of location on the transect (horizontal axis). In the lower graph, regions of erosion (negative $q''_{\text{sand,wc}}(x)$) and accretion (positive $q''_{\text{sand,wc}}(x)$) are identified (pink and yellow).

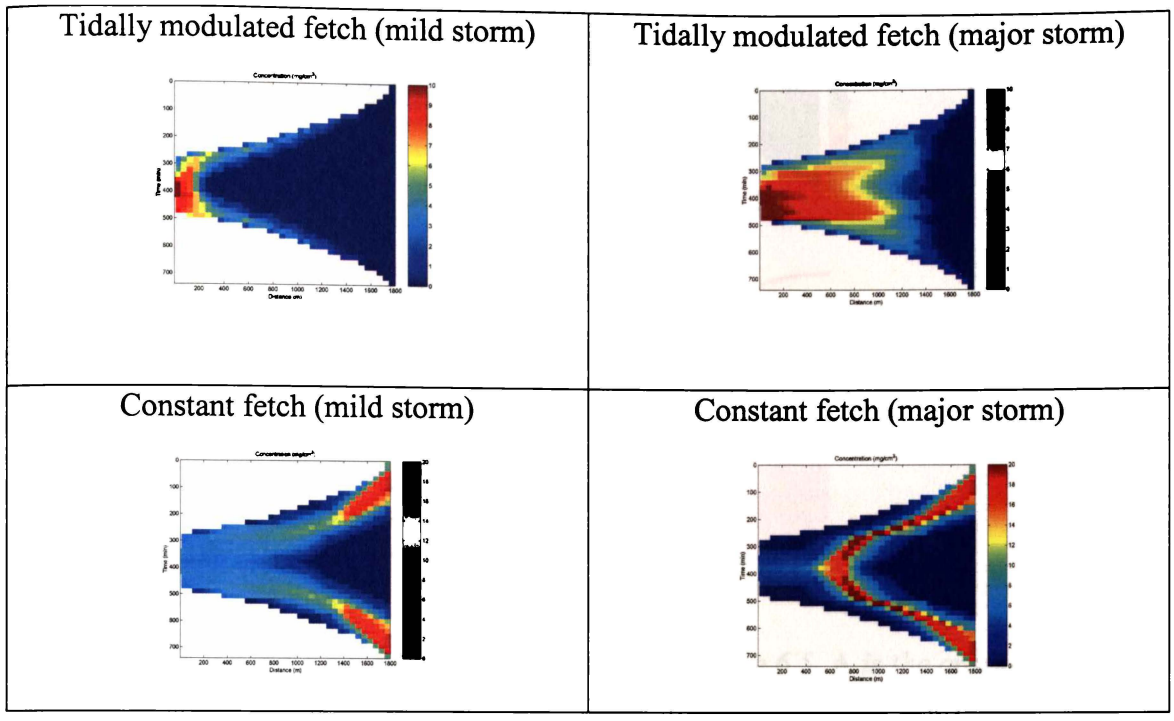

Figure 6.2: Concentration scenarios for schematic modelling (Figure 6.5).

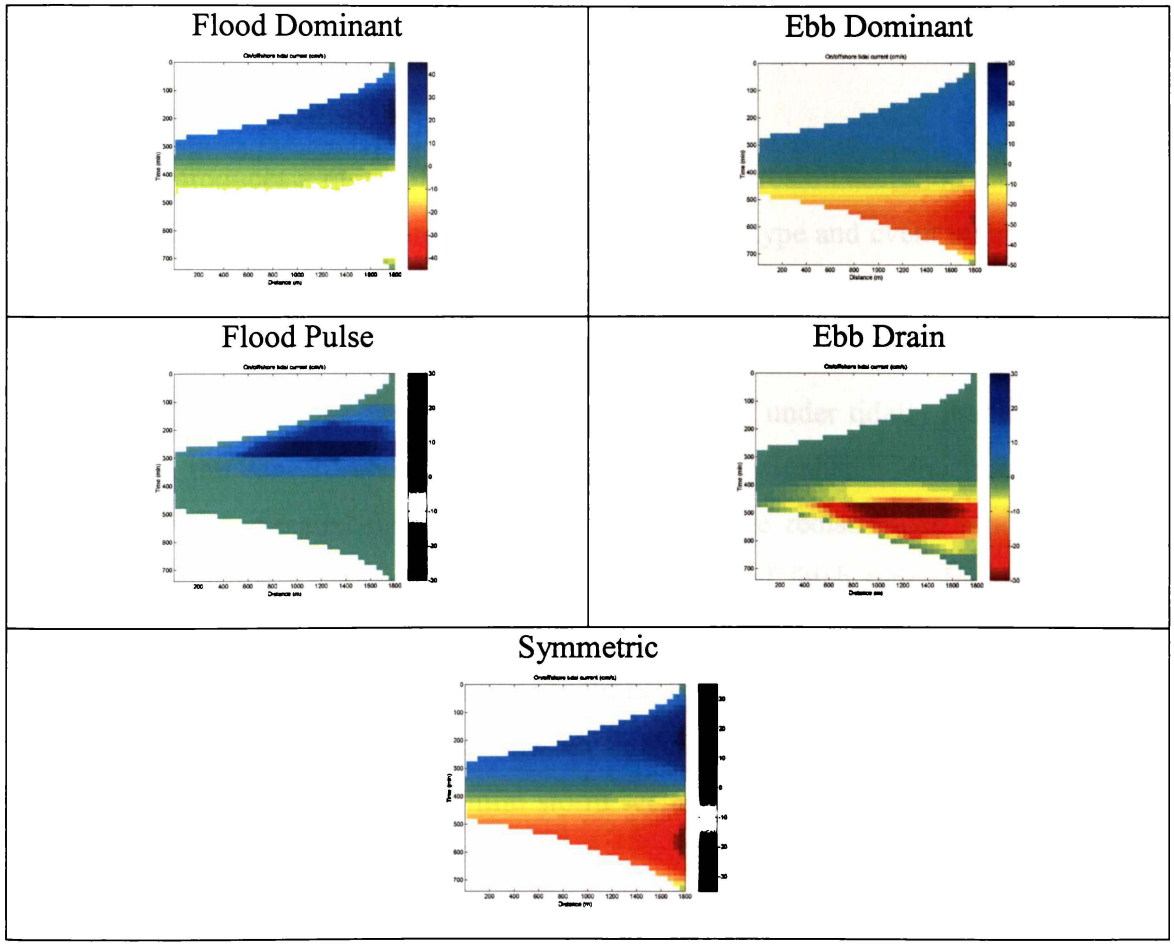

Figure 6.3: Mean current scenarios for schematic modelling (Figure 6.5). White areas are exposed sections of the transect.

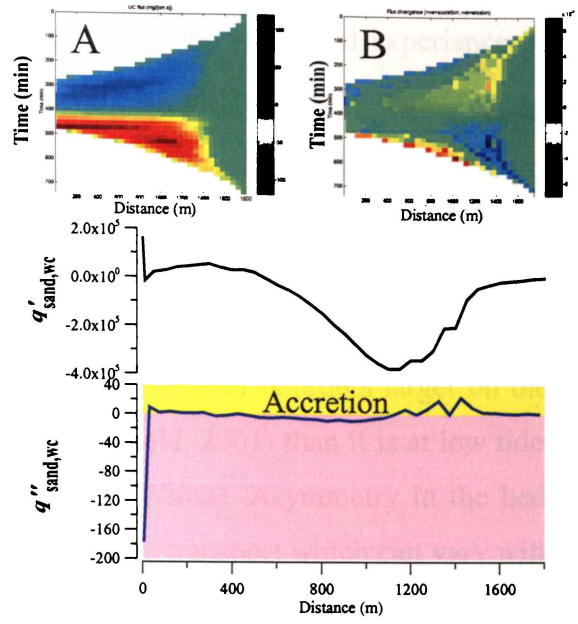

Figure 6.4: Legend for sand flux diagrams used in Figure 6.5. **A** *is the cross-shore sand flux,* $q_{\text{sand,wc}}(x,t)$ *and* **B** *the cross-shore gradient in* $q_{\text{sand,wc}}(x,t)$.

6.3.4 Discussion

The model produces a range of sediment-transport and erosion/accretion patterns under the various scenarios, suggesting that tidal regime, fetch type and event magnitude place important controls on intertidal flat sediment transport, erosion/accretion patterns and therefore cross-sectional shape. For instance, tidal asymmetry drives $Q_{\text{sand,wc}}(x)$ in the direction of the dominant flow under constant fetch, but under tidally modulated fetch, variation in the concentration field over the tide acts to enhance ebb transport, even under a flood-dominated tide. In contrast, ebb drainage redistributes sands from the upper flat onto the middle and lower flats regardless of fetch type. Increasing event magnitude not only results in higher concentrations and therefore greater flux, but also gives rise to different patterns in the concentration field and therefore different flux and erosion/accretion patterns. For example, erosion occurs across the entire profile under the ebb dominant, constant fetch, mild storm scenario, but for a major storm there is a zone of net deposition on the upper flat.

Differences in spatial patterns in concentration also result in different transport and erosion/accretion patterns. For instance, under tidally-modulated fetch, concentration is high on the upper flat (because fetch and bed-orbital speeds are large), but under

constant fetch the highest concentrations are encountered on the lower flat, where fully developed waves encounter *shallow* water and experience depth-limited breaking. As $\overline{U}$ is greatest on the lower flat, all else being equal, $Q_{\text{sand,wc}}$ would be larger under constant fetch, since, under this scenario, maximum tidal currents coincide with highest sand concentrations.

The wave flux would also be larger in constant fetch settings, at least at low tide, because wave-orbital speed asymmetry is orders larger on the lower flat for a constant fetch (e.g., Green and MacDonald, 2001) than it is at low tide (i.e., reduced fetch) for a tidally modulated fetch (e.g., Wiroa). Asymmetry in the bed-orbital speed provides a mechanism for onshore/offshore transport which can vary with elevation on the flat and also with the fetch type.

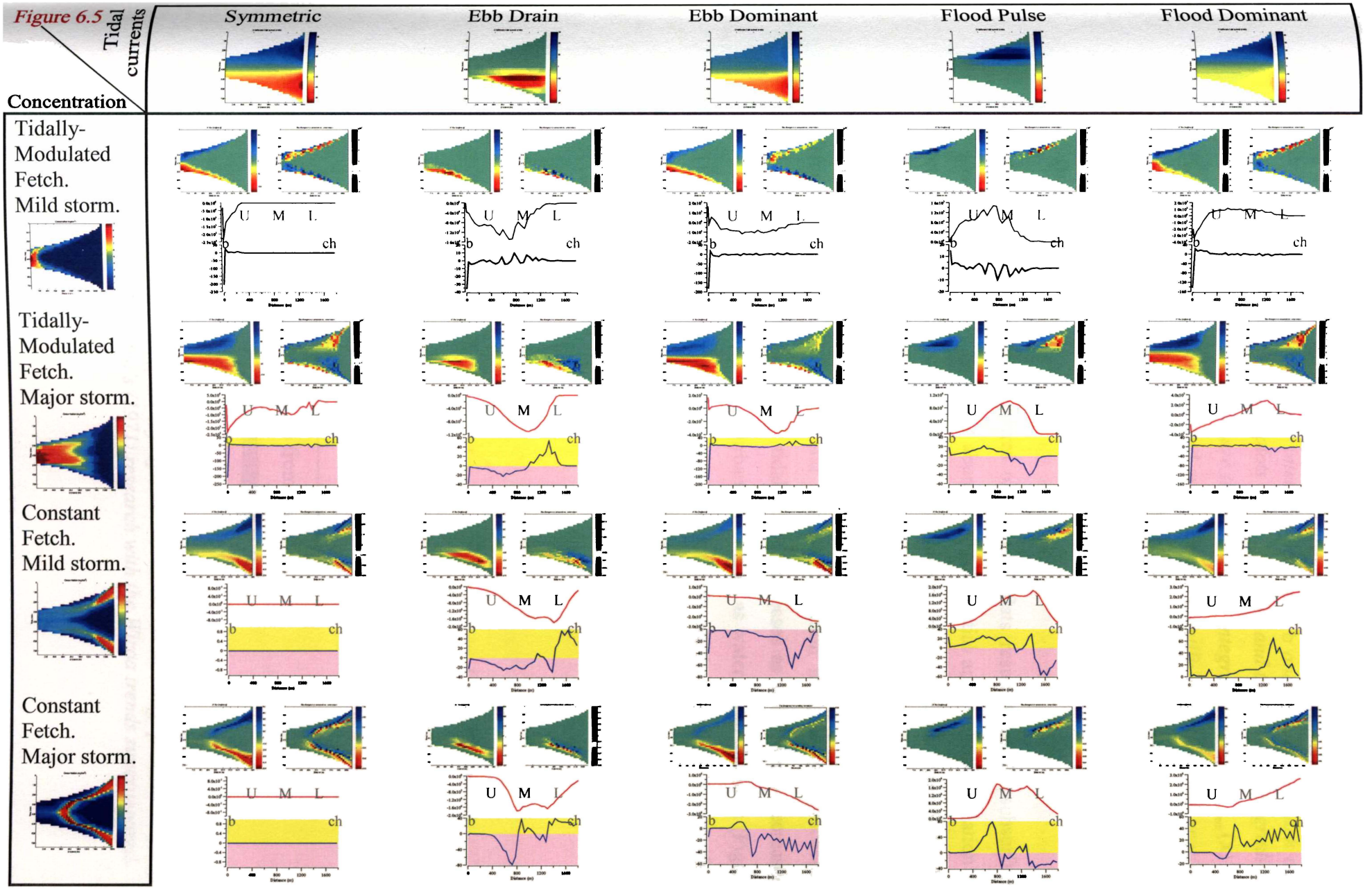
Figure 6.5
Tidal currents
Concentration
Symmetric
Ebb Drain
Ebb Dominant
Flood Pulse
Flood Dominant
Tidally-Modulated Fetch. Mild storm.
Tidally-Modulated Fetch. Major storm.
Constant Fetch. Mild storm.
Constant Fetch. Major storm.
U M L
b ch

Figure 6.5: Scenarios of cross-shore sand flux and the cross-shore gradient in the cross-shore sand flux for varying tidal and concentration conditions. U, M, L *are the geomorphic upper middle and lower intertidal flat while* b *and* ch *are the beach and channel. In each scenario the upper plots are* $q_{\text{sand, wc}}(x,t)$ *and the cross-shore gradient in* $q_{\text{sand, wc}}(x,t)$*, while the lower plots are the event (time) integrated terms* $q'_{\text{sand, wc}}(x)$ *(-) and* $q''_{\text{sand, wc}}(x)$ *(-), where yellow and pink regions identify accretion and erosion, respectively. White areas are exposed sections of the transect. See Figure 6.4 and the text for a detailed explanation on how to interpret the diagram.*

6.4 DISCUSSION

Geomorphic and sedimentary features of intertidal flats result from the subsurface geology; sediment supply, type, and abundance; and spatial and temporal variation in the forces which transport and redistribute sediment. Early research identified tidal currents and waves being primarily responsible for transporting intertidal flat sediments (e.g., Postma, 1967; Reineck, 1967). Allen (1971) and Dyer (1989) point out a fundamental feature of the spatial and temporal variation in these two processes: disturbance of bottom sediments by tidal action decreases as water depth decreases, while for wave action, sediment disturbance increases as water depth shallows (Figure 6.6). That is, the shallow upper sections of intertidal flats are the domain of waves while the seaward flats are the domain of tidal flows. Superimposed on Figure 6.6 are the skin friction terms and wave work for Wiroa, which support the Allen/Dyer assertion but also reveal spatial complexity.

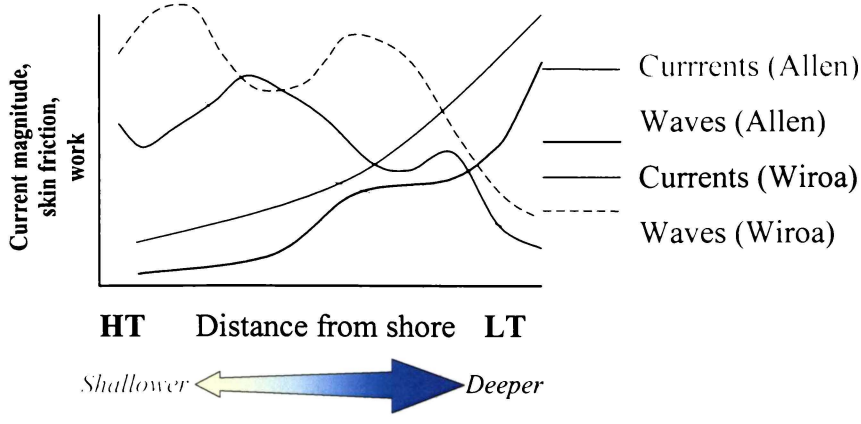

Figure 6.6: Schematic diagram of spatial variation in driving processes across intertidal flats based on Allen's (1971) research with the Wiroa trends superimposed.

Tidal currents have received far more attention in the estuarine sediment transport literature than other processes (e.g., waves), presumably because of their periodic nature, the ease with which they can be measured (and to some extent predicted), and the spatial trends in sedimentology, geomorphology and benthic biota which are observed on some flats (e.g., Evans and Collins, 1975; Frostick and McCave, 1979; Amos, 1995). The zonation which results from spatial variation in tidal currents is typically parallel to the bathymetry (e.g., Evans, 1965; Amos, 1995). In mixed-size sedimentary regimes, weakening tidal currents (across the flat) deposit coarser sediments on the lower-flat, and progressively finer sediments at higher elevations (Evans, 1965; Postma, 1967; Reineck, 1967; Collins *et al.*, 1981). Intermittently inundated regions experience very weak tidal flows and may become vegetated by halophytic plants such as mangroves and salt marsh species. Vegetation enhances accretion and deposition processes by 'baffling' already weak tidal currents (Carling, 1982), and therefore promotes shoreline advance.

Wave action on intertidal flats can modify or over-ride tidally-induced sedimentary patterns (e.g., grading). In the macrotidal Wash, decreasing tidal current with elevation causes sediment-size grading, however, waves intermittently deliver and deposit coarse sediments on the upper mud flats and salt marsh. This results in a stratigraphic sequence of alternating bands of mud and sand (Evans and Collins, 1975). Carling (1982) also observed wave-driven advection of coarse material onto marshlands during storms.

When waves are energetic, settling of fines is less likely, sands accumulate, and spatial variation in θ'_{w} and W_{w} may determine sedimentary patterns. This is the case at Wiroa, except on the channel margins, where $\theta'_{w} < \theta_{cr,sand}$, and in mangrove stands on the upper flats, where the wave boundary layer is biologically modified. Postma (1967) notes particle size may increase as depth decreases due to more effective wave penetration, or that particle size may decrease with elevation (reinforcing size-grading due to tidal currents) due to shoreward reductions in wave energy. It is worthwhile to note here that, although tides and waves redistribute sediments, sedimentary patterns ultimately depend on the availability and abundance of each size fraction. However, low mud abundance is not apparently a factor to the sandy flats at Wiroa, as mud is abundant in channels and nearby wave-sheltered locations.

Patterns in inundation/exposure and event-integrated work done by waves correspond to sedimentary and geomorphic features of the Wiroa flat. For instance, the low sloping upper flat (*U1*) resembles an accretionary feature built by shoreward moving sediment (e.g., $\bar{Q}_{susp,ww}$) and further aided by enhanced settling processes (see Section 5.6.6) within the intermittently inundated zone. *U1* also corresponds to the zone of maximum wave work (Figure 6.1), suggesting that slope there is related to wave energy in much the same way that beach slopes decrease in order to dissipate higher wave energy (e.g., Short, 1999). Similarly, lower W_w on the middle flats (induced by high tidal translation rates and smaller fetch) corresponds to steeper slopes. Thus, the complex process interactions which determine spatial variability in W_w at Wiroa – depth, wave period, wave energy, tidal translation rate, inundation duration, and time in excess of critical – would appear to be linked to sediment redistribution and geomorphic zonation.

Erosion and accretion are determined by flux divergence and the interaction of different transport mechanisms. For example, erosion from sandy middle flats and subsequent deposition on upper mud flats and marshes has been observed by Evans and Collins (1975), Carling (1982) and Bartholdy and Aagaard (2001), suggesting that waves promote accretion, growth, and reclamation of flats. In contrast, Krone (1966), Postma (1967) and Anderson and Pejrup (2001) claim that net sediment losses during episodic wave events balances longer term tidally-induced accretion and, consequently, waves are responsible for maintenance and dynamic equilibrium on intertidal flats. Most likely, both situations occur. In any case, accretionary mechanisms such as settling lag, scour lag, decreasing tidal flows with elevation and tidal asymmetry can be aided or abetted by wave action.

The discussion thus far has drawn primarily from meso-tidal settings (e.g., Wiroa and Okura) where tidal currents have a limited role in mobilising sands but are important in advecting wave-induced suspensions. As tidal energy increases or decreases, the relative role of the transport terms $Q_{sand,wc}$ and $Q_{sand,ww}$ will change and other terms may come into play. The familiar micro (0–2 m), meso (2–4 m) and macro (> 4 m) tidal-range classification of Davies (1964) is used here to represent regimes of tidal range and the tidal-current strength. Skin friction and transport terms are compared qualitatively in Table 6.1 for each tidal regime.

Microtidal range would be associated with a narrowing of intertidal regions and component geomorphic zones. Tidal currents are presumably incompetent across the flat and $Q_{sand,wc}$ would be small when compared with flats with higher tidal ranges. Comparatively, wave flux would increase in significance, however spatial trends in both $Q_{sand,wc}$ and $Q_{sand,ww}$ may be expected to yield similar sedimentary and geomorphic patterns to those discussed previously. Spatial variation in W_w is also likely to be similar to patterns discussed above, however, decline in W_w over the middle flats might be less significant than for higher tidal ranges because tidal translation rates are lower. Wave-current interaction, which only had a weak influence on sand entrainment at Wiroa, should not be anymore significant in a microtidal setting.

In macro-tidal estuaries with abundant sediment supply, the sedimentary patterns and general geomorphology of intertidal flats are largely controlled by tidal currents. Competent tidal currents can extend onto the upper flats and size-grading of sediments is common (e.g., Amos, 1995). As tidal translation rates are high, wave work over the middle flats is expected to be low. Wave work is also low on the lower flats compared to the strong tidal flows experienced there. However, on the upper regions of the flat, where tidal flows are presumably incompetent, only waves are capable of remobilising sediments, and there they may be responsible for local erosion or transport of coarse materials onto higher flats and marshlands, as already discussed. Strong tidal flows enhance $Q_{sand,wc}$ and advection of current-entrained sediment by the current, Q_{cc}, is most likely to be the largest flux component. Thus, as tidal range/energy increases, there are more potential entrainment and sediment transport mechanisms. While complexity and the range of processes may increase, strong tidal currents tend to dominate and control the overall intertidal flat geomorphology.

Tidal range	$\theta'_c > \theta_{cr}$	$\theta'_w > \theta_{cr}$	Q_{cc}	Q_{wc}	Q_{ww}	
Micro	x	✓	x	✓	✓	
Meso	x	✓	x	✓	*tmf*	✓
					cf	✓
Macro	✓	✓	✓	✓	*tmf*	✓
					cf	✓

Table 6.1: Entrainment and transport terms on estuarine intertidal flats of differing tidal range. The abbreviation "tmf" refers to tidally modulated fetches while "cf" refers to constant fetch. Q_{cc}, Q_{wc} and Q_{ww} are the transport terms for current entrainment with current advection, wave entrainment with current advection, and wave entrainment with wave advection, respectively.

As more wave and sediment transport data become available for a range of wave and tidal energies, comparison of intertidal flats and their transport processes should proceed in a quantitative fashion to facilitate development of morphodynamic models, such as those developed for beaches (e.g., Wright *et al.*, 1985; Masselink and Short, 1993). Non-dimensionalising elevation on the flat by dividing by the mean spring tidal elevation gives the relative tidal elevation for each location (e.g., Amos, 1995), which is a convenient and useful way to make spatial comparisons of geomorphic features and physical processes for a range of different settings. Zones of competency for tidal and wave motion should be considered alongside their associated time-integrated work terms (e.g., Figure 6.7).

By way of example, the mesotidal Wiroa flat is compared with an intertidal flat on the macrotidal Wash (Amos, 1995) in Figure 6.7. The *intermittently inundated* regions of the Wash occupy a wider relative tidal range than Wiroa, suggesting that infilling on the upper flats of the Wash is more advanced. The consequence is that salt marsh and mud flats occupy much of the intermittently inundated zone where fine sediments accumulate and consolidate. Deposition of fines also occurs at Wiroa, but wave activity prevents accumulation, except in those areas sheltered by mangroves. Tidal competency for sands defines the region where sands grade into muds on the upper flats of the Wash, but at Wiroa tidal currents are incompetent everywhere and bed sediment distributions are controlled by waves: on the channel margins waves are incompetent and muddy sediments are found despite strong tidal flows; and on the upper flats mangrove sheltering promotes settling of fines. The absence of wave data from the Wash limits further comparison.

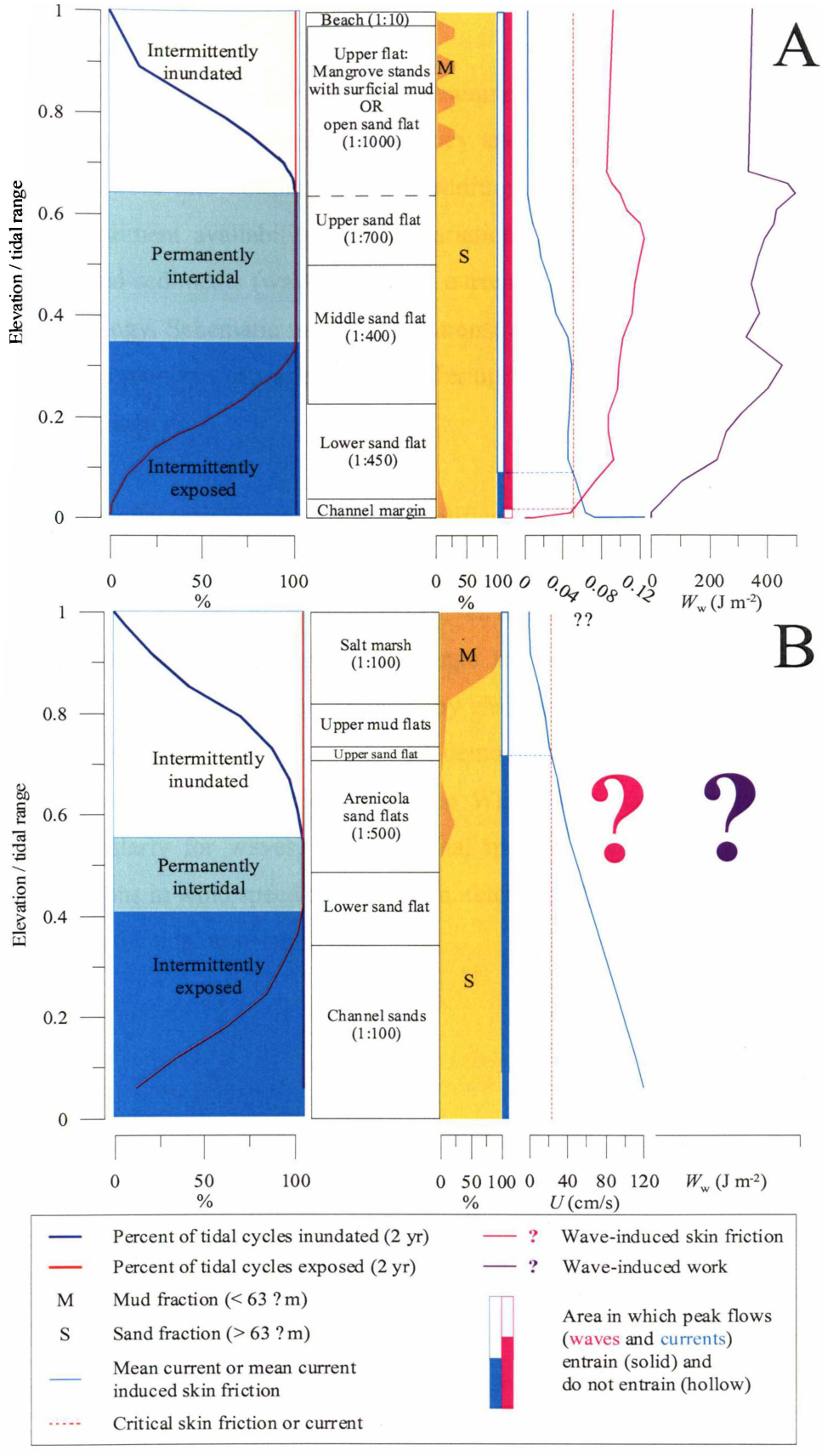

*Figure 6.7: Non-dimensional elevation (elevation/tidal range) plots of geomorphic features, inundation patterns, peak skin friction due to waves and currents, and event integrated work done at the bed by waves for **A** Wiroa Island and **B** The Wash* (Source: Amos, 1995). *Refer Section 6.2.1 for explanations on inundation/exposure index, skin friction and work terms.*

6.5 CONCLUSIONS

The Wiroa data show that waves control entrainment of local bed-sediment and that there is spatial correlation between competency and bed sediment size, and between time-integrated work and bottom slope. In addition to the constraints of subsurface geology and sediment availability, spatial variation in the processes responsible for redistributing bed sediments (waves and tidal currents) determines intertidal flat shape and geomorphology. Schematic modelling demonstrates that a wide range of sediment transport regimes/patterns can arise under differing fetch types, storm magnitudes and tidal current regimes.

Allen's (1971) model (see Figure 6.6) is a simplification of the way in which the driving processes vary across intertidal flats: tidal currents weaken with elevation while wave motions strengthen. The actual shape of the curves in Figure 6.6 is expected to vary for each setting. Furthermore, changing tidal range and energy alters the role of tidal currents and can influence wave generation (by changing fetch conditions) and spatial patterns in wave work. While Allen's model demonstrates the general trends in wave and tidal processes across intertidal flats, the Wiroa data suggest a more complex situation, particularly for waves, as bed-orbital motion is controlled by spatial and temporal variations in wind speed and direction, fetch length, wave height, wave period, penetration, and the tidal translation rate.

The primary aim of this research project was to gain an understanding of the spatial and temporal variation in physical processes (particularly waves) as they relate to sediment transport and geomorphology across an estuarine intertidal flat. This final chapter is a synopsis of the main discoveries pertaining to this research aim – other concluding remarks have been made at the end of each research chapter. Recommendations for future research are also made.

Although research on estuarine intertidal flats is dominated by investigations of a tidal nature, waves are considered by some researchers to be the most important sediment-transport process operating on estuarine intertidal flats (Postma, 1967; Dyer, 1989). Findings from the Wiroa experiments bear out this notion: sand and silt suspensions across the flat are switched on and off by wave activity, but not by tidal currents. That is, sediment distribution and geomorphic evolution of the Wiroa flats (and, most likely, other mesotidal intertidal flats) is controlled by wave-orbital motion at the bed. The same is true for the upper sections of macrotidal flats where tidal currents become incompetent.

Sand concentration near the bed (C_0) is controlled by wave-induced skin friction for three bottom/ripple regimes: when θ'_w is low, steep wave-orbital ripples dominate and $C_0 \propto \theta'^3_w$; as θ'_w increases, ripple crests are thought to become rounded and $C_0 \propto \theta'^1_w$; and eventually the bed is flattened and $C_0 \propto \theta'^3_w$. These relationships suggest that the reference concentration is a function of skin friction and ripple steepness as described by Nielsen's (1986) model for unbroken waves. The intermediate state ($C_0 \propto \theta'^1_w$), which has not previously been observed, may reflect the co-existence of ripples and flat beds, or a transitional bed of rounded ripples.

Suspended sands were confined to a near-bed layer about 10 cm thick. In this layer the $\overline{C}_{sand}$-profiles followed Nielsen's (1984) simple exponential model which implies a sediment diffusivity which is vertically uniform and which is typical of unbroken and spilling waves (Ogston and Sternberg, 2002). The mixing length was reasonably well

described by Nielsen's (1990) empirical equation, which implies that the mixing length is controlled by ripple height, near-bed wave orbital motion and settling velocity. Scatter in, and differences between, the Wiroa and Nielsen data are related to the way parameters are specified and to the reliance on empirical estimates of ripple dimensions. Surface turbulence under whitecaps rarely penetrates into the suspended-sand layer and was never observed to penetrate to the bed, suggesting that whitecaps do not influence entrainment only occasionally contribute to sediment mixing. Thus, the mechanics of sediment suspension on the intertidal flat are comparable to open coast settings under unbroken waves despite the short, choppy and whitecapped nature of estuarine seas.

Silt suspensions are also switched on by wave activity, however, because silt settles very slowly, it behaves like wash load and, following cessation of wave activity, settlement takes hours to days (e.g., Figure 5.7 and Green *et al.*, 2000). Consequently, silt concentration is unrelated to local bed shear stress, and the material in suspension is distributed homogeneously through the water column and is largely of non-local source. Although large silt fluxes were observed, hydrodynamic conditions across most of the flat prevent silt settling to the bed and consequently silt suspensions do not contribute to accretion and sedimentary patterns, with two exceptions: near the top of the intertidal flat $Q_{silt,ww}$ and enhanced settling give rise to ephemeral storm deposits at high tide; while at low tide, when the estuarine water body is confined to the tidal channels, fine sediments are likely to flocculate and settle to form a muddy channel-margin bed. An understanding of the silt transport equation requires measurement or modelling at an estuarine-wide scale.

Waves are the only entrainment mechanism on the Wiroa intertidal flat and as such waves control which sediments are mobilised, when and where. Sand transport is primarily determined by the interaction of tidal currents and the wave-induced concentration field, ($Q_{sand,wc}$), which are independent of one another and which both vary with location across the flat and with time through the tidal cycle. Consequently, sand transport and sand transport pathways are controlled by local circulation and the relative timing of strong tidal currents and high concentration suspensions, both of which are expected to vary from one flat to another.

At higher elevations on the Wiroa flat, sand transport due to waves was diabathic and in an onshore direction. Notwithstanding phase relationships between the velocity and concentration fields, increasing wave-orbital speed asymmetry with elevation up the flat suggests an increase in onshore transport under waves and the relative importance of $Q_{sand,ww}$ with respect to $Q_{sand,wc}$. Diabathic sediment transport under waves is thus a potential mechanism for the top-down accretion and growth intertidal flats.

Sand transport patterns are also expected to change from setting to setting under different tidal current regimes and fetch types, as noted above and shown by schematic modelling. Furthermore, changes in tidal range/energy influence tidal translation rates, intertidal flat width, and the competency and sediment flux associated with the mean current.

Despite the wide array of tidal ranges and current speeds expected on flats of differing tidal energy, Allen's (1971) paradigm is still expected to underpin the way in which wave and tidal energy vary across intertidal flats, albeit in a simplistic manner. Although the spatial patterns in competency and time-integrated work at Wiroa are not as simplistic as Allen's paradigm, they are broadly similar and they correspond to spatial variations in the sedimentary and geomorphic features of the flat. The implication is that waves are involved in shaping intertidal flats and controlling the way in which they evolve. Therefore, if an understanding how such systems function is to be gained, studies of physical processes, sediment transport and intertidal flat evolution must quantitatively consider wave action. Furthermore, the processes and transport mechanisms operating on intertidal flats are similar to those found in beach settings, but with more emphasis on tidal flows and possibly less emphasis on wave breaking processes. Results of the sort presented here can be used to help classify intertidal flats and thereby extend the beach morphodynamic framework (e.g., Wright *et al.*, 1985; Masselink and Short, 1993; Masselink and Turner, 1999) of which estuarine intertidal flats are an end-member.

Some specific recommendations for future research into processes and sediment transport on intertidal flats are listed below.

Many studies of intertidal flats, and certainly most texts on the subject, are from mud flats (e.g., Black *et al.*, 1998; Eisma *et al.*, 1998). In order to cover a range of sediment types more investigations on sandy and mixed sand/mud flats are required.

Wave, current, and sediment-transport measurements are required in all geomorphic subzones. Although this study attempted to measure currents, waves, and silt transport in every zone, sand transport was only measured on the lower and middle flats. As there is evidence from different studies to suggest that waves cause net erosion and net accretion on the upper sections of sand flats, it is pertinent that future studies make process/transport measurements in this region.

Efforts to better understand the influence of biological films on the entrainment threshold were not directly investigated in this thesis, however, entrainment measurements were in agreement with predictions for abiotic sediments at Wiroa. This suggests that biological films are not important to the sediment transport equation for the chosen measurement locations and time periods. However, in settings exposed to lower wave energy, and/or following periods of infrequent wave activity, biological films may bind and stabilise the sediment matrix (Grant, 1988; Lelieveld, 2000). Therefore, sediment transport on temperate and tropical estuarine flats is likely to be influenced by biological activity to one degree or another (or at one time or another), which justifies the ongoing research in this area that is essential to a wider understanding of sedimentation on intertidal flats.

An ability to measure mixed-size suspensions is crucial. At Wiroa, the two particle-size modes were amenable to identification and measurement with OBS and ABS. Combining instrument types according to their sensitivity for different sediment size fractions is one way in which instantaneous SSC can be measured for each size range. As estuarine waves have short periods, the concentration field fluctuates rapidly and therefore instrumentation must measure each size fraction separately and at a high sampling frequency.

Measurement of bedforms is crucial to understanding reference concentration, sediment mixing, and wave-advected transport mechanisms ($Q_{sand,ww}$). Empirical equations for ripple dimensions and evolution are inadequate due to their inability to account for lag effects, however the Wiroa data suggest that the predicted wave-orbital ripples are of the correct height and length order and that they play a significant role for SSC and mixing.

The shallow turbid fringe, which sweeps back and forth across the flats during storms and is known to carry the highest estuarine sediment concentrations (e.g., Dolphin and Green, 1997), is a challenging measurement environment. In such shallow water, unobtrusive measurements of waves and currents can be made by ADVs, while SSC may be measured using miniature OBSs, and/or near-bed ABSs deployed at an oblique angle. The detailed measurement of waves and silt/sand suspension in the shallow estuarine fringe which would significantly improve our understanding of intertidal flat sediment transport have yet to be made.

There is an inconsistency between pressure and velocity measurements made by some instruments on the Wiroa and Okura flats. The inconsistency is most likely due to pressure sensor frequency response under short-period waves. Although the manufacturers' specifications do not support this, data on frequency response are not readily available. Thus, frequency response testing is required to determine whether the inconsistency is a feature of the measurement process. In the meantime, the Wiroa data indicate the measurement of waves and bottom flows are satisfactorily achieved using current meters with high-frequency sampling capabilities.

Aagaard, T. and Masselink, G., 1999. The surf zone. In: A.D. Short (Editor), *Handbook of Beach and Shoreface Morphodynamics*. John Wiley and Sons Ltd., Chichester, England.

Allen, G.P., 1971. Relationship between grain size parameter and current patterns in the Gironde estuary. *Journal of Sedimentary Petrology*, 41(1): 74-88.

Amos, C.L., 1995. Siliciclastic tidal flats. In: G.M.E. Perillo (Editor), *Geomorphology and Sedimentology of Estuaries*. Developments in Sedimentology. Elsevier Science, pp. 273-306.

Anderson, F.E., 1972. Resuspension of estuarine sediments by small amplitude waves. *Journal of Sedimentary Petrology*, 42(3): 602-607.

Anderson, F.E., 1983. The northern muddy intertidal: Seasonal factors controlling erosion and deposition - A review. *Canadian Journal of Fisheries and Aquatic Sciences*, 40(Supplement No. 1): 143-159.

Anderson, T.J. and Pejrup, M., 2001. Suspended sediment transport on a temperate, microtidal mudflat, the Danish Wadden Sea. *Marine Geology*, 173: 69-85.

Arens, S.M., 1994. *Aeolian Processes in the Dutch Foredunes*, University of Amsterdam.

Bagnold, R.A., 1956. The flow of cohesionless grains in fluids. *Philosophical transactions of the Royal Society of London, Series A*, 249: 235-297.

Bagnold, R.A., 1963. Beach and nearshore processes. In: M.N. Hill (Editor), *The Sea*. Interscience, New York, pp. 507-528.

Bailard, J.A., 1981. An energetics total load sediment transport model for a plane sloping beach. *Journal of Geophysical Research*, 86(C11): 10938-10954.

Bailard, J.A. and Inman, D.L., 1981. An energetics bedload model for a plane sloping beach: Local transport. *Journal of Geophysical Research*, 86(C3): 2035-2043.

Bartholdy, J. and Aagaard, T., 2001. Storm surge effects on a back-barrier tidal flat of the Danish Wadden Sea. *Geo-Marine Letters*, 20: 133-141.

Battisto, G.M., Friedrichs, C.T., Miller, H.C. and Resio, D.T., 1999. Response of OBS to mixed grain-size suspensions during SandyDuck'97. In Proceedings of: *Coastal Sediments '99: Proceedings of the 4th International Symposium on Coastal Engineering and Science of Coastal Sediment Processes*, 1: 297-312, N.C. Kraus and W.G. McDougal (Editors). American Society of Civil Engineers, Long Island, New York.

Bell, R.G., Dumnov, S.V., Williams, B.L. and Greig, M.J.N., 1998. Hydrodynamics of Manukau Harbour, New Zealand. *New Zealand Journal of Marine and Freshwater Research*, 32: 81-100.

Bell, R.G., Hume, T.M., Dolphin, T.J., Green, M.O. and Walters, R.O., 1997. Characterisation of physical environmental factors on an intertidal sandflat, Manukau Harbour, New Zealand. *Journal of Experimental Marine Biology and Ecology*, 216: 11-31.

Bishop, C.T. and Donelan, M.A., 1987. Measuring waves with pressure transducers. *Coastal Engineering*, 11: 309-328.

Black, K., Hatton, D. and Rosenberg, M., 1993. Locally and externally-driven dynamics of a large semi-enclosed bay in southern Australia. *Journal of Coastal Research*, 9(2): 509-538.

Black, K., Hatton, D., Turnbull, J. and You, B., 1994. *Turbidity and light level monitoring in seagrass beds at Avalon and Clifton Springs*. Report for Marine Science & Ecology, Maunsell Pty Ltd & Port Geelong. Victorian Institute of Marine Sciences.

Black, K.P., 1983. *Sediment transport and tidal inlet hydraulics*. D.Phil Thesis, University of Waikato, Hamilton.

Black, K.P., Green, M.O., Healy, T., Bell, R.G., Oldman, J. and Hume, T.M., 1999. Lagrangian modelling techniques simulating wave and sediment dynamics determining sand-body equilibria. In: J. Harff, W. Lemke and K. Stattegger (Editors), *Computerized Modelling of Sedimentary Systems*. Springer, Berlin, pp. 3-21.

Black, K.P. and Rosenberg, M.A., 1991. Suspended sediment load at three time scales. In Proceedings of: *Coastal Sediments'91*: 313-327, ?? (Editor). ASCE.

Black, K.P. and Rosenberg, M.A., 1994. Suspended sand measurements in a turbulent environment: field comparison of optical and pump sampling techniques. *Coastal Engineering*, 24: 137-150.

Black, K.S., Paterson, D.M. and Cramp, A. (Editors), 1998. *Sedimentary Processes in the Intertidal Zone*. Geological Society Special Publications, Special Publication No. 139. The Geological Society, London, 409 p. pp.

Bretschneider, C.L., 1966. Engineering aspects of hurricane surge. In: A.T. Ippen (Editor), *Estuary and Coastline hydrodynamics*. McGraw-Hill, New York.

Brydsten, L., 1992. Wave-induced resuspension in the Öre estuary, northern Sweden. *Hydrobiologia*, 235/236: 71-83.

Bunt, J.A.C., Larcombe, P. and Jago, C.F., 1999. Quantifying the response of optical backscatter devices and transmissometers to variations in suspended particulate matter. *Continental Shelf reseach*: 593-610.

Carling, P.A., 1982. Temporal and spatial variation in intertidal sedimentation rates. *Sedimentology*, 29: 17-23.

Cavaleri, L., 1980. Wave measurement using pressure transducer. *Oceanologica Acta*, 3(3): 339-346.

Cavaleri, L., Ewing, J.A. and Smith, N.D., 1978. Measurement of the pressure and velocity field below surface waves. In Proceedings of: *Proceedings of the NATO Conference on Turbulent Fluxes through the Sea Surface, Wave Dynamics, and Prediction*, 1: 677, A. Favre and K. Hasselmann (Editors). Plenum Press, Marseille, France.

Collins, M.B., Amos, C.L. and Evans, G., 1981. Observations of some sediment-transport processes over intertidal flats, the Wash, U.K. In: S.D.-. Nio, R.T.E. Shuttenhelm and T.C.E. van Weering (Editors), *Holocene Marine Sedimentation in the North Sea Basin*. Blackwell Scientific, pp. 81-98.

Conner, C.S. and De Visser, A.M., 1992. A laboratory investigation of particle size effects on an optical backscatterance sensor. *Marine Geology*, 108: 151-159.

Dally, W.R., Dean, R.G. and Dalrymple, R.A., 1985. Wave height variation across beaches of arbitary profile. *Journal of Geophysical Research*, 90(C6): 11917-11927.

Davies, J.L., 1964. A morphogenic approach to the world's shorelines. *Zeitschrift fur Geomorphologie*, 8: 127-142.

Dingler, J.R. and Clifton, H.E., 1984. Tidal-cycle changes in oscillation ripples on the inner part of an estuarine sand flat. *Marine Geology*, 60: 219-233.

Doering, J.C. and Bowen, A.J., 1987. Skewness in the nearshore zone: A comparison of estimates from Marsh-McBirney current meters and colocated pressure sensors. *Journal of Geophysical Research*, 92(C12): 13173-13183.

Dolphin, T.J., 1992. *Low Amplitude Multiple Bar Systems in an Intertidal Fetch Limited Environment*. MSc Thesis, Auckland University, Auckland, 143 pp.

Dolphin, T.J. and Green, M.O., 1997. Sediment dynamics of an estuarine "Turbid Fringe". In Proceedings of: *Pacific Coasts and Ports: The combined 13th Australasian Coastal and Ocean Engineering Conference and 6th Australasian Port and Harbour Conference*, 1: 113-118. Centre for Advanced Engineering, University of Canterbury, Christchurch, New Zealand.

Dolphin, T.J., Green, M.O., Radford, J.D.J. and Black, K.P., 2001. Biofouling of Optical Backscatter Sensors: Prevention and Analytical Correction of Data. *Journal of Coastal Research*, Special Issue 34: 334-341.

Dolphin, T.J., Hamilton, C.L. and Green, M.O., 1999. *Wave, current and sediment suspension measurements on an intertidal-flat transect*. In: C.L. Hamilton's BSc(tech) Industry Report. Department of Earth Science, University of Waikato, Hamilton.

Dolphin, T.J., Hume, T.M. and Parnell, K.E., 1995. Oceanographic processes and sediment mixing on a sand flat in an enclosed sea, Manukau Harbour, New Zealand. *Marine Geology*, 128: 169-181.

Donelan, M.A., 1978. Whitecaps and momentum transfer. In Proceedings of: *Proceedings of the NATO Conference on Turbulent Fluxes through the Sea Surface, Wave Dynamics, and Prediction*, 1: 677, A. Favre and K. Hasselmann (Editors). Plenum Press, Marseille, France.

Downing, A., Thorne, P.D. and Vincent, C.E., 1995. Backscattering from a suspension in the near field of a piston transducer. *Journal of the Acoustical Society of America*, 97(3): 1614-1620.

Downing, A.J., 1992. *High Frequency Acoustic Monitoring of Suspensions of Marine Sediments*. Unpublished PhD thesis Thesis, University of East Anglia, Norwich, England.

Drabsch, J.M., Parnell, K.E., Hume, T.M. and Dolphin, T.J., 1999. The capillary fringe and the water table in an intertidal estuarine sand flat. *Estuarine, Coastal and Shelf Science*, 48(2): 215-222.

Du Toit, C.G. and Sleath, J.F.A., 1981. Velocity measurements close to rippled beds in oscillatory flow. *Journal of Fluid Mechanics*, 112: 71-96.

Dyer, K.R., 1986. *Coastal and Estuarine Sediment Dynamics*. John Wiley and Sons, Chichester, 342 pp.

Dyer, K.R., 1989. Sediment processes in estuaries: Future research requirements. *Journal of Geophysical Research*, 94(C10): 14327-14339.

Edelman, Joel, 2000. REF: IOS 71516. *pers comm.*: InterOcean Systems Inc.

Eisma, D., de Boer, P.L., Dijkema, K., Ridderinkhof, H. and Philippart, C., 1998. *Intertidal Deposits: River Mouths, Tidal Flats and Coastal Lagoons*. CRC Marine Science Series. CRC Press, Boca Raton.

Emery, W.L. and Thomson, R.E., 1998. *Data Analysis Methods in Physical Oceanography*. Pergamon, Oxford.

Evans, G., 1965. Intertidal flat sediments and their environments of deposition in the Wash. *The Quarterly Journal of the Geological Society of London*, 121(2): 209-245.

Evans, G. and Collins, M.B., 1975. The transportation and deposition of suspended sediment over the intertidal flats of the Wash. In: J. Hails and A. Carr (Editors), *Nearshore Sediment Dynamics and Sedimentation*. John Wiley and Sons, London, pp. 273-306.

Falmouth Scientific Inc., 1998. *3DACM User Manual.*

Folk, R.L., 1968. *Petrology of Sedimentary Rocks*. Hemphill's, Texas, 170 pp.

Forristall, G.Z., 1978. On the statistical distribution of wave heights in a storm. *Journal of Geophysical Research*, 83(C5): 2353-2358.

French, C.E., French, J.R., Clifford, N.J. and Watson, C.J., 2000. Sedimentation-erosion dynamics of abandoned reclamations: the role of waves and tides. *Continental Shelf Research*, 20(12-13): 1711-1733.

Frostick, L.E. and McCave, I.N., 1979. Seasonal shifts of sediments in an estuary mediated by algal growth. *Estuarine, Coastal and Marine Science*, 9: 569-576.

Gorman, R.M. and Neilson, C.G., 1999. Modelling shallow water wave generation and transformation in an intertidal estuary. *Coastal Engineering*, 36: 197-217.

Grant, J., 1988. Intertidal bedforms, sediment transport, and stabilization of benthic microalgae. In: P.L.e.a. de Boer (Editor), *Tide-Influenced Sedimentary Environments and Facies*. D. Reidel Publishing Co., pp. 499-510.

Grant, W.D. and Madsen, O.S., 1982. Movable bed roughness in unsteady oscillatory flow. *Journal of Geophysical Research*, 87(C1): 469-481.

Green, M.O., 1994. Wave-height distribution in storm sea: effect of wave breaking. *Journal of Waterway, Port, Coastal, and Ocean Engineering*, 120(3): 283-301.

Green, M.O., 1996. Introducing ALICE... *Water & Atmosphere*, 4(2): 8-10.

Green, M.O., 1999. Test of sediment initial-motion theories using irregular-wave field data. *Sedimentolgy*, 46: 427-441.

Green, M.O. and Bell, R.G., 1995. Wave influence on suspended-sediment fluxes in an estuary (Manukau Harbour, New Zealand). In Proceedings of: *Proceedings of the 12th Australasian Coastal and Ocean Engineering Conference combined with 5th Australasian Port and Harbour Conference*: 59-64, Melbourne, Australia.

Green, M.O., Bell, R.G., Dolphin, T.J. and Swales, A.J., 2000. Silt and sand transport in a deep tidal channel of a large estuary (Manukau Harbour, New Zealand). *Marine Geology*, 163: 217-240.

Green, M.O. and Black, K.P., 1999. Suspended-sediment reference concentration under waves: field observations and critical analysis of two predictive models. *Coastal Engineering*, 38: 115-141.

Green, M.O., Black, K.P. and Amos, C.L., 1997. Control of estuarine sediment dynamics by interactions between currents and waves at several scales. *Marine Geology*, 144: 97-116.

Green, M.O. and Boon, J.D., 1993. The measurement of constituent concentrations in nonhomogeneous sediment suspensions using optical backscatter sensors. *Marine Geology*, 110: 73-81.

Green, M.O., Dolphin, T.J., Swales, A. and Vincent, C.E., 1999. Transport of mixed-sediments in a tidal channel. In Proceedings of: *Coastal Sediments '99: Proceedings of the 4th International Symposium on Coastal Engineering and Science of Coastal Sediment Processes*, 1: 644-658, N.C. Kraus and W.G. McDougal (Editors). American Society of Civil Engineers, Long Island, New York.

Green, M.O. and MacDonald, I.T., 2001. Processes driving estuary infilling by marine sands on an embayed coast. *Marine Geology*, 178: 11-37.

Guza, R.T., Clifton, M.C. and Rezvani, F., 1988. Field intercomparisons of electromagnetic current meters. *Journal of Geophysical Research*, 93(C8): 9302-9314.

Guza, R.T. and Thornton, E.B., 1980. Local and shoaled comparisons of sea surface elevations, pressures, and velocities. *Journal of Geophysical Research*, 85(C3): 1524-1530.

Hanes, D.M., 1990. The structure of events of intermittent suspension of sand due to shoaling waves. In: B. le Mehaute and D.M. Hanes (Editors), *Sea*. Wiley, New York.

Hatcher, A., Hill, P., Grant, J. and Macpherson, P., 2000. Spectral optical backscatter of sand in suspension: effects of particle size, composition and colour. *Marine Geology*, 168: 115-128.

Hay, A.E., 1991. Sound scattering from a particle-laden, turbulent jet. *Journal of the Acoustical Society of America*, 90(4): 2055-2074.

Hay, A.E. and Sheng, J., 1992. Vertical profiles of suspended sand concentration and size from multifrequency acoustic backscatter. *Journal of Geophysical Research*, 97(C10): 15661-15677.

Heath, R.A., Greig, M.J.N. and Shakespeare, B.S., 1977. Circulation and hydrology of Manukau Harbour. *New Zealand Journal of Marine and Freshwater Research*, 11(3): 589-607.

Herbers, T.H.C., Lowe, R.L. and Guza, R.T., 1991. Field verification of acoustic doppler surface gravity wave measurements. *Journal of Geophysical Research*, 96(C9): 17023-17035.

Herbers, T.H.C., Lowe, R.L. and Guza, R.T., 1992. Field observations of orbital velocities and pressure in weakly non-linear surface gravity waves. *Journal of Fluid Mechanics*, 245: 413-435.

Hicks, D.M. and Green, M.O., 2001. Sand transport during moderate-energy events on the inner shelf at Mangawhai, New Zealand: a comparison among instrument-based and sand tracer measurements. *Continental Shelf Research*, submitted.

Hicks, D.M. and Hume, T.M., 1996. Morphology and size of ebb tidal deltas at natural inlets on open-sea and pocket-bay coasts, North Island, New Zealand. *Journal of Coastal Research*, 12(1): 47-63.

Hume, T.M. and Herdendorf, C.E., 1992. Factors controlling tidal inlet characteristics on low drift coasts. *Journal of Coastal Research*, 8: 355-385.

Hutt, J.A. and Black, K.P., 1997. Vertical attenuation of wave-induced pressure. In Proceedings of: *Pacific Coasts and Ports '97, Proceedings of the 13th Australiasian Coastal and Ocean Engineering Conference and the 6th Australasian Port and Harbour Conference*, 2: 1096. Centre for Advanced Engineering, Christchurch, New Zealand.

IAHR, 1989. List of sea-state parameters. *Journal of Waterway, Port, Coastal and Ocean Engineering*, 115(6): 793-808.

InterOcean, 1994. *S4 Users' Manual*. InterOcean Systems inc., San Diego.

Jackson, N.L. and Nordstrom, K.F., 1998. Aeolian transport of sediment on a beach during and after rainfall, Wildwood, NJ, USA. *Geomorphology*, 22(2): 151-157.

Jonsson, I.G. and Carlsen, N.A., 1976. Experimental and theoretical investigations in an oscillatory turbulent boundary layer. *Journal of Hydraulic Research*, 14(1): 45-60.

Kajiura, K., 1964. On the bottom friction in an oscillatory current. *Bulletin of Earthquake Research Institute, University of Tokyo*, 42: 147-174.

Kaminsky, G. and Kraus, N.C., 1993. Evaluation of depth-limited wave breaking criteria. *Waves'93, American Society of Civil Engineers*: pp. 180-194.

Kineke, G.C. and Sternberg, R.W., 1992. Measurements of high concentration suspended sediments using the optical backscatterance sensor. *Marine Geology*, 108: 253-258.

Kinsman, B., 1984. *Wind waves*. Dover Publications, Mineloa, New York, 676 pp.

Klein, G. deV., 1967. Comparison of recent and ancient tidal flat and estuarine sediments. In: G.H. Lauff (Editor), *Estuaries*. American Association for the Advancement of Science, Washington D.C., pp. 757.

Komar, P.D., 1998. *Beach Processes and Sedimentation*, 2nd Edition. Prentice-Hall, Inc., New Jersey, 544 pp.

Komar, P.D. and Miller, M.C., 1975. On the comparison between the threshold of sediment motion under waves and unidirectional currents with a discussion of the practical evaluation of the threshold. *Journal of Sedimentary Petrology*, 45: 362-367.

Kos'yan, R.D., 1985. Vertical distribution of suspended sediment concentrations seawards of the breaking zone. *Coastal Engineering*, 9: 171-187.

Kreyszig, E., 1993. *Advanced Engineering Mathematics*, 7th Edition. John Wiley and Sons, Singapore.

Krone, R.B., 1966. *Predicted suspended sediment inflows to the San Francisco bay system*. Report prepared for Central Pacific River Basins Comprehensive Water Polution Project, Federal Water Pollution Control Administration Southwest Region.

Larsen, L.H., Sternberg, R.W., Shi, N.C., Marsden, M.A.H. and Thomas, L., 1981. Field investigations of the threshold of grain motion by ocean waves and currents. *Marine Geology*, 42: 105-132.

Le Hir, P., Roberts, W., Cazaillet, O., Christie, M., Bassoullet, P. and Bacher, C., 2000. Characterisation of intertidal flat hydrodynamics. *Continental Shelf Research*, 20: 1433-1459.

Lee, D.-Y. and Wang, H., 1984. Measurement of Surface waves from subsurface gage, *Coastal Engineering*.

Lelieveld, S.D., 2000. *Effects of biota on intertidal sediment stability*. MSc Thesis, University of Waikato, Hamilton, 95 pp.

Longuet-Higgins, M.S., 1952. On the statistical distribution of the heights of sea waves. *Journal of Marine Research*, 11(3): 245-266.

Longuet-Higgins, M.S., 1956. The refraction of sea waves in shallow water. *Journal of Fluid Mechanics*, 1: 163-176.

Longuet-Higgins, M.S., 1975. On the joint distribution of the periods and amplitudes of sea waves. *Journal of Geophysical Research*, 80(18): 2688-2694.

Longuet-Higgins, M.S., 1980. On the distribution of the heights of sea waves: Some effects of nonlinearity and finite band width. *Journal of Geophysical Research*, 85(C3): 1219-1523.

Ludwig, K.A. and Hanes, D.M., 1990. A laboratory evaluation of optical backscatterance suspended solids sensors exposed to sand-mud mixtures. *Marine Geology*, 94: 173-179.

Lynch, J.F., Irish, J.D., Sherwood, C.R. and Agrawal, Y.C., 1994. Determining suspended sediment particle size information from acoustical and optical backscatter measurements. *Continental Shelf Research*, 14(10/11): 1139-1165.

MacDonald, T, C., 1977. Sediment suspension and turbulence in an oscillating flume. *CERC Tech Paper No*, 77-4.

Malvarez, G.C., Cooper, J.A.G., Jackson, D.W.T. and Navas, F., 2001. The role of wave action on sedimentation of tidal flats: Application of high spatial resolution numerical modelling in Strangford Lough, Northern Ireland. *Journal of Coastal Research*, Special Issue 34: 172-182.

Massel, S.R., 1996. *Ocean surface waves: their physics and prediction*. Advanced series on ocean engineering, 11. World Scientific, River Edge, N.J., 491 pp.

Masselink, G. and Pattiaratchi, C.B., 1998. The effect of sea breeze on beach morphology, surf zone hydrodynamics and sediment resuspension. *Marine Geology*, 146: 115-135.

Masselink, G. and Short, A.D., 1993. The effect of tide range on beach morphodynamics and morphology: a conceptual beach model. *Journal of Coastal Research*, 9(3): 785-800.

Masselink, G. and Turner, I., 1999. The effect of tides on beach morphodynamics. In: A.D. Short (Editor), *Handbook of Beach and Shoreface Morphodynamics*. John Wiley & Sons Ltd, Chichester, pp. 204-229.

McCave, I.N., Manighetti, B. and Robinson, S.G., 1995. Sortable silt and fine sediment size/composition slicing: Parameters for paleocurrent speed and paleoceanography. *Paleoceanography*, 10(3): 593-610.

McComb, P., Gorman, R., Black, K. and Kun, A.L., 2001. Measuring directional wave spectra using the 3D-ACM WAVE on fixed and taut-wire moorings. *IEEE Journal of Oceanographic Engineering*, 26(2): 171-180.

Miche, R., 1944. Undulatory movements of the sea in constant and decreasing depth. *Ann. de Ponts et Chaussees*, May-June, July-August: 25-78, 131-164, 270-292, 269-406.

Miller, R.L., 1976. Role of vortices in surf zone prediction: sedimentation and wave forces. *Social and Economical Paleontology and Mineralogy*, 24: 234-245.

Mitchener, H. and Torfs, H., 1996. Erosion of mud/sand mixtures. *Coastal Engineering*, 29: 1-25.

Möeller, I., Spencer, T., French, J.R., Leggett, D.J. and Dixon, M., 1999. Wave transformation over salt marshes: A field and numerical modelling study from North Norfolk, England. *Estuarine, Coastal and Shelf Science*, 49: 411-426.

Muir Wood, A.M., 1969. *Coastal Hydraulics*. MacMillan, London, England.

Neilson, C.G., 1998. *Wave Generation in a Large Intertidal Estuary*. MSc (Tech) Thesis, University of Waikato, Hamilton, New Zealand, 180 pp.

Nichols, M.M. and Biggs, R.B., 1985. Estuaries. In: R.A. Davis (Editor), *Coastal Sedimentary Environments*. Springer Verlag, New York, pp. 716 p.

Nielsen, P., 1981. Dynamics and geometry of wave-generated ripples. *Journal of Geophysical Research*, 86(C7): 6467-6472.

Nielsen, P., 1984. Field measurements of time-averaged suspended sediment concentrations under waves. *Coastal Engineering*, 8: 51-72.

Nielsen, P., 1986. Suspended sediment concentrations under waves. *Coastal Engineering*, 10: 23-31.

Nielsen, P., 1990. Coastal bottom boundary layers and sediment transport. In: P. Bruun (Editor), *Port Engineering*. Gulf Publishing Co., Houston, Texas, pp. 560-585.

Nielsen, P., 1992. *Coastal Bottom Boundary Layers and Sediment Transport*, 1st Edition. Advanced Series on Ocean Engineering, 4. World Scientific Publishing Co., Singapore, 324 pp.

Ogston, A.S. and Sternberg, R.W., 2002. Effect of wave breaking on sediment eddy diffusivity, suspended-sediment and longshore sediment flux profiles in the surf zone. *Continental Shelf Research*, 22(4): 633-655.

Osborne, P.D. and Greenwood, B., 1992. Frequency dependent cross-shore suspended sediment transport. 2. A barred shoreface. *Marine Geology*, 106: 25-51.

Pejrup, M., 1986. Parameters affecting fine-grained suspended sediment concentrations in a shallow micro-tidal estuary, Ho Bugt, Denmark. *Estuarine, Coastal and Shelf Science*, 22: 241-254.

Postma, H., 1961. Transport and accumulation of suspended matter in the Dutch Wadden Sea. *Netherlands Journal of Sea Research*, 1(1/2): 148-190.

Postma, H., 1967. Sediment transport and sedimentation in the estuarine environment. In: G.H. Lauff (Editor), *Estuaries*. American Association for the Advancement of Science, Washington D.C., pp. 757.

Reineck, H.E, 1967. Layered sediments of tidal flats, beaches, and shelf bottoms of the North Sea. In: G.H. Lauff (Editor), *Estuaries*. American Association for the Advancement of Science, Washington D.C., pp. 757.

Ridd, P. and Larcombe, P., 1994. Biofouling control for optical backscatter suspended sediment sensors. *Marine Geology*, 116: 255-258.

Ris, R.C., Holthuijsen, L.H. and Booij, N., 1994. A spectral model for waves in the near shore zone. In Proceedings of: *The 24th Conference on Coastal Engineering*: 68-78, B.L. Edge (Editor). American Society of Civil Engineers, New York.

Ryan, N.M. and Cooper, J.A.G., 1998. Spatial variability of tidal flats in response to wave exposure: examples from Strangford Lough, Co, Down, Northern Ireland. In: K.S. Black, D.M. Paterson and A. Cramp (Editors), *Sedimentary Processes in the Intertidal Zone*. Geological Society Special Publications. The Geological Society, London, pp. 221-230.

Sanford, L.P., 1994. Wave-forced resuspension of Upper Chesapeake Bay muds. *Estuaries*, 17(1b): 148-165.

Sarre, R., 1988. Aeolian sand drift from the intertidal zone on a temperate beach: potential and actual rates. *Earth Surface Processes and Landforms*, 14: 247-258.

Schoellhamer, D.H., 1995. Sediment resuspension mechanisms in Old Tampa Bay, Florida. *Estuarine, Coastal and Shelf Science*, 40: 603-620.

Sheng, J. and Hay, A.E., 1988. An examination of the spherical scatterer approximation in aqueous suspensions of sand. *Journal of the Acoustical Society of America*, 83(2): 598-610.

Sheng, J. and Hay, A.E., 1995. Sediment eddy diffusivities in the nearshore zone, from mulitfrequency acoustic backscatter. *Continental Shelf Research*, 15(2/3): 129-147.

Short, A.D., 1999. Wave-dominated beaches. In: A.D. Short (Editor), *Handbook of Beach and Shoreface Morphodynamics*. John Wiley and Sons Ltd, Chichester, pp. 173-203.

Sleath, J.F.A., 1978. Measurements of bed-load in oscillatory flow. *Journal of Waterways, Harbors, and Coastal Engineering Divission*, 104(WW4): 291-307.

Sobey, R.J., Chandler, B.D. and Harper, B.A., 1990. Extreme waves and wave counts in a hurricane. In Proceedings of: *Coastal Engineering*, 1: 358-370, B.L. Edge (Editor). ASCE, Delft, The Netherlands.

SonTek Inc., 1997. *ADV Operation Manual*. San Diego.

Soulsby, R.L., 1997. *Dynamics of Marine Sands*. Thomas Telford Publications, London, 249 pp.

Soulsby, R.L. and Whitehouse, R.J.S., 1997. Threshold of sediment motion in coastal environments. In Proceedings of: *Pacific Coasts and Ports: The 13th Australasian Coastal and Ocean Engineering Conference*, 1: 149-154. Centre for Advanced Engineering, Christchurch, New Zealand.

Sutherland, T.F., Lane, P.M., Amos, C.L. and Downing, J., 2000. The calibration of optical backscatter sensors for suspended sediment of varying darkness levels. *Marine Geology*, 162: 587-597.

Swart, D.H., 1974. *Offshore sediment transport and equilibrium beach profiles*. Deflt Hydraulics Lab. Publ. 131.

Tayfun, M.A., 1981. Breaking-limited wave heights. *Journal of Waterway, Port, Coastal and Ocean Engineering*, 107(2): 59-69.

Thorne, P.D., Hardcastle, P.J. and Soulsby, R.L., 1993. Analysis of acoustic measurements of suspended sediments. *Journal of Geophysical Research*, 98(C1): 899-910.

Thorne, P.D., Vincent, C.E., Hardcastle, P.J, Rehman, S. and Pearson, N., 1991. Measuring suspended sediment concentration using acoustic backscatter devices. *Marine Geology*, 98: 7-16.

Thornton, E.B. and Guza, R.T., 1983. Transformation of wave height distribution. *Journal of Geophysical Research*, 88(C10): 5925-5938.

Tonkin and Taylor, 1986. *Manukau Harbour Resources Study*. Manukau Harbour Maritime Planning Authority, Auckland.

van Straaten, L.M.J.U and Kuenen, Ph.H, 1958. Tidal action as a cause of clay accumulation. *Journal of Sedimentary Petrology*, 28(4): 406-413.

Vant, W.N., 1995. *Water quality survey of Manukau Harbour: Seventh annual report*. Consultancy Report. ARC301/7, NIWA, Hamilton.

Wallace, S. and Cox, R., 1997. Seagrass and wave hydrodynamics. In Proceedings of: *Pacific Coasts and Ports: The 13th Australasian Coastal and Ocean Engineering Conference*, 1: 69-73. Centre for Advanced Engineering, Christchurch, New Zealand.

Ward, L.G., Kemp, W.N. and Boynton, W.R., 1984. The influence of waves and sea grass communities on suspended particulates in an estuarine embayment. *Marine Geology*, 59: 85-103.

Webb, M.P. and Vincent, C.E., 1999. Comparison of time-averaged acoustic backscatter concentration profile measurements with existing predictive models. *Marine Geology*, 162: 71-90.

White, T.E., 1988. Status of measurement techniques for coastal sediment transport. *Coastal Engineering*, 35: 17-45.

Wiegel, R.L., 1964. *Oceanographical Engineering*. Theoretical and Applied Mechanics Series. Prentice-Hall, New York, 532 pp.

Williams, J.J., Bell, P.S., Thorne, P.D., Trouw, K., Hardcastle, P.J. and Humphery, J.D., 2000. Observed and predicted vertical suspended sediment concentration profiles and bedforms in oscillatory-only flow. *Journal of Coastal Research*, 16(3): 698-708.

Wright, L.D., Short, A.D. and Green, M.O., 1985. Short-term changes in the morphodynamic states of beaches and surf zones: an empirical predictive model. *Marine Geology*, 62: 339-364.

Xu, J.P., 1997. Converting near-bottom OBS measurements into suspended sediment concentrations. *Geo-Marine Letters*, 17: 154-161.

Young, I.R. and Verhagen, L.A., 1996. The growth of fetch limited waves in water of finite depth: Part 1. Total energy and peak frequency. *Coastal Engineering*, 29: 47-78.

Appendix Index

CURRENT METERS

Sensor Type	Manufacturer	Model	Sampling volume	Sampling rate Δt (s)	Portrait
EMCM	Marsh-McBirney [Ξ]	MMI	~$8x10^2$ cm^3 [⌖] Sensor ∅ = 5 cm	0.25	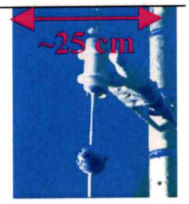
EMCM	InterOcean	S4A, S4DW	$1.2x10^5$ cm^3 [¤] Sensor ∅ = 25 cm	0.5	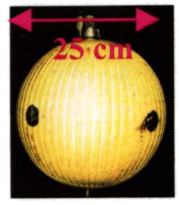
Acoustic (direct path)	Falmouth Scientific	3D-ACM WAVE	$2.9x10^3$ cm^3 [✦] Non-intrusive	0.186567 (5.36 Hz)	
Acoustic (doppler)	Sontek	Acoustic Doppler Velocimeter (ADV)	0.3 cm^3 [♌] Non-intrusive	0.2, 0.1 [†]	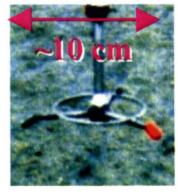

Table A1.1: Attributes of current meters used in this study. [Ξ]*sensor used on Alice.* [†] *sampling rates of 0.1 and 0.2 s used in this study.* [⌖] *estimate based on Edelman (2000) and Guza et al., (1988);* [¤]*(Edelman, 2000);* [✦]*(Falmouth Scientific Inc., 1998);* [♌]*(SonTek Inc., 1997).*

PRESSURE SENSORS

Sensor Type	Manufacturer	Model	Instrument size	Sampling rate Δt (s)	Portrait
Strain gauge (Adara)	NIWA	Dobie-O	11 x 20 cm	0.25	
Strain gauge (Druck)	NIWA	Dobie-A	16 x 35 cm	0.25	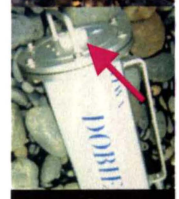
Strain gauge	InterOcean	S4A, S4DW	15 x 9 cm	0.5	
Silicon resonant oscillator (Druck)	Falmouth Scientific	3D-ACM WAVE	16 x 60 cm *or* 16 x 20 cm†	0.186567 (5.36 Hz)	
Quartz oscillator	Paroscientific[Ξ]		9 x 15 cm	0.25	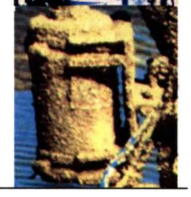

Table A1.2: Attributes of pressure sensors used during this study. Adara and Druck are pressure sensor manufacturers. [Ξ]sensor used on Alice. [†]3D-ACM WAVE dimensions when countersunk, as shown in portrait. Arrows indicate the location of pressure sensors on instrument housings.

Sensor/ instrument	Manufacturer	Model	Sampling volume	Sampling rate Δt(s)	
Acoustic Backscatter Sensor (ABS)	Aquatec electronics	ABS [Ξ]	Up to 128 1-cm-thick bins	0.20	
Optical Backscatter Sensor (OBS)	Downing & Associates	OBS-3 [Ξ,*]	~3 cm^3	0.25	
Automatic pump sampler	University of Waikato	Zelda	~2000 cm^3 (2 L)	15 s / sample	
Manual pump sampler	Purpose built		500 cm^3 (0.5 L)	9 s / sample	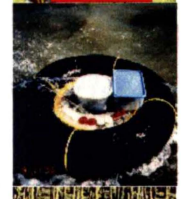
Sediment traps	Purpose built		Aspect ratio		
Alice traps			10		
Bed traps			6.5		

Table A1.3: Instruments used to collect data or physical samples for estimating SSC.

[Ξ] *The ABS is mounted on Alice while OBSs[*] are mounted on Alice and Dobie-o's.*

Appendix II: Sampling Strategies

TURBID FRINGE

Instrument	Sensor Elevation z (cm)	On Time (min:sec)	Cycle time (min)	Δt (s)
ADV	11	18:00	20	0.04
OBS	12	18:00	20	0.25
Dobie-A	0	06:49.6	10	0.20
Pump Sampler	11	00:10	10	

Table A2.1: Turbid Fringe Experiment sampling strategy. z is the sensor elevation above the bed, cycle time is the interval between the start of each burst and Δt is the sampling frequency in seconds.

BIMODAL-SIZE SUSPENSION

Alice Sensor	Sensor Elevation z (cm)	On time (min:sec)	Cycle time (min)	Δt (s)
EMCM	21, 55, 100, 167	08:32	60	0.25
Paroscientific	120	08:32	60	0.25
OBS	36, 76, 114, 193	08:32	60	0.25
ABS	120	10:00	60	0.20
Dobie-A	0	06:49.6	60	0.20

Table A2.2: Sampling strategy for Bimodal-size Suspension Experiments. Concentration estimates were made in 1-cm-thick bins using the ABS and at four locations using OBSs.

BIOFOULING

Instrument	Sensor Elevation z (cm)	On time (min:sec)	Cycle time (min)	Δt (s)
Dobie-A	0	04:16	30	0.25
OBS (unbrushed)	60	01:00	30	0.25
OBS (brushed)	60	01:00	30	0.25
Pneumatic brush	60	00:05	30	

Table A2.3: Sampling strategy for instruments deployed in the Biofouling Experiment.

PRESSURE-VELOCITY

1. Okura Estuary

Alice Sensor	Sensor Elevation z (cm)	On time (min:sec)	Cycle time (min)	Δt (s)
EMCM	14, 46, 82, 116	04:16	30	0.25
Paroscientific	25	04:16	30	0.25
ABS	60	05:00	30	0.20

Table A2.4.1: Sampling details for Green and MacDonald's (2001) Okura deployment. Estimates of concentration were made by the ABS in 1-cm-deep bins down to the bed.

2. Wiroa (estuarine)

Instrument	Orientation	Sensor Elevation (cm) z_p	Sensor Elevation (cm) z_u	On time (min:sec)	Cycle time (min)	Δt (s)
3D-ACM	vertical	0	16	08:00	15	0.18657 (5.36Hz)
3D-ACM	horizontal†	25	25	08:00	15	0.20
Dobie-A	vertical	17.5	n/a	06:49.6	15	0.20
Dobie-A	horizontal*	12	n/a	06:49.6	15	0.20

*Table A2.4.2: Sampling parameters, sensor elevations and orientation. †3D-ACM mounted with the pressure transducer facing into the waves. * This Dobie was moved during the experiment such that the pressure sensor was facing in one of three directions relative to the wave approach: into the waves, away from the waves and side on to the waves.*

3. Mangawhai (open coast)

Sensor	Sensor Elevation z (cm)	Δt (s)	On time (min:sec)		Cycle time (min)	
			12-m depth	7-m depth	12-m depth	7-m depth
EMCM	29,64,110,177	0.25	8:32	17:04	90	60
Paroscientific	120	0.25	8:32	17:04	90	60
ABS	120	0.20	10:00	10:00	90	60
Video	120	n/a	00:30	00:30	30	30

Table A2.4.3: Sampling details for Green's (1999) Mangawhai deployment. Δt is the sampling interval. IBB is the interval between bursts. Estimates of concentration were made by the ABS in 1-cm-deep bins down to the bed.

4. Taranaki (open coast)

Instrument	Sensor Elevation (cm)* z_p	z_u	On time (min:sec)	Cycle time (min)	Δt (s)
3D-ACM	571 (209)	555 (225)	18:00	60	0.18657 (5.36Hz)
3D-ACM	575 (205)	559 (221)	18:00	60	0.18657 (5.36Hz)
S4DW	620.5 (159.5)	613 (167)	18:00	60	0.5
S4DW	620.5 (159.5)	613 (167)	18:00	60	0.5
S4A	619.5 (160.5)	612 (168)	18:00	60	0.5
Dobie-A	209.5 (570.5)	n/a	17:04	60	0.5
Dobie-A	209.5 (570.5)	n/a	17:04	60	0.5
Dobie-A	209.5 (570.5)	n/a	17:04	60	0.5
Tower transducer	156.6 (623.5)	n/a	18:00	20	0.5

*Table A2.4.4: * Sensor elevations are relative to the bed; figures in brackets are distances below the top of the upper horizontal cross-member. z_p is the pressure sensor elevation and z_u is current meter elevation.*

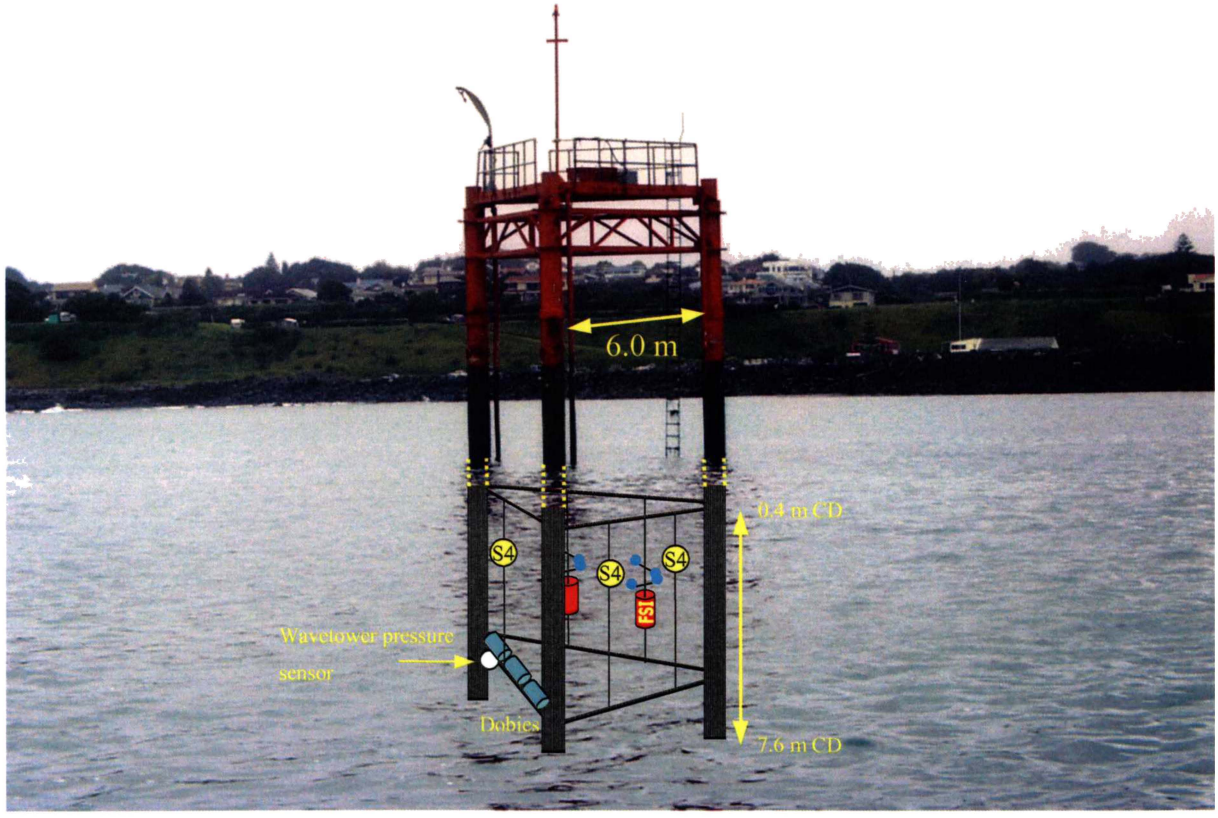

Figure A2.1: Schematic/photograph of the Port of Taranaki wave tower. Red cylinders depict the FSI 3D-ACMs, yellow spheres the InterOcean S4s, and blue cylinders the NIWA Dobies.

TRANSECT EXPERIMENT

Phase 1

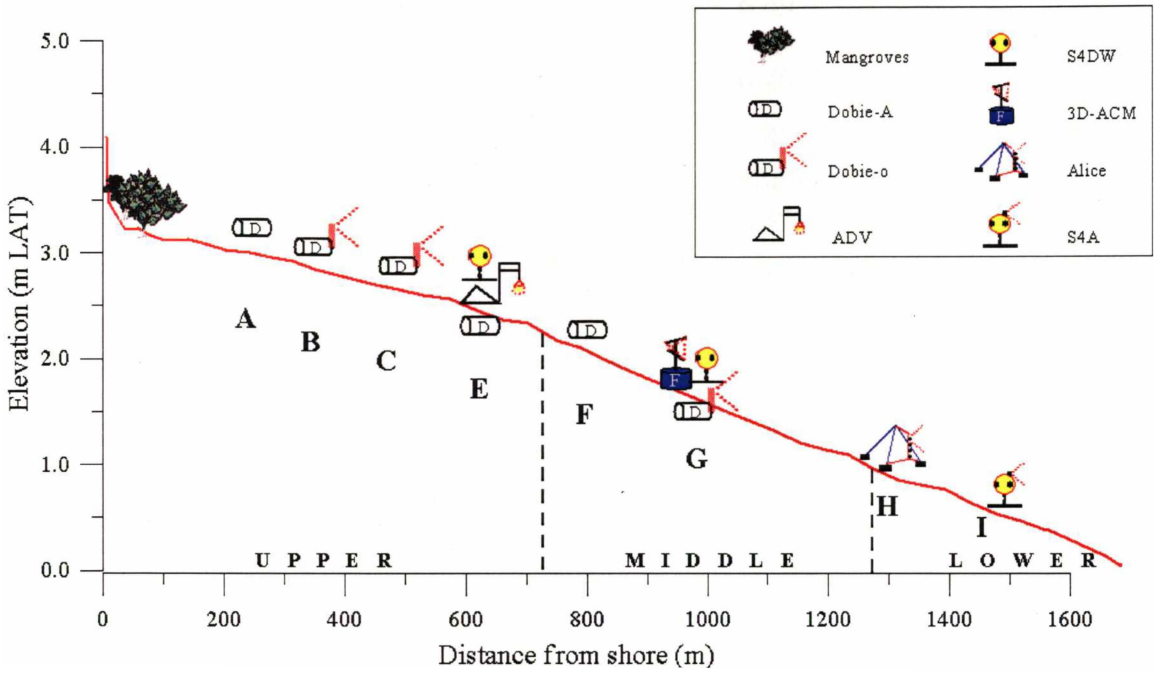

Figure A2.2: Location of instruments during Phase I of the Transect Experiment. The letters used to identify each station correspond to the last character of the station ID in Table A2.5.1.

Phase I Station ID	Instrument	Bed elevation*	Sensor elevation (cm)	On Time (min:sec)	IBB (min)	Δt (s)
W1A	Dobie-A	2.999	$z_p = 0$	6:49.6	30	0.20
W1B	Dobie-O	2.883	$z_p = 0$ $z_{OBS} = 10$	6:49.6	30	0.20
W1C	Dobie-O	2.717	$z_p = 0$ $z_{OBS} = 10$	6:49.6	30	0.20
W1E	ADV	2.467	$z_u = 11$	6:49.6	30	0.20
	Big Kahuna		$z_{OBS} = 24$	continuous		0.20
	Dobie-a		$z_p = 0$	6:49.6	30	0.20
	Manual Sampling		z = 10, 24, 45, 91	00:12	30	n/a
W1F	Dobie-A	2.065	$z_p = 0$	6:49.6	30	0.20
W1G	Dobie-O	1.59	$z_p = 0$ $z_{OBS} = 10$	6:49.6	30	0.20
	3D-ACM*		$z_p = 15$ $z_u = 31$	09:00	30	0.186567 (5.36 Hz)
	S4DW		$z_p = 34$ $z_u = 41.5$	05:00	30	0.50
W1H	Alice	0.792	Refer Table A2.5.3			
W1I	S4A‡	0.55	$z_p = 34$ $z_u = 41.5$	01:00‡ 05:00	15 30	0.50

*Table A2.5.1: Instrument deployment details. *denotes elevations (*m*) above Lowest Astronomical Tide datum (LAT). Sensor elevation (z) is the distance above the bed and subscripts* p, u *and* OBS *refer to pressure, velocity, and optical backscatter sensor elevations, respectively. ‡The S4A was set to run dual-mode, which is where two separate sampling strategies are run simultaneously – a 1-minute average every 15 minutes and a 5-minute burst every 30 minutes, in this case. * 3D-ACM WAVE, hereinafter referred to as 3D-ACM.*

Phase 2

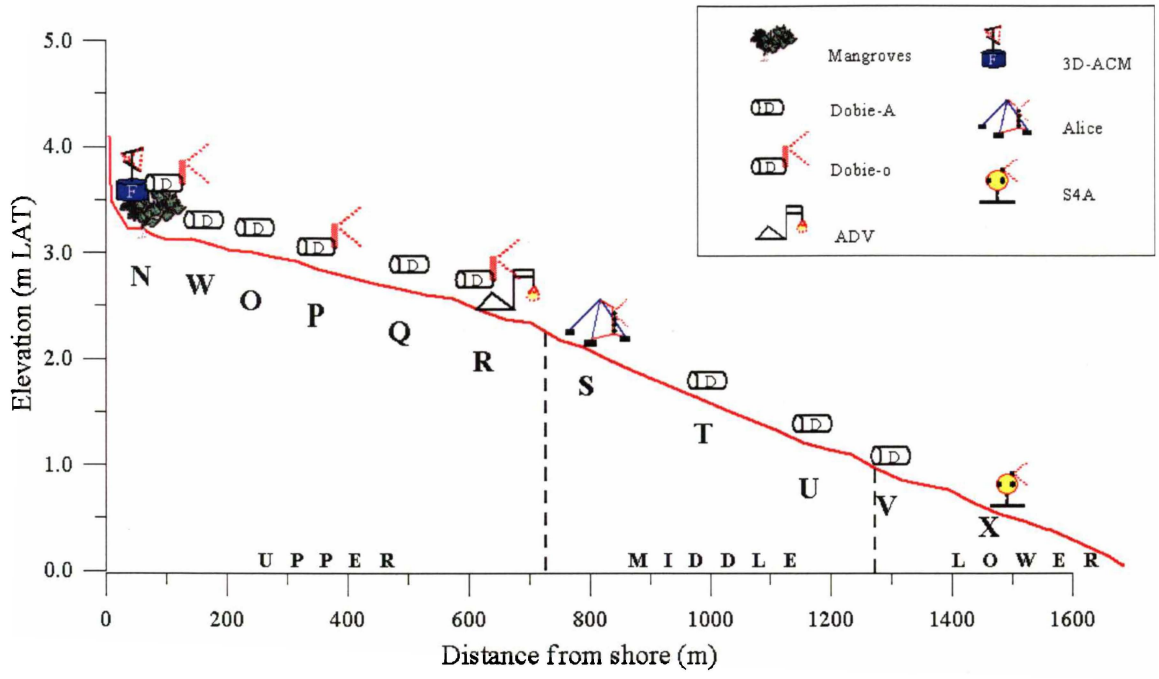

Figure A2.3: Location of instruments during Phase II of the Transect Experiment. The letters used to identify each station correspond to the last character of the station ID in Table A2.5.2.

Phase II Station ID	Instrument	Bed elevation*	Sensor elevation (cm)	On Time (min:sec)	IBB (min)	Δt (s)
W2N	Dobie-O	3.359	$z_p = 0$ $z_{OBS} = 10$	6:49.6	30	0.20
	3D-ACM*	3.364	$z_p = 6$ $z_u = 22$	09:00	30	0.186567 (5.36 Hz)
W2W	Dobie-A	not surveyed	$z_p = 0$	6:49.6	30	0.20
W2O	Dobie-A	2.999	$z_p = 0$	6:49.6	30	0.20
W2P	Dobie-O	2.883	$z_p = 0$ $z_{OBS} = 10$	6:49.6	30	0.20
	3D-ACM*	2.895	$z_p = 17$ $z_u = 33$	09:00	30	0.186567 (5.36 Hz)
W2Q	Dobie-A	2.717	$z_p = 0$	6:49.6	30	0.20
W2R	ADV	2.467	$z_u = 11$	6:49.6		0.10
	Dobie-O	2.467	$z_p = 0$ $z_{OBS} = 10$	6:49.6	30	0.20
W2S	Alice	2.065	Refer Table A2.5.3			
W2T	Dobie-A	1.59	$z_p = 0$	6:49.6	30	0.20
W2U	Dobie-A	not surveyed	$z_p = 0$	6:49.6	30	0.20
W2V	Dobie-A	0.792	$z_p = 0$	6:49.6	30	0.20
W2X	S4A‡	0.55	$z_p = 34$ $z_u = 41.5$	01:00‡ & 05:00	15 30	0.5

*Table A2.5.2: Instrument deployment details. *denotes elevations (m) above Lowest Astronomical Tide datum (LAT). Sensor elevation (z) is the distance above the bed and subscripts* p, u *and* OBS *refer to pressure, velocity, and OBS elevations, respectively. ‡The S4A was set to run dual-mode, which is where two separate sampling strategies are run simultaneously – a 1-minute average every 15 minutes and a 5-minute burst every 30 minutes, in this case. * 3D-ACM WAVE, hereinafter referred to as 3D-ACM.*

Alice Sensor	Sensor Elevation (cm)	On time (min:sec)	IBB (min)	Δt (s)
EMCM	13.5, 45.5, 82, 115.5	04:16	30	0.25
Paroscientific	25	04:16	30	0.25
OBS	18, 50, 124	04:16	30	0.25
ABS	45	05:00	30	0.20
Sonar*			30	

*Table A2.5.3: Sampling strategy for sensors on Alice during the Transect Experiment. The ABS sampled 64 1-cm-thick bins meaning that the last 12–20 bins were located below the bed. *An Imagenex 675 kHz sonar gave planimetric and profile images of the sea bed.*

Appendix III: Instrument Calibrations

This appendix describes the calibration procedures performed for Marsh-McBirney (MMI) electromagnetic current meters and Dobie, S4 and 3D-ACM pressure sensors.

A3.1 Zero-offset tests for Marsh-McBirney current meters

The zero-offset for each MMI current meter was determined by immersing the sensors (one at a time) in a bucket of still water. The output signals (V_x and V_y) were recorded for a period 10-s with a sampling interval of 1 s (Table A3.1). Velocity is adjusted accordingly.

	X1	Y1	X2	Y2	X3	Y3	X4	Y4
10-s mean	-0.52	0.86	-0.51	0.36	-0.88	-0.69	1.25	0.22

Table A3.1: MMI zero-offsets (x- and y-axis) obtained from 10-s averages of the velocity readings (cm/s) in still water.

A3.2 Static calibration for pressure sensors

Two static calibrations were performed. Prior to the Transect Experiment only prototype Dobie-O's were calibrated. Dobie-A was calibrated as described below but this was done by the manufacturer (NIWA). The 3D-ACMs were factory calibrated and on their maiden deployment and thus were not calibrated prior to deployment. In any case, the chamber used for pre-experiment calibrations was too small to use for calibrating the 3D-ACMs and S4s. Subsequently the S4A and one 3D-ACM were checked using a newer and larger chamber shown in Figure A3.1. In both calibrations, an independently calibrated pressure sensor was mounted in the chamber wall.

Pre- and post-experiment calibrations followed the same procedure. Instruments were sealed in a water filled chamber and the pressure raised to the maximum desired pressure for calibration: ~4200 hPa for Dobie calibrations and ~2800 hPa for S4A and 3D-ACM calibration verifications. The chamber pressure was then released incrementally with a 5-min stop at each pressure stage. The calibration data (Figures A3.2 & A3.3) are 60-s averages made in the last minute of each 5-min interval. A lower pressure range was used for calibration verifications (S4 and 3D-ACM) which is more

appropriate for the shallow-water conditions in which the instruments were deployed and better resolution is achieved (i.e., data points are more closely spaced).

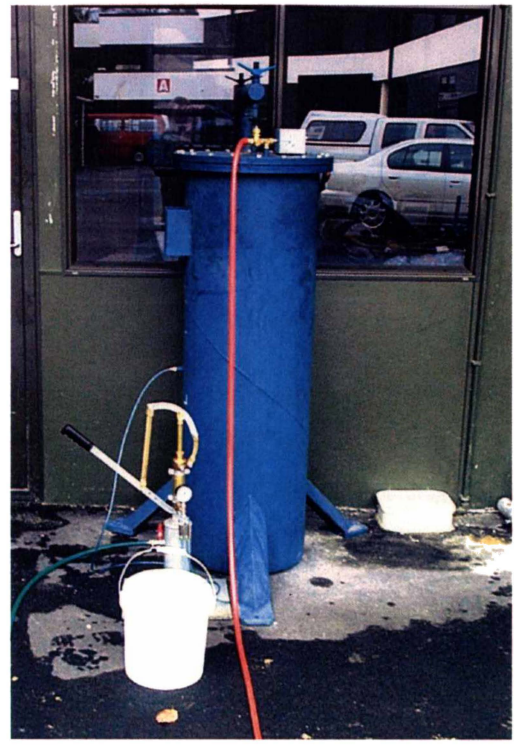

Figure A3.1: Chamber used for post-Transect Experiment calibrations. Photograph courtesy of Iain MacDonald.

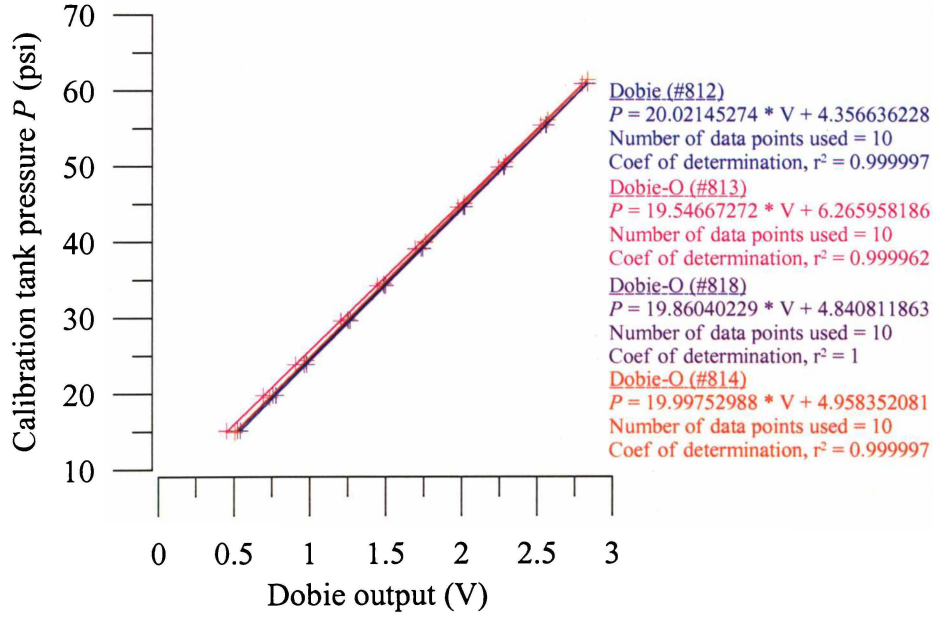

Figure A3.2: Dobie calibration data. V is the Dobie output (volts) and P is the chamber pressure in psi.

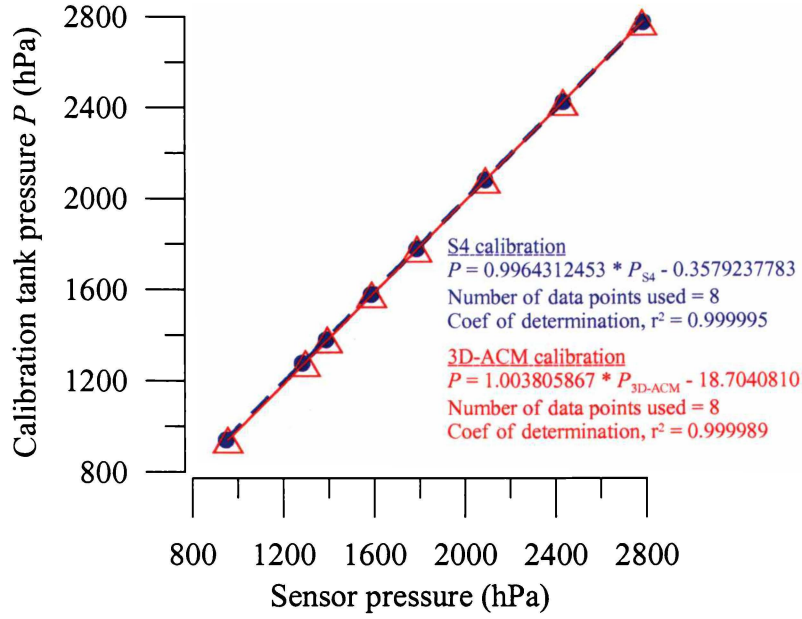

Figure A3.3: Verification of S4 and 3D-ACM pressure sensors using calibration tank. P is the pressure measured by the sensor mounted in the tank wall and P_{S4} and $P_{3D\text{-}ACM}$ are the pressures measured by the S4 and 3D-ACM.

Appendix IV: Timeline of Instrument Operational Periods for the Transect Experiment

The following tables are time-lines for each instrument deployed on the Wiroa intertidal-flat during the Transect Experiment. The first three tables represent the first part of the experiment, and the forth table is from the second part of the experiment when instruments were relocated and additional Dobies were deployed.

Yellow-fill on the date labels indicates a maintenance visit (battery replacement and data offloads) to the site. Red-fill on the date label indicates a visit to the field site for the purposes of collecting suspended sediment samples with the pump system described in Section 2.3 and 2.4. Indicated on the tables are labels which represent the various instrument problems encountered:

Mem full

Instrument memory was filled before servicing. Instrument stopped logging.

Bat. monitor failure

The proto-type Dobie-O battery monitor failed and caused premature logging stop.

"obtime" logging error

Ongoing error in 3D-ACM due to hardware or firmware fault

Delay-start error

Ongoing error in 3D-ACM due to hardware or firmware fault

Failed (battery)

Power failure prior to instrument servicing

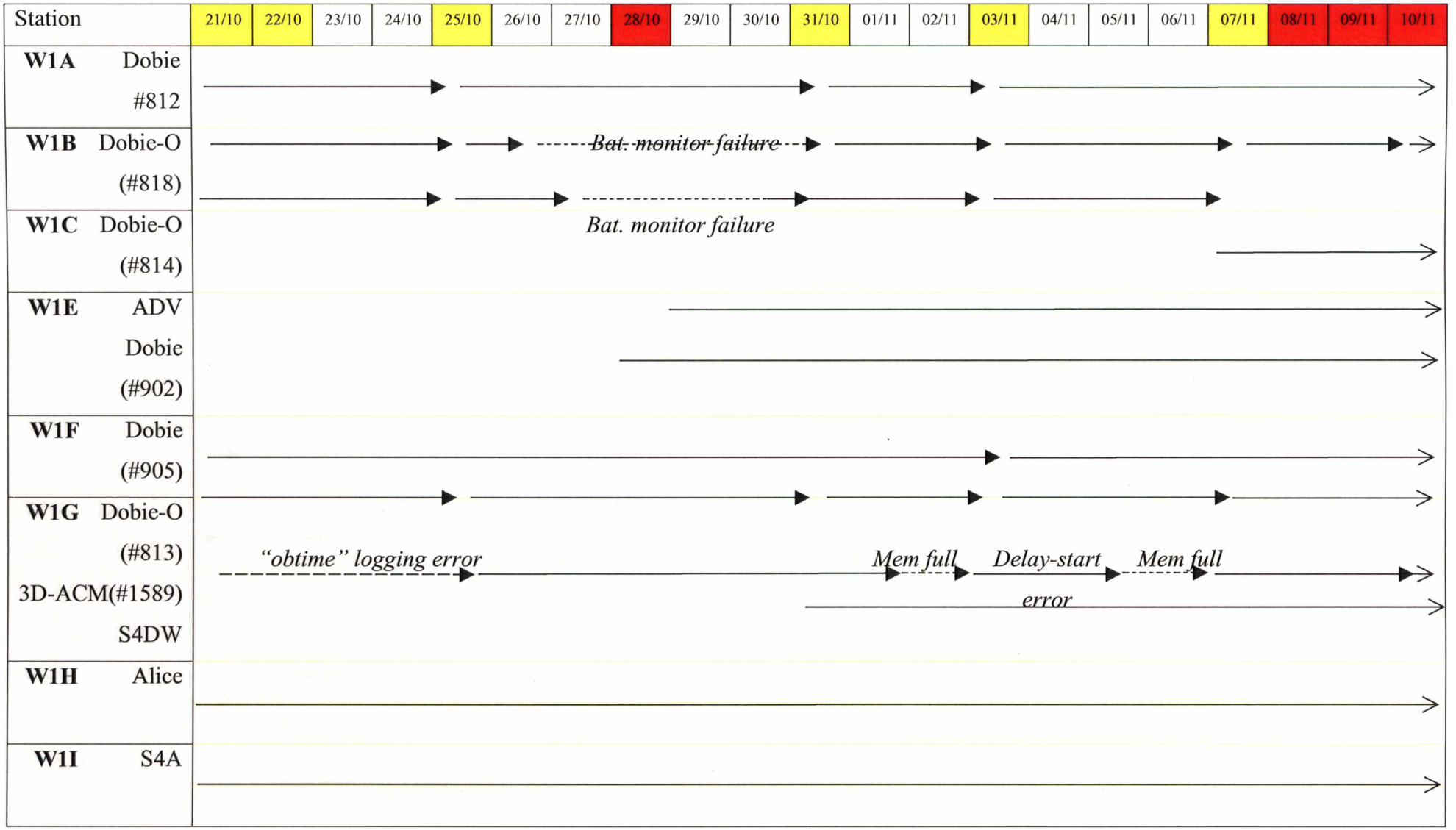
Station
21/10
22/10
23/10
24/10
25/10
26/10
27/10
28/10
29/10
30/10
31/10
01/11
02/11
03/11
04/11
05/11
06/11
07/11
08/11
09/11
10/11
W1A Dobie #812
W1B Dobie-O (#818)
Bat. monitor failure
W1C Dobie-O (#814)
Bat. monitor failure
W1E ADV Dobie (#902)
W1F Dobie (#905)
W1G Dobie-O (#813) 3D-ACM(#1589) S4DW
"obtime" logging error
Mem full
Delay-start error
Mem full
W1H Alice
W1I S4A

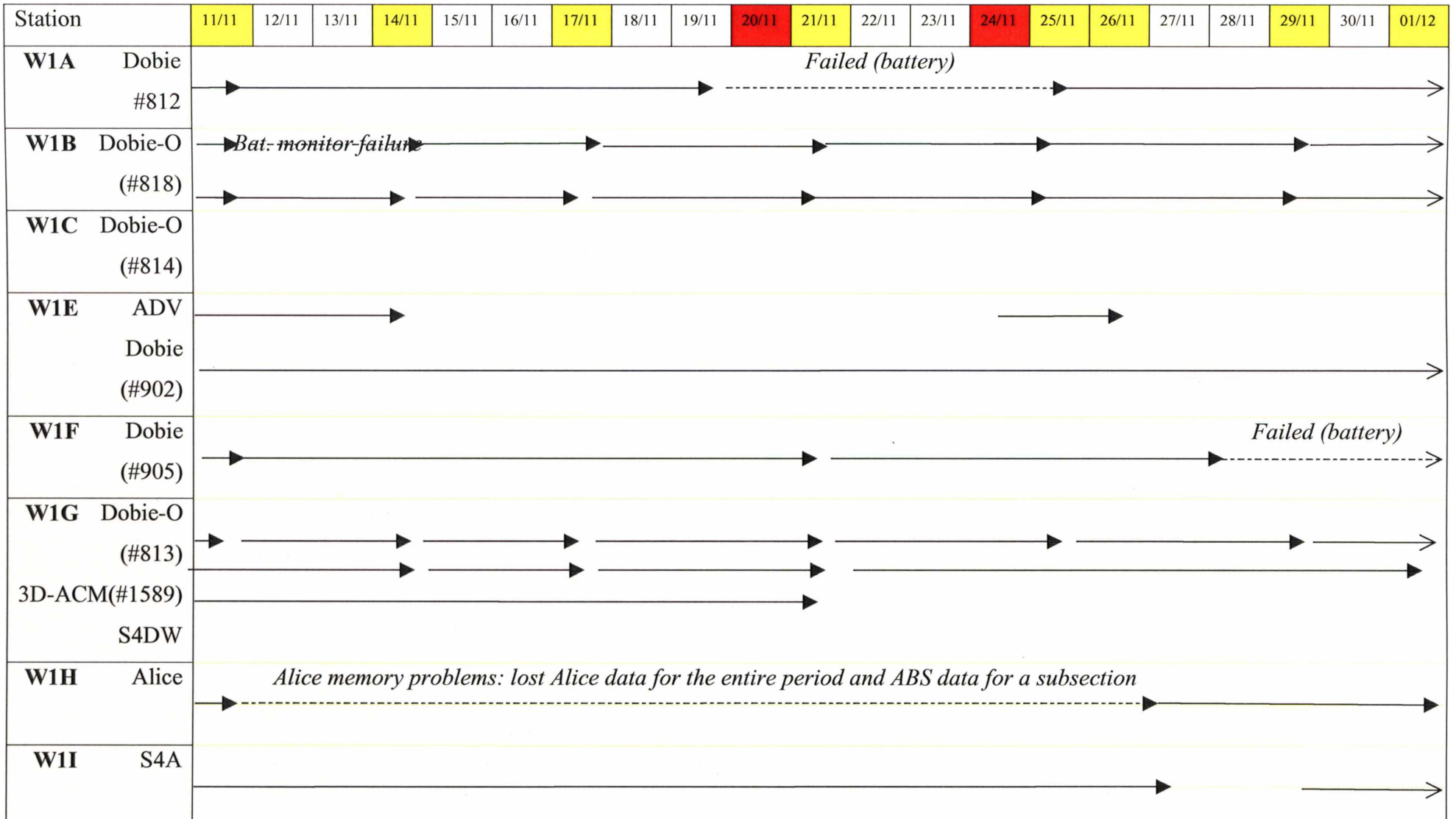
Station
11/11
12/11
13/11
14/11
15/11
16/11
17/11
18/11
19/11
20/11
21/11
22/11
23/11
24/11
25/11
26/11
27/11
28/11
29/11
30/11
01/12
W1A Dobie #812
Failed (battery)
W1B Dobie-O (#818)
Bat. monitor failure
W1C Dobie-O (#814)
W1E ADV Dobie (#902)
W1F Dobie (#905)
Failed (battery)
W1G Dobie-O (#813)
3D-ACM(#1589)
S4DW
W1H Alice
Alice memory problems: lost Alice data for the entire period and ABS data for a subsection
W1I S4A

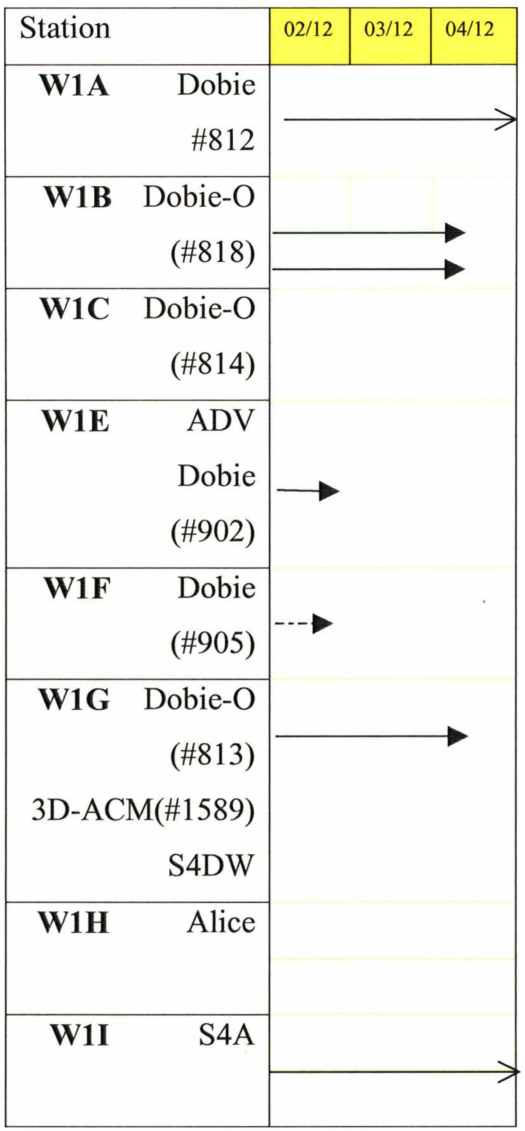
Station
02/12
03/12
04/12
W1A Dobie #812
W1B Dobie-O (#818)
W1C Dobie-O (#814)
W1E ADV Dobie (#902)
W1F Dobie (#905)
W1G Dobie-O (#813)
3D-ACM(#1589)
S4DW
W1H Alice
W1I S4A

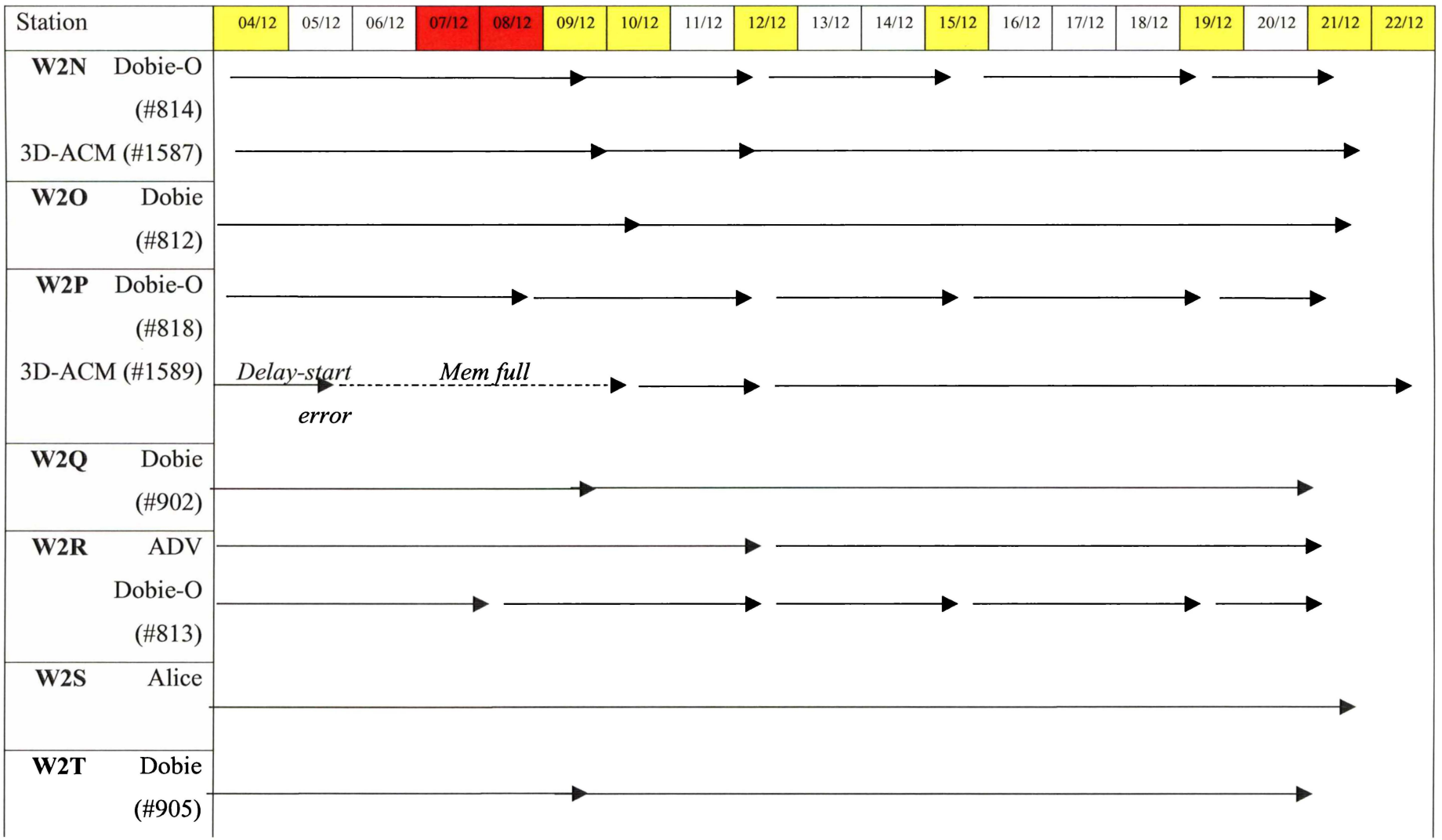
Station
04/12
05/12
06/12
07/12
08/12
09/12
10/12
11/12
12/12
13/12
14/12
15/12
16/12
17/12
18/12
19/12
20/12
21/12
22/12
W2N Dobie-O (#814)
3D-ACM (#1587)
W2O Dobie (#812)
W2P Dobie-O (#818)
3D-ACM (#1589)
Delay-start error
Mem full
W2Q Dobie (#902)
W2R ADV
Dobie-O (#813)
W2S Alice
W2T Dobie (#905)

W2U	Dobie (#911)	
W2V	Dobie (#908)	
W2W	Dobie (#912)	
W2X	S4A	

Appendix V: Wave direction and correction for horizontally displaced sensors

A5.1 Determination of wave propagation direction

The wave propagation axis, Φ_w, is defined as the axis of maximum variance in the filtered velocity data (see section 2.5.1) from each burst. The axis holding the maximum variance was determined by rotating the velocity components $\tilde{u}_{CM}(t)$ and $\tilde{v}_{CM}(t)$ from 0–180° at 1° increments. At each rotation the variance of the velocity component parallel to the axis of rotation ($\tilde{v}_{CM}(t)$) was recorded and the rotation axis with maximum variance taken as Φ_w.

In most coastal environments this is sufficient to identify the direction of incident wave travel $\bar{\phi}_w$ as the range of possible directions is limited to a 180° (or less) sector. However, on wide intertidal-flats waves may approach from any direction. For intertidal flats exposed only to locally generated waves, wind records and a first principles knowledge of wave refraction may be used to determine wave direction in most cases, unless bathymetry is particularly complex.

At the Wiroa intertidal flat, $\bar{\phi}_w$, was determined by investigating diagnostic plots (e.g., Figure A5.1) which include graphical and text information pertaining to Φ_w, $\tilde{u}_{CM}(t)$, $\tilde{v}_{CM}(t)$, wind speed and direction, $\bar{h}$, $\bar{T}$, residual (mean) velocity vector and shoreline orientation. In most cases it was not difficult to determine the direction on the wave propagation axis which waves were travelling towards[3]. Where $\bar{\phi}_w$ was not obvious and/or if the velocity data were scattered such that direction was not obvious, bursts were not considered for analysis.

---

[3] To maintain consistency with velocity data, the wind vector in Figure A5.2 and the wave direction $\bar{\phi}_w$ are defined as the bearing in the direction of travel.

A5.2 Correction of pressure–velocity phase, $\varphi_{h\text{-}Uw}$, for horizontally displaced sensors

Comparison of pressure and velocity data requires that both sensors are located at the same horizontal coordinate, which is the case for 3D-ACM and S4 instruments (within a few centimetres), but is not the case for Alice. On Alice, pressure and velocity sensors are horizontally separated by a distance of 1.7 m. Thus, when making direct comparisons between pressure and velocity signals with Alice data there is an inherent phase lag between the two signals which is dependent on the direction of wave travel.

In order to correct for horizontal sensor displacement, the bearing between sensors was used to determine the actual horizontal offset associated with $\bar{\phi}_w$ for each burst of wave data (Figure A5.2) as follows. The offset distance for a given wave direction O_w is

$$O_w = \cos\alpha^* O_I$$

where O_I is the offset distance between sensors (1.7 m for Alice) and α^* is the angle between the bearing of $\bar{\phi}_w$ and the bearing between the sensors ϕ_I:

$$\alpha^* = \bar{\phi}_w - \phi_I$$

as pictorially shown in Figure A5.2.

The measured pressure–velocity phase $\varphi_{h\text{-}Uw}$ was then adjusted by adding the phase offset (°)

$$\varphi'_\omega = \left[\frac{O_w}{2\pi/k}\right] * 360$$

at each ω in the $\varphi_{h\text{-}Uw}$ spectrum. Note that when $\phi_I = \bar{\phi}_w \pm 90°$ wave crests arrive at the sensors simultaneously and φ'_ω is zero at all ω.

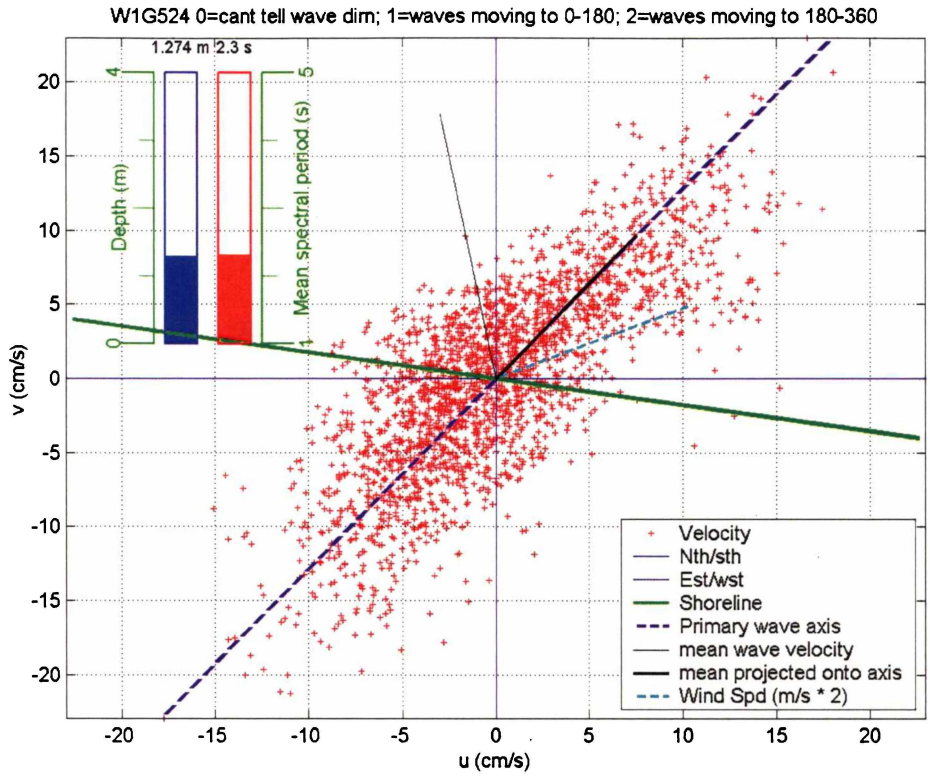

Figure A5.1: Example of diagnostic plot used for determining wave direction. Each burst of wave data was plotted in this way and wave direction was decided using: Φ_w *(purple dashed line) and wind speed and direction (pale blue dashed line).*

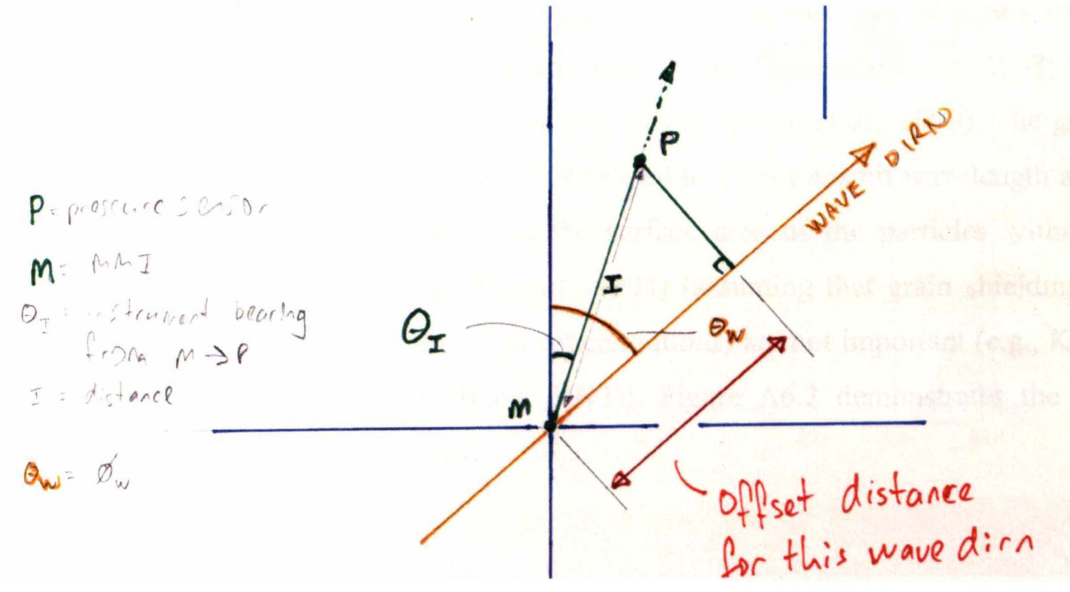

Figure A5.2: Schematic of geometric quantities used to determine the phase offset φ'_ω

Appendix VI: Suspended Sediment Concentration Measurement

A6.1 Suspended Sediment Concentration Measurement

Estimates of SSC were made from OBS data, ABS data and water samples (see section 2.5). Water samples were filtered using standard procedures (see Dolphin *et al.*, 1999) and the resulting concentration was expressed as the mass of sediment per fluid volume (mg/L). Estimates from OBS and ABS data can be problematic as backscatter is a function of both SSC and grain size, and calibration with native sediments is usually required. When suspended particle size is nonuniform and/or size varies with time, sensor response is partly due to the changes in the particle size distribution and consequently the raw data can be difficult to interpret (e.g., White, 1988; Ludwig and Hanes, 1990; Thorne, *et al.*, 1991; Conner and De Visser, 1992; Hay and Sheng, 1992; Thorne, *et al.*, 1993; Lynch, *et al.*, 1994; Bunt *et al.*, 1999).

OBS sensitivity (that is, voltage output per mg/L of suspended sediment; see Figure A6.1) has been shown to be five to ten times greater for silt than sand suspensions (Ludwig and Hanes, 1990; Conner and De Visser, 1992; Green and Boon, 1993; Black and Rosenberg, 1994; Xu, 1997; Battisto, *et al.*, 1999; Green *et al.*, 1999). The greater sensitivity to finer particles (Figure A6.1) is related to OBS transmit wavelength and to backscattering which is proportional to the surface area of the particles within the illuminated sampling volume (Lynch *et al.*, 1994) (assuming that grain shielding and multiple scattering (associated with high concentrations) are not important (e.g., Kineke and Sternberg, 1992; Green and Boon, 1993)). Figure A6.2 demonstrates the latter concept for sand and silt size ranges.

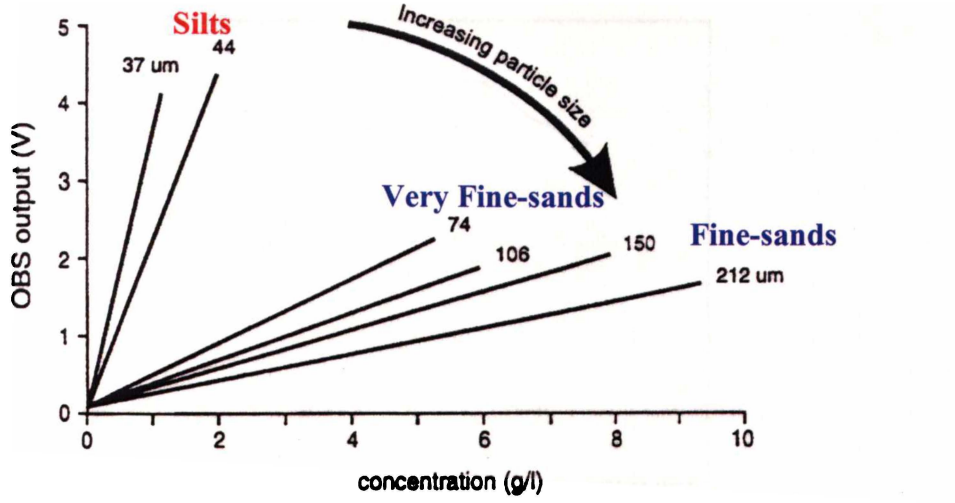

Figure A6.1: OBS sensitivity. Textural descriptions are from (Folk, 1968). Source: Bunt et al. (1999).

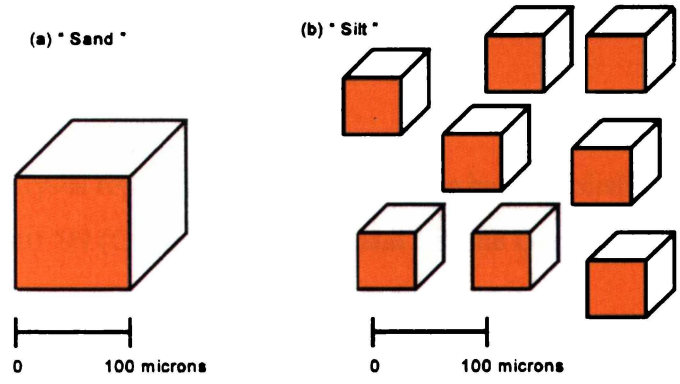

Figure A6.2: Comparison of the surface area of a sand particle (a) with silt particles (b) of the same combined mass. OBS response is proportional to surface area (orange) which is greater for a silt suspension than a sand suspension of the same volume/concentration. Source: Battisto et al. (1999).

For the ABS, variation in backscatter strength with grain size is described by the form factor (Figure A6.3) as investigated and described by Hay (1991), Hay and Sheng (1992) and Thorne *et al.* (1993). ABS sensitivity varies with acoustic frequency and is most sensitive for $k_{ABS}.a_s \sim 1$ (Lynch *et al.*, 1994), where k_{ABS} is the acoustic wavenumber and a_s is the particle radius. As the form function is nearly flat in the range $k_{ABS}.a_s \sim 1$ the ABS response there is approximately proportional to particle volume.

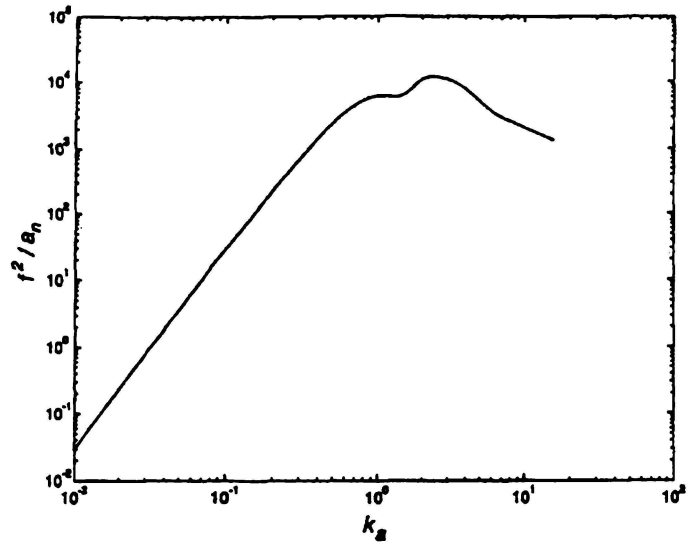

Figure A6.3: Form factor for ABS. Source: Lynch et al. (1994)

A6.4 Measuring mixed-size suspensions using optical and acoustic backscatter sensors

The results and analyses reported in this section have been published in the Proceedings of Coastal Sediments '99 (Green *et al.*, 1999) and Marine Geology (Green *et al.*, 2000).

Although Ludwig and Hanes (1990) recommended against the use of OBSs in environments with mixed sediment sizes, Green and Boon (1993) demonstrated that silt and sand fractions in a mixed suspension produce partial sensor responses as if each fraction were the only fraction present. Battisto *et al.* (1999) subsequently employed this concept to make estimates of SSC in a mixed size suspension where the partial response from one constituent was unchanging. As the partial response of each grain size is a function of the SSC and the OBSs sensitivity to that size, the partial response will decay in those size ranges for which the sensor is insensitive. As OBS and ABS are sensitive in different size regions (silts and sands respectively) it has been suggested that they could be used together in order to separately determine the silt and sand concentrations of a suspension (Thorne *et al.*, 1991; Green and Boon, 1993; Lynch *et al.*, 1994). Bimodal-size Suspension Experiments were conducted (see section 2.3.2) to test the performance of the OBS in measuring only the silt constituent and the ABS in measuring only the sand constituent. Area and volume size-analyses (Figure A6.8) suggest that Manukau Harbour suspensions are suitable for the testing and application of this technique.

Much of the following work has been presented at the Coastal Sediments'99 conference and published in those proceedings (refer Green *et al.*, 1999).

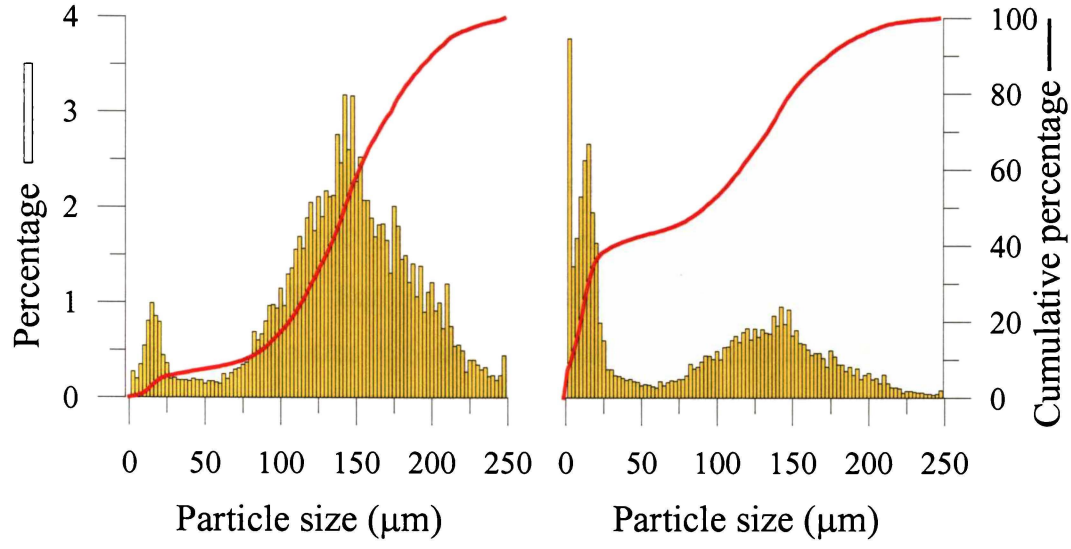

Figure A6.8: Comparison of grain size analysis by volume (left graph) and by area (right graph) for suspended sediment (trap) sample. In the volume analysis particles < 40 μm occupy around six percent of the total distribution whilst in the area analysis they occupy ~ 41 %. Consequently, although silts have a comparatively small mass/volume they register a larger OBS response than sands for a given mass/concentration.

Turbidity tank tests – OBS calibration

The aim of the OBS turbidity tank tests was to quantify sensitivity for the silt and sand fractions and then, assuming a partial response for each size fraction (following Green and Boon, 1993), investigate the competency of OBSs in measuring silt concentration in a mixed suspension. That is, can the OBS be used as a "silt meter" for mixed (silt:fine-sand) suspensions in Manukau Harbour?

OBS sensor response R is described by:

$$R = SC + O \qquad \text{(Eqn A6.1)}$$

where S is the sensitivity (V/[mg/L]) and R (V) initially varies linearly with concentration C, but becomes nonlinear at higher concentrations (> 10^4 mg/L; Kineke and Sternberg (1992)). O is the sensor offset. Using Green and Boon's observations

eqn A6.1 can be rewritten in terms of the constituent silt and sand concentrations, C_{silt}, C_{sand}, and sensitivities, S_{silt}, S_{sand}:

$$R = (S_{silt}C_{silt}) + (S_{sand}C_{sand}) + O \qquad \text{(Eqn A6.2)}$$

To determine S_{silt} and S_{sand} each OBS was calibrated in the turbidity tank (described in section 2.4.2) using Poutawa Channel bed sediments which had been wet sieved into silt (10-30 μm) and sand (100-200 μm) fractions. Eight concentrations were measured in the range 0–400 mg/L. Eqn A6.1 was then fitted to the data using a least-squares technique to give estimates of S and O for each sensor and each sediment. In each case the coefficient of determination (r^2) exceeded 0.99 and estimates of S_{silt} were approximately ten times greater than S_{sand}, as is commonly reported in the literature for 'silt:sand' comparisons (refer Section A6.1).

As the OBS is less sensitive to sand, simply ignoring the partial response to sand ($S_{sand}.C_{sand}$) in a 'silt:sand' suspension gives:

$$C_{silt,estimated} = \frac{(R-O)}{S_{silt}} \qquad \text{(Eqn A6.3)}$$

and an associated error due to any sand in suspension:

$$E_{silt} = \left[\frac{C_{silt,estimated}}{C_{silt,true}} - 1\right] * 100 \qquad \text{(Eqn A6.4)}$$

where

$$C_{silt,true} = \frac{(R - O - S_{sand}C_{sand})}{S_{silt}} \qquad \text{(Eqn A6.5)}$$

Eqn 5.4 then reduces to:

$$E_{silt} = 100\frac{C_{sand}}{C_{silt}}\frac{S_{sand}}{S_{silt}} \qquad \text{(Eqn A6.6)}$$

With the relative sensitivities known ($S_{sand}/S_{silt} \sim 0.1$), the ratio C_{sand}/C_{silt} required to generate given error was determined and some examples presented in Table A6.1. These results show that OBSs are relatively insensitive to sand in mixed suspensions and, with the exception of high C_{sand}/C_{silt} ratios (e.g., > 2), can be used as "silt meters", for Manukau sediments. Application of this technique requires knowledge of local suspended sediment sizes and their associated sensitivities.

C_{sand}/C_{silt}	0.1	1	10
E_{silt}	1 %	10 %	100 %

Table A6.1: Error generated for given ratios of C_{sand}/C_{silt} by ignoring the sand constituent and assuming $S_{sand}/S_{silt} \sim 0.1$

Turbidity tank tests – ABS

ABS measurement of backscattered acoustic pressure $<P^2>$ has been described previously in eqn 2.8 and, according to the ABS form factor, has greater sensitivity in the sand than silt size range for typical ABS frequencies (Sheng and Hay, 1988; Thorne *et al.*, 1991; Lynch *et al.*, 1994). Following Green and Boon's partial response model for OBS, similar consideration was made for the ABS: in a mixed-size suspension $<P^2>$ is the sum of the backscatter from each of the two size constituents, $<P^2_{sand}>$ and $<P^2_{silt}>$, as if they were the only constituents present:

$$\left\langle P^2 \right\rangle = \left\langle P^2_{sand} \right\rangle + \left\langle P^2_{silt} \right\rangle \qquad \text{(Eqn A6.7)}$$

where backscattered pressure is related to concentration in each bin as:

$$\left\langle P^2 \right\rangle = \frac{C_r c A_0^2}{a_s \rho_s} S^2_{a_s} B_r^2 \exp[-4\alpha_w r] \exp[-4 \int_0^r \alpha_s dr'] \qquad \text{(Eqn A6.8)}$$

for which eqn 2.8 is the inversion (terms are described previously in section 2.4.3). Collecting the system constant A_0 and sediment related terms together gives:

$$\frac{A_0^2 S_{a_s}^2}{a_s \rho_s} = \frac{\langle P^2 \rangle}{C_r c B_r^2 \exp[-4\alpha_w r] \exp[-4 \int_0^r \alpha_s dr']} \qquad \text{(Eqn A6.9)}$$

Eqn A6.9 was evaluated with C and $<P^2>$ determined in a series of turbidity tank tests separately using the sieved silt and sand fractions separately. Each test consisted of eight concentrations in the range 0–400 mg/L. The term $\exp[-4\int_0^r \alpha_s dr']$, which describes sound attenuation due to sediment, was assumed to be insignificant (i.e. =1). The ratio $[A_0^2 S_{a_{silt}}^2 / a_{silt}\rho_{silt}] / [A_0^2 S_{a_{sand}}^2 / a_{sand}\rho_{sand}]$ describes the relative sensitivity of each ABS frequency to the silt/sand size fractions (Table A6.2). The form function for the 1.97 MHz ABS has the most favourable relative sensitivity although sensitivity to sand and not silt is very encouraging for all three ABS frequencies.

ABS frequency	1.08 MHz	1.97 MHz	4.38 MHz
$\frac{A_0^2 S_{a_{silt}}^2 / a_{silt}\rho_{silt}}{A_0^2 S_{a_{sand}}^2 / a_{sand}\rho_{sand}}$	0.020	0.005	0.022

Table A6.2: The ratio $[A_0^2 S_{a_{silt}}^2 / a_{silt}\rho_{silt}] / [A_0^2 S_{a_{sand}}^2 / a_{sand}\rho_{sand}]$ for each ABS frequency, measured in turbidity tank tests, indicates the relative sensitivity of ABS to silt/sand suspensions. The silt and sand components of the ratio are calculated as the average of the eight estimates made in the turbidity tank

The percentage error in estimating $<P_{sand}^2>$ by simply ignoring $<P_{silt}^2>$ is then:

$$E_{sand} = \left[\frac{\langle P_{silt}^2 \rangle}{\langle P_{sand}^2 \rangle}\right] * 100 \qquad \text{(Eqn A6.10)}$$

and substituting with eqn. A6.8:

$$E_{sand} = \left(\frac{C_{silt}}{C_{sand}} \frac{A_0^2 S_{a_{silt}}^2 / a_{silt}\rho_{silt}}{A_0^2 S_{a_{sand}}^2 / a_{sand}\rho_{sand}}\right) * 100 \qquad \text{(Eqn A6.11)}$$

Sound attenuation due to sediment is again assumed insignificant and has been omitted in the formulation of eqn 5.11. Using the results from Table A6.2 in eqn A6.11 it is then

possible to calculate E_{sand} for ratios of C_{sand}/C_{silt} (A6.4). The error due to ignoring silt in a silt:sand suspension is very low, particularly for the 1.97 MHz ABS for which silt concentrations 20 times larger than sand concentrations yield only a 10% error. Thus, the 1.97 MHz ABS is the most successful 'suspended-sand meter' for effectively estimating fine-sand (100-200 μm) concentrations in silt:sand suspensions as the silts are essentially invisible to it. This is not unexpected as acoustic devices can only measure down to around 25 μm (Lynch *et al.*, 1994).

ABS frequency	E_{sand} = 1 %	E_{sand} = 10 %	E_{sand} = 100 %
1.08 MHz	0.5	5	50
1.97 MHz	2	20	200
4.38 MHz	0.45	4.5	45

Table A6.4: Ratios of C_{silt}/C_{sand} which generate specified errors for each ABS frequency.

Field data – Poutawa Channel

Field data from the Poutawa Channel deployment are summarised in Figure A6.9 and have been reported in detail in Green *et al.* (1999) and Green *et al.* (2000). C_{silt} and C_{sand}, which are based on OBS and ABS data, are fundamentally different, due to differences in the behaviour of sand and silt suspensions in the tidal channel.

ABS *C*-profile shapes are in agreement with a two-layer diffusion model for sand suspensions (Green *et al.*, 1999) and concentrations vary on a 6-h cycle, which is exactly phase and roughly proportional to the mean current $\overline{U}_{z=100}$ (Figure A6.9). *C*-profile shape and correlation between tidal currents, local bed shear and ABS concentration are consistent with the turbidity tank results show that the ABS is sensitive to sand in suspension, not silt.

The suspension profiles measured by the OBS array were vertically uniform, which implies a suspension of particles with a vanishingly small settling velocity, i.e., silt. The observed variation with water depth and current-direction was explained by the advection up and down the channel of a horizontal gradient of suspended silt (Green *et al.*, 2000). Toward the end of the flood tide 'clean' ocean water pushes silty water past the instrument station (fall in SSC in Figure A6.9) and up onto the intertidal flat. The return of the turbid suspension early in the ebb tide is due to Alice's close proximity to the intertidal flats (Figure 2.1). OBS estimates of SSC in the channel increased when silt

entrained by waves on adjacent intertidal flats was advected down the Poutawa Channel on the outgoing tide. The *C*-profile shape inferred from the OBS array and correlation with the tide demonstrates OBS measured the advection of a silt suspension, which is consistent with the turbidity tank results: OBS are sensitive to silt in suspension, not sand. However, OBS estimates of C_{silt} were in error near the bed during peak flow when C_{sand} became large.

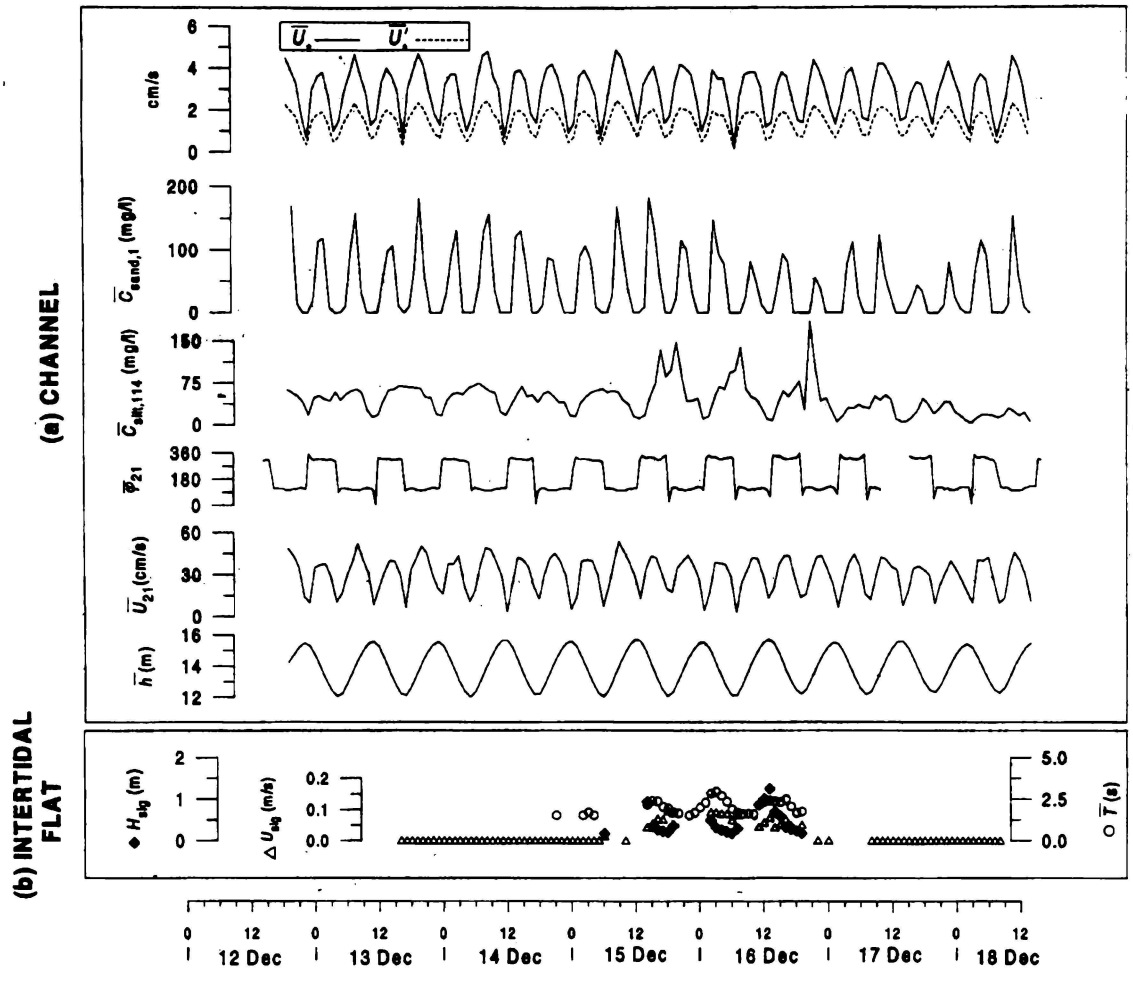

Figure A6.9: Bimodal-size Suspension Experiment time series from (a) the Poutawa Channel and (b) the adjacent intertidal flat. Source: Green *et al.*, (2000).

Appendix VII: Estuarine Wave Height Distributions

Although not used for sediment transport calculations, Rayleigh-based wave statistics were used for description and characterisation of estuarine waves. This appendix presents the results of an analysis of 658005 waves, which were measured by seven deployments of S4, 3D-ACM and Alice instruments, during the Transect Experiment.

A7.1 Definitions

The heights and periods of individual waves were determined using the time-series of sea-surface elevations $\eta(t)$ (see section 2.5.1). Each wave was defined by successive zero-upcrossings, the elapsed time between each crossing being the wave period, T_z, with wave height:

$$H_z = \eta_{max} - \eta_{min}$$

For identifying individual waves using zero-crossings is preferred to using successive wave crests or troughs because of irregularities in the sea-surface elevation (which is particularly relevant for choppy seas), while up-crossings and down-crossings are not considered to be significantly different if a large number of waves (e.g., 70–250 per burst for Transect Experiments) are sampled (IAHR, 1989).

A7.2 Wave height distributions

Longuet-Higgins (1952) demonstrated that heights of waves with a linear Gaussian surface and a narrow range of wave periods are described according to the single-parameter Rayleigh model. Subsequently, it has been shown that ocean wave heights are more or less Rayleigh distributed (e.g., Forristall, 1978; Thornton and Guza, 1983; Sobey *et al.*, 1990; Green, 1994, 1999). In estuaries, it is pertinent to check the Rayleigh assumption as there are few investigations of estuarine wave heights. Although estuarine waves are confined to a narrow period range (due to limited fetch) and might then be expected to be Rayleigh distributed, the sea-state of estuarine waves is choppy, 'confused' and disorganised, unlike ocean swells.

The empirical exceedence probability distribution was calculated using wave data from seven deployments during the Transect Experiment. The empirical exceedence probability distributions are compared with the probability distribution of Rayleigh wave heights:

$$P_R = (H / H_{rms}) = \exp[-(H / H_{rms})^2]$$

The results are presented graphically for each instrument deployment in Figure A7.1. The χ^2 (chi-square) goodness-of-fit test is used to test if the difference between the empirical exceedence and Rayleigh distributions is due to chance alone. The critical value of χ^2 from the chi-square table at the 99% level with 13 degrees of freedom is 4.107 [χ^2 p=0.99, df=16-2-1=13]. The χ^2 test statistic is given as:

$$\chi^2 = \sum_{i=1}^{k} \frac{(O_i - E_i)^2}{E_i}$$

where O_i and E_i are the observed and expected frequencies corresponding to class i, and k is the number of classes. In all cases, the test statistic was less than the tabulated critical value, indicating that there is no significant difference between the empirical and the Rayleigh distributions at the 99% level (Table A7.1). Noted and discussed in section 2.5.1 is the systematic overprediction of frequency of high waves by the Rayleigh distribution. Following Green (1994) the error in calculating H_s was estimated using Tayfun's (1981) N:

$$N = \left[\frac{\pi}{7\sqrt{2}} \frac{\tanh(k_0 \bar{h})}{k_0 \sqrt{2m_0}} \right]$$

where k_0 is the mean apparent wavenumber which is related to ϖ through the linear dispersion relation (Green, 1994). N was evaluated for waves at Wiroa and is displayed in Figure A7.2.

Location		χ^2 test statistic (eqn. 3.23)	Tabulated critical χ^2
W2P	3D-ACM	0.038415	4.107
W2S	Alice	0.021694	4.107
W1G	3D-ACM	0.011716	4.107
W1G*	S4DW	0.017341	4.107
W1H	Alice	0.005786	4.107
W1I	S4A	0.012713	4.107
W2X	S4A	0.023934	4.107

Table A7.1: χ^2 goodness-of-fit test results for the empirical exceedence and Rayleigh distributions.

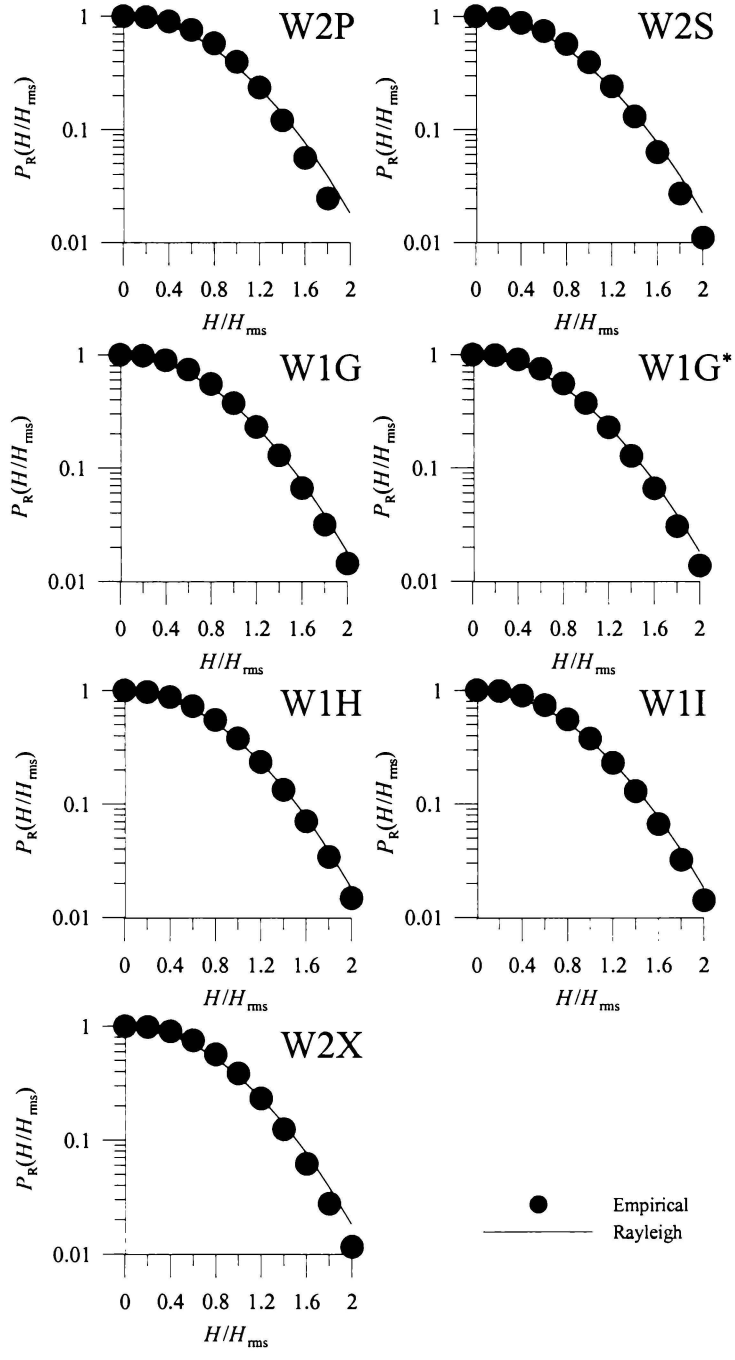

Figure A.41: Empirical exceedence probability and Rayleigh distributions for seven deployments on the Wiroa Intertidal flat. The S4 deployed alongside the 3D-ACM at W1G is indicated as W1G.*

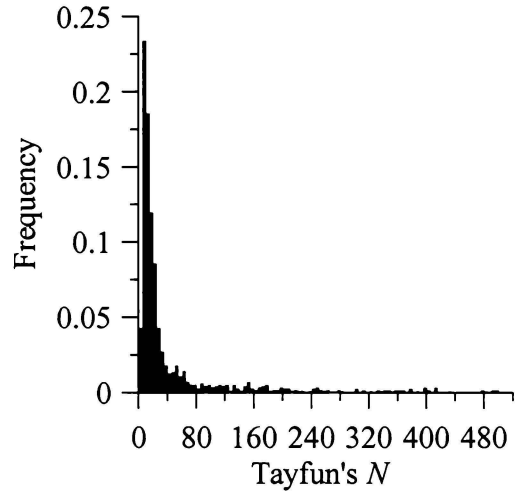

Figure A4.12: Frequency distribution of Tayfun's N for waves at Wiroa Island. Most waves fall in the 10–40 category.

Journal of Coastal Research	(ICS 2000 Proceedings)	334–341	New Zealand

Biofouling of Optical Backscatter Sensors: Prevention and Analytical Correction of Data

T.J. Dolphin†, M.O. Green‡, J.D.J. Radford‡ and K.P. Black†

†Coastal Marine Group
Department of Earth Sciences
University of Waikato
Private Bag 3105
Hamilton, New Zealand

E-mail: t.dolphin@waikato.ac.nz
‡NIWA
National Institute of Water and Atmospheric Research
P.O. Box 11-115
Hamilton, New Zealand

ABSTRACT

DOLPHIN, T.J.; GREEN, M.O.; RADFORD, J.D.J., AND BLACK, K.P., 2001. Biofouling of Optical Backscatter Sensors: Prevention and Analytical Correction of Data. *Journal of Coastal Research, Special Issue 34,* (ICS 2000 New Zealand). ISSN 0749-0208.

Optical backscatter sensors (OBSs) are highly sensitive to the effects of biofouling. In this paper we introduce preventive and corrective measures which deal with the problem. We developed a pneumatic brush which, in a 160-day experiment, was shown to prevent biofouling. The brush is small (1x10 cm), self-contained, requires no/low field maintenance, has good endurance and can easily be adapted for OBS arrays. Data from the clean (brushed) OBS were used along with biofouled data from a second co-located OBS to develop an analytical method for estimating suspended-sediment concentration (SSC) from biofouled OBS data. The method involves correcting for two effects of biofouling, drift (D) and attenuation (A). D is an apparent increase through time in OBS offset, and A is an apparent decrease in sensitivity. Two separate datasets were used to develop and then test the method. Using the first dataset, we estimate D by fitting a cubic spline through clear-water data points. A is then related to D empirically. Using the second dataset we test how accurately the method works. Good results can only be obtained if sufficient clear-water data points are available for estimating D.

ADDITIONAL INDEX WORDS: *Biofouling, optical backscatter sensor, suspended sediment.*

INTRODUCTION

Optical backscatter sensors (OBSs), which are perhaps the most widely used device for measuring suspended-sediment concentration (SSC), operate by transmitting infrared (IR) light into the surrounding water and measuring the amount of light backscattered from particles in suspension. Estimation of SSC from raw OBS data can be problematical for a number of reasons: optical backscatter is a function of both SSC and sediment grain size, with some research having been directed at this problem (e.g., LUDWIG and HANES, 1990; CONNER and DE VISSER, 1992; GREEN and BOON, 1993; BLACK and ROSENBERG, 1994; XU, 1997; BUNT *et al.*, 1999); at high mud concentrations (>10 g/L) OBS response is non-linear (KINEKE and STERNBERG, 1992); at low SSC, OBS response may be related to phytoplankton concentration (SCHOELLHAMER, 1993); and various marine organisms can obscure the transmitted or backscattered light. In regard to the latter, fish, algal slime and encrusting organisms are the primary offenders.

This paper addresses the problem of biofouling of the OBS caused by encrusting organisms such as, in our case, barnacles. Two approaches to solving the problem are taken. In the first, we present an efficient and effective mechanical brush which prevents establishment of encrusting organisms. In the second, we present an analytical method for estimating SSC from OBS data which is contaminated due to biofouling of the OBS sensor.

FIELD SITE

The deployment took place in the Manukau Harbour (Figure 1), which is a large meso-tidal estuary on the west coast of North Island, New Zealand. The harbor is largely infilled and strong tidal currents (>1 m/s) flow along channels which dissect extensive subtidal and intertidal flats. Bed sediments are predominantly fine sands. On the intertidal flats, sediment resuspension is driven by locally generated wind-waves. In the absence of

waves, SSC on the intertidal flat is low (~0–50 mg/L) but during periods of wave activity

Instruments were deployed on the intertidal flat adjacent to and some 800 m offshore from Wiroa Island (Figure 1). The site was inundated by up to 1.2–2.1 m of water for approximately 7 hours each tidal cycle. Measurements were made over a period of 160 days.

METHODS

A small frame with two OBSs (Downing OBS-3), a CR10X datalogger and a DOBIE wave gauge were deployed on the Wiroa Island intertidal flat. The frame consists of a buried base to which CR10X and battery housings were attached, and a 1-m vertical shaft with an 80-cm adjustable horizontal arm to which OBSs were mounted. The OBSs were attached at each end of the adjustable arm (so as to prevent cross-talk), 60 cm above the bed and oriented facing into the expected incident wave field. This orientation was chosen to minimize variations in the suspension that might be caused by the presence of the instrument frame. A DOBIE was mounted on the bed at the base of the vertical shaft.

To prevent colonization of the sensor face by marine organisms, one OBS was fitted with a pneumatic brush (described below); the other was unprotected and experienced biofouling. The OBSs sampled simul-taneously at 4 Hz for 1 minute every 30 minutes. Prior to detailed analysis, out-of-water data points were removed using the tidal record from DOBIE and visual examination of OBS burst means and standard deviations as a guide. The first five seconds of OBS data were also removed to allow for stabilization of the signal at power-up (typically <1 s).

Midway through the experiment, the unprotected OBS was manually serviced to remove barnacles from the sensor face. The two resulting datasets (from experiment start to servicing and from servicing to experiment end), which both comprise a clean time-series (OBS_{clean}) and a biofouled time-series (OBS_{biof}), were used to develop and then test an analytical method for estimating SSC from biofouled OBS data.

Each OBS was laboratory calibrated in a 180-L turbidity tank using local bed sediments (fine sands; mean grain size of 200 μm). The tank comprises a 1.5-m long column with a recirculating pump at the base. Suspended sediment falls down through the water column and is pumped back to the top where it is ejected through four opposing nozzles. SSC in the tank was measured by extracting a sample through a nozzle mounted at the same elevation as the OBS. Samples were then filtered to establish SSC and this was compared to the raw OBS concentrations in excess of 1600 mg/L have been measured (DOLPHIN and GREEN, 1997).

response. Both OBSs responded linearly (r^2=0.99) to increasing SSC over the range 0–1600 mg/L:

$$C = GR \tag{1}$$

where C is suspended-sediment concentration (mg/L), G is gain (mg/[LmV]) and R, the sensor response (mV), is

$$R = R_{obs} - R_0$$

where R_{obs} is the observed sensor response and R_0 is the electronic offset, defined as the OBS output in clear (tap) water.

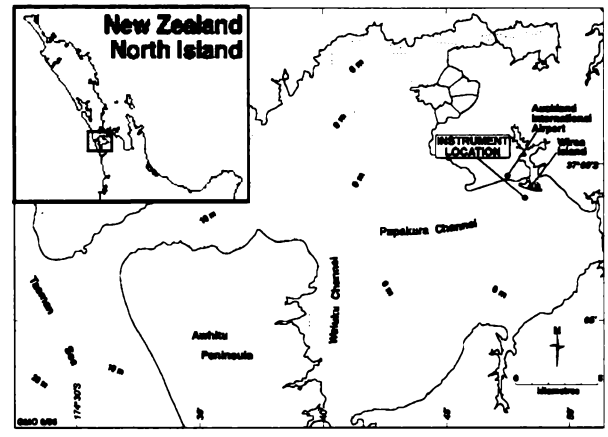

Figure 1. Map of Manukau Harbour showing instrument location.

Water samples collected from the site revealed a discrepancy between the bed sediments used for laboratory calibration (mean size = 200 μm) and the actual material in suspension, which at OBS elevations were mainly silts (mean size = 20 μm). An adjustment to G is required. In laboratory experiments where only glass particles with a constant refractive index were used, CONNER and DE VISSER (1992) show that the OBS gain is 10 times greater for 37-μm particles compared to 106-μm particles. Using natural sediments, similar findings were made by LUDWIG and HANES (1990), although GREEN and BOON (1993), BLACK and ROSENBERG (1994) and XU (1997) report lower gain factors of 5.8–5.9, 1.8 and 4.6–6, respectively. Variation in G may result from differences in the way grain-size is estimated and variations in refractive properties of natural sediments. Using very similar sediments from a nearby site, GREEN *et al.* (1999) showed that the OBS is 10 times more sensitive to silt (10–30 μm) than to fine sand (100–200 μm). Therefore, for the purposes of inverting our field data, we decreased G obtained in the turbidity tank by a factor of 10.

BIOFOULING PREVENTION

OBS data are especially sensitive to contamination caused by organisms adhering to the sensor face. There are several ways of preventing this. An ideal method for preventing biofouling should be self-contained, require no maintenance in the field, outlast the experiment duration and prevent even the initial stages of biofouling so as to yield a completely unfouled record. Various antifoulant coatings have been used, but these may require maintenance in the field (recoating), may only be suitable for short-term experiments and can themselves alter transmission and detection of light as the coating degrades. Furthermore, the OBS-3 manufacturer-recommended antifoulant (TBTA) is illegal in many countries. In comparison, automated mechanical cleaners are self-contained, usually require no maintenance in the field and can provide good-quality data (e.g., BLACK *et al.*, 1994; RIDD and LARCOMBE, 1994). They can operate either by removing fouling material or by preventing it from forming. The latter is preferable because it yields a completely unfouled record and is less likely to cause damage by scraping of debris across the sensor face. Post-deployment removal of encrusting organisms can also damage the sensor which, through removal of the protecting epoxy, can reduce the life-span of the instrument.

To prevent biofouling we designed and deployed a brush similar to those used by BLACK *et al.* (1994) and RIDD and LARCOMBE (1994), but driven by pneumatics. It consists of a soft brush that is swept across the sensor face by a small pneumatic actuator or piston (1x10 cm). The actuator is driven by compressed air sourced from a regulated dive-cylinder and is attached to the OBS by an adjustable bracket. When retracted, the brush is positioned outside of the OBS's field of view, 12 mm from the edge of the sensor. Laboratory tests with and without the mounted brush confirmed that the retracted device was not 'visible' to the OBS. The brushed OBS (OBS_{clean}) was calibrated with the mounted brush in the retracted position. Brushing was controlled by the CR10X (which also recorded OBS data), but could have easily been designed to operate independently of the logging system. With the use of a manifold, the system can also be adapted for boundary-layer OBS arrays (e.g., 5 x OBS-3 in GREEN *et al.*, 1999).

The rate at which biofouling occurs varies with location, season, temperature, nutrient supply and so on. Prevention of biofouling is achieved by using an appropriate brushing frequency for the deployment environment. An important advantage of the shallow-water pneumatic system is that, in extreme biofouling environments, the sensor can be brushed frequently without compromising experiment duration. The soft brush, in combination with frequent brushing, also eliminates the possibility of OBS damage caused by scraping of debris across the OBS face (e.g., RIDD and LARCOMBE, 1994).

In our experiment, OBS_{clean} was brushed at 30-minute intervals, just prior to the start of each burst (although brushing frequency can be more or less frequent than data collection). Over 7700 brush cycles (two sweeps each cycle) were completed during the experiment with minimal wear on the brushing system and no apparent damage to the OBS. Comparison of the two OBSs (Figure 2) near the end of the experiment shows how effective the brush was in preventing biofouling.

The field data are shown in Figure 3. R_{clean} is the burst-averaged output from OBS_{clean} and R_{biof} is the burst-averaged output from OBS_{biof} (where both outputs are adjusted for electronic offset). In the absence of wave activity (i.e., 'clear water') R_{clean} always returned to zero indicating that OBS_{clean} was unfouled and the brush was functioning effectively.

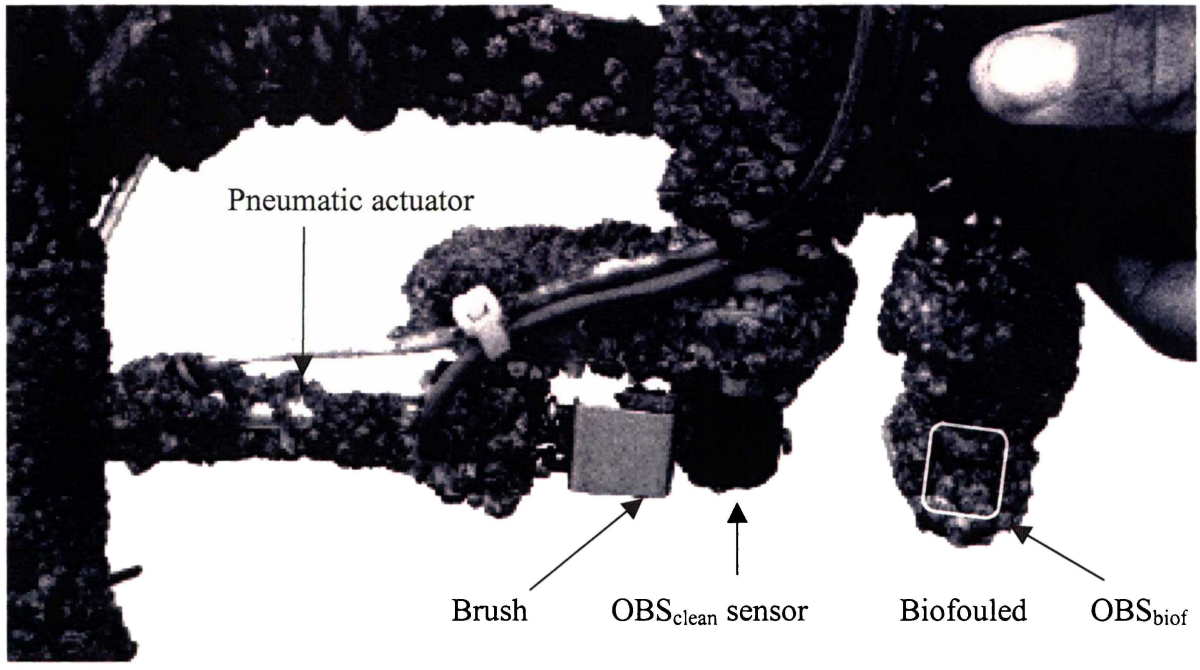

Figure 2. Comparison of brushed (OBS$_{clean}$) and unbrushed (OBS$_{biof}$) sensors following severe biofouling by barnacles (mainly *Eliminus modestus*).

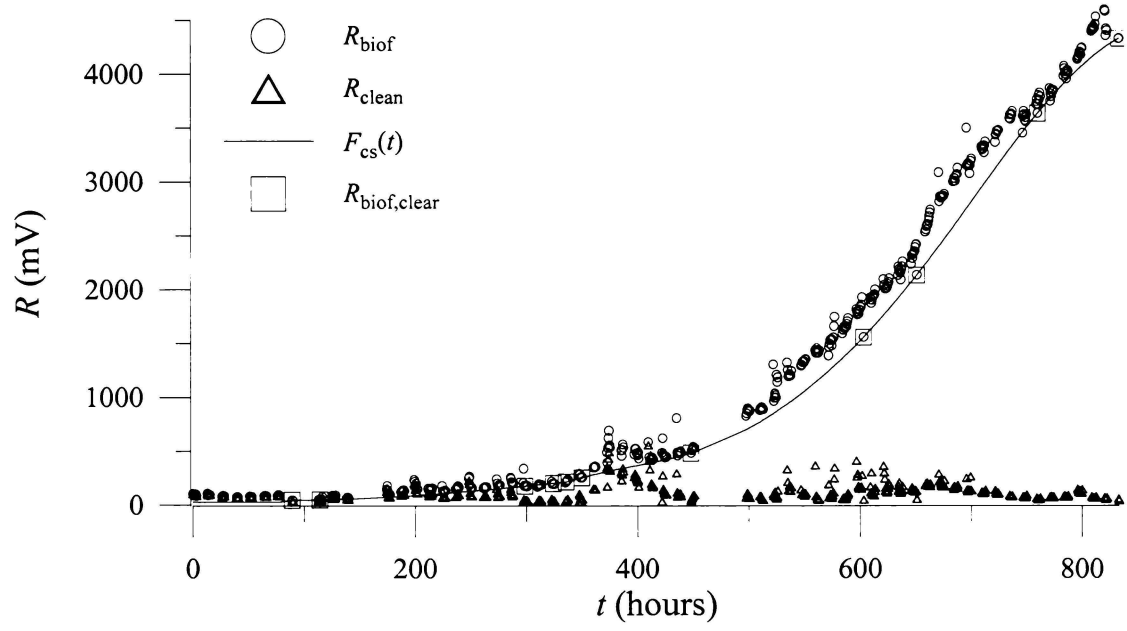

Figure 3. Comparison of biofouled and unfouled data. Square symbols are clear-water OBS$_{biof}$ output (corresponding to near-zero wave activity) used for estimating drift.

ANALYTICAL CORRECTION OF BIOFOULED DATA

We assume that the biofouled component of the signal varies in some systematic way that can be described and corrected for. We hypothesize that the build-up of organisms on the sensor face causes a 'drift' (D) and 'attenuation' (A) of the OBS signal. D is an apparent increase through time in the OBS offset which is due to reflection of IR light from the back of encrusting organisms. A is an apparent decrease in the sensitivity (i.e., voltage output per mg/L of suspended sediment, which is the inverse of gain, G) which results from reduced transmission of IR light out to the sampling volume and reduction in penetration of backscattered light back to the detectors (Figure 4). For the biofouled sensor, then, SSC is related to R by :

$$C = G\left(\frac{R-D}{A}\right) \tag{2}$$

Therefore, if D and A are known, then Eq. 2 can be used to estimate accurately SSC from the biofouled sensor.

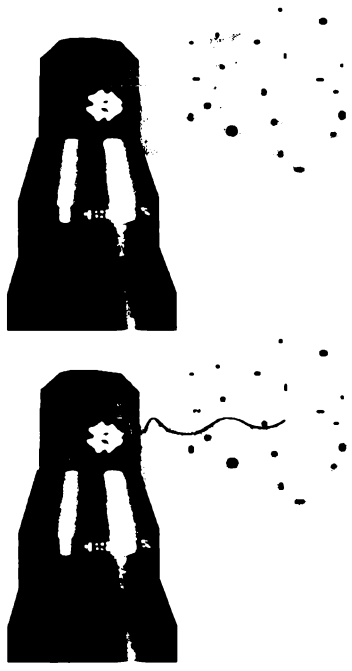

Figure 4. An encrusting life-form obscures the OBS IR-emitting-diode and photoreceptors, which results in attenuation of the signal, for two reasons. Firstly, transmission out to the sampling volume is obscured. Secondly, reception is reduced as backscattered light is blocked by the organism's exoskeleton.

In the following, we use the first dataset to evaluate D and A. We then use the second dataset to test how well Eq. 2 performs in estimating SSC from biofouled OBS data.

Evaluation of D and A (first dataset)

Drift due to biofouling has been modeled as an exponential trend (e.g., RIDD and LARCOMBE, 1994; BELL *et al.*, 1997). However, biofouling may not be a continuous, steady process as implied by an assumed exponential drift. To obtain a more accurate model of drift, we fitted a cubic spline $F_{cs}(t)$ to the variation through time (t) of $R_{biof,clear}$, which is the burst-averaged output from OBS_{biof} for bursts when the water was essentially clear (i.e., $C \approx 0$ mg/L). Since suspension events at the field site are driven by waves (GREEN *et al.*, 1997), clear-water bursts correspond to times of zero or near-zero wave activity. Eleven clear-water bursts were identified from DOBIE wave data in the first dataset and are shown in Figure 3 together with $F_{cs}(t)$. These bursts were used to evaluate D because in clear water all backscattered light must be due to reflection from encrusting organisms.

Attenuation is evaluated as:

$$A = \frac{(R_{biof} - D)}{R'_{biof}} \tag{3}$$

where D is evaluated from the cubic spline previously described and R_{biof} is the burst-averaged output from OBS_{biof}. The term R'_{biof} is the burst-averaged output that should have been obtained had OBS_{biof} not been biofouled:

$$R'_{biof} = \frac{(G_{clean} R_{clean})}{G_{biof}} \tag{4}$$

$G_{clean}R_{clean}$ is the true SSC as measured by OBS_{clean} (Eq. 1) and G_{biof} is the instrument gain for OBS_{biof}.

A is plotted against D in Figure 5, which reveals the following correlation over the range $0 < D < 500$ mV:

$$A = G_A D + O_A \tag{5}$$

where G_A is -2.03×10^{-3} (1/mV) and O_A is forced to be 1 ($r^2 = 0.80$; n=115). Eq. 5 was fitted only to data from bursts for which $C_{clean} > 50$ mg/L (see Figure 5), which was meant to ensure that there was sufficient signal to raise estimates of A above some base noise level. For $D > 500$ mV there is no discernible relationship between D and A.

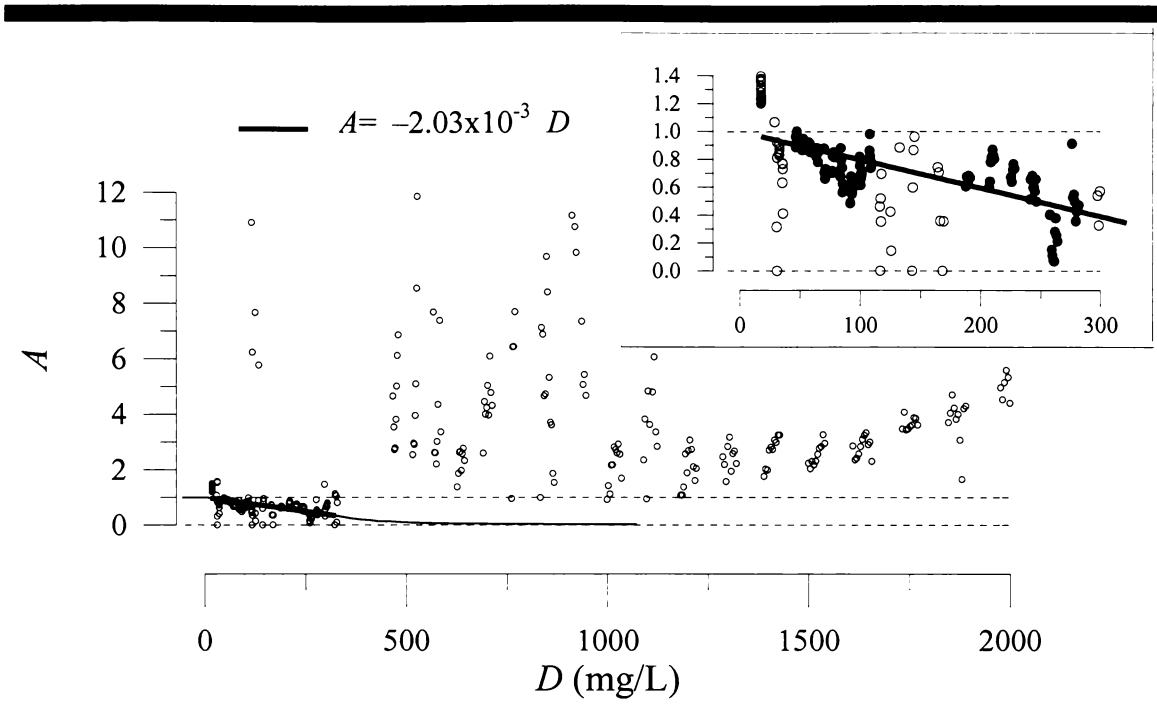

Figure 5. Scatterplot of D and A. The heavy line is Eq. 5, which was fitted to bursts for which $C_{clean} > 50$ mg/L (solid symbols) over the range $0 < D < 500$ mV. The thin line shows how A should change for $D > 500$ mV.

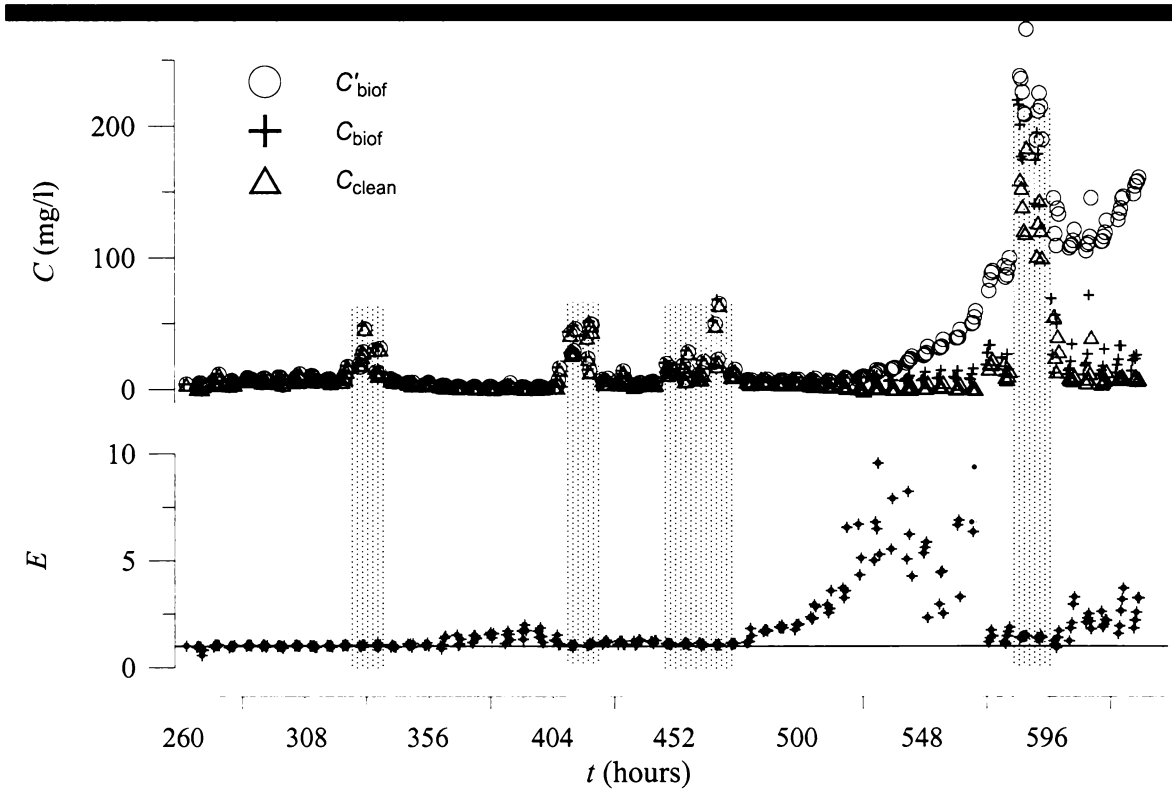

Figure 6. Estimates of SSC, second dataset. Stippled patches highlight suspension events.

Test of Equation 2 (second dataset)

To test Eq. 2, we used data from the second dataset (i.e., from servicing to end of experiment) to calculate and compare C_{biof} (i.e., SSC estimated from OBS_{biof}, corrected for the effects of biofouling) with C_{clean} (i.e., SSC estimated from OBS_{clean}).

C_{biof} was estimated using Eq. 2, with D and A as described previously. C_{clean} was estimated using Eq. 1. C_{biof} and C_{clean} are compared in Figure 6.

C_{clean} is the true SSC, or at least the best estimate of the true SSC. Therefore, if D and A perfectly correct for biofouling, then $C_{biof}/C_{clean} = 1$. The relative error in C_{biof} is shown in Figure 6, defined as:

$$E = \frac{C_{biof}}{C_{clean}} \tag{6}$$

To give an indication of the magnitude of the biofouling correction, we also show in Figure 6 C'_{biof}:

$$C'_{biof} = G_{biof} R_{biof} \tag{7}$$

which is the estimate of SSC that would have been obtained had no correction for biofouling been made.

DISCUSSION

Colonization by encrusting organisms on the OBS was effectively prohibited by our pneumatic brush, which swept the sensor face twice every 30 minutes. The result was a clean record of OBS data, from which we were able to estimate SSC. The brush is intended as a biofouling prevention device, the success of which depends on an appropriate brushing frequency for the deployment environment. In the event that biofouling initiates between brushing cycles, only weakly attached organisms will be dislodged. In comparison, semi-rigid wiper blades can remove moderately-well adhered organisms, thereby requiring a lower cleaning frequency than their softer-brush counterparts. However, the trade-off for a lowered cleaning frequency is occasional data contamination due to biofouling (although we can correct for this, to a point) and potential damage as sharp skeletal materials are dragged across the sensor face (e.g., RIDD and LARCOMBE, 1994). In any case, a preventive non-damaging device will always be preferential.

When a biofouling preventive measure has failed or is unavailable, Eq. 2 can be used to estimate SSC from biofouled data if D and A are known. Figure 6 shows that Eq. 2, with $F_{cs}(t)$ fitted to clear-water data points and then interpolated to evaluate D, and Eq. 5 used for A, provided good estimates of SSC from the biofouled OBS data. The error was low when SSC rose above the OBS response threshold (stippled patches). When SSC was below the OBS response threshold, noise in the two signals yielded some large, but meaningless, errors (see E in Figure 6).

The success of Eq. 2 depends upon the accuracy of D. To estimate D, a function is fitted to only those bursts where backscatter is low (SSC $\approx$ 0; R = D). Exponential, power, cubic-spline and piece-wise linear functions for D are shown in Figure 7 for the present dataset. Exponential and power functions are not satisfactory, primarily because they do not pass through all clear-water data. We use here a cubic spline in preference to a piece-wise linear fit because it takes into account the recent history of the drift. This seems reasonable because growth rates are more likely to change smoothly rather than abruptly, which would otherwise be implied by a piece-wise linear fit. The cubic spline interpolations of D gave good results, generally slightly under-estimating SSC as D increases, which is the sign of an increasingly attenuated signal.

Attenuation was hypothesized to be a function of drift, which seems reasonable as both are manifestations of the effect biofouling has on OBS output. However, as A can only be estimated during suspension events (when the true OBS signal is high), the range of data points available for estimating A was limited. Whilst there is some scatter in these points the correlation coefficient indicates a strong relationship (r^2=0.8). Eq. 5 may be specific to the environment and type of biofouling (barnacles). For application of Eq. 2 elsewhere, a pilot experiment could be conducted to derive an empirical equation for A that is suited to local conditions. This requires good estimates of SSC (either water samples or OBS_{clean}) in addition to OBS_{biof}. If that is not possible, and the biofouling is of a similar nature, it may be possible to use Eq. 5 with the coefficients used herein.

SSC estimates made using Eq. 2 should be constrained to the domain of Eq. 5, which terminates at $D \sim 500$ mV or 10% of the OBS maximum linear response (Figure 5). Beyond this point the true attenuation function is not adequately described by Eq. 5, which should approach zero asymptotically (Figure 5). Also, as $A \rightarrow 0$ and where R is low, care must be taken to avoid multiplication of system noise. Further research, perhaps focused on controlled laboratory experiments, is required to refine the attenuation function.

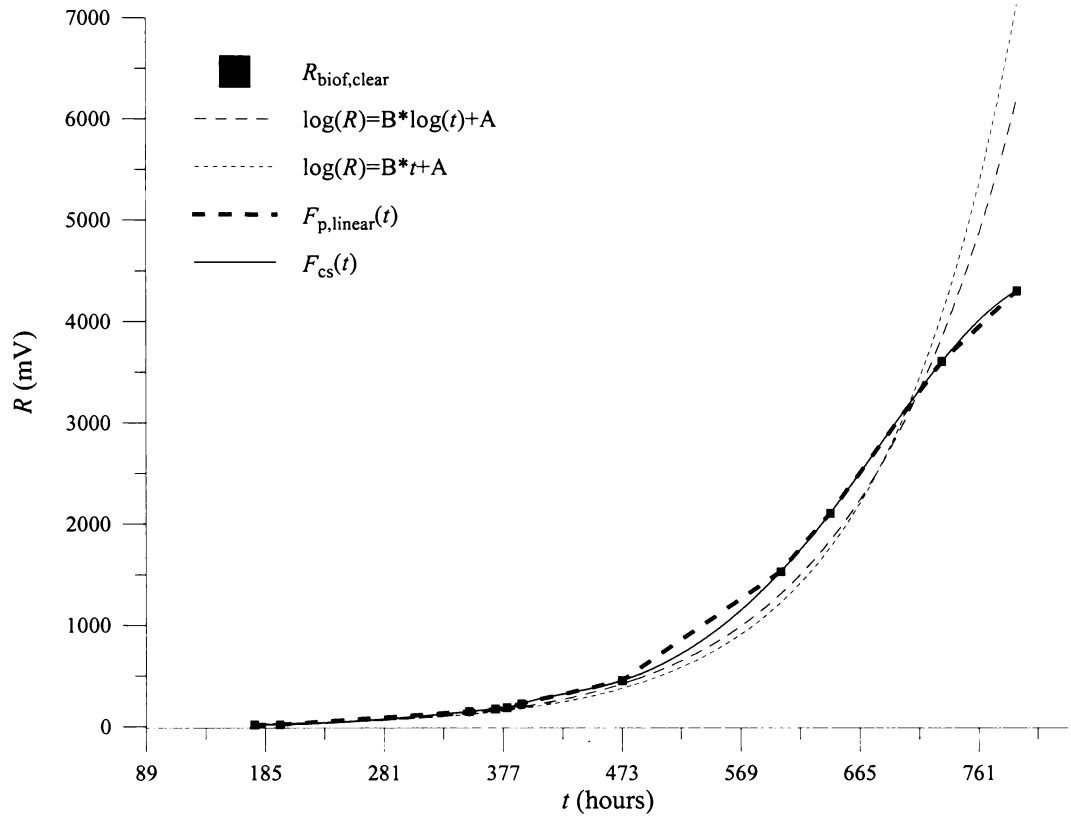

Figure 7. Estimates of D fitted to clear water data. $F_{p,linear}(t)$ and $F_{cs}(t)$ are piece-wise linear and cubic spline functions fitted to $R_{biof,clean}$ versus t.

CONCLUSIONS

An effective method of OBS biofouling prevention, using soft brushes and pneumatics, is presented. In Manukau Harbour, where biofouling can ruin OBS data in a matter of days, we found that a brushing interval of 30 minutes was sufficient to prevent grief. Biofouling preventive brushes extend the useful record length and result in reliable data.

SSC can be estimated from biofouled data using Eq. 2. D (the apparent increase through time in the OBS offset) is found by fitting a cubic spline to clear-water data points. If clear-water data points are not available then the method cannot be used. A (the apparent decrease in the sensitivity) is found to be related to D, although this relationship may need to be redefined for the local biofouling conditions. Our data show that the method cannot be applied when $D > 10\%$ of the instrument's maximum linear response.

ACKNOWLEDGEMENTS

The authors would like to acknowledge the Department of Earth Sciences, University of Waikato and the New Zealand Foundation for Research, Science and Technology, contract C01618 for funding this project. For their voluntary assistance in the field we also thank Earth Sciences students Hamish Saunders, Bronwen Riddle, Adam Paterson and Jens Kruger.

LITERATURE CITED

BELL, R.G.; HUME, T.M.; DOLPHIN, T.J.; GREEN, M.O., and WALTERS, R.A., 1997. Characterisation of physical environmental factors on an intertidal sandflat, Manukau Harbour, New Zealand. *Journal of Experimental Marine Biology and Ecology,* 216, 11–31.

BLACK, K.P. and ROSENBERG, M.A., 1994. Suspended sand measurements in a turbulent environment: field comparison of optical and sampling techniques. *Coastal Engineering*, 24, 137–150.

BLACK, K.P.; HATTON, D.; TURNBULL, J., and YOU, B., 1994. Turbidity and light level monitoring in seagrass beds at Avalon and Clifton Springs. *Report for Marine Science and Ecology, Maunsell Pty Ltd and the Port of Geelong Authority*. Victorian Institute of Marine Sciences, November, 1994. 44 p.

BUNT, J.A.C.; LARCOMBE, P., and JAGO, C.F., 1999. Quantifying the response of optical backscatter devices and transmissometers to variations in suspended particulate matter. *Continental Shelf Research,* 19, 1199–1220.

CONNER, C.S. and DE VISSER, A.M., 1992. A laboratory investigation of particle-size effects on an optical backscatter sensor. *Marine Geology,* 108, 151–159.

DOLPHIN, T.J. and GREEN, M.O., 1997. Sediment dynamics of an estuarine "Turbid Fringe". *Proceedings of Pacific Coasts and Ports '97 – 13th Australasian Coastal and Ocean Engineering Conference and 6th Australasian Port and Harbour Conference,* (Christchurch, New Zealand), Vol.1, pp. 113–118.

GREEN, M.O.; BLACK, K.P., and AMOS, C.L., 1997. Control of estuarine sediment dynamics by interactions between currents and waves at several scales. *Marine Geology,* 144, 97–116.

GREEN, M.O.; DOLPHIN, T.J.; SWALES, A., and VINCENT, C.E., 1999. Transport of mixed-size sediments in a tidal channel. *Proceedings Coastal Sediments '99* (ASCE), (New York, U.S.A.),Vol 1, pp. 644–658.

GREEN, M.O. and BOON, J.D., 1993. The measurement of constituent concentrations in nonhomogenous sediment suspensions using optical backscatter sensors. *Marine Geology,* 110, 73–81. KINEKE, G.C. and STERNBERG, R.W., 1992. Measure-ments of high-concentration suspended sediments using the optical backscatter sensor. *Marine Geology,* 108, 253–258.

LUDWIG, K.A. and HANES, D.M., 1990. A laboratory evaluation of optical backscatterance suspended-solids sensors exposed to sand mud mixtures. *Marine Geology,* 94, 173–179.

RIDD, P. and LARCOMBE, P., 1994. Biofouling control for optical backscatter suspended sediment sensors. *Marine Geology,* 116, 255–258.

SCHOELLHAMER, D.H., 1993. Biological interference of optical backscatterance sensors in Tampa Bay, Florida. *Marine Geology*, 110, 303–313.

XU, J.P., 1997. Converting near-bottom OBS measure-ments into suspended sediment concentrations. *Geo-Marine Letters*, 17, 154–161.

Appendix IX: $q_{sand,wc}$ and $q''_{sand,wc}$ scenarios (enlarged diagrams from Figure 6.5)

Tidally modulated fetch, mild storm, symmetric tide

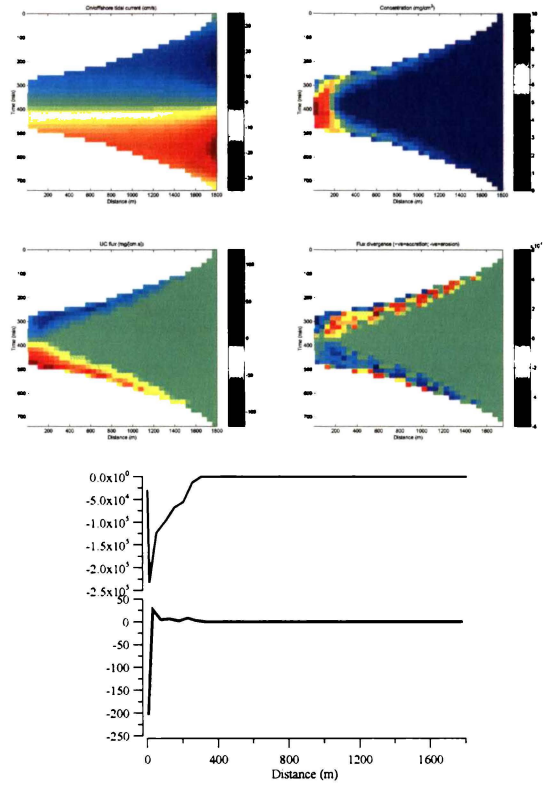

Tidally modulated fetch, major storm, symmetric tide

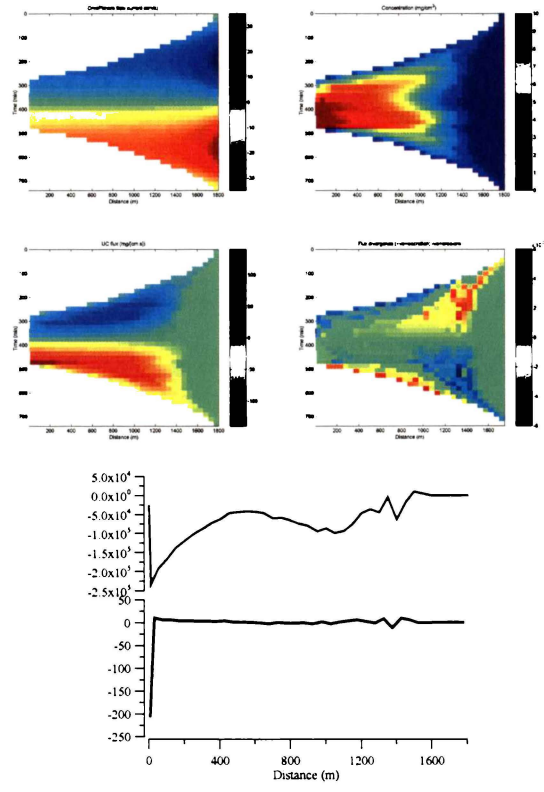

Constant fetch, mild storm, symmetric tide

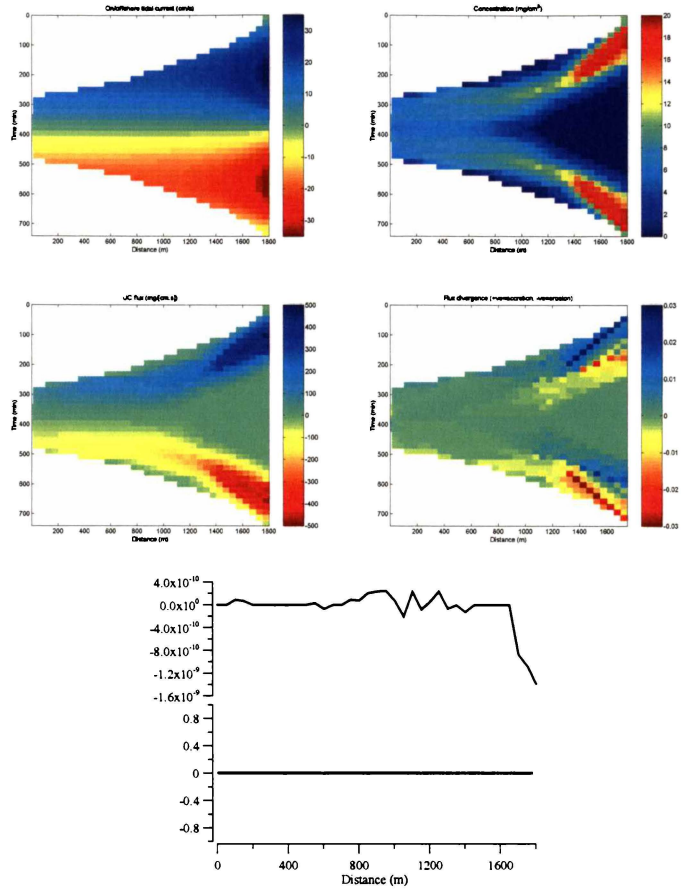

Constant fetch, major storm, symmetric tide

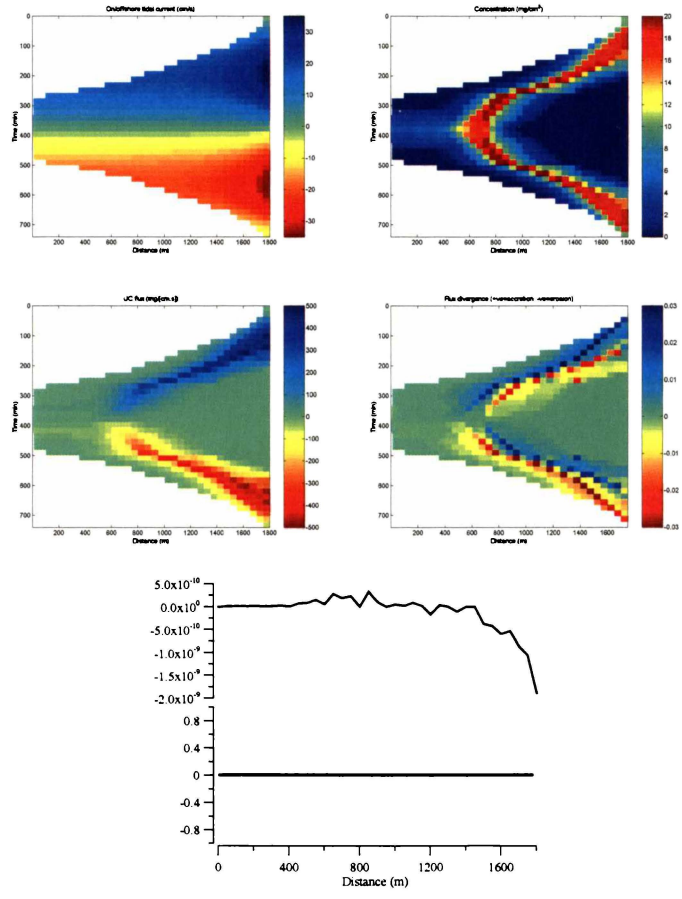

Tidally modulated fetch, mild storm, flood dominant

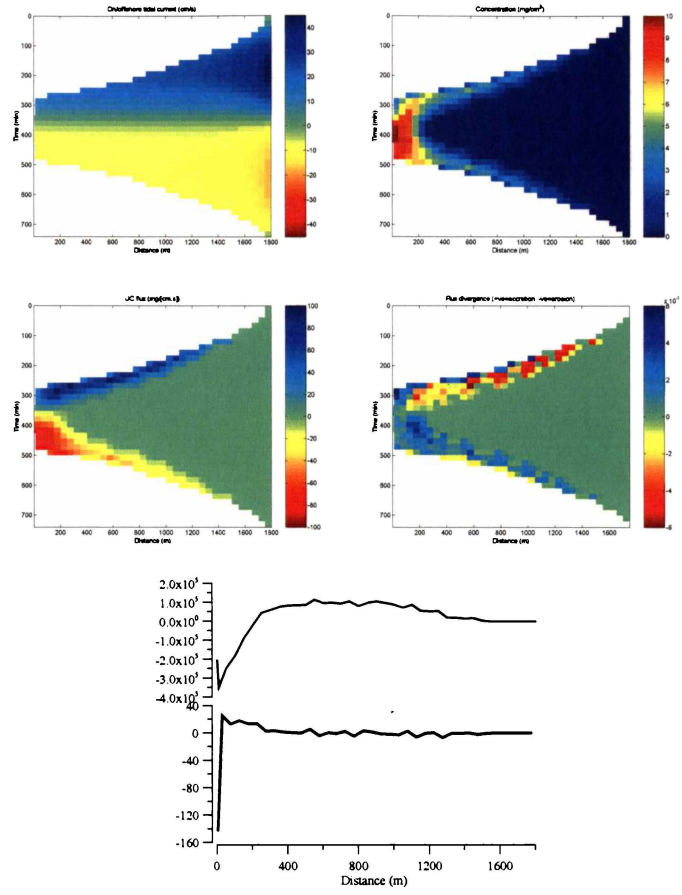

Tidally modulated fetch, major storm, flood dominant

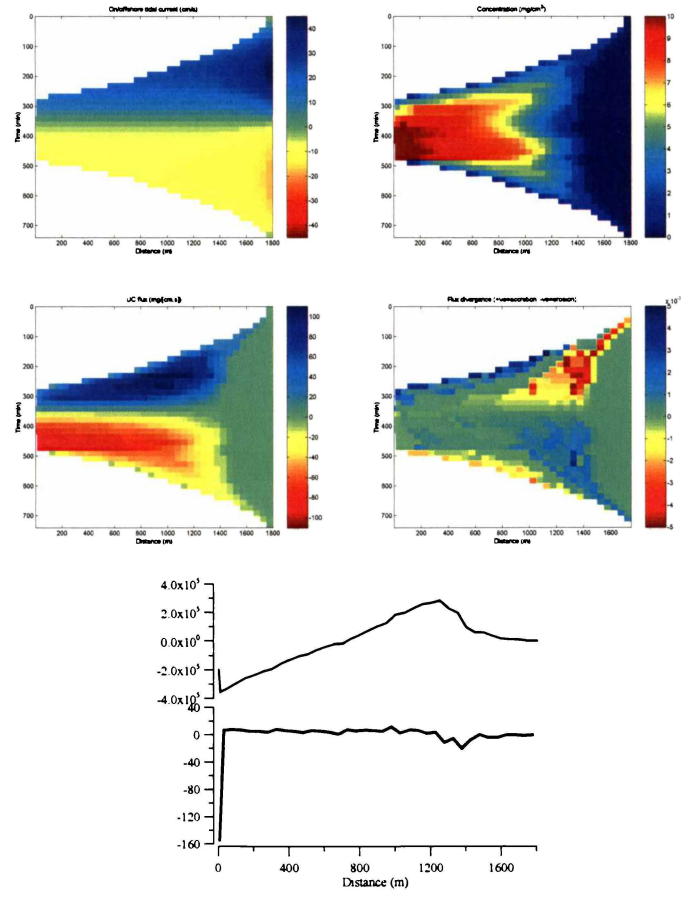

Constant fetch, mild storm, flood dominant

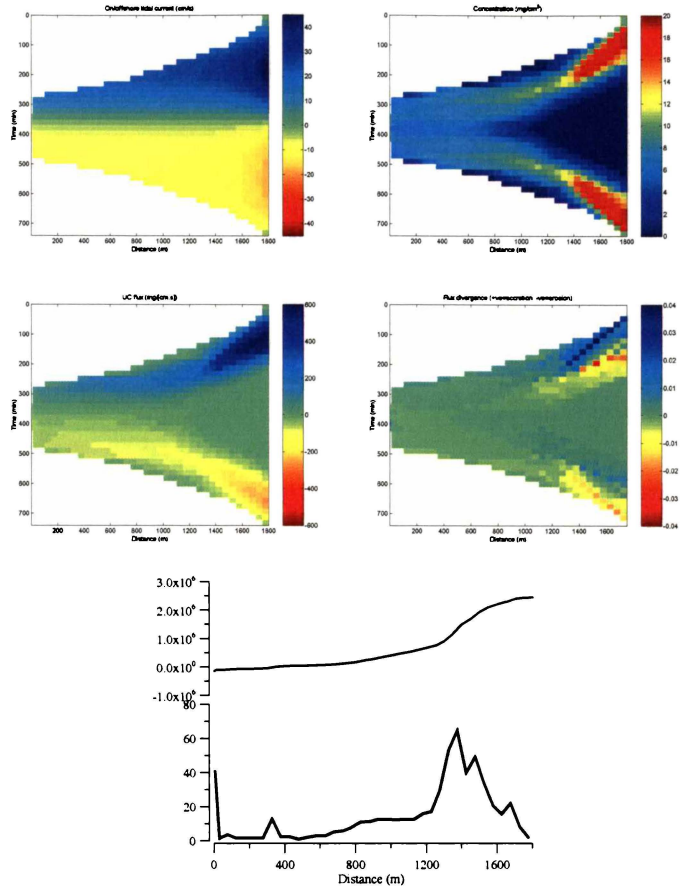

Constant fetch, major storm, flood dominant

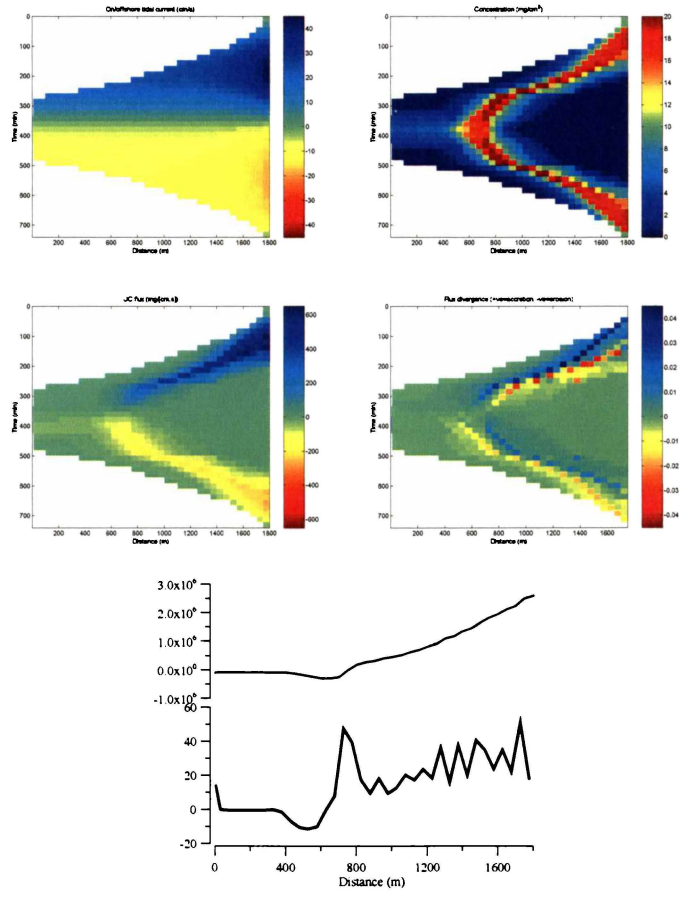

Tidally modulated fetch, mild storm, ebb dominant

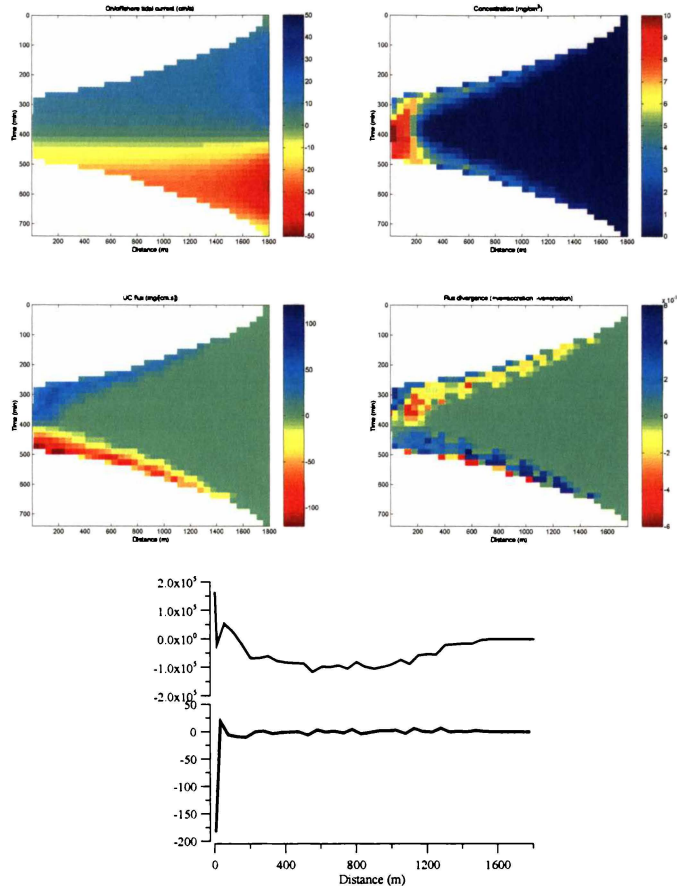

Tidally modulated fetch, major storm, ebb dominant

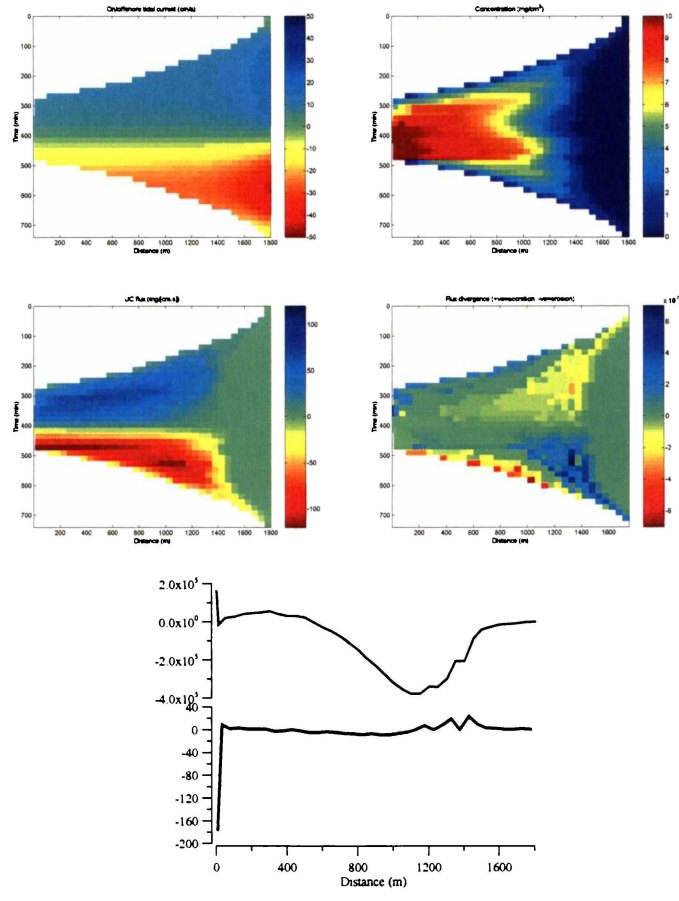

Constant fetch, mild storm, ebb dominant

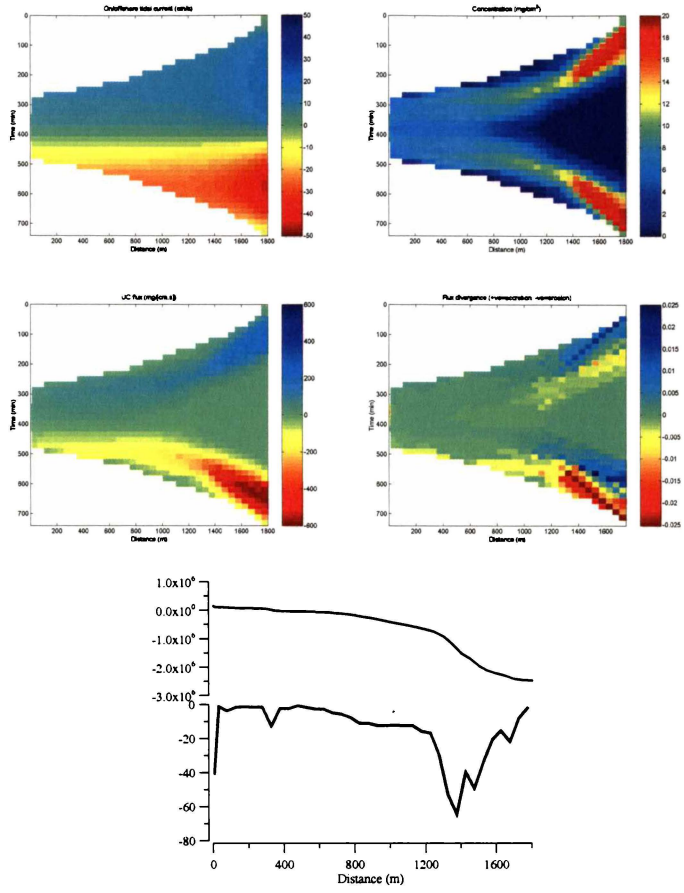

Constant fetch, major storm, ebb dominant

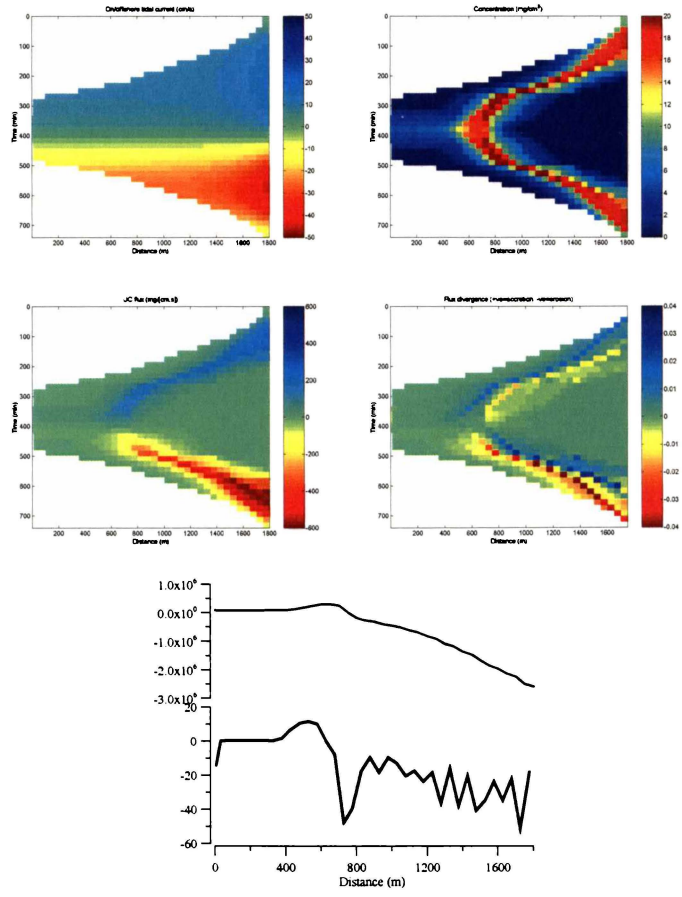

Tidally modulated fetch, mild storm, ebb drain

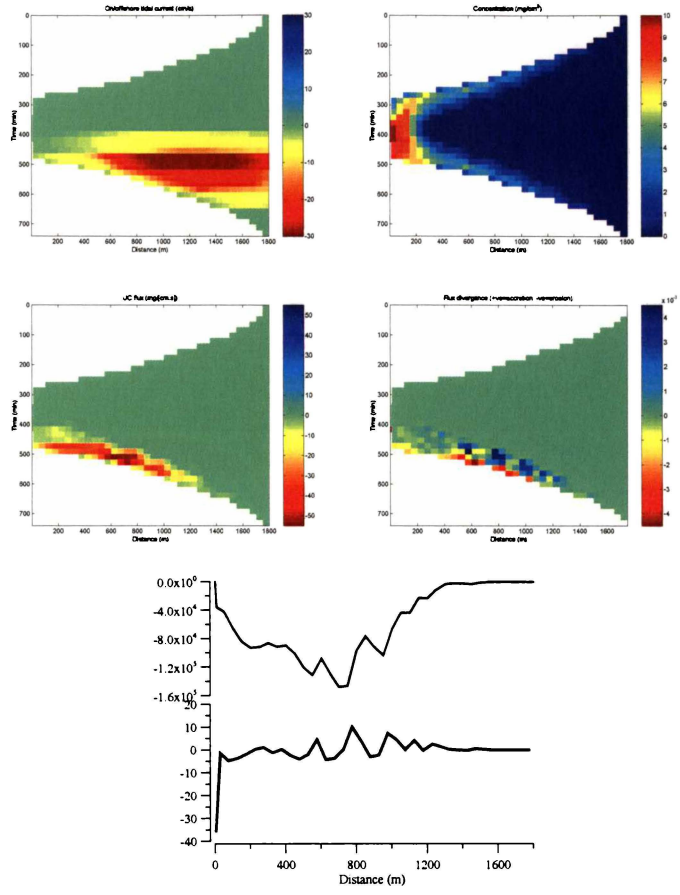

Tidally modulated fetch, major storm, ebb drain

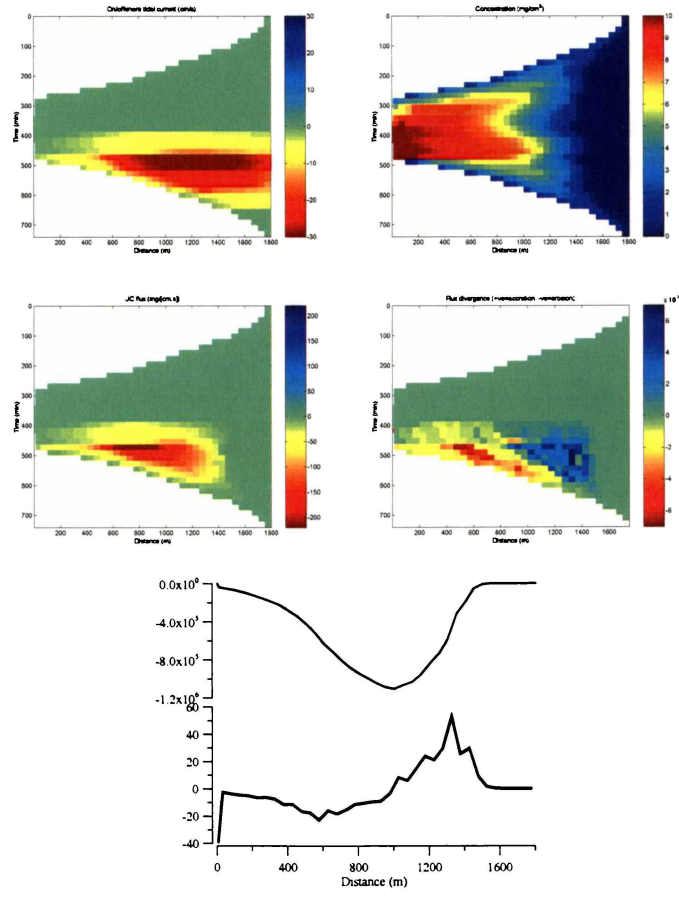

Constant fetch, mild storm, ebb drain

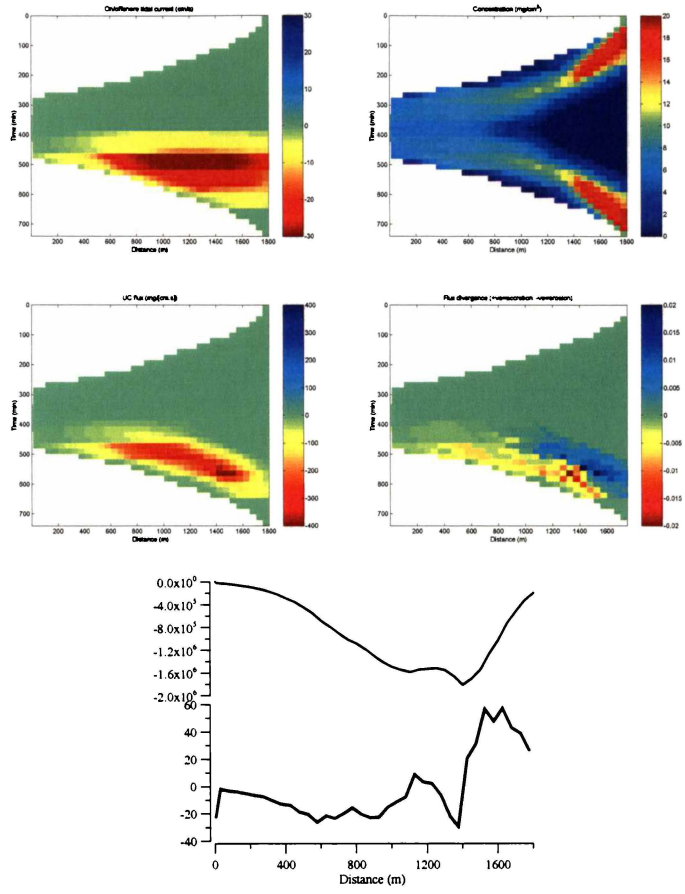

Constant fetch, major storm, ebb drain

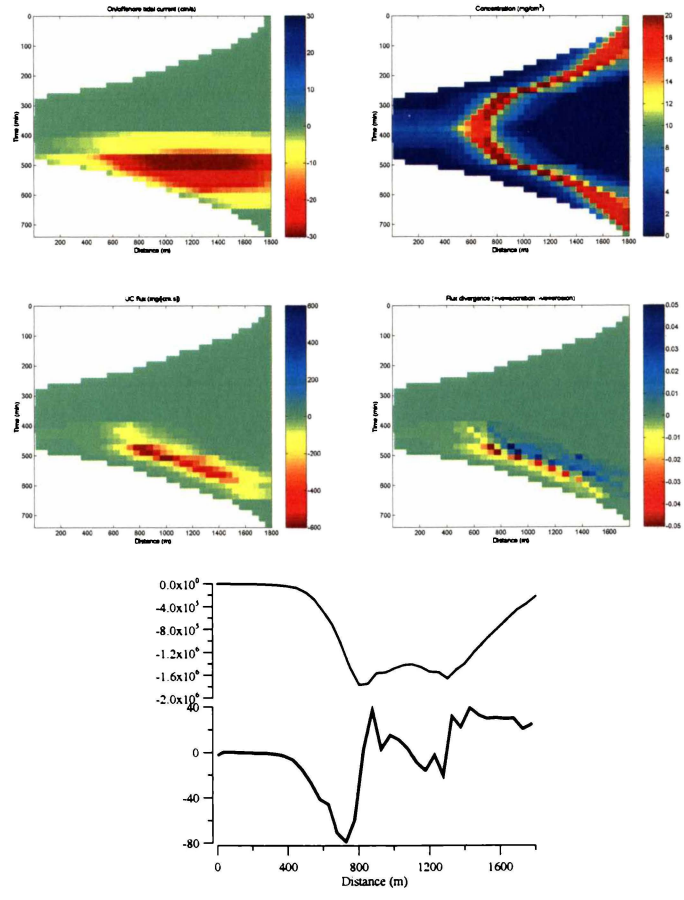

Tidally modulated fetch, mild storm, flood pulse

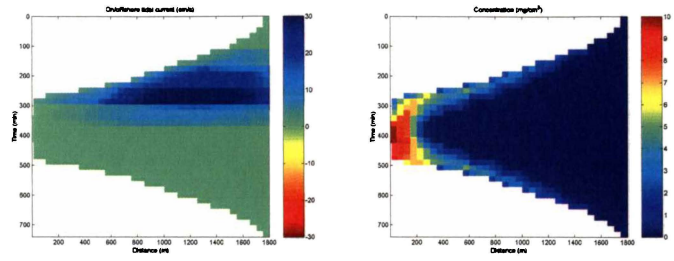

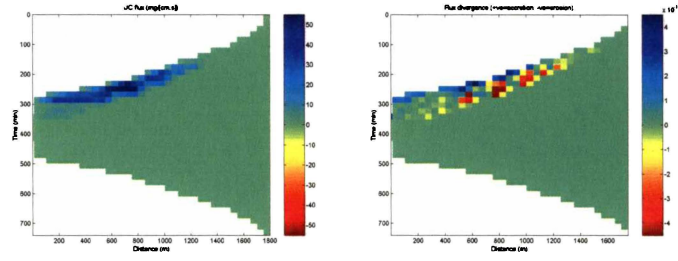

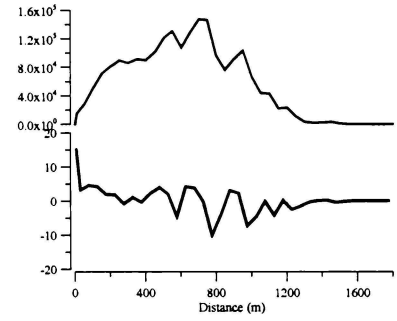

Tidally modulated fetch, major storm, flood pulse

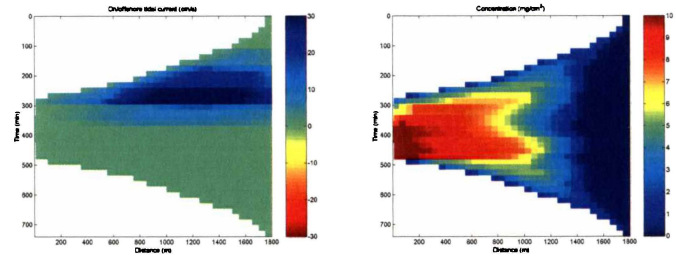

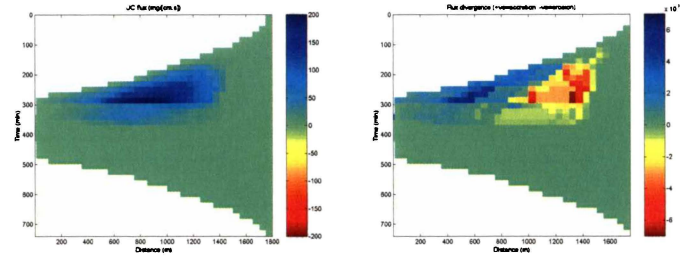

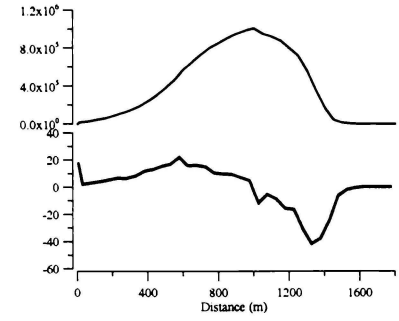

Constant fetch, mild storm, flood pulse

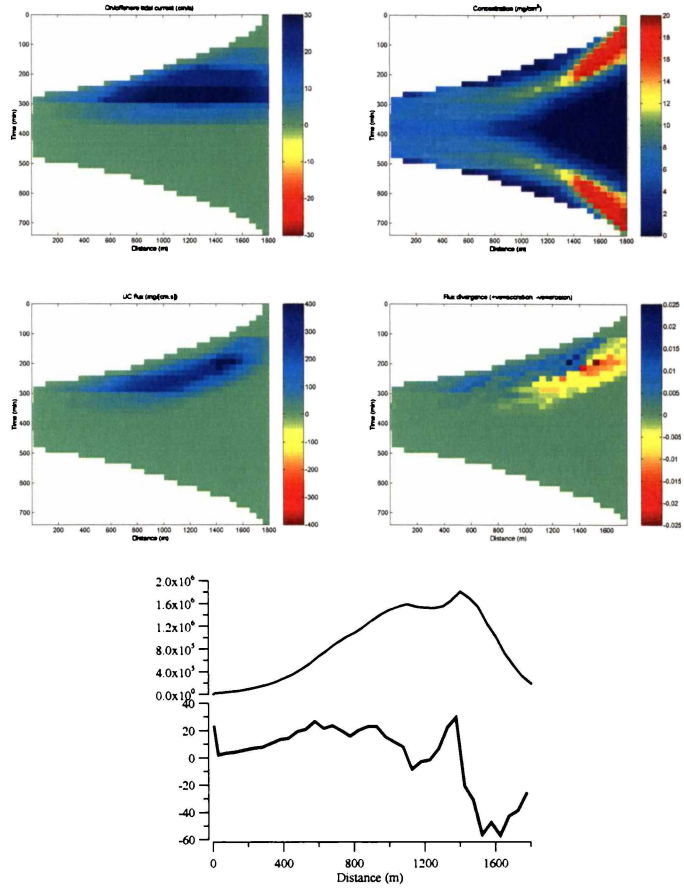

Constant fetch, major storm, flood pulse